On the Atomistic Simulation Approach Towards the Structural Stability of the ZnS Nanoparticles

by

Mohammad Khalkhali

A thesis submitted in partial fulfillment of the requirements for the degree of

Doctor of Philosophy

in

Materials Engineering

Department of Chemical and Materials Engineering

University of Alberta

Abstract

Recently, ZnS quantum dots have attracted a lot of attention since they can be a suitable alternative for cadmium-based quantum dots, which are known to be highly carcinogenic for living systems. Suitable optoelectronic properties and non-toxic nature of ZnS quantum dots capacitate exiting applications for these nanomaterials especially in the field of biomedical imaging. The ability to tune the optoelectronic properties of quantum dots based solely on size of these nanoparticles, which is due to the quantum confinement effect, has raised significant interest both in experimental and computational studies. Nevertheless, the structural stability of nanocrystalline ZnS seems to be a challenging issue since they potentially prone to autonomous structural evolutions in ambient conditions. Thus, it is essential to build an understanding about governing factors controlling structural changes of ZnS nanoparticle before they can be safely implemented, especially for *in vivo* applications.

Using the molecular dynamics technique, we have studied the structural evolution of ZnS nanoparticles at bare and hydrated states. Accuracy of molecular dynamics simulation highly depends on the reliability of the empirical potential it uses. Although multiple empirical potentials have been suggested for ZnS, there was no comprehensive study on comparing the performance of these potentials. Hence, this study started with a through review of available empirical potentials of ZnS in literature. The performance of each potential is tested through comparing the ZnS properties calculated using empirical potentials with experimental or higher level first principle calculation results. Based on the obtained results and the nature of our study which is focused on the noncrystalline ZnS, we chose the proper potential.

The study of the structural evolution of 1 to 5 nm freestanding ZnS nanoparticles in vacuum revealed that relaxed configurations of bare ZnS nanoparticles larger than 3 nm consist of three regions: a) a crystalline core, b) a distorted network of 4-coordinated atoms surrounding the crystalline core, and c) a surface structure entirely made of interconnected

3-coordinated atoms. Decreasing the size of the ZnS nanoparticle to 2 nm causes the crystalline core to disappear. Further reducing the size makes all of the atoms to become 3-coordinated and adopt a bubble-like structure. The simulation results also showed that polarity of nanoparticles is also affected by their structural evolutions. The non-polar ideal initial structures change to polar structures after relaxation at 300 K. For NPs smaller than 3 nm, where surface structure is predominant, magnitude of dipole moment of zinc-blende and wurtzite nanoparticles are similar due to the similarity of their surface structures. Increasing the size makes the crystalline core dominant so, dipole moments converge to the bulk values. The bulk wurtzite structure at 300 K shows a natural dipole moment of 0.3855 D per ZnS along the unit cell c direction because of the slight C_{3v}-distortion of the elementary ZnS tetrahedron. On the other hand, zinc-blende lattice does not have a polar nature due to the T_d symmetry. As a result, increasing the size makes bare zinc-blende and wurtzite nanoparticles less and more polar, respectively.

Structural analyses of ZnS nanoparticle in water showed that the 3-phase structure of bare nanoparticles is not formed in the hydrated state. Bulk of hydrated nanoparticles has more crystalline structure, however, the inhomogeneity in their surface relaxation makes them more polar comparing to bare nanoparticles. This inhomogeneity is more severe in hydrated wurtzite nanoparticles, causing them to show larger dipole moments. Analyzing the structure of water in the first hydration shell of the surface atoms show that water is mainly adsorb to the nanoparticles' surface through Zn-O interaction. This interaction causes the structure of water in the first hydration shell to be discontinuous and positions of water molecules have the same pattern as positions of Zn atoms on the surface of nanoparticles. Long residence time of water molecules in the first hydration shell of surface Zn atoms, can affect the interaction of nanoparticle with other nanoparticles and the arouse solution.

Preface

Chapter 3 of this thesis was published as **M. Khalkhali, Q. Liu and H. Zhang**, "**A comparison of different empirical potentials in ZnS**", *Modeling Simul. Mater. Sci. Eng.*, vol. 22 (2014), 085014 (22pp). I was responsible for the data collection and analysis as well as the manuscript composition. Chapter 4 of this thesis has been accepted for publication as **M. Khalkhali, H. Zeng, Q. Liu and H. Zhang**, "**A size-dependent structural evolution of ZnS nanoparticles**", *Sci. Rep.* 5, 14267 (2015). I was responsible for the data collection and analysis as well as the manuscript composition. Chapter 5 of this thesis has been prepared for publication as **M. Khalkhali, H. Zeng, Q. Liu and H. Zhang**, "**The structural evolutions of ZnS nanoparticles in hydrated and bare states**". I was responsible for the data collection and analysis as well as the manuscript composition. The paper represented in Appendix D was published as **H. Zhang, M. Khalkhali, Q. Liu, and J. F. Douglas**, "**String-like Cooperative Motion in Homogeneous Melting**", *J. Chem. Phys.*, 138, 12A538 (2013). I was partially responsible for the data collection and analysis. In all the aforementioned publications Dr. Hao Zhang contributed to manuscript composition and edits and Dr. Qingxia Liu contributed to revisions. Dr. Hongbo Zeng contributed to revisions of corresponding manuscripts of Chapter 4 and 5.

To my parents, for all the sacrifices they made to make my life and my accomplishments, including this thesis, possible.

Acknowledgements

I would like to express my appreciation to my supervisor **Dr. Hao Zhang** whose passionate support gave me the freedom to develop my ideas. I would like to thank **Dr. Qingxia Liu** and **Dr. Hongbo Zeng** as well, for all of their supports during this study. I also need to thank my dear friends **Dr. Abolfazl Noorjahan**, **Dr. Ata Kamyani**, and **Dr. Pouyan Motamedi** for all the constructive scientific discussions, help and support they provided during my PhD studies. I would also like to acknowledge Financial supports from the **Natural Sciences and Engineering Research Council of Canada (NSERC-CRD)**, **The Canadian Centre for Clean Coal/Carbon and Mineral Processing Technologies (C^5MPT)**, and **Teck Metals Ltd**. This research was enabled in part by support provided by **WestGrid (www.westgrid.ca)** and **Compute Canada Calcul Canada (www.computecanada.ca)**, which are funded in part by the **Canada Foundation for Innovation**, **Alberta Innovation** and **Science, BC Advanced Education**, and the participating research institutions.

Contents

List of Figures

List of Tables

Chapter 1

Introduction

It might be an after-dinner lecture in 1959 by Richard Feynman (1918 - 1988), "There's Plenty of Room at the Bottom ", which triggered an inspiration that has led to the rapidly developing field of nanotechnology [18]. Although some have questioned the degree to which Feynman influenced the rise of nanotechnology, it is without a doubt that the scientific world has traveled toward Feynman's vision of manipulating and controlling things at the atomic scale in the last 60 years and still has far to go. Probably the most important product of the fast developing field of nanotechnology are nanomaterials. In principle, nanomaterials are a new class of materials with one, two or three external in the nano-domain dimensions (1-100 nm). According to this definition, nanomaterials can be categorized into three shapes: nanoparticles (NPs) which have their three dimensions in the nanoscale, nanoplates which have one nano-sized dimension, and nanowires, nano-objects with two nano-sized dimensions and the third dimension being significantly longer [19]. In a different terminology, nanoparticles, nanowires and nanoplates are called zero, one and two dimensional nanomaterials. Over the past 50 years, the rapid growth of the nanotechnology has enabled us to fabricate nanomaterials in variety of shapes and sizes and propose exiting new applications. The main feature of the nanomaterials in any shape is their large surface to volume ratio which results in a large contribution of the surface in the system energy. On the nanoscale, the thermodynamic effect of surface can lead to equilibrium atomic structures that differ from of the material on larger scales. The reactivity of nanomaterials, due to their high surface to volume ratio, can also differ from the bulk material greatly. This can lead to a potential harm to environment and living organisms which might has been underestimated during the rapid growth of nanotechnology. The first step to avoid these undesirable side effects is to construct a detailed understating of physics of the nanoscale which enables us to predict the properties of nanomaterilas and how they interact with their environment [20].

1.1 Atomistic Simulations

Despite of considerable development in nano-fabrication techniques in past decades, our understanding of physics of the nano-level is still limited. Although, the development of tools of experimental studies, specially the electron microscopy, has enhanced our general understanding of nano-scale phenomena, there are still considerable details which are untouchable by these studies. Theoretical and numerical studies have shown to be a promising approach to accompany the experiments and develop our understanding about nanomaterials.

Electronic structure methods based on quantum mechanic calculations (first-principle methods) are the most accurate simulation tools available to us. The theory of quantum mechanics relies on the fact that energy and all other related properties of a system can be calculated by solving Schrödinger's equation. For a theoretical materials scientist, development of Schrödinger's equation is probably the most exiting discovery happened in the world of physics. This, in principle, gives us all we need to understand the matter as we now knew the underlying equations that describe it. Unfortunately, exact solution of Schrödinger's equation is only feasible for the simplest systems. As a result, different electronic structure methods have been developed to estimate the solution of the Schrödinger's equation by means of different mathematical approximations [21]. Despite all the developments in hardware and software technologies, the computational expense of the first-principle methods is still a crucial limitation which makes them technically impractical for systems beyond hundreds of atoms and time scales over hundreds of picoseconds [22].

Atomistic simulations, in which we are only concerned with atoms, rather than electrons and sub-atomic particles, are the best alternative offering a compromise between computational speed and accuracy. These sets of simulation methods which are also known as molecular mechanics, use empirical potentials and laws of classical mechanics to model atomic interactions. Molecular dynamics (MD) simulations in particular, enable the study of dynamics and atomic level evolutions of relatively large systems (up to millions of atoms or even more) in a practical time period (nanoseconds). This can result in calculation of dynamical properties like heat and mass transfer, diffusion, surface absorption, and geometry evolution of nanomaterials. Overall, MD enables the study of systems and processes with more realistic dimensional and time scales. The accuracy of molecular mechanic methods, however, is greatly dependent on the reliability of the empirical potential they use to model interatomic interactions. As a result, it is quite important to verify the reliability of empirical potentials by testing their ability to reproduce different material properties.

Figure 1.1: Different size colloidal QDs excited by ultraviolet light showing a wide range of colours [1].

1.2 ZnS nanoparticles

Among all nanomaterials which have gradually found their ways into our daily lives, II-VI semiconductor nanomaterials are of great technological interest due to their unique opto-electronic properties. When the size of a zero-dimensional semiconductor nanomaterial is small enough to exhibit quantum properties (generally sizes less than 5 nm), it is called quantum dot (QD). The name was first proposed by Reed in late 1980s [23]. The most exciting quantum mechanical property of QDs is the quantum confinement effect which happens in semiconductor crystallite whose size is in the order of the size of its exciton Bohr radius [24]. Due to the small size of QDs, the electrons are confined and the energy levels can be modeled using the particle in a box model. In principle, as the size of the QD decreases, the size of the band gap (the difference between the valence and conduction bands energy) increases. Thus, more energy is needed to excite an electron (moving it from valance to conduction band), so more energy would be released when the electron returns to its ground state, consequently. This means that the optoelectronic properties of QDs are highly tunable. Example of this is shown in Figure 1.1 which shows florescent QDs fluoresce a wide range of colors when changing their sizes [1].

QDs show a promising future in variety of optoelectronic applications such as solar cells, LEDs, diode lasers, quantum computing and biomedical imaging. The latter, especially, has attracted a lot of attention recently where the wide absorption and luminescent efficiency, a high resistance to photobleaching, and high chemical stability of quantum dots make them an ideal candidate to substitute organic fluoroscopes [25, 26].

In spite of all promising properties of QDs, the rapid development of QD technology has also raised serious concerns about safety, mainly because the most studied II-VI semiconductor nanomaterials contain cadmium (CdSe, CdTe and CdS), which is known to be highly carcinogenic for living systems [27]. Various modifications such as adding a ZnS

shell or polyethylene glycol (PEG) coating have been suggested to modify QDs with toxic elements. However, the cytotoxicity of Cd containing QDs is still a major concern [28].

Zn-based QDs such as ZnS have been introduced as a suitable alternative since Zn is inherently an essential biological element [29]. Furthermore, the band gap of ZnS is more than 1 eV wider than the others in the II-VI family, which enables a wider spectrum to be tuned by varying the size of ZnS nanostructures. Generally, the size of QDs for biomedical applications is smaller than 5 nm for two main reasons: to get the best use out of the quantum confinement effect and to avoid accumulation of QDs in the body. It has been reported that large QDs are generally accumulated in the reticuloendothelial system, such as liver, spleen and lymphatic system for several months, but the QDs with sizes less than 5 nm could be removed by kidney quickly [30]. Unfortunately, utilizing ZnS nanoparticles in this size range has shown to be challenging since noncrystalline ZnS has the potential to undergo uncontrolled structural changes in ambient conditions[20]. As a result, the structural stability of ZnS NPs as a function of different factors such as size, environment, aggregation, temperature, and pressure have been highlighted in experimental and numerical studies. However, we still have a vague picture of details of the structural evolution of these nanoparticles on which applicability of them is highly depended.

At standard temperature and pressure (STP: 298 K and 1 bar), bulk ZnS exists in two crystal structures: zinc-blende ($ZB : F\bar{4}3m$) and wurtzite ($WZ : P6_3mc$). ZB which is also known as sphalerite, is the stable phase of ZnS at standard condition while WZ is more stable above 1020 °C. If we consider the Zn and S atoms separately, they make FCC and HCP arrangements in ZB and WZ structures, respectively. In both structures the Zn and S atoms are connected through a tetrahedral bond structure to form the ZnS molecule. At higher pressures (above 15 GPa), ZnS acquires the high density rocksalt structure ($RS : Fm\bar{3}m$). These three structure are shown in Figure 1.2.

The solid state phase transformation to RS phase is not technically significant as not many high pressure applications suggested for ZnS NPs. Reversible and irreversible phase transformations between ZB and WZ phases, or between each of these phases and the distorted structure, however, have attracted a lot of attention, since they were observed to occur under ambient conditions. One of the first experimental works on the structural stability on ZnS NPs is done by Qadri et al. [31]. They showed the XRD diffraction peaks from the WZ phase, in the initially pure 30 Å ZB samples which were annealed at 400 °C in vacuum for 45 minutes. The ZB-WZ phase transformation at 400 °C and in vacuum is also reported for ZnS NPs in other studies [32]. Similar study was performed by Yang et al. reported temperatures as low as 250 °C for ZB-WZ phase transformation when increasing the pressure just for 1 GPa [33]. These temperatures are much lower than the bulk trans-

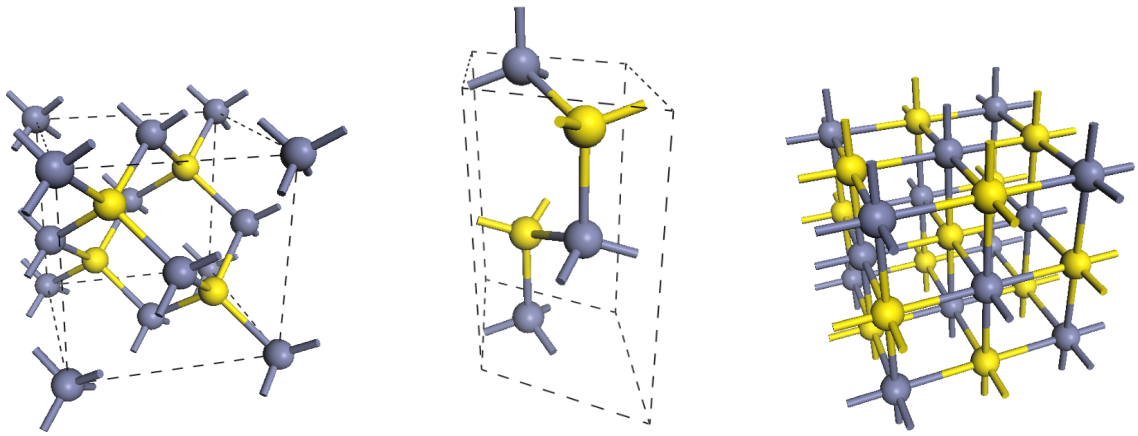

(a) (b) (c)

Figure 1.2: Three phase structure of ZnS: (a) zinc-blende ($ZB : F\bar{4}3m$), (b) wurtzite ($WZ : P6_3mc$), and (c) rocksalt ($RS : Fm\bar{3}m$).

formation temperature of 1020 °C. One other important observation of all of these studies was that the size of the ZnS NPs increased significantly after annealing. This suggests agglomeration is one of the controlling factors in phase stability of ZnS NPs.

The structural change in 3 nm ZnS NPs is also reported as a function of aggregation states of NPs [34]. Reversible switching between distorted structure of dispersed or weakly aggregated NPs and crystalline structure of strongly aggregated NPs in reported as a result of changing the aggregation state. Dispersed and aggregated states were achieved using slow drying and ultrasonic agitation, respectively. More studies has been done in the same research group at University of California-Berkley, focusing on structural stability of ZnS NPs. They also reported the reversible structural transformations between distorted and crystalline ZB structures induced at room temperature by absorption-desorption of methanol and water [35, 36]. XRD results showed that the minimum energy structural configuration of particles in methanol at room temperature does not have a crystalline nature. However, binding of water leads to a dramatic structural modification, significantly reducing distortions of the surface and interior and generating a structure close to that of ZB. They also used the UVvis. absorption spectroscopy to show that there was no change in the onset of absorption, indicating that no coarsening occurred, and the structural enhancement was a sole effect of water binding. Molecular dynamics simulations and thermodynamic analysis were also used to complement the experimental results. The thermodynamic analysis, which makes use of surface energy data, showed that for sizes smaller than 7 nm WZ nanoparticles are more thermodynamically stable than ZB and the ZB-WZ transformation is thermodynamically possible in temperatures as low as 25 °C [2]. Molecular dynamics simulation was also confirmed the enhancement of crystallinity by absorption of water to

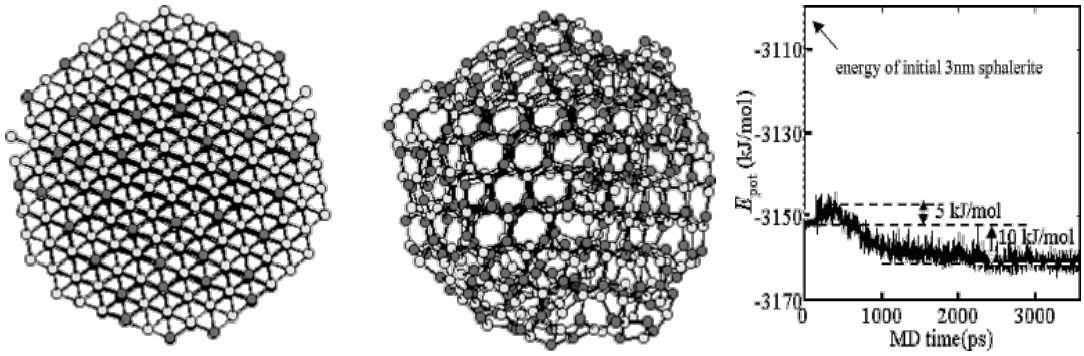

(a) (b) (c)

Figure 1.3: Results of MD simulation of a free standing 3 nm ZB NP [2]. (a) Initial configuration viewed along the [111] direction, (b) The energy-minimized structure obtained by the MD, and (c) Potential energy evolution. The [001] hexagonal channels of WZ at (b) were considered as the sign of ZB-WZ phase transformation. According to (c), the activation energy of this phase transformation was reported to be 5 KJ/mol.

the surface of NPs. The MD simulations of Zhang et al. have one more interesting and at the same time strange result too: they reported that a 3 nm free standing (in vacuum) ZB ZnS NP experienced phase transformation WZ structure at 300 K [2] in a relatively short (3.6 ns) MD simulation (Figure 1.3). Clear phase transformation from ZB-WZ in dispersed ZnS NPs had been never reported experimentally. Moreover, observing a complete phase change in a short MD simulation at room temperature, where kinetics is the controlling factor, is extraordinary.

Using computational techniques, another group mainly based in the Royal Institution of Great Britain have also studies the ZnS nanostructures excessively. In one of their early studies, they introduced an interatomic potential for ZnS and surface energies of the most observed surfaces of ZB and WZ structure were calculated using the lattice static approach [37]. Using the calculated surface energies, they found the low energy crystal morphologies following the Gibbs criteria, and predicted a dodecahedron shape for the ZB phase and a prismatic shape for the WZ phase [20]. The derived interatomic potential along with density functional theory (DFT) technique are used to perform global minimization through the simulated annealing [38, 39] and genetic algorithm [40] procedures to find the the best possible estimate of the global energy minimum of ZnS small clusters. In the very small $(ZnS)_n$ clusters with $10 \leqq n \leqq 49$ the minimum energy structure was bubble-like cluster, a hollow spheroidal structures where all atoms are three-coordinated. For $50 \leqq n \leqq 80$ clusters, the global minimum energy structures are "double bubbles" or onion-like clusters in which one bubble is formed inside another one. Crystal structure of large clusters ($n = 256$ *and* $n = 512$) obtained by global minimization, mainly consisted of four-coordinated atoms but deviated from the two bulk phases of ZnS found in nature and

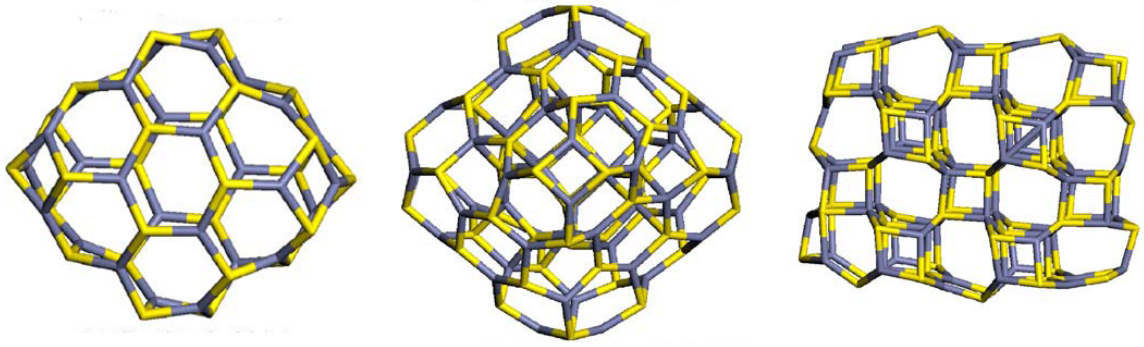

(a) (b) (c)

Figure 1.4: Three structure observed for $(ZnS)_n$ clusters after global minimization [3]. (a) bubble-like ($10 \leqq n \leqq 49$), (b) double-bubbles ($50 \leqq n \leqq 80$), and BCT ($80 \leqq n \leqq 512$).

were shown to be similar to the BCT zeolite structure. However, the energy of WZ clusters were found to be so close to BCT ones and it was suggested that their relative energies may be reversed by solvation effects [3]. The formation of bubble-like clusters was also reported during early stages of ZnS formation in aqueous solution [41].

Another approach to predict stable configuration of a NP is to calculate frequent crystalline surface energies and construct the most stable shape using Wulff construction. Applying surface energies calculated using first-principle computer simulations, Barnard et al. used this approach to study the effect of shape and size on stability of ZnS ZB [42] and WZ [43] NPs. Similar to what suggested by the lattice static study of Hamad et al. [37], they showed that ZB rhombic dodecahedron enclosed entirely by non-polar 110 facets is the most stable ZnS shape regardless of the NP size. However adding polar facets to ZB nanostructures will make core/shell crystalline/amorphous structure thermodynamically favorable. Furthermore, deviation from rhombic dodecahedron enables some thermodynamic paths from ZB to WZ transformation by decreasing the size [43]. While this approach provides valuable thermodynamic information about phase stability of the ZnS NPs, it does not come close to dynamics. Moreover, Wulff configurations can not be made in all sizes and more realistic model of a NP would include imperfect facets, edges and corners which affect the NP's surface energy significantly.

In addition to alternating optoelectronic properties of a single NP, structural and configurational changes can also affect intrinsic forces between NPs. Semiconductor NPs interactions can be decomposed into coulomb and van der Waals components. Although NPs are generally charge neutral, they exhibit large static permanent dipoles causing considerable coulomb interactions [44]. Dipole-Dipole interactions are of a great importance as they are shown to be the governing factor in agglomeration [45], oriented attachment [46], and sta-

bilization of superlattice structures [47] of non-metallic NPs. There has been considerable number of studies on finding the origin of large permanent dipole in ionic NPs. Large DM is expected in WZ NPs due to the polar nature of WZ lattice but should be absent in ZB NPs due to the T_d symmetry of ZB lattice. Li and Alivisatos's study on CdSe nanorods has shown a permanent DM was proportional to the volume of nanorods. They considered the origin of the DM was due to the natural polar character of the WZ structure [48]. Nann and Schneider have also shown that a small crystallographic deviations from the ideal WZ structure could result in a large permanent dipole moment [49]. On the other hand, Shim and Guyot-Sionnest have shown a linear dependence of the large DM to the radius of both WZ CdSe and ZB ZnSe nano crystals [44]. Since the large DM has been observed for both ZB and WZ structures, they concluded that this linear size dependence is not due to the polar character of the WZ lattice but due to the faceted surface structure of nano crystals. Later study of Shanbhag and Kotov showed that minor deviations from a symmetric tetrahedral shape of ZB CdS nanocrystals could result in large DMs [50]. Cho et al. has shown that dipole moment of PbSe nanocrystals with centrosymmetric rocksalt lattice was large enough to result in the formation of nanowires through oriented attachment of nanocrystals [51]. Considering a random distribution of polar facets and probability of lacking of central symmetry, they showed that about 89% of possible shapes of PbSe nanocrystals were polar. Self-assembly of ZnS nanocrystals into ellipsoidal shapes has also been explained by charge-charge, charge-dipole, and dipole-dipole interactions of non-symmetric ZnS NCs along the [111] direction [52]. ZnS nanowires with length as long as 10 µm have been also successfully fabricated via oriented attachment of ZnS nanocrystals [53].

1.3 Objectives of this study

The background mentioned above shows that in spite of the numerous theoretical and experimental researches on ZnS NPs in the past two decades, our understanding of the structural evolution in these important nanomaterials is still not complete. This is more crucial in studies based on atomistic simulations as their results are sometime contradictory. Some other challenges like the particle-particle interactions and the effect of the structural evolutions on them have remained almost untouched. Regarding to the increasing interest in potential applications of ZnS NPs, it seems necessary to enhance our knowledge about the reliability of these materials. The post fabrication structural evolutions of these nanostructures is one of the main factors governing their applicability.

As mentioned in Section 1.1, a reliable interatomic potential is essential for an accurate atomistic simulation. Some conflicts in the atomistic simulation studies of ZnS are due to the inaccurate potentials. Due to the lack of a comprehensive study on available empirical potentials in the literature, a sound decision can not be made about choosing an appropriate one. Thus, this work started by a comprehensive study which aimed to address advantages

and disadvantages of each empirical potential of ZnS proposed in literature. After choosing the suitable interatomic potential, molecular dynamics was used as the main simulation tool to study the structure of the ZnS NPs. NPs with different initial structures and size were simulated in different environments. Simulation were performed in comparable length and time scales to the experimental conditions. The structure of NPs was examined in details with different analytical methods. The effect of size and environment on particle-particle interactions have also been studied. At the end of this study, we hope to provide an insight of dynamics of structural evolutions of ZnS NPs which can help to find a proper fabrication and post-fabrication treatments to render best performance of ZnD NPs in their future applications.

Chapter 2

Methodology

2.1 Interatomic potential

Basically, all simulation methods in the atomic scale start with the calculation of the internal energy. The internal energy of a solid is a many-body quantity explicitly depended on the positions and momenta of electrons and nucleus of all atoms in the system. The calculation of the ground state internal energy requires to solve the Schrödinger's equation for the collection of atoms of interest. However, exact solution of Schrödinger's equation is only feasible for the simplest systems. As mentioned in section 1, variety of first-principle methods have been developed to estimate the solution of the Schrödinger's equation by means of different mathematical approximations. However, this is still an intractable problem to solve and the computational expense of the first-principle methods is still a crucial limitation which makes them technically impractical for systems beyond hundreds of atoms. Thus approximations must be made to simplify the situation. Atomistic simulation methods, tackle this problem by subsuming the effect of the electrons and nuclei into interatomic interactions. Depending on the nature of the system, different kinds of interatomics interaction might be considered to model the internal energy of the system accurately. The parameter of the interatomic interaction are derived empirically by fitting different properties of the system to the experimental or higher level first-principle calculation results. The collection of all interatomic interactions which defines the system under the study is called interatomic potential or force field. As explained in section 1, The accuracy of an atomistic simulation method is highly depended on the interatomic potential used to model the interaction of atoms. Interatomic interactions can be divided into to main groups: bonded and non-bonded interactions. Bonded interactions which act between covalently bonded atoms usually are not considered for ionic crystalline solids. Instead, a model which was first introduced by Born and Mayer [54] is used which assumes that the interatomic potential of ionic-bonding materials consists of two main non-bonded interactions: long-range electrostatic and short-range. Here we explain different components of the Born model.

2.1.1 Electrostatic interaction

The charged nature of the ionic species gives rise to the Coulombic interaction which can typically represent up to 90% of the total energy. Electrostatic energy between two charged atoms is represented by Coulomb's law:

$$U_c(r_{ij}) = \frac{q_i q_j}{4\pi\epsilon_0 r_{ij}} \tag{2.1}$$

where ϵ_0 is the permitting of free space, q_i and q_j are the charges on atoms i and j, and r_{ij} is their distance. Despite the simplest form of the Coulomb energy, it is in fact the most complicated atomic interaction to evaluate in an atomistic simulation. It is because Coulomb energy shows a slow decay in respect to separation distance of atoms due to the $\frac{1}{r}$ term, which makes it the long-range component of the interatomic potential. For finite clusters, like nanoparticles in vacuum, it may be practical to calculate the pure Coulomb interaction between all atoms, but, this approach is not technically possible for infinite periodic systems. The most applied solution to overcome ill-defined Coulomb energy problem is proposed by Ewald [55].

Ewald summation

The heart of the Ewald'd idea to overcome convergence problem is a technique that separates Coulomb term into two components, one of which is rapidly convergent in real space, and the second decays quickly in reciprocal space. Here we provide a simplified overview of the Ewald method, mainly based on description provided by Kittle [56]. For more details readers are encouraged to read Ref. [55] and Ref. [57].

In a lattice of non-overlapping, spherical ions of positive or negative charges, the electrostatic potential, ψ, felt by the ion i can be written as:

$$\psi_i = \sum_{j \neq i} \frac{q_j}{r_{ij}} \tag{2.2}$$

where q_i is the charge of ion j at the distance of r_{ij} from ion i. Note that the $\frac{1}{4\pi\epsilon_0}$ coefficient is omitted in this definition. Considering the entire system is charge neutral and contains an infinite number of positive and negative charges situated at distances r_{ij}^{+} and r_{ij}^{-} from ion i, respectively, Equation 2.2 can be rewritten as:

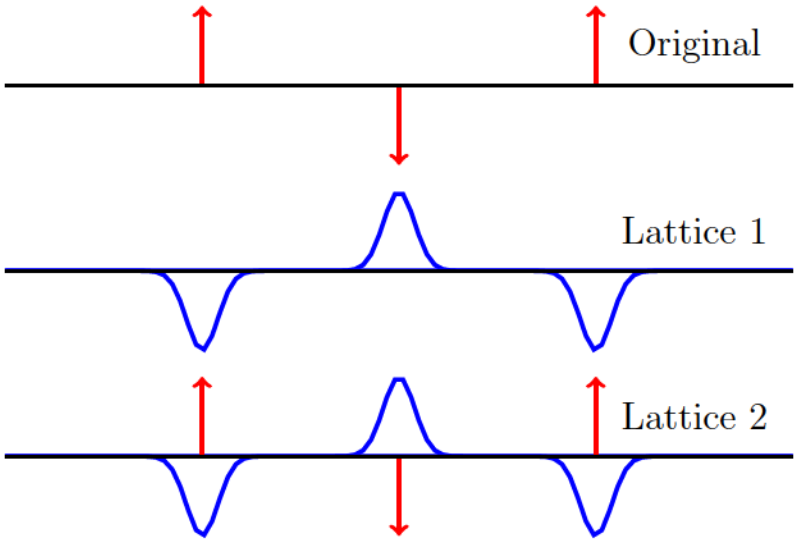

Figure 2.1: The representation of the Ewald summation in 1D.

$$\psi_i = q\left(\sum_{j^+\neq i}\frac{1}{r_{ij}^+} + \sum_{j\ \neq i}\frac{1}{r_{ij}^-}\right) \tag{2.3}$$

Now consider that we add two charge distributions, like Gaussian distribution, to each lattice site in a way that distribution 1 has the sign same as the point charge at that lattice site and distribution 2 has the opposite sign. Similarly, we can define two auxiliary lattices such lattice 1 includes distribution 1 and lattice 2 contains distribution 2 and point charges. When these two components are combined they reduce to the original set of point charges. Definition of lattice 1 and lattice 2 are illustrated in Figure 2.1.

Accordingly, we can define ψ_1 and ψ_2 corresponding to the contributions of lattice 1 and 2 to the total potential energy, ψ. Figure 2.1 shows that charge distribution in lattice 2 is dominated by point charges and resembles delta-like charge distribution. Therefore, its effect on the potential can be computed more rapidly in the real space and convergence will be faster if the Gaussian width of the charge distribution is narrower. On the other hand, potential of lattice 1 is more conveniently calculated in reciprocal space where it converges faster when Gaussian distributions are wider. Therefore, an optimum width of the Gaussian peaks as well as cut-off distances in real and reciprocal spaces should be calculated. One well known approach is to define these parameters by minimizing the total number of real and Fourier terms to be evaluated for a given specified accuracy [58] which leads to

$$\eta_{opt} = \left(\frac{N\pi^3}{V^2}\right)^{\frac{1}{3}} \tag{2.4}$$

$$r_{max} = \left(\frac{-ln(A)}{\eta}\right)^{\frac{1}{2}} \tag{2.5}$$

$$G_{max} = 2\eta^{\frac{1}{2}}(-ln(A))^{\frac{1}{2}} \tag{2.6}$$

where η is the peak width parameter, N is the total number of charges, V is the unit cell volume, A is the level or the accuracy and r_{max} and G_{max} are cut-offs in real and reciprocal spaces, respectively. The definition of the potential dictates that the charge distribution at the reference point does not contribute to ψ_1 or ψ_2. Therefore, we can rewrite the potential of lattice 1 as

$$\psi_1 = \psi_{recip} - \psi_{self} \tag{2.7}$$

where ψ_{recip} is the potential of the continuous series of Gaussian distribution in the reciprocal space and ψ_{self} is the potential caused by the charge distribution at the reference point. ψ_{recip} as well as its associated charge density can be expanded in terms of Fourier series

$$\psi_{recip} = \sum_{\mathbf{G}} c_{\mathbf{G}} e^{i(\mathbf{G}.\mathbf{r})} \tag{2.8}$$

$$\rho = \sum_{\mathbf{G}} \rho_{\mathbf{G}} e^{i(\mathbf{G}.\mathbf{r})} \tag{2.9}$$

where $c_{\mathbf{G}}$ and $\rho_{\mathbf{G}}$ are Fourier coefficients and $\mathbf{G}$ is a reciprocal lattice vector (where the special case $\mathbf{G} = 0$ is excluded). The potential energy can be related to its charge distribution through Poisson's equation

$$\nabla^2 \psi_{recip} = -4\pi\rho \tag{2.10}$$

combing Equations 2.8, 2.9 and 2.10 we can write

$$c_{\mathbf{G}} = 4\pi \frac{\rho_{\mathbf{G}}}{\mathbf{G}^2} \tag{2.11}$$

Our basic assumption is that each ion j with poison of $\mathbf{r}$ in the lattice is the centre of a

Gaussian charge distribution whose density is

$$\rho(\mathbf{r}) = q_j \left(\frac{\eta}{\pi}\right)^{\frac{3}{2}} e^{-\eta r^2} \tag{2.12}$$

Now, to evaluate $\rho_{\mathbf{G}}$, we multiple both sides of the 2.9 by $e^{-i(\mathbf{G}.\mathbf{r})}$ and integrate over the volume of the cell. The charge distribution to be considered in this case is that originating on the ion points within the cell and also that of the tails of the distributions originating in all other cells. However, it can be shown that the integral of the total charge times $e^{-i(\mathbf{G}.\mathbf{r})}$ over a single unit cell is equal to the integral of the charge density originating in a single cell times $e^{-i(\mathbf{G}.\mathbf{r})}$ over all space. Accordingly, we have

$$\begin{aligned}
\rho_{\mathbf{G}} \int_{cell} e^{i(\mathbf{G}.\mathbf{r})}.e^{-i(\mathbf{G}.\mathbf{r})} &= \rho_{\mathbf{G}}.V_{cell} \\
&= \int_{all\ space} \sum_j q_j \left(\frac{\eta}{\pi}\right)^{\frac{3}{2}} e^{-\eta(r-r_j)^2} e^{-i(\mathbf{G}.\mathbf{r})} d\mathbf{r} \\
&= \sum_j q_j \left(\frac{\eta}{\pi}\right)^{\frac{3}{2}} e^{-i(\mathbf{G}.\mathbf{r}_j)} \int_{all\ space} e^{-(i\mathbf{G}.\boldsymbol{\zeta}+\eta\boldsymbol{\zeta}^2)} d\boldsymbol{\zeta} \\
&= \left(\sum_j q_j e^{-i(\mathbf{G}.\mathbf{r}_j)}\right) e^{-\frac{\mathbf{G}^2}{4\eta}} \\
&= S(\mathbf{G}) e^{-\frac{\mathbf{G}^2}{4\eta}}
\end{aligned} \tag{2.13}$$

where S($\mathbf{G}$) is the structural factor of the unit cell under consideration. Using the calculated value for $\rho_{\mathbf{G}}$, we can now calculate $c_{\mathbf{G}}$ through Equation 2.11 and substituting $c_{\mathbf{G}}$ in Equation 2.8 gives

$$\psi_{recip} = \frac{4\pi}{V} \sum_{\mathbf{G}} S(\mathbf{G}) G^{-2} e^{i(\mathbf{G}.\mathbf{r}) - \frac{\mathbf{G}^2}{4\eta}} \tag{2.14}$$

ψ_{self} at the reference ion point, i, due to the central Gaussian distribution is

$$\psi_{self} = \int_0^\infty \frac{\rho}{r} (4\pi r^2) dr = 2q_i \left(\frac{\eta}{\pi}\right)^{\frac{1}{2}} \tag{2.15}$$

and so

$$\psi_1 = \frac{4\pi}{V} \sum_{\mathbf{G}} S(\mathbf{G}) G^{-2} e^{i(\mathbf{G}.\mathbf{r}) - \frac{\mathbf{G}^2}{4\eta}} - 2q_i \left(\frac{\eta}{\pi}\right)^{\frac{1}{2}} \tag{2.16}$$

ψ_2 can be partitioned into three contributions from each ion in respect to the reference

point: contributions from the point charge of ion j, from the part of the Gaussian distribution centred on j and lying inside a sphere of radius r_j, and from that part falling outside the sphere, respectively.

$$\psi_2 = \sum_j q_j \left[\frac{1}{r_j} - \frac{1}{r_j} \int_0^{r_j} \rho(\mathbf{r}) d\mathbf{r} - \int_{r_j}^{\infty} \frac{\rho(\mathbf{r})}{r} d\mathbf{r} \right] \tag{2.17}$$

substituting $\rho(\mathbf{r})$ and carrying out some mathematical manipulations, we have

$$\psi_2 = \sum_j \frac{q_j}{r_j} ercf(\eta^{\frac{1}{2}} r_j) \tag{2.18}$$

where $erfc(x)$ is the complimentary error function. Finally, we can write the total potential of the reference ion i in the field of all the other ions in the crystal as

$$\psi(i) = \frac{4\pi}{V} \sum_{\mathbf{G}} S(\mathbf{G}) G^{-2} e^{i(\mathbf{G}.\mathbf{r}) - \frac{\mathbf{G}^2}{4\eta}} - 2q_i \left(\frac{\eta}{\pi}\right)^{\frac{1}{2}} + \sum_j \frac{q_j}{r_j} ercf(\eta^{\frac{1}{2}} r_j) \tag{2.19}$$

and the total electrostatic energy of the system can be calculated as

$$U_{es} = \frac{1}{2} \times \frac{1}{4\pi\epsilon_0} \sum_i q_i \psi_i \tag{2.20}$$

2.1.2 Short-range interactions

As implied in their name, short-range interactions have a fast converging nature which makes it tractable to use cut-off to evaluate them. In a many-atom system, short-range interaction can be considered between two, three or more atoms.

$$U_{sr} = \frac{1}{2} \sum_{i,j}^{N} U_{ij} + \frac{1}{6} \sum_{i,j,k}^{N} U_{ijk} + ... \tag{2.21}$$

The first and second terms in Equation 2.21 are two- and three-body interactions, respectively. The two-body or the pair potential is described by two atomic interactions: repulsive and attractive. The physical origin of the repulsive term is related to the Pauli principle: when the electronic clouds surrounding the atoms starts to overlap, the energy of the system increases abruptly. Thus, this term dominates in short atomic distances. At the large atomic distances, however, attractive part is dominating to assure the cohesion of the system. This attraction is described by van der Waals dispersion forces. Combining attractive and repulsive interactions, two-body potential will have a form like Figure 2.2.

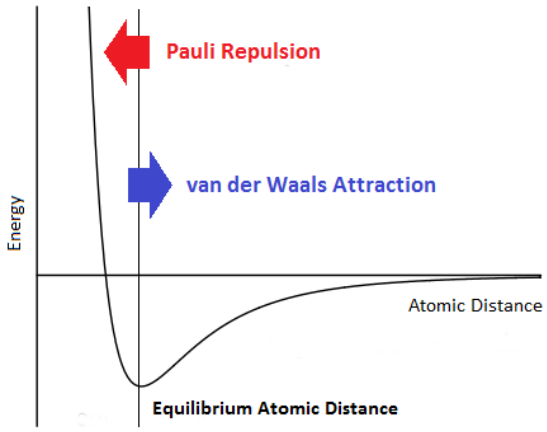

Figure 2.2: Two-body short-range interaction.

There is no doubt that the simplest and the most widely used pair potential model is the Lennard-Jones potential

$$U_{LJ} = 4\epsilon \left[\left(\frac{\sigma}{r_{ij}} \right)^{12} - \left(\frac{\sigma}{r_{ij}} \right)^{6} \right] \tag{2.22}$$

where ϵ is the depth of the potential well (potenital value at the equilibrium atomic distance) and σ is the distance at which the potential equals to zero. For ionic solids the most commonly used pair potential is the Buckingham potential

$$U_{Buckingham} = Ae^{\left(-\frac{r_{ij}}{\rho}\right)} - \frac{C}{r_{ij}} \tag{2.23}$$

where A, rho, and C are potential parameters. There has been a constant debate about advantages and disadvantages of these two formulations. As explained by Buckingham in his original paper [59], the Buckingham potential describes the repulsion term from the Pauli principle by a more realistic exponential function, comparing to the inverse twelfth power used by the Lennard-Jones potential. On the other hand, some point out that the Buckingham potential remains finite even at the very small atomic distances which can cause the infamous "Buckingham catastrophe" at short range. This is especially more important when it is used in simulations of charged systems with small atomic distances. Moreover, the Lennard-Jones potential is quicker to compute due to the simple formulation.

The three-body term is often used to take into account the semicovalent nature of the semiconductors atomic bonds. The simplest and the most frequently used formulation is

the harmonic angle potential

$$U_{\theta_{ijk}} = \frac{k}{2}(\theta_{ijk} - \theta_0)^2 \tag{2.24}$$

where k is the harmonic constant and θ_0 is the equilibrium angle between atoms i, j, and k. Generally, higher order interactions like 4-body potentials are avoided because they require high computational time which technically makes simulations time consuming.

2.1.3 Polarizability

The Coulomb interaction introduced previously assumes the electronic orbitals are fixed and changing the lattice conditions has no effect on them or in other words, atoms are not polarizable. An atom or ion is polarizable if it develops a dipole moment when placed in an electric field. It is generally unreasonable to assume that the dipole moment of an atom is fixed, since both the magnitude and direction readily alter depending on the nature of the system being studied. The simplest and most successfully implemented method for taking into account the polarization of ions within the Born model is the shell model developed by Dick and Overhauser [60]. In this model, an ion ($q_{ion} = q_c + q_s$) is considered to have two parts: the core, which carries atomic mass and part of the total charge (q_c), and the massless shell, which takes the polarizable charge (q_s). The shell and core are electrostatically screened from each other but connected through a harmonic spring. The shell is allowed to move relative to the core, forming a dipole, and the degree of polarisation is dependent on the value of the harmonic spring constant and the shell charge.

$$V_{core-shell} = \frac{1}{2}k_s r^2 \tag{2.25}$$

When polarizable ions are modeled using shell model, short-range interaction are considered to act only between shells while Coulomb interaction acts on both shells and cores [61]. The physical basis of this consideration is that the short-range interactions are a result of electron cloud interactions and since shells mimic the valence electrons, the short range-forces must act between them.

There are two ways to implement shell model in the molecular dynamics (MD) simulation. One approach is to treat shells as massless species like the original definition of the shell model. In this implementation which is usually called relaxed shell model [62], the shell cannot be treated dynamically and instead the procedure is first to relax the shell by applying the force minimization at each time step and then integrate the motion of the finite mass core by conventional molecular dynamics. Since an additional minimization is

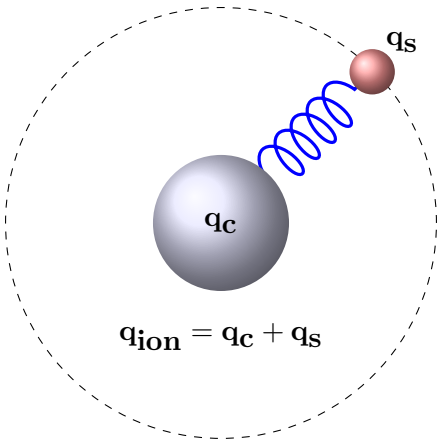

Figure 2.3: Representation of the shell model of Dick and Overhauser.

required in each time step, the computational cost per time step for this algorithm is considerably high. Another approach which is more popular in molecular dynamics simulations is the adiabatic shell model of Mitchell and Fincham [63]. In this method the shell is given a small portion of ion mass and its motion is integrated by conventional molecular dynamics technique. The shell mass should be small enough to ensure that the core-shell spring frequency is well above the vibrational frequencies of the lattice. From classical mechanics, the frequency of core-shell spring can be calculated as

$$\upsilon = \frac{1}{2\pi}\sqrt{\frac{k_s}{x(x-1)M}} \tag{2.26}$$

where x is the fraction of the ion mass assigned to shell and M is the ion mass. Equation 2.26 shows that smaller shell constants require smaller shell masses to satisfy adiabatic conditions. Technically, this means much smaller MD time steps are required to capture the fast movement of the light shells.

2.2 Lattice Dynamics

Lattice dynamics is based on the study of the vibrations of the atoms in a crystal. Understanding lattice dynamics in essential to have a complete picture vibrational frequencies and effect of these vibration on thermodynamic properties of crystalline materials. In these study, lattice dynamic simulations are used to calculate the phonon dispersion of ZnS lattices which are represented in chapter 3. Owing much to Dove [61], we represent the lattice dynamics calculation of a very simple system here, which can be a base of understanding these calculations for more complicated systems.

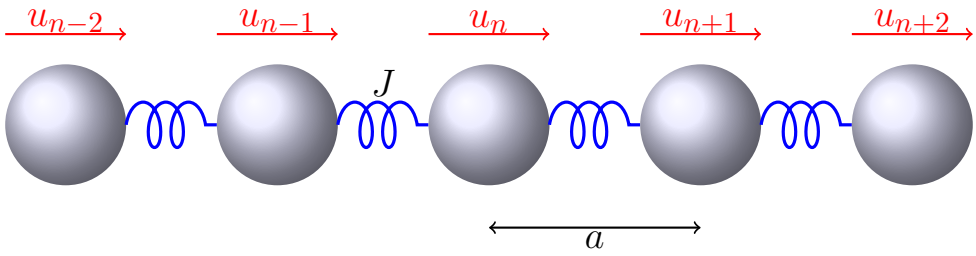

Figure 2.4: Linear chain model. J is the harmonic force constant, u represents the displacement, and a in the equilibrium lattice constant.

The simplest model can be used to explain the atomic vibrations is a linear chain of atoms with unit mass m which are separated by lattice constant a (Figure 2.4).

Here we just consider *nears-neighbor interaction* which means each atom is just feel the force of its immediate neighborer. If the energy between to atoms separated by distance a is $\phi(a)$, the total energy of a chain of N atoms will be

$$E = N\phi(a) \tag{2.27}$$

Now, consider that each atom moves by finite displacement u. If u is small enough in comparison with a, the energy of the atomic chain can be calculated using Taylor series

$$E = N\phi(a) + \sum_{s\geq 1} \frac{1}{s!} \frac{\partial^s \phi}{\partial u^s} \sum_n (u_n - u_{n+1})^s \tag{2.28}$$

where u_n is the displacement of the n^{th} atom so displacement between atoms n and $n+1$ will be $r = a + (u_n - u_{n+1})$. Thus the derivative of ϕ in respect to u is equivalent to the derivative with respect to r. Since a is the equilibrium lattice constant (distance at which there is no force on atoms), the first term in Equation 2.28 ($s = 1$) is zero. As u is small to a we may expect the dominant contribution comes from the quadratic term. Considering only the quadratic term ($s = 2$) and neglecting all higher terms is called *harmonic approximation*. The higher order terms which are neglected here are called *anharmonic terms*. The second derivative of ϕ in respect to u, $j = \frac{\partial^2 \phi}{\partial u^2}$, is called *harmonic force constance*. Now, we can write the Newton equation of motion for the n^{th} atom as

$$m\frac{\partial^2 u_n}{\partial t^2} = -\frac{\partial E}{\partial u_n} = -J(2u_n - u_{n+1} - u_{n-1}) \tag{2.29}$$

Harmonic equation equation of motion has a known solution which is a sinusoidal wave. Thus, the motion of the whole system will be a set of traveling waves. The aim of lattice

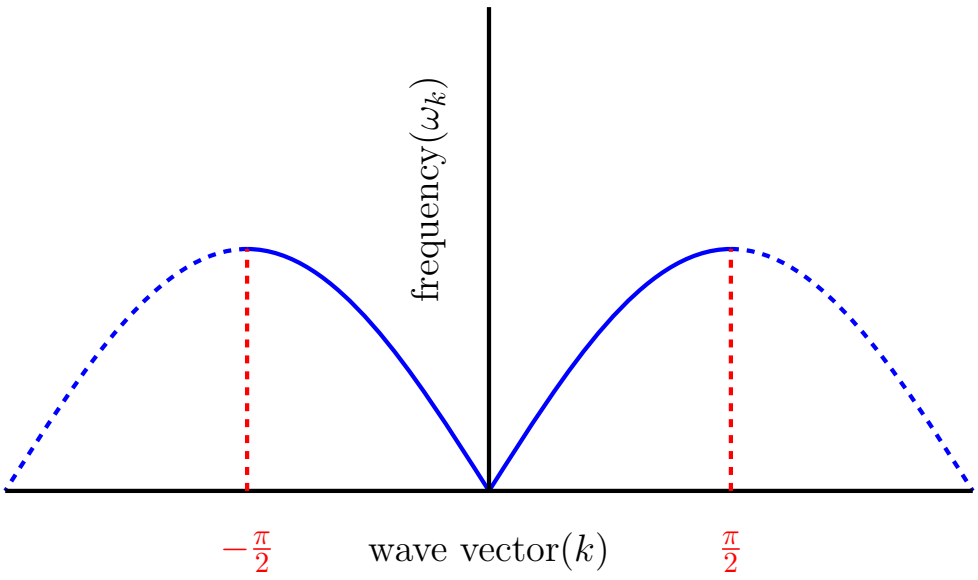

Figure 2.5: Dispersion curve for the one-dimensional mono atomic chain.

dynamics calculations is to find the set of frequencies of these waves. The mathematical representation of time-dependent motion of n^{th} which is a linear superposition of each of traveling waves can be written as

$$n_n(t) = \sum_k \widetilde{u}_k exp(i[kx - \omega_k t]) \tag{2.30}$$

where k is the wave vector ($k = 2\pi/\lambda$), ω_k is the corresponding angular frequency ($\omega_k = 2\pi\nu$), $\widetilde{u}_k$ is the amplitude, and x is the displacement which is restricted to values $x = na$. By substituting Equation 2.30 into Equation 2.29 and applying some simple mathematical manipulations we can obtain an expression for the angular frequency as a function of wave vector

$$\omega_k = \left(\frac{4J}{m}\right)^{1/2} |sin(ka/2)| \tag{2.31}$$

by taking only positive roots we obtain the behaviour of the angular frequency as shown in Figure 2.5 which is called dispersion curve.

When k approaches to zero, we can take the linear approximation of Equation 2.31 and write

$$\omega_k(k \longrightarrow 0) = a\left(\frac{4J}{m}\right)^{1/2}|k| \tag{2.32}$$

This give the phase velocity c, which is equivalent to the velocity of sound in the crystal

$$c = \frac{\omega}{k} = a\left(\frac{4J}{m}\right)^{1/2} \tag{2.33}$$

Because of this relation, a vibrational mode as Figure 2.5, which goes to zero in the limit of small k, is called *acoustic mode*. If the atomic chain consists of two atom types with different masses the corresponding solution of the wave equation will result in two simultaneous equations. In addition to the *acoustic mode*, solving this system of equations gives rise to the *optic mode*. Frequencies in *optic mode* are flat at small k but not equal to zero. They are large in respect to *acoustic branch* and vary weakly with k. We will not representing the lattice dynamic formulations for more complicated cases here. For detailed explanation of the lattice dynamic formulation for more complicated systems, reader are referred to reference [61].

2.3 Molecular Dynamics

The molecular dynamics simulation method is based on Newtons second law or the equation of motion, $F = ma$. Knowing the force on each atom, it is possible to determine the acceleration of each atom in the system. Integrating the equations of motion then yields a trajectory that describes the microscopic state of a system as it varies with time. A microscopic state of a system is described by Hamiltonian, $\mathbf{H}$, as a sum of the kinetic (K) and the potential (U) energies, which are functions of the Cartesian momentum and coordinate of each particle, respectively

$$\mathbf{H} = K(\mathbf{p}) + U(\mathbf{r}) \tag{2.34}$$

where $\mathbf{p} = (\mathbf{p}_1, ..., \mathbf{p}_N)$ and $\mathbf{r} = (\mathbf{r}_1, ..., \mathbf{r}_N)$ are sets of atomic positions and momenta, respectively. We discussed the potential energy in Section 2.1 and we know that the kinetic energy takes the familiar quadratic form

$$K = \sum_{i=1}^{N} \frac{1}{2m_i}(p_{ix}^2 + p_{iy}^2 + p_{iz}^2) \tag{2.35}$$

where m_i is the mass of particle i, and $p_{ix},\ p_{iy},\ p_{iz}$ are the x, y, and z components of its momentum. From the classical mechanics the Hamiltons equations of motion can be written as

$$-\frac{\partial H(r,p)}{\partial r_i} = \frac{dp_i}{dt} = f_i \tag{2.36}$$

$$-\frac{\partial H(r,p)}{\partial p_i} = \frac{dr_i}{dt} = \frac{p_i}{m_i} \tag{2.37}$$

The first expression in Hamiltonian's equations of motion gives us the force acting on each atom which can provide us with the trajectory of the atom by applying the Newton's second law. The second term gives the velocity of each atom which leads to the temperature of the system. The Hamiltonian's equations of motion is integrated in each time step to move particles to new positions and to get new velocities at these new positions. As a result, not only is the configuration space of the system explored but information about the dynamics of the system is also gathered during the MD simulation.

At the heart of each MD simulation, there is a numerical integration method which integrates the 6N first order differential equations resulted by Hamiltonian's equations of motion. The performance of the simulation and accuracy of results are highly depended on the integrator. The Verlet algorithm [64], which is both time reversible and simple, is commonly used to perform the numerical integration. In this work, we used one variant of this algorithm called leapfrog Verlet. The name leapfrog comes from one of the ways to write this algorithm, where positions and velocities "leap over" each other. The leapfrog Verlet algorithm requires values of position $\mathbf{r}$ and force $\mathbf{f}$ vectors at time t while the velocities $\mathbf{v}$ are half a time step behind $(t - \frac{1}{2}\Delta t)$. The first step is to calculate the velocities at $t + \frac{1}{2}\Delta t$ by integration of the force:

$$v(t + \frac{1}{2}\Delta t) = v(t - \frac{1}{2}\Delta t) + \frac{\Delta t}{m} f(t) \tag{2.38}$$

The positions are then calculated using the new velocities:

$$r(t + \Delta t) = r(t) + \Delta t v(t + \frac{1}{2}\Delta t) \tag{2.39}$$

It is usually required to have the velocity at time t because properties such as total energy

of the system are depended on both position and velocity of atoms. In the leapfrog Verlet algorithm, the velocity at t is calculated by taking average of $v(t - \frac{1}{2}\Delta t)$ and $v(t + \frac{1}{2}\Delta t)$.

2.3.1 Simulation at different ensembles

In statistical mechanics, an ensemble is defined as a collection of all possible systems which have different microscopic states but have an identical macroscopic or thermodynamic state. Similarly, an ensemble average is the average taken over a large number of ensembles of the system considered simultaneously. Molecular dynamics provides the time evolution of the microscopic state of the system under the study. On the other hand, an experimental observable is usually obtained from a large number of replicas of the macroscopic sample which provides ensemble average of an observable. The connection between MD results and experiments can be made through the ergodic hypothesis, which states that over long periods of time, the time average of observable A equals its ensemble average :

$$A_{obs} = \langle A \rangle_{ens} = \lim_{t \to \infty} \langle A \rangle_t \tag{2.40}$$

This means that to make a relation between MD results and experiments, it is necessary to let the simulated system evolve in the phase space for a sufficiently long time and fulfill the quasi-ergodic theorem. Considering different thermodynamic parameters we can define four ensembles:

- Microcanonical ensemble (NVE) : The thermodynamic state characterized by a fixed number of atoms, N, a fixed volume, V, and a fixed energy, E which corresponds to an isolated system.
- Canonical Ensemble (NVT): Thermodynamic state in which number of atoms, N, volume, V, and a temperature, T are fixed.
- Isobaric-Isothermal Ensemble (NPT): This ensemble is characterized by a fixed number of atoms, N, a fixed pressure, P, and a fixed temperature, T.
- Grand canonical Ensemble (μVT): The ensemble characterized by a fixed chemical potential, μ, a fixed volume, V, and a fixed temperature, T.

Handling the NVE ensemble is tractable since MD by definition enables the conservation of energy. However, some modifications are necessary to fix other thermodynamic quantities, e.g. the temperature or pressure. There are three distinguished approaches to control the thermodynamic ensembles in MD:

1. Strong-coupling control: the system variable couples to the thermodynamic quantity is scaled to give exact preset derived value

2. Weak-coupling control: the system variable couples to the thermodynamic quantity is corrected at each integration step to move the system towards derived value of the thermodynamic quantity

3. Stochastic control: some degrees of freedom are added to the equation of motion and they are modified in order to give desire distribution to the system variable.

4. Extended system methods: variables representing an external system which fix the desired thermodynamic quantity are added to the Hamiltonian and the equations of motion are derived from the extended Hamiltonian.

The first two method are deterministic, stable and easy to implement, but they cannot capture the fluctuations of thermodynamic quantities. It means the sampling of the system is not accurate which is troublesome when the dynamics of the system is of interest. Stochastic thermostats are safer options and there is still ongoing research in this field mostly because these thermostats are proven to satisfy ergodicity. However, the common stochastic thermostats, like Andersen thermostat, are disable to preserve the kinetics of the system yet. The extended system methods are the most accurate and implemented controls which can rigorously prob dynamics in the course of MD simulations. In this study, temperature and pressure are controlled in this scheme using Nosé-Hoover thermostat and barostat.

Nosé-Hoover thermostat

The Nosé-Hoover thermostat is a name given to the algorithm proposed by Hoover [65] to improve the original Nosé formulation for the NVT ensemble [66]. Let's first review the idea of Nosé to simulate canonical ensemble.

Nosé showed that the canonical distribution can be generated with smooth, deterministic, and time-reversible trajectories [65]. He assigned additional generalized coordinate s and its conjugate momentum p_s to the heat bath. s is defined to be the scaling factor of velocities

$$\mathbf{v} = s\frac{d\mathbf{r}}{dt} = s\frac{\mathbf{p}}{m} \tag{2.41}$$

the kinetic and potential energies associated with s also are defined as

$$U_s = (N_f + 1)k_B T_0 \ln s, \quad K_s = \frac{1}{2}Q\frac{ds}{dt} = \frac{p_s^2}{2Q} \tag{2.42}$$

where Q is effective mass of the thermostat, T_0 is the temperature of the heat bath (desired

temperature) and N_f is the number of degrees of freedom in the system. Nosé's augmented Hamiltonian then can be written as

$$H_{Nosé} = K(\mathbf{p}) + U(\mathbf{r}) + \frac{1}{2}Q\frac{ds}{dt} + \frac{p_s^2}{2Q}(N_f+1)k_BT_0\ln s \tag{2.43}$$

Accordingly, the Hamiltonian equations of motion for the extended system would be

$$\begin{aligned}
\frac{d\mathbf{r}_i}{dt} &= \frac{\mathbf{p}_i}{m_i s^2} \\
\frac{d\mathbf{p}_i}{dt} &= \mathbf{f}_i \\
\frac{ds}{dt} &= \frac{p_s}{Q} \\
\frac{dp_s}{dt} &= \sum_i \frac{\mathbf{p}_i}{m_i s^3} - (N_f+1)\frac{k_BT_0}{s}
\end{aligned} \tag{2.44}$$

The Nosé thermostat treats the extended system as an NVE ensemble. He proved that it yields NVT ensemble for the system in ($\mathbf{r}$, $\mathbf{p}$/s) coordinates, which was of course the whole point of the definitions of additional coordinates (s,p_s). The Nosé's Hamiltonian can generate canonical ensemble independent of Q however, this parameter controls the efficiency and accuracy of coupling.

Nosé thermostat was a major advance but it has one problem: the scaling of velocity with s leads to scaling of time. The Hoover improvement to the Nosé formulation was to avoid time scaling by replacing s with thermodynamic friction coefficient $\zeta = p_s/Q$. Nosé added one degree of freedom to the system by introducing s. Hoover removed that degree of freedom by taking the formulation back to the real time. The equation of motion in Hoover's version after applying ζ and replacing Nosé's (N_f+1) with N_f is read

$$\begin{aligned}
\frac{d\mathbf{r}_i}{dt} &= \frac{\mathbf{p}_i}{m_i} \\
\frac{d\mathbf{p}_i}{dt} &= \mathbf{f}_i - \zeta\mathbf{p}_i \\
\frac{d\zeta}{dt} &= \frac{1}{Q}\left(\sum\frac{\mathbf{p}^2}{m} - N_f k_BT_0\right) \equiv \frac{1}{\tau_T^2}\left(\frac{T(t)}{T_0} - 1\right)
\end{aligned} \tag{2.45}$$

The effective mass of thermostat is usually defined as $Q = N_f k_B T\tau_T^2$ where τ_T is the time constant of thermostat. The friction coefficient, ζ, is controlled by the first order differential equation which is a function of velocity, $\mathbf{v}$. As a result, it is important to let $\mathbf{v}$ reach self consistency through more iterations when implementing Nosé-Hoover thermostat in a leapfrog scheme. Corresponding Hamiltonian to the Hoover formulation which is equivalent

to the Helmholtz free energy can be written as

$$H_{NVT} = A = K(\mathbf{p}) + U(\mathbf{r}) + \frac{1}{2}Q\zeta^2 + N_f K_B T \int_0^t \zeta(t')dt' \tag{2.46}$$

In this study this formulation which is called Nosé-Hoover thermostat is used in all molecular dynamics simulation to control the temperature.

Nosé-Hoover barostat

The idea of extended system can also be applied to include external constant pressure. This idea was first developed by Anderson [67]. In the original Andersen method, the isotropic simulation cell is allowed to change its size but not the shape to control the system pressure. Parrinello-Rahman extended the Anderson method to allow the cell shape change [68]. Similar to his thermostat, Nosé added a new degree of freedom to the Andersen dynamics which generates NPT ensemble through scaling of time. Hoover proposed a straightforward method to extend his formulation for canonical ensemble to the isothermal-isobaric case [65]. This was done by introducing a new reduced coordinate $x \equiv \frac{r}{V^{1/D}}$ for D dimensional system. The equation of motion 2.45 now can be extended as

$$\begin{aligned}
\frac{d\mathbf{x}_i}{dt} &= \frac{\mathbf{p}_i}{m_i V^{1/D}} \\
\frac{d\mathbf{p}_i}{dt} &= \mathbf{f}_i - (\eta + \zeta)\mathbf{p}_i \\
\frac{d\zeta}{dt} &= \frac{1}{\tau^2}\left(\frac{T(t)}{T_0} - 1\right) \\
\frac{d\eta}{dt} &= \frac{1}{Q}V(P(t) - P_0) \\
\frac{dV}{dt} &= D\eta V
\end{aligned} \tag{2.47}$$

While the canonical case is well reproduced by Hoover formulation, the NPT simulation using Equation 2.47 results in a distribution function which does not sample exactly the NPT ensemble. Melchionna et al. solved this problem by modifying Hoover formulation via introducing the effective mass of barostat [69]:

$$
\begin{aligned}
\frac{d\mathbf{r}_i}{dt} &= \frac{\mathbf{p}_i}{m_i} + \eta(\mathbf{r}_i + \mathbf{R}_0) \\
\frac{d\mathbf{p}_i}{dt} &= \mathbf{f}_i - (\eta + \zeta)\mathbf{p}_i \\
\frac{d\zeta}{dt} &= \frac{1}{\tau^2}\left(\frac{T(t)}{T_0} - 1\right) \\
\frac{d\eta}{dt} &= \frac{1}{Q'}V(P(t) - P_0) \\
\frac{dV}{dt} &= D\eta V
\end{aligned}
\tag{2.48}
$$

where $Q' = N_f k_B T \tau_p^2$ is the effective mass of the barostat, τ_p^2 is the barostat time constant, and $\mathbf{R}_0$ is the center of mass of the system. Corresponding Hamiltonian which is equivalent to Gibbs free energy can be written as

$$
H_{NPT} = G = K(\mathbf{p}) + U(\mathbf{r}) + \frac{1}{2}Q\zeta^2 + \frac{1}{2}Q'\eta^2 + \int_0^t (N_f K_B T \zeta(t') + k_B T_0)dt' \tag{2.49}
$$

In this study, Melchionna modification of the Hoover algorithm which is called Nosé-Hoover barostat is used to control pressure in MD simulations.

2.3.2 Periodic boundary condition

The length-scale of any atomistic simulation is limited meaning the finite number of atoms can be handles in each simulation cell. Physically, this means a large fraction of the atoms is on the surface or affected by the surface. This is not an issue when we are interested in the properties of an isolated system like free standing nanoparticles in vacuum. In fact, modeling the surface effect is what we want in these cases. However, this arrangement is not satisfactory when the goal of simulation is to model bulk properties. It is not practical to increase the size of the MD simulations cell to the sizes in which bulk properties can be modeled in a single simulation cell. The problem of surface effect can be overcome by applying periodic boundary condition (PBC) [64]. In this method, the simulation cell is replicated to make translated images of itself. When an atom moves in the original box during the simulation, its periodic images in neighboring cells move in the exact same manner. Thus if an atom passes one of the cell walls, one of its images enters the original cell from the opposite wall. A two dimensional representation of PBC is shown in Figure 2.6.

Although PBC removes the unwanted effect of the boundaries, some care still should be taken to avoid interaction of atoms in the original cell with their images. This effect which is called the minimum image convention is specially important for the non-bonded interactions. If the cell dimensions are smaller than the cut-off of the non-bonded interactions, atoms in

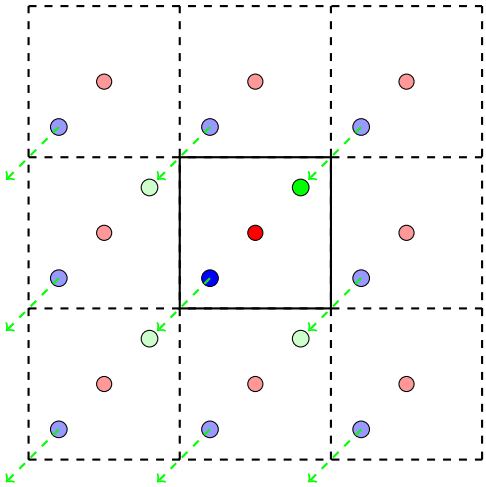

Figure 2.6: Periodic boundary condition representation in 2D space. The green arrow shows the movement of an atom out of the box. Once one atom moves out of the original box, one of its images enters the box from opposite boundary.

the original cell would feel the effect of their images. As a rule of thumb, the simulation cell dimensions should be at least twice the cut-off distance. By its very nature, Ewald summation satisfies the minimum image convention but, PBC should be used carefully if other methods are used to handle Coulomb long range interactions.

2.4 Density functional theory

As mentioned in Section 1, the most accurate simulation tools in the atomic level are quantum mechanic calculations (first-principle methods). In this study, we used first-principle calculations with the density functional theory (DFT) nature to validate empirical potentials for our MD simulations. DFT as a higher level simulation method is commonly used to validate or derive the empirical potential parameters. In this section, we provide an overview on the theory behind DFT owing much to [22]. It is worth to mention that the purpose of this section is not to present a comprehensive review of all the science behind DFT technique but, a short and clear representation of the basic equations important to understand how DFT works.

The key difference between an atomistic simulation and a quantum mechanical method is that in quantum mechanics atoms are treated as systems made of nuclei and electrons. As a result, now we need to know the position of both electrons and nuclei to calculate the energy of a many-atom system. A key property of atoms which helps applying quantum mechanics is that atomic nuclei is much heaver than an individual electron. This fact enables us to use Born-Oppenheimer approximation and separate electrons and nuclei into two apart mathematical problems. First step is to find the lowest energy state of elec-

trons in field of fixed position nuclei. This state is called *ground state* of electrons and ground state energy, E, can be expressed as a function of nuclei positions. Calculating the ground state energy of electrons requires to solve Schrödinger's equation. The most famous representation of Schrödinger's equation is $\hat{\mathrm{H}}\Psi = E\Psi$ which is the time independent and non-relativistic form. In this equation, H is the Hamiltonian operator and Ψ is a set of solutions, or eigenstates, of the Hamiltonian. Each Ψ_i has an associated eigenvalue, E_i that satisfies the equation. Hamiltonian for a many-atom system can be expressed as

$$\hat{H} = \frac{h^2}{2m}\sum_{i}^{N}\nabla_i^2 + \sum_{i}^{N}V(\mathbf{r}_i) + \sum_{i}^{N}\sum_{j<i}U(\mathbf{r}_i,\mathbf{r}_j) \tag{2.50}$$

where the three terms are kinetic energy of electrons, interaction between electrons and nuclei, and interaction between electrons, respectively. Note that the electron spin is neglected in this presentation in order to simplify the notation. The electron-electron interaction term in Hamiltonian is the most critical and complicated to solve. The form of this term tells us that an individual electron wave function, ψ_i cannot be found unless we consider all other individual electron wave functions in the system simultaneously. We can define the probability that N electrons are in a particular sets of coordinates, $\{\mathbf{r}\}$, as $\psi^*(\{\mathbf{r}\})\psi(\{\mathbf{r}\})$ where the asterisk indicates the complex conjugate. Accordingly, the density of electrons at the particular position in the space can be written in terms of individual electron wave functions as

$$n(\mathbf{r}) = 2\sum_{i}^{N}\psi_i^*(\mathbf{r})\psi_i(\mathbf{r}) \tag{2.51}$$

$n(\mathbf{r})$ is the function of three coordinates but it contains considerable amount of quantum information. It means that if we can reformulate the Schrödinger's equation in a way that its components become functions of electron density rather than wave functions, the dimensions of the Schrödinger's equation decreases from 3N to three. This idea divides electronic structure methods into two main categories: *wave-function-based methods* whose object is the calculation of the full electron wave functions and the *density functional theory* methods which use electron density to find the ground state energy.

2.4.1 DFT formulation

The entire field of DFT is based on the two fundamental theorems developed and proved by Kohn and Hohenberg [70]. These theorems enable us to reformulate the problem of finding the ground-state energy in terms of the total density of the electrons rather than by dealing with the many-body wave functions. Kohn-Hohenberg theorems can be written as

- The ground-state energy from Schrödinger's equation is a unique functional of the electron density.
- The electron density that minimizes the total energy of the functional is the exact ground-state density.

The first theorem states that the ground-state electron density can determine all ground-state properties including the energy and the wave function through a mathematical relation which has a functional form. This tells us that the energy functional exists but it does not give any information about its formulation. The second theorem gives us a very important characteristic of the energy functional: if we know the form of the functional, electron density which is obtained from its energy minimization is the "true" solution of the Schrödinger's equation.

We can divide the energy functional into three parts: the kinetic energy, the interaction with the external potential due to positively charged nuclei, and the electron-electron interaction.

$$E[n(\mathbf{r})] = K[n(\mathbf{r})] + U_{ee}[n(\mathbf{r})] + V_{ext}[n(\mathbf{r})] \tag{2.52}$$

V_{ext} is system dependent so, the contribution of V_{ext} can be written explicitly in terms of the electron density as soon as we define the system

$$V_{ext}[n(\mathbf{r})] = \int V(\mathbf{r})n(\mathbf{r})dr \tag{2.53}$$

We still need to define the kinetic and electron-electron functionals. Let's consider an imaginary system in which electrons do not interact. For such a system the kinetic energy and electron density are well defined:

$$\begin{aligned} K_s[n(\mathbf{r})] &= \frac{h^2}{m}\sum_i^N \int \psi_i^* \nabla^2 \psi_i d^3r \\ n(\mathbf{r}) &= \sum_i^N |\psi_i(\mathbf{r})|^2 \end{aligned} \tag{2.54}$$

The interaction of an individual electron with other electrons can also be formulated with the classical Coulomb interaction:

$$U_H = e^2 \int \frac{n(\mathbf{r}')}{\mathbf{r} - \mathbf{r}'} d^3\mathbf{r}' \tag{2.55}$$

U_H which is called the Hartree potential, includes the self-interaction contribution because the electron we are considering is also part of the total electron density. Now, we can rewrite the energy functional as

$$E[n(\mathbf{r})] = K_s[n(\mathbf{r})] + U_H[n(\mathbf{r})] + V_{ext}[n(\mathbf{r})] + E_{XC}[n(\mathbf{r})] \tag{2.56}$$

where E_{XC} is the exchange-correlation energy which is the sum of the error made in using a non-interacting kinetic energy and the error caused by the unphysical self-electron-electron interaction. Now it is the time to introduce the next milestone in developing DFT, the work of Kohn and Sham [71]. Kohn and Sham showed that the task of finding the right electron density can be changed into solving a set of equations in which each equation only involves a single electron.

$$\left[\frac{h^2}{2m}\nabla^2 + v_{ext}(\mathbf{r}) + v_H + v_{xc}(\mathbf{r})\right]\psi_i(\mathbf{r}) = \varepsilon_i\psi_i(\mathbf{r}) \tag{2.57}$$

where v_{XC} is the local multiplicative potential which is the functional derivative of the exchange-correlation energy with respect to the density:

$$v_{xc}(\mathbf{r}) = \frac{\delta E_{xc}(\mathbf{r})}{\delta n(\mathbf{r})} \tag{2.58}$$

To solve the Kohn-Sham set of equations, we need to define the Hartree potential, v_H, and to define the Hartree potential we need to know the electron density, $n(\mathbf{r})$. However, the electron density itself is the function of single-electron wave functions, ψ_i, and to find the ψ_i we again need to solve Kohn-Sham equations! To break this circle the problem is usually treated with the following iterative algorithm:

1. Define an initial, trial electron density, $n_j(\mathbf{r})$.
2. Solve Kohn-Sham equation and fine single-electron wave functions, $\psi_i(\mathbf{r})$.
3. Calculate $n_{j+1}(\mathbf{r})$ using single-electron wave functions and Equation 2.54.
4. Compare $n_j(\mathbf{r})$ with $n_{j+1}(\mathbf{r})$. If the two densities are the same (or practically close), $n_j(\mathbf{r})$ is the ground-state electron density, and it can be used to compute the total energy. Otherwise, update the $n_j(\mathbf{r}) = n_{j+1}(\mathbf{r})$ and begin the process from step 2.

Kohn-Sham equations nicely formulate the problem of finding the ground state energy but, there is still one term in this equation which need to be specified: the exchange-correlation function.

2.4.2 Exchange-correlation functional

The existence of the exchange-correlation functional is guaranteed by the Hohenberg-Kohn theorem but its general form is still one of the biggest mysteries in the quantum world. There is one specific case however, in which this functional can be derived. This system is the homogeneous electron gas (HEG) in which the electrons are subject to a constant external potential and electron density is constant at all points in space; $n(\mathbf{r}) = C$. The exchange-correlation energy can be decomposed into exchange and correlation terms linearly:

$$E_{xc}[n(\mathbf{r})] = E_x[n(\mathbf{r})] + E_c[n(\mathbf{r})] \tag{2.59}$$

The exchange term for the HEG, ϵ_x, can be explained by a simple analytic form

$$\epsilon_x[n(\mathbf{r})] = -\frac{3}{4}\left(\frac{3}{\pi}\right)^{1/3} \int n(\mathbf{r})^{4/3} d\mathbf{r} \tag{2.60}$$

Analytic functional form for the correlation term of the HEG, ϵ_c, is not known but numerical quantum Monte Carlo calculations could provide accurate values of the correlation energy. Several approaches have been proposed to calculate analytical form of ϵ_c based on the fitting different formulations on the quantum Monte Carlo results.

Knowing ϵ_{xc}, now E_{XC} at each position in the space can be approximated to be the exchange-correlation potential of HEG with the same electron density as that position. Thus, we can write

$$E_{xc}[n(\mathbf{r})] = \int n(\mathbf{r})\epsilon_x[n(\mathbf{r})] d\mathbf{r} \tag{2.61}$$

This approximation uses only the local density to define the approximate exchange-correlation functional, so it is called the local density approximation (LDA). The LDA gives us a way to completely define the Kohn-Sham equations, and many material properties such as structure, vibrational frequencies, elastic moduli and phase stability have been successfully predicted using it. However, it is important to remember that the results obtained by LDA do not exactly true solutions of Schrödinger's equation because we are not using the true exchange-correlation functional.

If the local gradient in the electron density is also used in addition to the local electron density, the resultant exchange-correlation functional is called generalized gradient approximation (GGA). Since there are many ways to include information from the gradient of

the electron density in a GGA functional, large number of distinct GGA functionals are defined. The next big step in improvement of exchange-correlation functional approximation was the development of the exact exchange functional. The exact exchange energy is also called Hartree-Fock exact exchange energy because it is formulated using Kohn-Sham orbitals, $\phi_i(\mathbf{r})$, instead of electron density, $n(\mathbf{r})$.

$$E_x^{HF}(\mathbf{r}) = -\frac{1}{2} \sum_{i,j}^{\text{occupied states}} \int dr dr' \frac{\phi_i^*(\mathbf{r}')\phi_j^*(\mathbf{r})\phi_j(\mathbf{r}')\phi_i(\mathbf{r})}{|\mathbf{r}-\mathbf{r}'|} \tag{2.62}$$

If a exchange-correlation functional is constructed as a linear combination of the Hartree-Fock exact exchange functionals and any number of exchange and correlation density functionals, it is called hybrid exchange-correlation functional. One of the most popular hybrid functionals is B3LYP: Becke, three-parameter, Lee-Yang-Parr:

$$E_{xc}^{B3LYP} = E_{XC}^{LDA} + \alpha_1(E_x^{HF} - E_x^{LDA}) + \alpha_2(E_x^{GGA} - E_x^{LDA}) + \alpha_3(E_c^{GGA} - E_c^{LDA}) \tag{2.63}$$

where E_x^{GGA} is the Becke 88 exchange functional, E_c^{GGA} is the Lee-Yang-Parr correlation functional, and α_1, α_2, and α_3 are three numerical parameters chosen empirically to optimize the functional to predict set of molecular properties (bond lengths, formation energies, etc.) [22].

2.4.3 Basis set

Regardless of the quantum chemical calculation method we use, the essential input is the representation of the molecular orbitals. Basis set is a mathematical representation of the molecular orbitals within a molecule. It can also be interpreted as the set of rules which limit each electron position in particular region of space. In general, an atomic orbital may be formulated as a product of a radius, r and an angle-dependent component such as

$$\phi_{nlm}(\mathbf{r}) = R_n(r)Y_{lm}(\theta,\varphi) \tag{2.64}$$

where n is the main quantum number, l is the angular-momentum quantum number, m is magnetic quantum number of the individual atom and $Y_{lm}(\theta,\varphi)$ is the spherical harmonics function which give atomic orbitals their characteristic shapes [72]. The first approximation for the orbital shape is developed by Slater [73]. The general expression for Slater-Type Orbitals (STO) is

$$\phi_{abc}^{STO}(x,y,z) = Nx^a y^b z^c e^{-\zeta r} \tag{2.65}$$

where N is a normalization constant, a, b, c are constants that control angular momentum ($l = a + b + c$) and ζ controls the orbital width. STOs are very reasonable approximations for the true atomic orbitals but they are slow in computing due to their ill-behaving exponential function. Boys proposed the Gaussian Type Orbitals (GTO) which are much faster computationally [74]:

$$\phi_{abc}^{STO}(x, y, z) = N x^a y^b z^c e^{-\zeta r^2} \tag{2.66}$$

The advantage of the GTO approach is that numerical evaluation of integrals is much easier than with STOs. However, GTOs approximate the orbital shapes poorly comparing to STOs. To compensate for this loss of accuracy, it is possible to use a linear combination of enough GTOs to mimic a STO which is usually called STO-nG. If a basis set uses only one STO, GTO or STO-nG to construct each atomic orbital, it is called *minimal* basis set. Similarly, double-zeta, triple-zeta and ... are basis sets that use two, three or more basis functions for each atomic orbital.

Since it is computationally expensive to use double-zeta for every orbital, double-zeta is usually considered only for the valence orbitals. The basis sets which split the inner and outer orbitals are called split-valence basis sets. The common naming of split-valance basis sets is like $\mathrm{A}_1 - \mathrm{A}_2\mathrm{A}_3G$ (such as 3-21G) where A_1 is the number of GTO forming STO-nG of the inner orbitals, and A_2 and A_3 are the number of GTO in the first and second STO-nGs in the double-zeta valance orbitals.

When the atoms are brought close together, the polarization effect distorts the shape of the atomic orbitals. This shape distortion can be seen as changing in the pure nature of an orbital, like s, to a hybrid nature like s + p. Polarized basic sets which usually recognized by adding asterisks to the name of split-valance basis sets, (like 6-21G*) take this effect into the account.

When an atom is in an anion or in an excited state, it is important to model the valance electrons more accurately. To do this, diffuse basis sets are utilized which have small ζ exponents. Using diffuse basis sets is specially important when modeling anions as it can affect the results significantly. Diffuse basis sets are usually represented by the '+' signs. The terminology we used to name basis sets is developed by Nobel Prize-winning theoretical chemist, John Pople and the basis sets with this structure were developed in his group.

Let's end this section by emphasizing on an important thing to remember when reporting

the results of a DFT calculation: the results of DFT are highly depended on the functional and basis set used for calculations. Thus, these parameters should be reported along with the simulation results.

Chapter 3

Empirical potentials of ZnS

3.1 Introduction

The technological importance of ZnS comes from two main reasons: 1) it is an important II-VI semiconductor and 2) the main resource for production of zinc metal. The former is due to the large direct band gap of ZnS which can be readily controlled by tailoring the structure and configuration of particles, especially in nanoscale [75]. This property, which can lead into wide range of optoelectronic applications, has been a motivation of various studies on ZnS nanostructures over the past few decades. Although the rapid growth of nanotechnology has enabled us to fabricate nanostructures with a variety of geometries, our understanding of their structural and configuration evolution is still limited. For ZnS nanostructures in particular, uncontrollable changes in structure and configuration which can occur in ambient conditions have been a challenging issue questioning reliability of their optoelectronic applications[20]. Prediction of ZnS nanomorphology is inherently difficult experimentally as thermodynamic properties of nanomaterials differ from bulk materials greatly [42]. In the past two decades, atomistic simulation methods have become important tools to compliment experimental studies by providing fundamental understanding of mechanisms of structural and configurational evolutions in ZnS nanostructures. Some of the computational studies on ZnS nanostructures were reviewed by Hamad et. al. [76] and Feigl et. al. [20]. Several other works on ZnS nanostructures studied equilibrium configurations of nanoparticles [2, 42, 43] and nanowires [77], effect of environment [78, 79] and pressure [80] on structural transformation of nanoparticles, and mechanical properties of ZnS nanowires and thin film [81].

ZnS mineral, sphalerite, as the primary source of zinc metal is mainly recovered by flotation process. Unlike most of the other sulfide minerals, sphalerite does not respond well to flotation. Therefore, sphalerite flotation requires activation by heavy-metal ions to

A modified version of this chapter has been published as **M. Khalkhali, Q. Liu and H. Zhang**, "**A comparison of different empirical potentials in ZnS**", *Modeling Simul. Mater. Sci. Eng.*, vol. 22 (2014), 085014 (22pp).

enable adsorption of collectors [82]. The activation of sphalerite has been surveyed extensively; however, conflicts still remain in regard to the mechanism of activation on the atomic scale. Computational studies of the ZnS activation process is mainly focused on the effect that the presence of activators has on the surface properties. The influence of the presence of lead [83] iron and copper [84, 85] species on (110) surface properties was studied using quantum mechanical methods. This technique is also reported in the studies of interaction of collectors and activators on sphalerite surface [86, 87].

Although atomistic simulation methods have proven to be promising approaches to address various problems so far, it should be kept in mind that their applicability is limited mainly by two factors: their accuracy in modelling interatomic interactions and their computational demands. Electronic structure methods based on quantum mechanic calculations are the most accurate available methods. Theory of quantum mechanics relies on the fact that energy and all other related properties of a system can be calculated by solving the Schrödinger's equation. However, exact solution of Schrödinger's equation is only feasible for the simplest systems. As a result, different electronic structure methods have been developed to estimate the solution of the Schrödinger's equation by means of different mathematical approximations[21]. Despite all the developments in hardware and software technologies, the computational expense of the first-principle methods is still a crucial limitation which makes them technically impractical for systems beyond hundreds of atoms [22].

Molecular mechanic methods which use empirical potentials and laws of classical mechanics to model atomic interactions are the best alternative, offering a compromise between computational speed and accuracy [88]. Molecular dynamics (MD) simulations in particular, enable the study of dynamics and atomic level evolutions of relatively large systems (up to millions of atoms or even more) in a practical time period (nanoseconds). This can results in calculation of dynamical properties like heat and mass transfer, diffusion, surface absorption, and geometry evolution of nanoparticles. MD also can be applied to derive relations between thermodynamic quantities, namely, temperature, pressure, volume, and energy[89]. Overall, MD enables the study of systems and processes with more realistic dimensional and time scales. The accuracy of molecular mechanic methods, however, is greatly dependent on the reliability of the empirical potential they use to model interatomic interactions. As a result, it is quite important to verify the reliability of empirical potentials by testing their ability to reproduce different material properties.

In this paper we focus on five empirical potentials proposed for ZnS in literature. Different material properties calculated using these potentials are compared with the corresponding experimental values or higher order first-principle calculations. ZnS properties studied in this paper are important factors in the ZnS applications mentioned above. As a result,

the ability to reproduce these properties can be considered to be good criteria to choose the appropriate empirical potential for computational studies of ZnS.

The five different potential functions of ZnS studied in this paper are developed by Wright and Jackson [90], Hamad et. al. [37], Wright and Gale [91], Grünwald et. al. [88], and Benkabou et. al. [92]. To avoid redundancy, we will name potentials by their short terms as IP1, IP2, IP3, IP4 and IP5 respectively. The first four potential functions are based on the Born model of solids, which assumes the interatomic potential of ionic-bonding materials consists of two main parts: long-range electrostatic and short-range energies. Thus, the potential energy for each atom can be written as:

$$U_i = \frac{1}{2}\sum_{j\neq i}\frac{q_i q_j}{4\pi\epsilon_0 r_{ij}} + \frac{1}{2}\sum_{j\neq i} V_{ij}(r_{ij}) + multibody\,potentials \tag{3.1}$$

where the first and second terms are Coulomb and pair potentials. The Ewald summation method [57] is used in this paper to evaluate the long-range Coulombic interactions. The Shell model is also used in the first three potentials to add the prioritization effect. The shell model, proposed by Dick and Overhauser [60], defines a simple mechanical description to handle polarization. In this model, ions are considered to have two parts: the core which carries atomic mass and the shell which takes the polarizable charge. Core and shell are connected by a spring so the shell can displace from the core to model polarizability. The sum of the core and shell charges represents the total charge of ion and they interact with harmonic spring potential[93]:

$$V_{core-shell} = \frac{1}{2}k_s r^2 \tag{3.2}$$

In a potential developed by Benkabou et. al., a totally different approach than the Born model is applied. In this approach, parameters of Teresoff potential [94, 95], which is based on the bond ordering concept, are optimized to reproduce structural and mechanical properties of ZnS. These parameters are just introduced for Zn-S pairs and Zn-Zn and S-S interactions have not been taken into account.

Among the empirical potentials studied in this paper, IP1 and IP2 have been used in molecular dynamics and lattice dynamics simulations repeatedly. IP1 has been used to study the surface properties of ZnS [2, 96], mechanical properties of ZnS nanowires and thin films [81], the structural evolution of ZnS nanoparticles in vacuum [2], in presence of water [78], and during aggregation [97]. IP2 has also applied to study the structure of ZnS surfaces [37], nanoclusters and nanoparticles [3, 39], and embryonic growth in aqueous

solution [41]. A more through version of IP3 which also includes two-body parameters for Fe-S and Mn-S interactions, has been used to investigate mechanisms of uptake and incorporation of cadmium, iron and manganese impurities in sphalerite via lattice dynamics surface studies [98]. The pressure induced phase transformation in CdSe/ZnS Core/Shell nanocrystals, has been modelled via molecular dynamics study which implemented IP4 [80].

3.2 Structural and Mechanical Properties

Structural and mechanical properties of ZnS were calculated using different interatomic potential formulations and compared with experimental values. These properties are the main material characteristics used in the derivation of interatomic potentials. In the other words, potential parameters are optimized to fit calculated properties to the experimental ones. A powerful force field is the one that can predict more materials properties, especially those that are not used in the process of deriving potential parameters.

In potential derivation procedures, the lattice parameters which minimize the total energy of the system are usually optimized by fitting to experimental values. Experimental values are usually obtained at room temperature while the physical meaning of energy minimization is lowering the temperature down to 0 K. However, this process is commonly acceptable as thermal expansion in solids is negligible at low temperatures.

There are two main approaches to calculate elastic constants via atomistic simulation methods: 1) method based on strain (or stress) fluctuations and 2) the direct method which calculates elastic constants from stress-strain relation of material subjected to an external load. Fluctuation methods are based on the fact that elastic constants are equal to the second derivatives of the deformation energy with respect to strain:

$$\sigma_{ij} = \frac{\partial U}{\partial \epsilon_{ij}} \Rightarrow C_{ij} = \frac{\partial^2 U}{\partial \epsilon_i \partial \epsilon_j} \tag{3.3}$$

where U, ϵ, σ and C_{ij} are deformation energy, strain, stress and corresponding elastic constant, respectively. Thus, by subjecting the structure to twelve deformations (three pair of uniaxial and three pairs of pure shear) in a way that each deformation constructs a small fluctuation along one strain vector while keeping the rest zero, the elastic stiffness matrix can be calculated [99].

In the direct method, elastic constants are achieved via constant pressure MD. External pressure is applied in different directions to calculate corresponding elastic moduli. The

major advantage of the direct method is that it is potentially capable of considering the dynamics of the system. However, variation of strain and stress during MD simulations makes it necessary to use average values to calculate stress-strain behaviour. Consequently, one needs to run long simulations and make sure that strain equilibrates before each step of stress [100].

In this study we used GULP code [99] which applies the fluctuation method within the lattice dynamics calculations. The lattice constant values at 300 K and 0 GPa are also calculated using constant pressure molecular dynamic simulation within DL_POLY classic code [101]. Details of MD simulations are explained in section 3.6. Although some of the lattice constant and mechanical properties are reported for these potentials in their original papers, we recalculated all structural and mechanical constants. This helps us to provide more consistent comparison between different potentials.

Three different crystal structures have been reported for ZnS in literature. Under standard conditions, ZnS can adopt two crystal structures which are zinc-blende (ZB:$F\bar{4}3m$) and wurtzite (WZ:$P6_3mc$). Due to the similarity of unit cell volume and bond lengths, there is a small energy difference between these two structures. At higher pressures, the high density rocksalt structure (RS:$Fm\bar{3}m$) becomes more stable. Table 3.1 shows calculated lattice and mechanical constants for three ZnS phases for each potential. Values reported in the original papers (numbers in parentheses) and corresponding experimental results are also represented where available. As rocksalt phase is not stable in standard condition, the experimental value for lattice constant of this structure has been calculated by extrapolating lattice volume at higher pressures to 0 GPa [6].

Table 3.1: Comparison of mechanical and structural properties calculated via different potentials of ZnS (lattice parameters are in Å and mechanical properties are in GPa).

	IP1	IP2	IP3	IP4	IP5	exp.
			ZB			
a	5.403	5.410	5.450	5.475	5.367	
	(5.407)	(5.41)	(5.45)	(5.48)	(5.406)	
$a(300K)$	5.401	5.431	5.459	5.501	-	5.409[a], 5.412[b], 5.41[c]
C_{11}	91.834	105.563	107.060	106.200	98.435	107.1[d], 104.6[e], 94.2[c]
	(91.7)	(105.1)	(107.1)	(150.1)	(98.0)	
C_{12}	58.285	67.727	59.821	73.386	80.949	66.7[d], 65.3[e], 56.8[c]
	(58.2)	(67.8)	(59.4)	(51.4)	(73.0)	

Continued on the next page

Table 3.1 – Continue

	IP1	IP2	IP3	IP4	IP5	exp.
C_{44}	60.103 (44)	42.909 (43.1)	32.977 (33.2)	51.740 (62.2)	20.019	46.55[d], 46.13[e], 43.6[c]
B	69.468	80.339 (80)	75.128 (75.6)	84.324 (83.4)	86.778 (81.6)	74.8±3.2 f, 79.5[g]
			WZ			
a	3.867 (3.91)	3.876 (3.87)	3.894 (3.89)	3.895 (3.89)	3.795	
$a(300K)$	3.824	3.851	3.889	3.863	-	3.816[g], 3.85[c], 3.8230[k]
c	6.092 (6.05)	6.088 (6.10)	6.191 (6.20)	6.241 (6.26)	6.198	
$c(300K)$	6.247	6.291	6.312	6.353	-	6.252[g], 6.29[c], 6.2565[k]
C_{11}	124.556 (108.5)	124.720 (124.2)	110.722 (111.3)	130.568 (161.4)	107.444	124.2[h], 122.2[i], 131.2[c]
C_{12}	46.349 (54.9)	60.092 (59.8)	55.733 (55.6)	68.052 (53.8)	79.442	60.15[h], 59.1[i], 66.3[c]
C_{13}	42.484 (53.2)	59.092 (58.0)	58.739 (57.9)	56.769 (28.2)	73.426	45.54[h], 46.0[i], 50.9[c]
C_{33}	115.389 (86.8)	113.211 (113.0)	124.195 (126.4)	137.103 (213.1)	113.471	140.0[h], 138.5[i], 140.8[c]
C_{44}	40.270 (26.8)	37.403 (37.3)	37.525 (37.7)	32.459 (32.4)	12.504	28.64[h], 28.23[i], 28.6[c]
C_{66}	39.103 (34.4)	32.314	27.496	31.258 (53.8)	14.001	32.03[h], 32.4[c]
B	69.519	79.713	76.560 (76.4)	84.582 (82.3)	86.772	80.1[g], 75.8[j]
			RS			
a	5.075	5.050	5.376	5.194 (5.20)	4.754	5.06[b]
C_{11}	122.560	127.818	228.319	108.697 (73.2)	501.082	-

Continued on the next page

Table 3.1 – Continue

	IP1	IP2	IP3	IP4	IP5	exp.
C_{12}	77.298	81.177	76.840	88.973 (45.3)	0.000	-
C_{44}	77.298	96.671	67.046	88.973 (45.3)	11.522	-
B	92.385	96.724	127.333	95.548 (54.6)	167.027	103.6[b]

(a) Ref. [102] (b) Ref. [6] (c)Ref. [103]
(d) Ref. [104] (77 K) (e) Ref. [104] (298 K)
(f) Ref. [105] (g) Ref. [7] (h)Ref. [106]
(i) Ref. [107] (j) Ref. [108] (k)Ref. [109]

As seen in table 3.1, there is a wide range of experimental data values for mechanical properties. As mechanical properties are one of the main parameters used in derivation of empirical potentials, the values calculated by each potential is strictly dependent on corresponding experimental values used in derivation process. Likely due to the use of different calculation methods, there are a few noticeable differences between mechanical properties calculated in this study and those reported in original papers. Keeping in mind the inherent uncertainty of experimental results, IP2 potential seems to have better overall agreement with experimental lattice constants and mechanical properties of three ZnS phases.

As expected, all of the potentials overestimate 300 K lattice constant of zinc-blende phase since experimental results (which are obtained in room temperature) are fitted to those calculated via energy minimization. However, almost all potentials can reproduce experimental wurtzite lattice constants at 300 K. It can be seen that wurtzite lattice constant a is overstimulated by energy minimization while c is underestimated. Nevertheless, increasing temperature causes lattice constant to approach their experimental values. One improvement which can easily be applied to potential derivation methods by using lattice constants calculated by NPT MD simulations at 300 K and 0 GPa in the optimization procedure instead of those obtained via energy minimization.

3-body potentials are very short-ange in nature and usually do not go further than first neighbour atomic distance. Considering a Zn atom, first, second, third , and fourth neighbours are S, Zn, S, Zn atoms at $\frac{\sqrt{3}}{4}a$, $\frac{\sqrt{2}}{2}a$, $\frac{\sqrt{10}}{4}a$, and a distances, where a is the lattice

constant. In case of zinc-blende ZnS ($a = 5.41$), first, second, third and fourth neighbour distances would be $2.343\mathring{A}$, $3.825\mathring{A}$, $4.277\mathring{A}$, and $5.41\mathring{A}$, respectively. The atomic distances in wurtzite are similar to zinc-blende because of their alike densities. Therefore the cut-off distance of $6\mathring{A}$, which was proposed for IP3 potential, seems to be too high for 3-body interactions as it goes beyond the fourth neighbour. The effect of high 3-body cut-off is noticeable in rocksalt ZnS which is a more compact phase. As can be seen in table 3.1, there is a large difference between rocksalt properties calculated by IP3 and other potentials. We have tried different 3-body cut-offs for IP3 potential without changing the formulation itself and results are given in table 3.2.

Table 3.2: Effect of changing 3-body cut-off on structural and mechanical properties calculated via IP3 potential (lattice parameters are in Å and mechanical properties are in GPa).

	Zn-S 6.0 Å	Zn-S 3.0 Å
	ZB	
a	5.450	5.441
C_{11}	107.060	104.636
C_{12}	59.821	58.180
C_{44}	32.977	32.907
B	75.128	73.665
	WZ	
a	3.894	3.902
c	6.191	6.110
C_{11}	110.722	107.221
C_{12}	55.733	55.219
C_{13}	58.739	58.314
C_{33}	124.195	109.103
C_{44}	37.525	40.604
C_{66}	27.496	26.002
B	76.560	74.100
	RS	
a	5.376	5.200
C_{11}	228.319	140.585
C_{12}	76.840	96.586
C_{44}	67.046	79.523
B	127.333	111.252

Table 3.2 shows that changing 3-body cut-offs improves rocksalt properties predicted by IP3 potential. Except for C_{11} and C_{33} of wurtzite which become softer, it seems that changing 3-body cut-off has no significant effect on other properties of zinc-blende and wurtzite phases.

Using the shell model inherently causes MD simulations to become more complicated. Firstly, the shell model introduces a new specie into the system which will increase the simulation time. Additionally, handling shells in MD simulations requires more care especially in higher temperatures and pressures. We will discuss MD simulation of shell model in the section 3.6. Adding many-body terms in potential formulations can also slow down MD simulations. This made us interested in investigating how removing the shell model and 4-body term affects material properties predicted by IP2 and IP3 potentials. Table 3.3 compares the structural and mechanical properties before and after removing shell model and 4-body term from IP2 and IP3 potentials.

Table 3.3: Comparison of mechanical and structural properties calculated by IP2 and IP3 potential with and without shell model and 4-body potential (lattice parameters are in Å and mechanical properties are in GPa).

	IP2 (No Shell)	IP2	IP3 (No 4-bd)	IP3 (No Shell)	IP3
			ZB		
a	5.410	5.410	5.450	5.450	5.450
C_{11}	105.563	105.563	107.060	107.060	107.060
C_{12}	67.727	67.727	59.821	59.821	59.821
C_{44}	64.950	42.909	32.977	65.652	32.977
B	80.339	80.339	75.128	75.567	75.128
			WZ		
a	3.868	3.876	3.894	3.888	3.894
c	6.116	6.088	6.191	6.209	6.191
C_{11}	140.254	124.720	110.719	133.816	110.722
C_{12}	55.883	60.092	55.716	43.691	55.733
C_{13}	49.321	59.092	58.695	43.615	58.739
C_{33}	131.596	113.211	124.227	137.704	124.195
C_{44}	42.264	37.403	37.537	46.837	37.525
C_{66}	42.185	32.314	27.501	45.350	27.496
B	79.932	79.713	76.540	76.609	76.560
			RS		
a	5.050	5.050	5.376	5.376	5.376
C_{11}	127.818	127.818	228.316	228.319	228.319
C_{12}	81.177	81.177	76.816	76.840	76.840
C_{44}	96.671	96.671	67.048	67.046	67.046
B	96.724	96.724	127.316	127.333	127.333

Table 3.3 clearly shows that omitting 4-body potential from IP3 formulation does not significantly affect structural and mechanical properties. On the other hand, removing the shell model does show noticeable effect on wurtzite and zinc-blende properties for both potentials. In some cases, (IP2: zinc-blende C_{44} and wurtzite C_{11}, C_{44} and C_{66}, IP3: zinc-blende C_{44} and wurtzite C_{12}, C_{44} and C_{66}) removing the shell model results in deviations from the experimental values while other cases (IP2: wurtzite C_{13}, C_{33}, IP3: wurtzite C_{11}, C_{13} and C_{33}) approach to experimental values after removing the shell model.

3.3 Phonon dispersion

Calculation of phonon dispersion spectra in solid crystals is interesting as it can be used to obtain some material properties such as heat capacity, thermal expansion coefficient and phonon-electron interaction. Phonon-electron interaction is especially attractive in semiconductor materials like ZnS as it can govern the optoelectronic properties. Phonon dispersion data is also one of the material properties which can be readily used in empirical interatomic potential development. Since phonon data was not used as a fitting parameter in developing any of the potentials mentioned in this study, the ability of each potential to reproduce experimental data can be a good way to test them.

In this section, experimental phonon dispersion data of zinc-blende and wurtzite ZnS is compared with those calculated via empirical potentials. Phonon dispersion calculations were performed using the module within GULP software and experimental results were obtained from Raman scattering study of Cheng et. al. [4]. The details of calculation process can be found elsewhere[99]. However, it is important to mention that calculation of Born effective charge and high frequency dielectric constant tensor is necessary in ionic materials to add a correction responsible to break degeneracy of the Transverse Optical (TO) and Longitudinal Optical (LO) modes. Thus, theses tensors are calculated for each potential formulation and represented in table 3.4 along with corresponding experimental values.

Table 3.4: Born effective charges and high frequency dielectric constants.

	IP1	IP2	IP3	IP4	IP5	exp.
			ZB			
Z^*_{xx}	0.66	1.82	1.46	1.18	-	2.15[a]
ϵ^{∞}_{zz}	4.14	3.35	4.9	-	-	5.2[b] , 4.4[c]
			WZ			
Z^*_{xx}	0.63	1.80	1.44	1.18	-	
Z^*_{zz}	0.72	1.86	1.55	1.18	-	
ϵ^{∞}_{xx}	4.01	3.32	4.82	-	-	
ϵ^{∞}_{zz}	4.43	3.41	5.09	-	-	

(a) Ref. [110] (b) Ref. [111] (c)Ref. [112]

Table 3.4 shows that IP1 potential underestimates ZnS ionicity compared to the experimental results. As mentioned above, the Born effective charge of IP4 ZnS, which does not include the shell model, is equal to the nominal charge of cores. Atoms are not charged

in IP5 so Born effective charge can not be defined. For both IP1 and IP4, the dielectric constant tensor is equal to unit matrix. Using the information calculated in table 3.4, phonon dispersion relation for zinc-blende and wurtzite phases are calculated and shown in figure 3.1. Phonon band structures are drawn along ΓX and ΓA directions for ZB and WZ structures respectively where Γ, X, and A are high symmetry points in the Brillouin zone. Γ refers to the centre of the Brillouin zone (k = 0,0,0) while X and A are k = $0, \frac{1}{2}, 0$ and k = $0, 0, \frac{1}{2}$ in corresponding Brillouin zones of zinc-blende and wurtzite structures respectively. In figure 3.1, solid lines represent experimental results obtained from Raman scattering study of Cheng et. al. [4] and filled diamonds are values calculated using interatomic potentials.

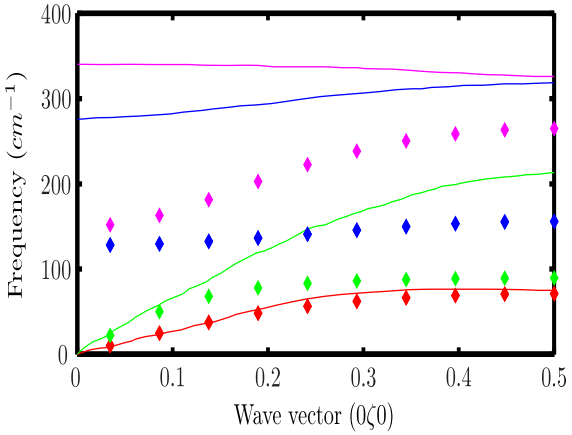
Frequency (cm^{-1})
Wave vector (0ζ0)

(a)

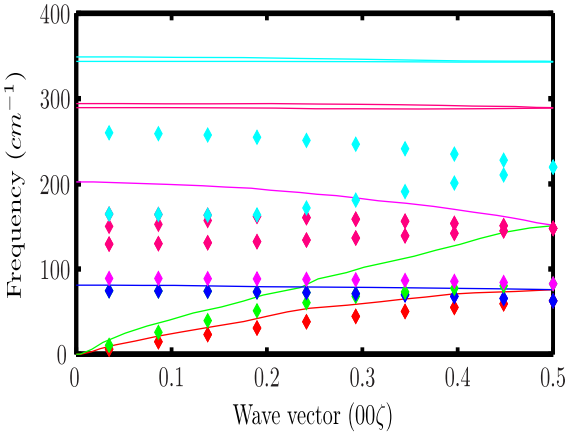
Frequency (cm^{-1})
Wave vector (00ζ)

(b)

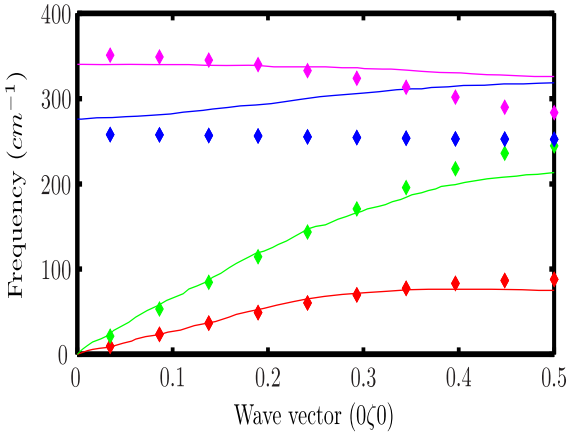
Frequency (cm^{-1})
Wave vector (0ζ0)

(c)

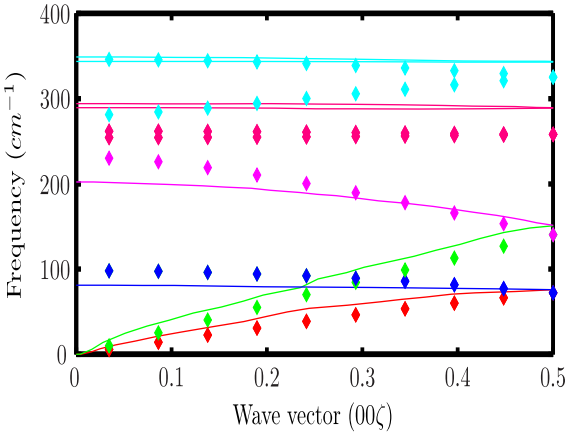
Frequency (cm^{-1})
Wave vector (00ζ)

(d)

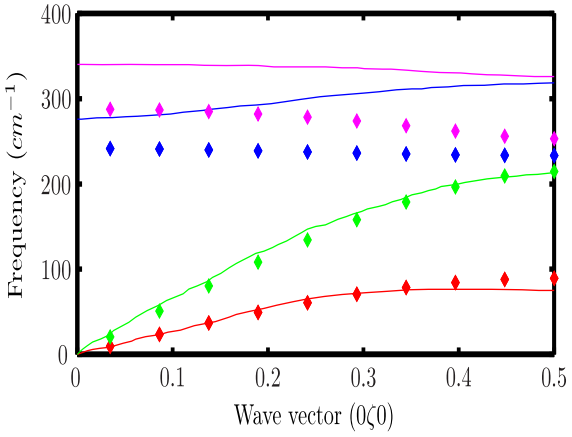
Frequency (cm^{-1})
Wave vector (0ζ0)

(e)

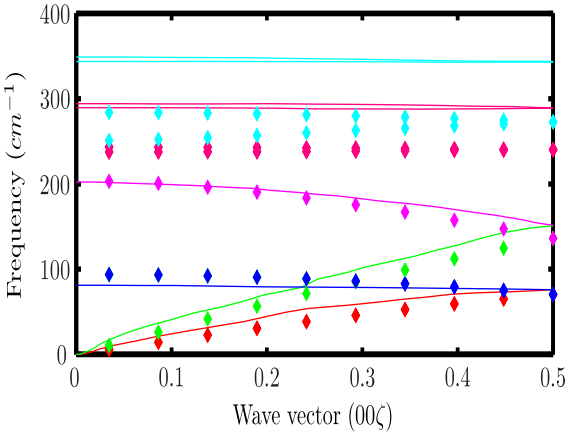
Frequency (cm^{-1})
Wave vector (00ζ)

(f)

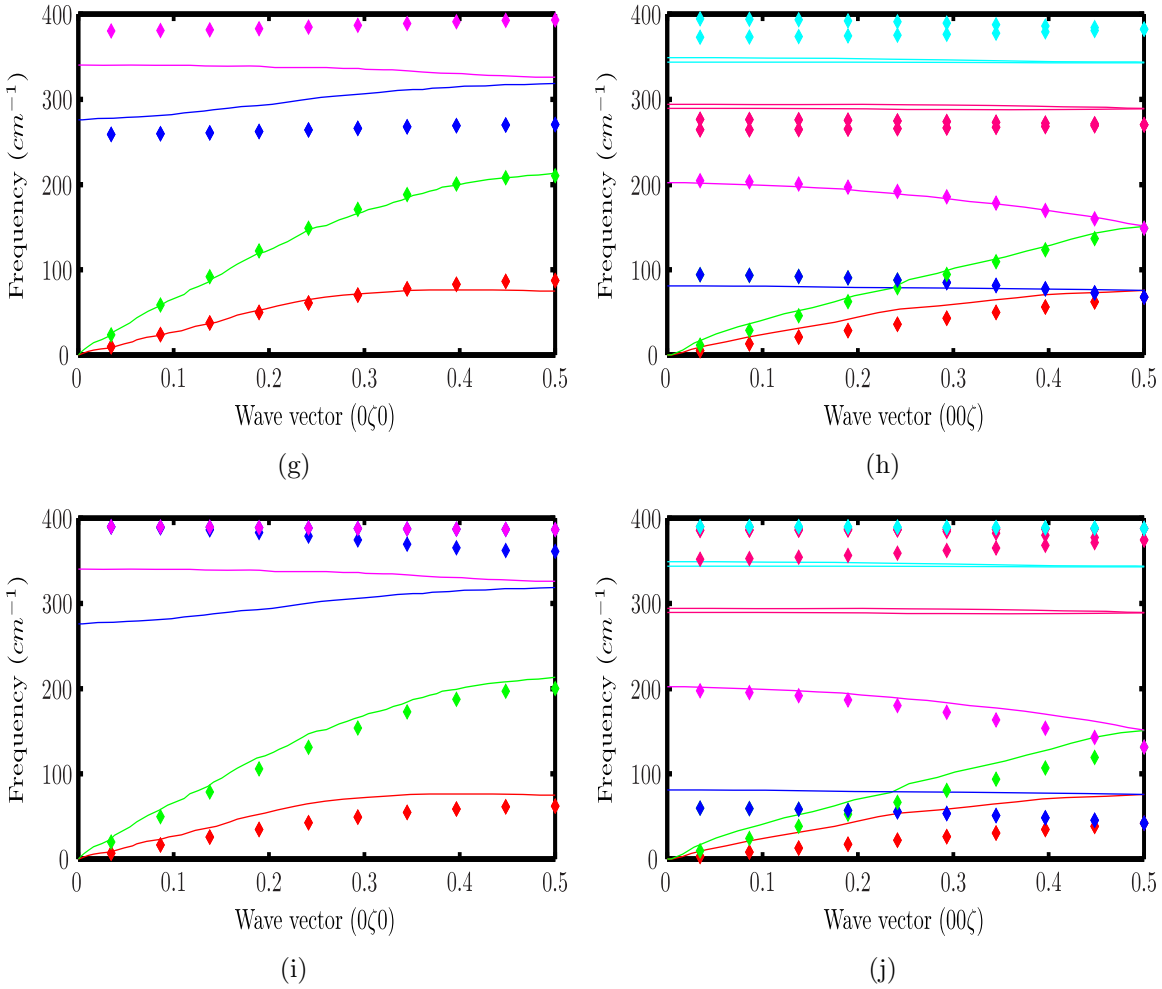

Figure 3.1: Phonon dispersion relations of ZnS calculated with (a,b) IP1, (c,d) IP2, (e,f) IP3, (g,h) IP4, and (i,j) IP5. Right and left figures are correspond to zinc-blende and wurtzite phases respectively. The solid lines represent experimental results taken from [4] and filled circles are calculated phonon frequencies

Except for IP1, acoustic phonons calculated using empirical potentials are in good agreement with the experiment. All potentials show weakness in the calculation of optic phonons. This is worse for IP5 as there is no LO/TO splitting in Γ point. As pointed out by Wright and Gale [91], this is because of the fact that species do not carry charge in IP5. Among the other three, it seems IP2 potential can reproduce better Γ point phonon frequencies for zinc-blende ZnS. Phonon dispersion relations obtained by IP4 also shows an acceptable agreement to experimental values despite its simple formulation.

3.4 Surface energy and structure

There is a considerable number of studies on surface properties of ZnS using first-principle and molecular mechanics methods. High surface to volume ratio in nanostructures, makes surface properties a crucial topic in nanoscience. As a result, the ability of an interatomic potential in predicting surface properties can be an important factor for using it in nanoscience.

The energy penalty to cleave a bulk material and form a surface is defined as the surface energy. By this definition, surface energy for any stable material is a positive value (making a free surface is endothermic) and can be calculated as:

$$E_s = \frac{[U_s - nU_{coh}]}{A} \tag{3.4}$$

where E_s is surface energy, U_s is the energy of system that contains surface, n is number of atoms in the same system, U_{coh} is cohesive energy per atom in periodic bulk system, and A is the surface area.

There are two main approaches for calculating surface energy by atomistic simulation methods. In the first method, which we call the 3D method, a system with two free surfaces is made by introducing vacuum gaps. This can be done by increasing the simulation cell length along one axis making a slab with two free surfaces normal to the increased dimension. It should be kept in mind that the simulation is still running in a 3D periodic environment so the vacuum gap should be sufficiently large to avoid interaction of free surfaces with their images. The slab itself should be thick enough to ensure that properties converge to bulk properties at the centre of the slab. The advantage of the 3D method is that it can be used with codes that can only handle 3D boundary conditions. This is crucial especially when there is long range electrostatic interaction in the system (like ZnS) as many of the available MD codes have not implemented the two-dimensional Ewald summation. The main disadvantage of this method is the necessity of a larger simulation box due to the presence of vacuum gaps which will increase the simulation time.

In the second method (2D method), a system with a single surface and two regions is made. Region 1 contains surface and all layer below surface allowed to relax and atoms in region 2 are assumed to have no displacement from relaxed bulk structure. The 2D method is more efficient and became possible for ionic system by introducing the 2D version of Ewald summation by Parry [113] (know as Parry summation).

We used both methods within GULP code to calculate (110) surface energy of zinc-blende ZnS. Since both methods produced similar results for all potentials, we used 2D

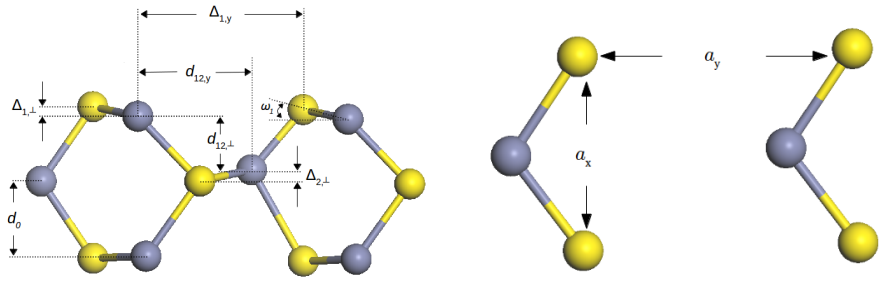

(a) Top view (b) Side view

Figure 3.2: Side and top views of the relaxed surface geometry for the (110) surface of cubic ZnS (After Duke and Paton[5]).

method to calculate other surface energies. (110) is found to be the most stable surface of zinc-blende ZnS in nature. Duke and Paton [5] studied atomic geometries of (110) surface of ZnS using low-energy electron diffraction (LEED) analysis. The relaxed (100) surface structure and its structural parameters suggested by Duke and Paton is shown in figure 3.2 schematically. Table 3.5 represents ZnS(110) surface properties calculated by different potential formulations. Corresponding experimental and first-principle values are represented where available.

Structural relaxation of different surfaces of II-VI semiconductors is well established by numerical and experimental studies. It has been observed that anions move outward from the surface and cations move inward[37]. It seems all potentials except IP1 can predict this surface reconstruction. This potential has also been used in other studies to calculate ZnS(110) properties [83, 96]. Unfortunately, we could not reproduce results reported in these studies (E_s=0.53[83], 0.65[96]; $\Delta_{1,\perp}$=0.42 [83], 0.28[96]). To check accuracy of our calculations, we used the surface configuration already relaxed by IP2 potential as the input for IP1 surface calculations and we ended up with the same surface properties reported in table 3.5. IP5 potential is also predicting a less stable (110) surface which is probably due to the fact that this potential does not consider charged species. The effect of charges become more considerable when the system has free surfaces as coulomb forces acting on surface atoms are not homogeneous in three dimensions.

Table 3.5: (110) surface geometry parameters (as shows in figure 3.2). All distances are in Å and ω angle is in degrees.

	IP1	IP2	IP3	IP4	IP5	DFT[a,b]	exp.[c]
a_x	3.821	3.825	3.854	3.871	3.795		3.825
a_y	5.403	5.410	5.450	5.475	5.367		5.409
$\Delta_{1,\perp}$	-0.013	0.370	0.531	0.128	0.744	0.320, 0.55	0.59
$\Delta_{1,y}$	4.426	4.252	4.162	4.318	4.330	4.345, 4.21	4.296
$d_{12,y}$	2.871	2.947	2.997	2.887	3.197	3.006, 3.12	3.149
$d_{12,\perp}$	1.700	1.566	1.544	1.720	1.285	1.590, 1.49	1.403
$\Delta_{2,\perp}$	-0.009	0.094	0.091	0.031	0.058	0.072, 0.000	0.000
d_0	1.967	1.888	1.891	1.898	1.837	2.001, 1.87	1.912
ω_1	179.250	17.702	22.406	6.335	35.673	15.9	28.0

(a) Ref. [84] (b) Ref. [85] (c)Ref. [5]

In addition to (110) surface of ZB structure, we also studied other most observed surfaces in ZB and WZ nanoparticles. (100) and (111) surfaces are known to be probable facets in ZB nanostructures [42] as well as (0001), $(10\bar{1}0)$ and $(11\bar{2}0)$ in WZ ones[43]. It should be taken into consideration that (100), (111) and (0001) surfaces are polar surfaces which inherently exhibit a dipole moment. Polar surfaces would be unstable, showing high surface energies unless dipoles are removed. In this study, dipole moments were removed by forming surface vacancies with the same procedure described by Hamad et. al. [37]. Another important fact about polar surfaces is that they can be made by cleaving along Zn or S layers. As a result, we can end up with Zn or S terminated surfaces. In table 3.6 calculated surface energies using empirical potentials and DFT calculations are shown. DFT results for ZB and WZ phases are taken from two works of Feigl, Barnard and Russo [42, 43].

Table 3.6: Comparison of the surface energies (J/m^2) of ZnS in ZB and WZ structures, calculated using different empirical potentials (Zn and S denote Zn-terminated and S-terminated surfaces, respectively).

		IP1	IP2	IP3	IP4	IP5	DFT[a]
				ZB			
(110)		0.825	0.515	0.439	0.554	1.176	0.43
(100)	Zn	1.845	1.532	1.161	1.111	1.773	2.03
(100)	S	1.724	1.295	1.038	1.121	1.652	2.03
(111)	Zn	1.369	0.851	0.676	0.856	1.513	1.36
(111)	S	1.407	0.981	0.863	0.897	1.418	1.36
				WZ			
(0001)	Zn	1.368	0.828	0.661	0.858	1.475	1.394
(0001)	S	1.658	0.961	0.879	0.907	1.418	1.394
$(10\bar{1}0)$		0.862	0.520	0.439	0.575	1.028	0.431
$(11\bar{2}0)$		0.854	0.500	0.384	0.562	1.156	0.427

Ref. [42] for ZB and Ref. [43] for WZ surface energies.

Table 3.6 shows that all empirical potentials and DFT calculations predict the same trend in surface energies. (110) is the most stable surface in ZB phase followed by (111) and (100). In WZ phase, $(11\bar{2}0)$ has the smallest energy but the difference between this surface and $(10\bar{1}0)$ energies is negligible, suggesting similar stability for both surfaces.

3.5 Behaviour under pressure

As mentioned before, ZnS can be found in two fourfold coordinated (Z = 4) crystal structures in nature: zinc-blende ($F\bar{4}3m$) and wurtzite ($P6_3mc$). The first and second neighbour distances in both structures are similar. As a result, there is a small difference between unit cell volume of the two structures. There has been a considerable amount of theoretical and experimental studies showing that ZnS undergoes phase transformation from fourfold to sixfold rocksalt structure ($Fm\bar{3}m$) at high pressures. High pressure x-ray diffraction showed that this transformation results in a large volume change (13-17%) in pressure range from 12 to 18 GPa [6, 7, 114]).

In this section, we examine interatomic potentials ability to model ZnS under pressure by comparing high pressure lattice dynamic results with experiments. Enthalpy and volume per atom are calculated for 3 phases using lattice dynamic code within GULP software. Coexistent pressure of fourfold and sixfold coordinated phases can be approximated by the

point of equal enthalpy of both phases in Fig.3.3.

Figure 3.3e clearly shows that IP5 potentials can not model ZnS crystal structures correctly as rocksalt is more stable than zinc-blende and wurtzite at all pressures. This can be justified by the fact that IP5 potential does not consider interaction between similar atoms. These interactions (especially anion-anion interactions) become more important in more condense phases like rocksalt where atomic distances are smaller. IP3 potential predicts rocksalt structure to be unstable at all pressures between 0 to 30 GPa. As shown in section 3.2, mechanical properties of rocksalt calculated by IP3 potential could be improved by changing the high 3-body cut-off suggested in the original paper to a smaller value. We expect that the ability of IP3 potential in modelling pressure induced phase transformation to be improved by changing the 3-body cut-off as well. Figure 3.3f confirms that by changing the 3-body cut-off to 3.0 Å transition pressure calculated by IP3 lies in the range reported in experimental studies. The relative volume change with increasing pressure is calculated for the four potentials that showed acceptable transition pressure values in Fig.3.3. Resultant P-V graphs are plotted in figure 3.4 and compared with three different experimental values.

Increasing pressure causes considerable divergence of wurtzite (and zinc-blende) relative volume from experimental values in figure 3.4a and Figre 3.4c. This is expected as IP1 and IP4 potentials underestimated and overestimated bulk modulus, respectively (Table 3.1). The parameters of the equation of state (like the Murnaghan formulation) can be obtained by fitting to high density ZnS phase (rocksalt) experimental P-V data. Properties in ambient pressure can then be derived by extrapolation of the equation of state to 0 Gpa. Using this method, relative volume of rocksalt to wurtzite phase (V_{RS}/V_{ZB}) in ambient pressure is reported to be 0.81 [6, 7]. IP4 potential overestimates V_{RS}/V_{ZB} at ambient pressure and this is the main reason for the large difference between calculated and experimental values in figure 3.4c. This difference is larger in figure 3.4d as IP3 potential overestimates both relative volume and bulk modulus of the rocksalt phase. Thus, even modifying the 3-body cut-off, can not make this potential predict ZnS properties in high density structure state accurately. Generally, it seems IP2 potential offers better modeling of ZnS under high pressure. Results of this section are summarized in table 3.7.

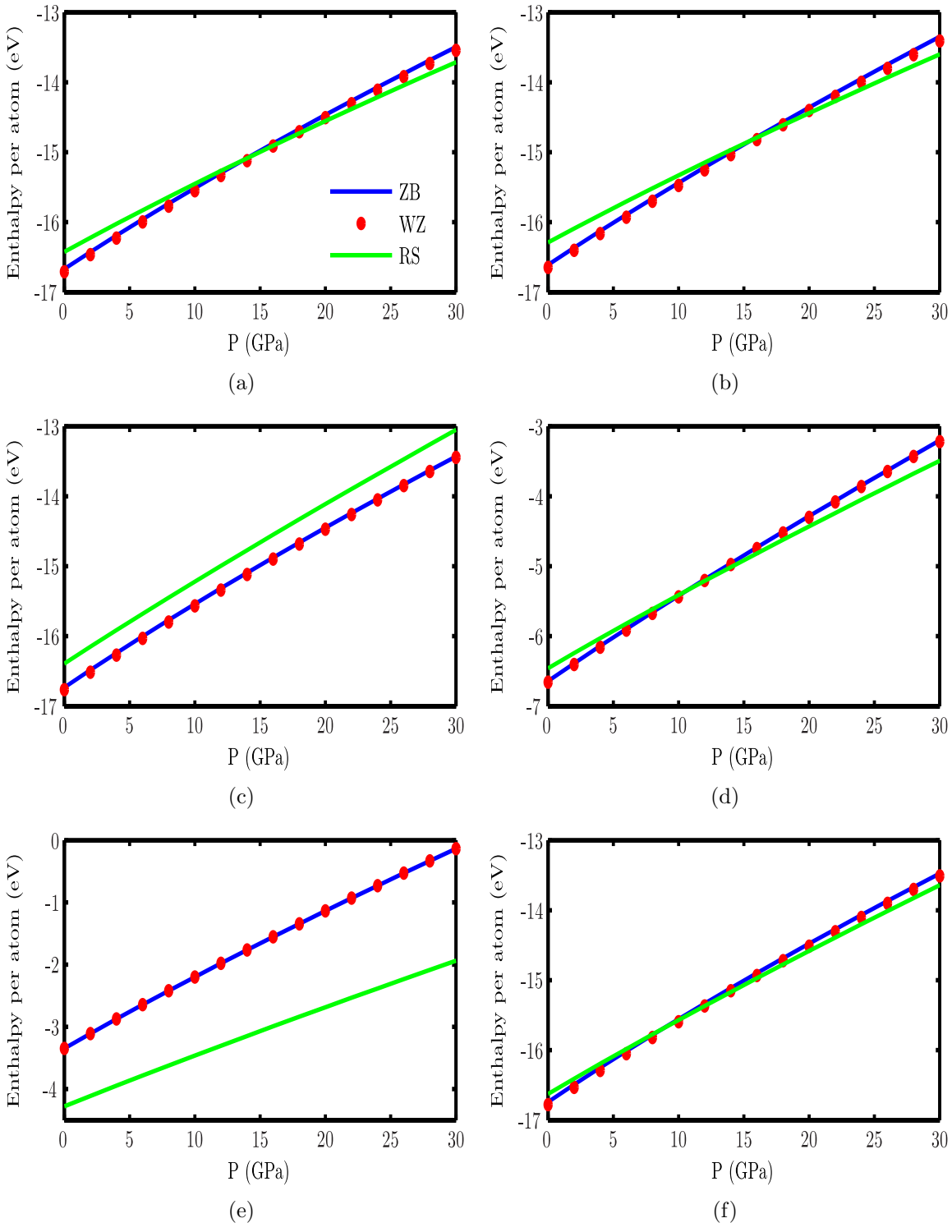

Figure 3.3: Enthalpy per atom as a function of Pressure for bulk ZnS: (a) IP1, (b) IP2, (c) IP3, (d) IP4, (e) IP5, and (f) IP5 with the new 3bd cut-off.

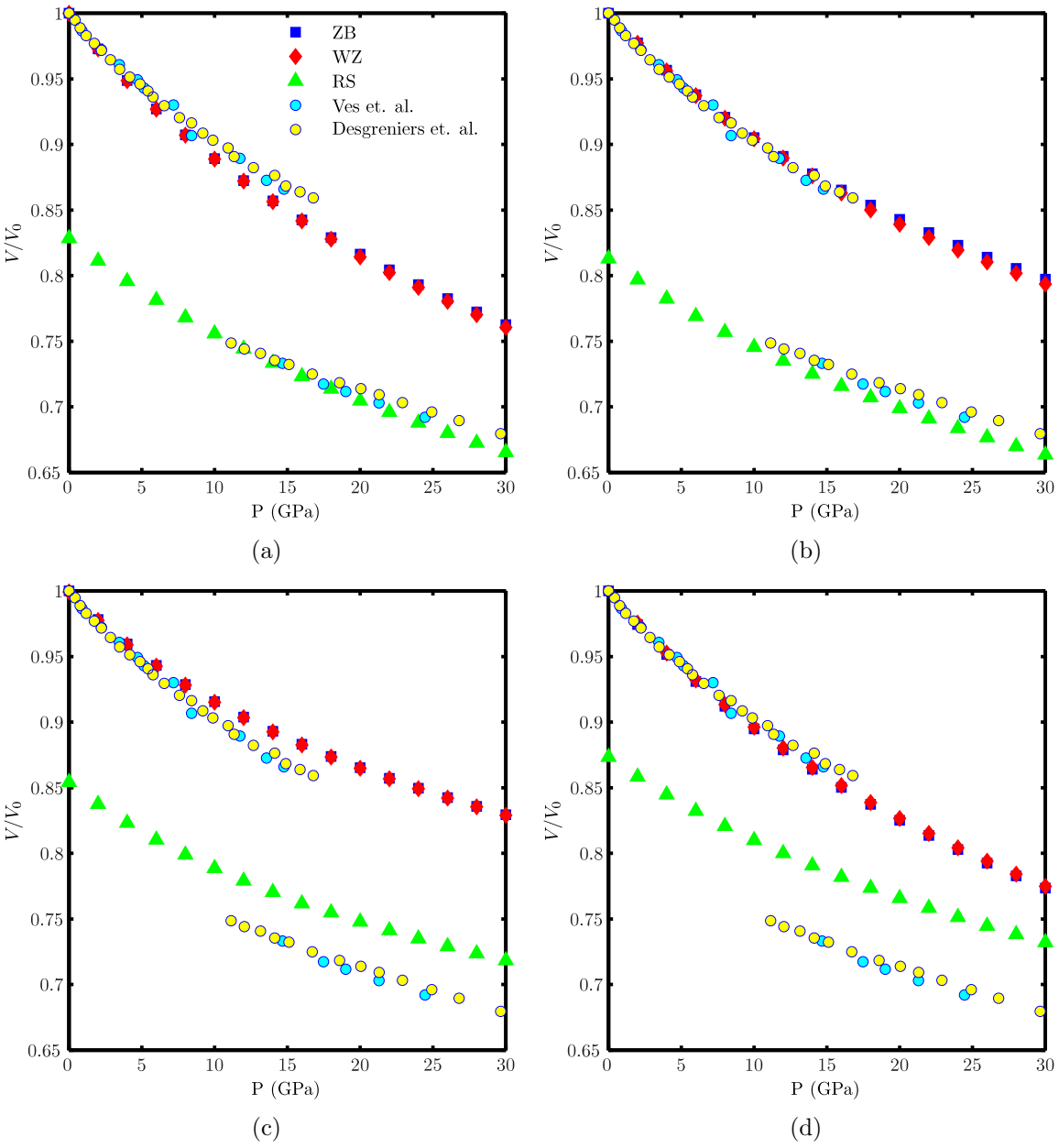

Figure 3.4: Pressure-volume relation of ZnS fourfold and sixfold phases for (a) IP1, (b) IP2, (c) IP4, and IP3 with the modified 3-body cut-off potentials. Resultant graphs are compared with experimental values of Ves et. al.[6] and Desgreniers et. al.[7]

Table 3.7: Comparison of behaviour of four interatomic potentials of ZnS under pressure. V_T/V_0, ΔV_T, and P_T are relative volume, volume change, and pressure, of phase transformation respectively

	IP1	IP2	IP3	IP4	exp.
V_T/V_0	0.856	0.863	0.892	0.903	0.865[a],0.853[b]
$\Delta V_T(\%)$	14.3	17.0	9.6	13.8	16[a],17[b]
$P_T(GPa)$	14	16	10	12	14.7[a],14.6[b]

(a) Ref. [6] (b) Ref. [7]

3.6 Thermal expansion

The ability of a force field to model a material at higher temperatures enables many opportunities to investigate high temperature phenomena in atomistic scales. One of the physical properties that can be readily calculated by MD is the volume change with respect to temperature. When the experimental values are available, thermal expansion calculated by MD can be used as one of the factors to verify the ability of a force field to model high temperatures.

There are a considerable number of studies on crystal structure of ZnS at low temperatures. However, there is not much experimental data available above room temperature. Two sets of published experimental data on ZnS thermal expansion are neutron diffraction high temperature lattice parameter measurement by Moss et. al. [115] and diatometery linear expansion by Roberts et. al. [8].

In this section, we compare thermal expansion of ZnS modelled with different potentials with experimental values. Nosé-Hoover isothermal-isobaric ensemble (NPT) at 0 GPa were used within DL_POLY code to calculate volume change with temperature of 6x6x6 zinc-blende super cell with 3D periodic boundary condition. Final configuration of simulation at each temperature is used as the initial configuration for the next one to accelerate the equilibration.

For the potentials containing shell model, the adiabatic method as described by Mitchell and Fincham [63] is used. In this method the shell is given a small portion of ion mass and its motion is integrated by standard techniques. The shell mass should be small enough to ensure that the core-shell spring frequency is well above the vibrational frequencies of the lattice. From classical mechanics, the frequency of core-shell spring can be calculated as

$$\upsilon = \frac{1}{2\pi}\sqrt{\frac{k}{x(x-1)M}} \tag{3.5}$$

where x is the fraction of the ion mass assigned to shell, M is the ion mass and k is the shell constant. Equation 3.5 shows that smaller shell constants require smaller shell masses to satisfy adiabatic conditions. Technically, this means much smaller MD time steps are required to capture the fast movement of the light shells. In addition to slowing down the simulations, light shells are problematic at higher temperatures due to their much higher vibrational frequencies in respect to the lattice.

For sulfur, we chose $x = 0.1$ which results in core-shell frequencies of 48 THz and 34 THz for IP2 and IP3 potentials, respectively. These frequencies are well above known vibration modes in ZnS. For IP1 potential, we had to choose x as small as 0.01 to make the zinc core-shell frequency in the same range as sulfur. To keep consistency, time step of 0.1 fs was used for all potentials and NPT simulations were run for 100 ps. Final lattice dimensions were calculated by taking the average of the last 10 ps of each simulation. It should be mentioned that we were unable to run MD simulations for ZnS described by IP5 potential. The system seems to be unstable at all high temperatures.

The temperature at which the zinc-blende to wurtzite phase transformation occurs is known to be around 1300 K (1273[116], 1295[109]). Moss et. al. also showed that ZnS keeps its complete cubic structure up to 1300 K[9]. MD calculated and experimental values of thermal expansion are given in figure 3.5.

MD results should be treated with caution when they are used to calculate thermal expansion. The simulation cell should be equilibrated carefully and average cell dimensions should be calculated when fluctuation in cell dimensions is in a same order of magnitude as thermal expansion. Considering this, it seems IP2 potential shows a better agreement with experimental thermal expansion results. Thermal expansion behaviour of wurtzite is also calculated and seen to be fairly similar to zinc-blende for all potentials. The energy difference between the two phases is very small (about 0.5%) with a slightly more stable wurtzite in all temperatures.

3.7 Potential energy hyper-surface

Derivation of force field parameters by fitting to a potential energy hypersurface obtained from first-principle methods is one of the main ways to develop empirical interatomic potentials. An ab-initio energy hypersurface is usually calculated by changing the geometry of

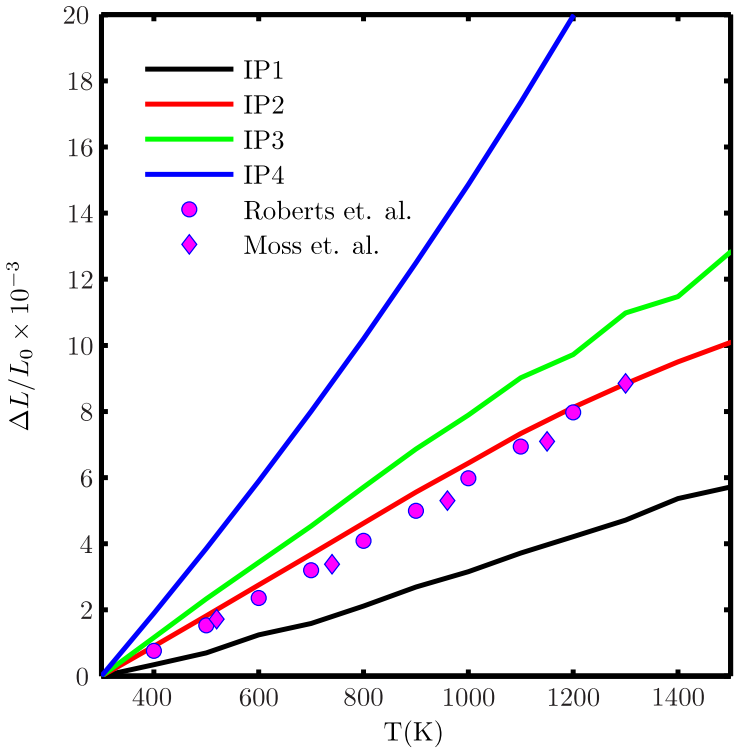

Figure 3.5: Thermal expansion of zinc-blende ZnS calculated by MD using different potential formulations. Experimental results are taken from Roberts et. al.[8] and Moss et. al.[9] works.

periodic solids, gas phases or both. Potential energy hypersurface calculated from a reliable first-principle method, can also be a good criterion to compare different empirical force fields.

In this section, we compare energy hypersurfaces calculated using empirical potentials with those obtained from the density functional theory (DFT) calculations. Gaussian optimized basis sets for ZnS by Heyd et. al. [117] and middle-range hybrid exchange-correlation functional of Henderson, Izmaylov, Scuseria and Savin (HISS) [118] were used in the periodic boundary condition code [119] within GAUSSIAN program [120] to calculate the first-principle energy hypersurface. The basis set and functional which we used in this study have shown reliable results in structural and band gap calculations of ZnS. We also checked the reliability of our DFT calculations by calculating optimized lattice constants for all three ZnS phases which were in a very good agreement with the experimental values ($a_{ZB} = 5.413, a_{WZ} = 3.3.828, c_{WZ} = 6.260, a_{RS} = 5.071$).

Two different strategies were used to calculate the potential energy hypersurfaces for ZnS in zinc-blende crystal structure. In the first set of calculations, we constructed potential energy hypersurface by changing the zinc-blende ZnS unit cell volume. The lattice constant was changed from 5 to 5.8 Å with 0.01 Å increments and potential energy calculated at each step. As shown in the previous sections, this range of volume change covers expansion due to increasing temperature from 0 to 2000 K and compression due to increasing pressure from 0 to 30 GPa for all empirical potentials. As absolute energy values calculated with DFT and interatomic potential methods can not be compared directly, energy difference is calculated for each method:

$$\Delta E = E - E_0 \tag{3.6}$$

where E is the potential energy calculated at each step and E_0 is the minimum energy of corresponding empirical potential or DFT calculation. Since the minimum of each potential formulation occurs at its equilibrium lattice constant, we shifted all minimums to the lattice constant calculated via DFT (which is a good choice as it has a good agreement with experimental value). This enabled us to compare the curvature of each empirical potential energy hypersurface with the one calculated from DFT.

Anharmonicity of the energy hypersurface is noticeable in figure 3.6 as the slope of diagram is bigger in the compression mode (a $<$ 5.41 Å) compared to the expansion mode (a $>$ 5.41 Å). IP2 potential has better agreement with DFT energy calculations in compression mode which can verify the more favourable results we obtained for this potential in section 3.5. In expansion mode, which can be related to the thermal expansion, IP2 and IP3 potentials

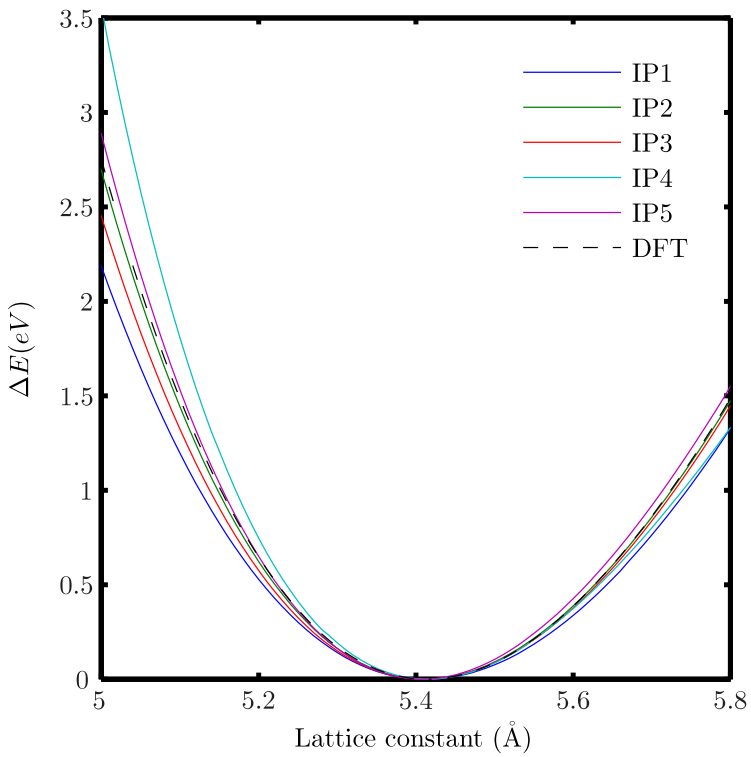

Figure 3.6: Energy hypersurfaces calculated via changing zinc-blende unit cell volume.

exhibit a better fit to DFT results. This is again in agreement with the thermal expansion results calculated in section 3.6.

Uniform volume change of zinc-blende unit cell can not include the effect of the three body interaction in the empirical potential formulations as the value of S-Zn-S angle stays the same when lattice dimensions are changed uniformly in all directions. Also, the effect of polarization can not be captured with changing cubic unit cell volume uniformly as minimum energy always happens when cores and shells occupy the same positions. In order to capture the effect of presence of three-body and shell model terms in empirical potential formulations, we used another strategy to calculate energy hypersurface for zinc-blende ZnS unit cell. In this method, one Zn atom was moved from its equilibrium position in zinc-blende unit cell, $(\frac{1}{4}a,\frac{1}{4}a,\frac{1}{4}a)$, toward and away from the S atom at (0,0,0) along [1,1,1] direction (a is the unit cell). To stay on [1,1,1] direction, fractional position of Zn atom should always have the format like (α,α,α). To build the energy hypersurface, α was changed from 0.15 to 0.35 with 0.01 increments. In order to include polarization of core-shell units, all shells were let to relax at each step while cores were fixed. figure 3.7 shows the resultant energy hypersurfaces.

Compared to figure 3.6, energy hypersurfaces in figure 3.7 show more anharmonicity.

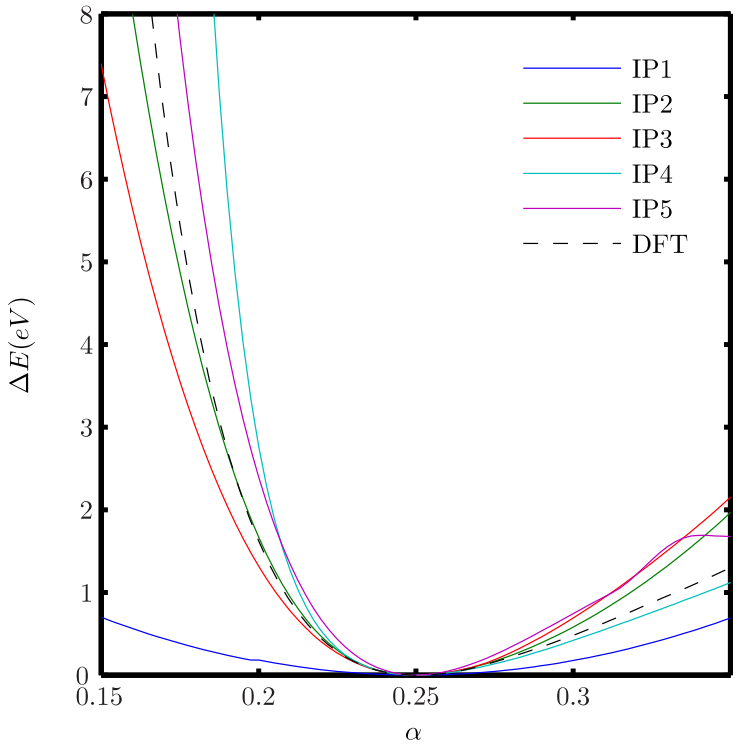

Figure 3.7: Energy hypersurfaces calculated via changing Zn atom fractional position (α,α,α) in zinc-blende unit cell.

The slope of the DFT energy hypersurface is much bigger in the first half of the diagram where $0.15 < \alpha < 0.25$. This part of the diagram is equivalent to the moving of a Zn atom from its equilibrium fractional position at (0.25,0.25,0.25) toward the S atom placed at the origin. IP2 represents the best agreement with DFT calculation in this region. Although IP2 diverges from DFT energy hypersurface in the second half of the figure. 3.7 and IP4 fits better in this region, calculating R^2 values showed IP2 have the best overall agreement with the DFT results.

3.8 Conclusion

The performance of five different empirical potentials for ZnS were tested and compared in this paper. This was done by calculating different ZnS properties via empirical potentials and comparing them with corresponding experimental results or DFT calculations. Properties tested in this paper are mechanical and structural properties, phonon dispersion relation, surface energy and structure, behaviour under pressure, thermal expansion and energy hypersurface. In section 3.2 we showed that lattice constants of ZB and WZ phases calculated by all empirical potentials are in acceptable agreement with the experiment. In RS phase, however, IP3 and IP5 could not reproduce experimental lattice constant. This also happened for mechanical properties as elastic constants calculated for RS phase via IP3 and IP5 are very different from those calculated by other three potentials. We showed that mechanical and structural properties of RS phase calculated by IP3 potential can be improved by modifying its 3-body cut-off distance.

In Section 3.3 phonon dispersion relations for ZB and WZ phases were studied. Except for IP1, all other empirical potentials seemed to be able to reproduce acoustic branch. All potentials showed weakness in predicting optical phonons. This was worse for IP5 as there was no LO/TO splitting due to the fact that atoms are charge neutral.

Surface properties of ZnS were studied in section 3.4. Previous theoretical and experimental studies showed that (110) surface of ZnS experiences a considerable geometry change after relaxation. This surface relaxation includes the movement of anions to the out of the surface. This surface reconstruction was observed by all empirical potentials except IP1. Relaxed surface structures calculated by IP2 and IP3 were more similar to the experiment.

IP1, IP2 and IP4 have been shown to be able to predict the pressure induced phase transformation in section 3.5. We also have shown changing 3-body cut-off distance enables IP3 to show a pressure induced phase transformation. It was also observed that the P-V relation calculated by IP2 represents better agreement with experimental results. Thermal expansion calculated by this potential has also shown better accordance to the experimental

results. Finally, the energy hypersurface obtained from DFT calculations showed a better agreement to IP2 compared to the other empirical potentials.

Considering these results, we should emphasize that one general comment can not be made on reliability of particular empirical potentials. The choice of potential is highly depended on the application that molecular mechanic simulation aims for. Each of these potentials is designed to reproduce some specific ZnS properties. Except for IP5, we were able to run molecular dynamic simulations for temperatures as high as 1500 K. We noticed that more care should be taken when using potentials that include shell model when running simulations at higher temperatures. Simulation speed is also highly depended on complexity of potential formulation. Thus, potentials like IP4 offer much higher simulation speed than more complicated ones like IP3.

Chapter 4

Structure of ZnS nanoparticles in vacuum

4.1 Introduction

II-VI semiconductor nanomaterials are of great technological interest due to their unique optoelectronic properties. The quantum confinement effect makes it possible to tune the frequency range of emitted light (colour) from semiconductor nanostructures, usually known as quantum dots (QDs), by controlling their sizes[24]. Because they also have wide absorption and luminescent efficiency, a high resistance to photobleaching, and high chemical stability, quantum dots are an ideal candidate for use in biomedical imaging applications, where they can be used in place of organic fluoroscopes [25]. Owing to the rapid growth of nanotechnology, a variety of synthesis procedures have been proposed to fabricate II-VI semiconductor nanoparticles (NPs) in different sizes, shapes and structures [76]. The typical QD size is smaller than 5 nm mainly to make the best use of the quantum confinement effect. Moreover, studies have shown that the level of toxicity of QDs also decreases with decreasing sizes. It has been reported that large QDs are generally accumulated for several months in the reticuloendothelial system, such as liver, spleen and lymphatic system, but QDs smaller than 5 nm could be removed quickly by the kidney [30].

The rapid development of QD technology has raised serious concerns about its applicability, mainly because the most studied II-VI semiconductor nanomaterials contain cadmium (CdSe, CdTe and CdS), which is known to be highly carcinogenic for living systems [27]. Various modifications such as adding a ZnS shell or polyethylene glycol (PEG) coating have been suggested to modify QDs with toxic elements. However, the cytotoxicity of Cd containing QDs is still a major concern [28]. Zn-based QDs such as ZnS have been introduced as a suitable alternative for QDs with Cd components since Zn is considered to be

A modified version of this chapter has been been accepted for publication in Scientific Reports as **M. Khalkhali, H. Zeng, Q. Liu and H. Zhang**, "**A size-dependent structural evolution of ZnS nanoparticles**" *Sci. Rep.* 5, 14267 (2015)

an essential biological element [29]. Furthermore, the band gap of ZnS is more than 1 eV wider than the others in the II-VI family, which enables a wider spectrum to be tuned by varying the size of ZnS nanostructures. However, the structural stability of nanocrystalline ZnS has been shown to be a challenging issue limiting its applicability since a ZnS NP has the potential to undergo uncontrolled structural changes [20].

At standard temperature and pressure (STP: 298 K and 1 bar), bulk ZnS exists in two crystal structures: zinc-blende ($ZB : F\bar{4}3m$) and wurtzite ($WZ : P6_3mc$). ZB structure has slightly lower energy at standard condition while WZ is more stable above 1020 °C. At higher pressures (above 15 GPa), the high density rocksalt structure ($RS : Fm\bar{3}m$) becomes more stable. It has been shown that at the nanoscale, the phase transformation behaviour of ZnS can deviate greatly from bulk. For ZnS nanostructure, the temperatures as low as 400 °C [31] and 250 °C [33] have been reported for the ZB-to-WZ phase transformation at standard pressure and 1 GPa, respectively. However, pressure-induced transformations to the RS phase have been shown to increase to 19.6 GPa in ZnS NPs [121].

The structural transformation of ZnS NPs has also been reported at room temperature. Zhang et al. showed that reversible structural transformations at room temperature could be induced by the absorption-desorption of methanol and water [35]. They found that absorption of water to the surface of ZB ZnS NPs increased crystallinity, a finding also supported by MD simulation results [78]. MD has also been used to study the structural relaxation of a freestanding 3 nm ZnS NP at 300 K [2] as well as the aggregation behaviour of NPs with the same size [97]. A phase transformation from ZB to WZ structure was reported in both cases. Haung and Banfield have shown that WZ grows on the surface of coarsened ZB particles during aggregation at 500 K [122]. The crystal growth of WZ, however, was kinetically controlled by WZ-ZB interface radius, and no pure WZ particles were observed in coarsened samples.

Using MD and DFT calculations, Hamad and Catlow studied $(ZnS)_n$ clusters with sizes ranging from 1 to 4 nm ($18 < n < 512$) [3]. They showed that small clusters ($n < 80$) adopted bubble-like or onion-like structures, which predominantly consisted of arrangements of 3-coordinated atoms. Crystal structures of large clusters ($n = 256\ and\ n = 512$) obtained by simulated annealing, mainly consisted of 4-coordinated atoms but deviated from the two bulk phases of ZnS found in nature and were shown to be similar to the BCT zeolite structure [3]. Applying surface energies calculated using first-principle computer simulations into a thermodynamic model, Barnard et al. studied the effect of shape and size on the stability of ZnS ZB [42] and WZ [43] NPs. They found that the rhombic dodecahedron shape, enclosed entirely by non-polar {110} facets, was the most stable ZnS shape regardless of the size of the particle [42]. However, it has been shown that adding polar facets to ZB

nanostructures would make coreshell crystalline/amorphous structure thermodynamically favourable. Deviation from the rhombic dodecahedron shape enabled some thermodynamic paths from ZB to WZ transformation by decreasing the size [43]. In contrast, high energy WZ nanostructures with low prism aspect ratios or lower indexed pyramidal capping facets were prone to transform to ZB, especially when the size increased [43].

In this paper we aim to provide details about how the freestanding ZnS NP size affects structural evolution in standard condition. Structural and configurational evolutions of ZnS NPs were studied using classical MD method. Different structural analyses including radial distribution function (RDF), angular distribution (AD), Honeycutt-Andersen indices, root mean square displacement (RMSD) and coordination number (CN) calculations were performed to characterize the relaxed structures of NPs. In perfect ZB and WZ lattices, each ion is connected to four dissimilar ions with a tetrahedral bond geometry in which all bond angles are equal to 109.47°. Based on bond angles and CN population analyses, we show that the structure of relaxed ZnS NPs bigger than 2 nm consist of three regions: a) a 4-coordinated crystalline core at which Zn and S ions keep their initial tetrahedral arrangement, b) a distorted network of 4-coordinated ions which environs the crystalline core and c) the surface structure which consists of a network of 3-coordinated ions. The stability and size of each region is highly dependent on the crystal structure and size of the ZnS NP. The 4-coordinated tetrahedral bond structure completely disappears in 2 nm ZnS NPs and decreasing the size down to 1 nm results in a bubble-like structure in which all atoms are 3-coordinated. The effect of this structural evolution on NPs' dipole momenta (DM) has also been studied since dipole-dipole interactions are of great importance in non-metallic nanoparticles, as they are found to govern the inter-particle interactions which can vary the behaviour of the mixture of NPs from agglomeration to self-assembly into ordered structures. Results of DM calculations show that in relatively smaller NPs where the surface effect is dominant, DM is controlled by the surface structure. Due to the similarity of the surface structure of ZB and WZ NPs, their DM is similar when the size is smaller than 3 nm. However, in NPs bigger than 3 nm, the direction and magnitude of DM approach the bulk values. This implies that ZB NPs become less polar while the polarity of WZ NPs increases due to the considerable polar nature of WZ lattice.

4.2 Results

4.2.1 Structural Evolution

The Radial Distribution Function

The radial distribution function of atom B in the distance r from atom A ($g(r)$) can be readily calculated from MD trajectories as,

$$g(r) = \frac{< n(r)/v(r) >}{N_A N_B / V} \tag{4.1}$$

where $n(r)$ is the number of B atoms found in the shell between r and $r + dr$, $v(r)$ is the volume of the shell, N_A and N_B are the total number of atom A and atom B in the system, V is the total volume of the system, and $< ... >$ denotes the ensemble average. For the small dr, $v(r)$ can be approximated as $v(r) = 4\pi r^2 dr$ and equation 4.1 can be rewritten as

$$g(r) = \frac{< n(r) >}{4\pi r^2 dr \rho_A N_B} \tag{4.2}$$

where ρ_A is the number density of atom A in the system. In a special case where A and B are the same, N_B is equal to $N - 1$, where N is the total number of A atoms in the system. Some care should be taken into consideration when calculating RDF for a freestanding NP. As the NP has undercoordinated atoms on its surface, its $n(r)$ is lower than what is calculated for the bulk. This means the intensity of RDF peaks of NPs are lower than bulk even for the initial structure. It is especially important for 1 and 2 nm NPs because of their high surface-to-volume ratio. While the position of RDF peaks of relaxed NPs can be compared with the bulk, making a direct comparison between the intensities of RDF peaks is not accurate. A RDF diagram of a NP with the same size and at the same temperature but with no structural relaxation may be used as a reference to study the crystal structure change in the relaxed NP. This reference RDF is made for each NP by cutting a sphere with the same size as the NP from the trajectories of 1 ns NPT simulation of the periodic bulk structure at 300 K and 0 atm. One other issue in the RDF calculations of freestanding NPs is that the volume is not defined for non-periodic systems. As a result ρ should be defined carefully. In our RDF calculations, we used the number density of the bulk ZnS as a normalizing factor, ρ. This puts the intensities of NPs' RDF peaks on the same order of magnitude with each other as well as the bulk. Figure 4.1 shows the calculated RDFs for Zn-Zn pairs in ZB and WZ NPs with different sizes. RDF plots of unrelaxed structures are calculated as explained above. $n(3.5 < r < 4.5)$, the number of Zn-Zn pairs whose distances are between 3.5 and 4.5 Å (area under the first RDF peak), is also shown in Fig. 4.1.

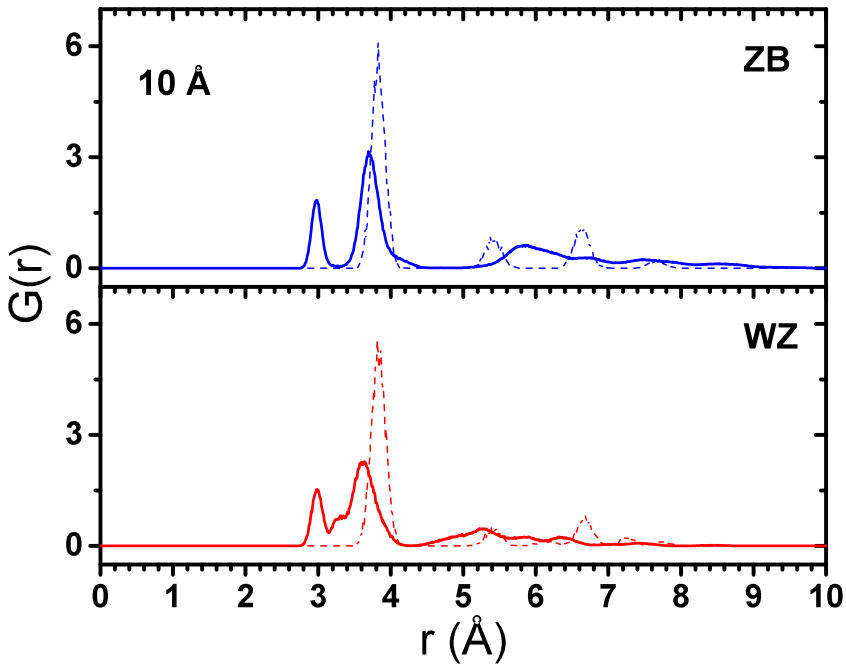
10 Å
ZB
WZ
G(r)
r (Å)
0
3
6
0
1
2
3
4
5
6
7
8
9
10

(a)

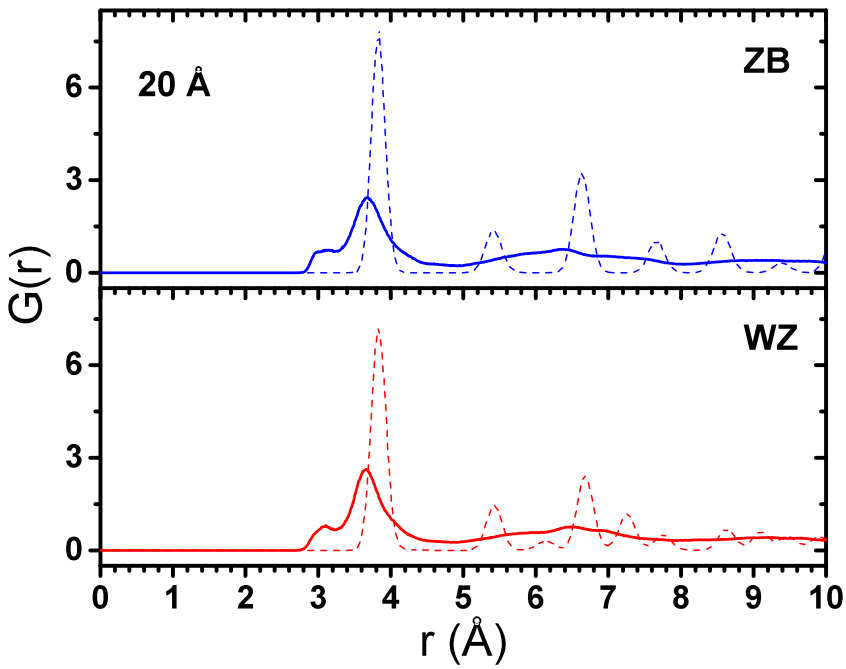
20 Å
ZB
WZ
G(r)
r (Å)
0
3
6
0
1
2
3
4
5
6
7
8
9
10

(b)

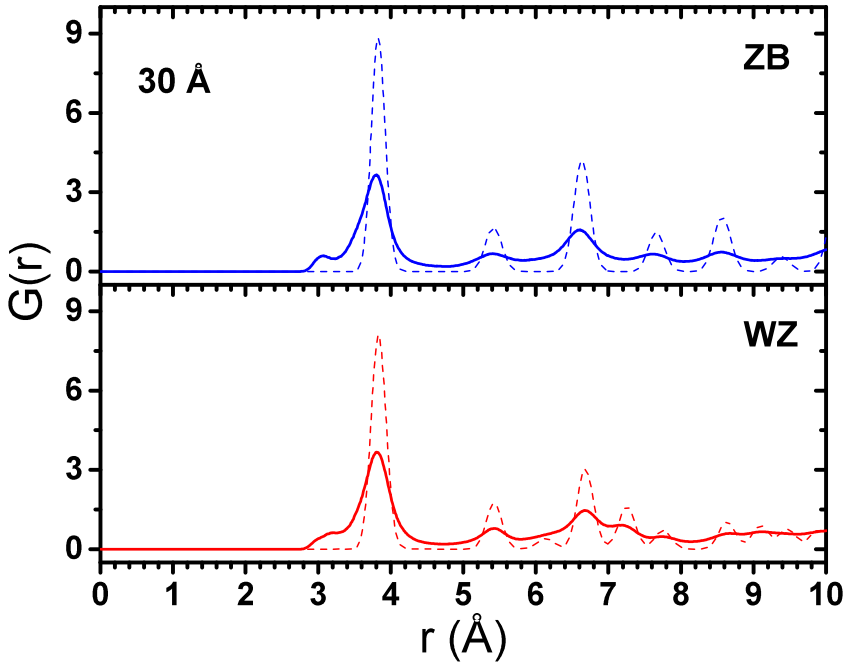
30 Å
ZB
WZ
G(r)
r (Å)
0
3
6
9
0
1
2
3
4
5
6
7
8
9
10

(c)

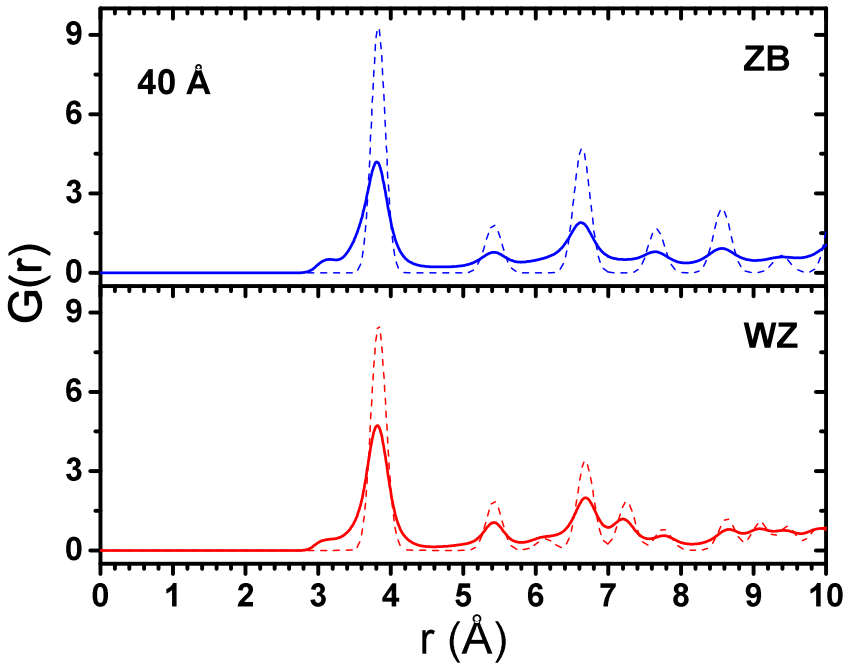
40 Å
ZB
WZ
G(r)
r (Å)
0
3
6
9
0
1
2
3
4
5
6
7
8
9
10

(d)

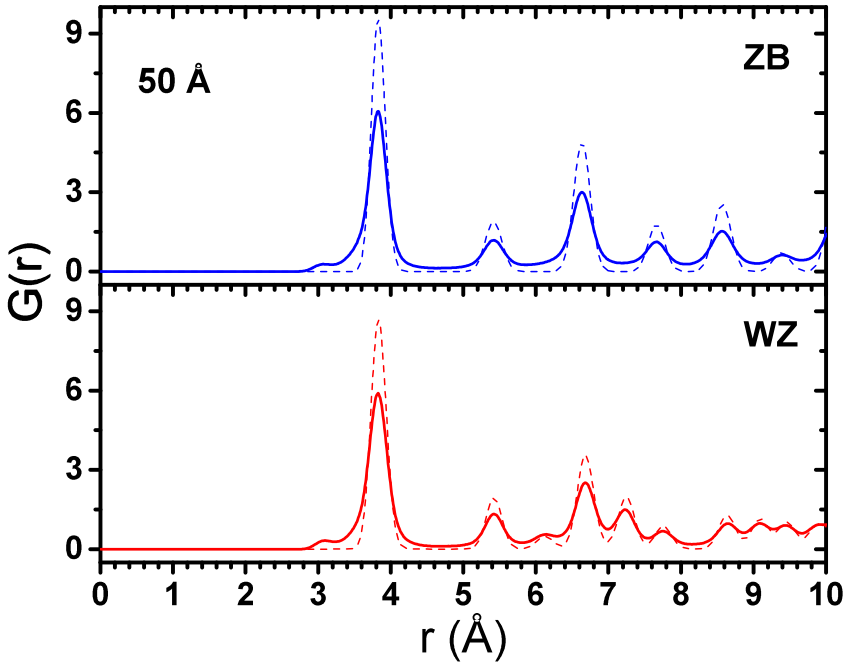

(e)

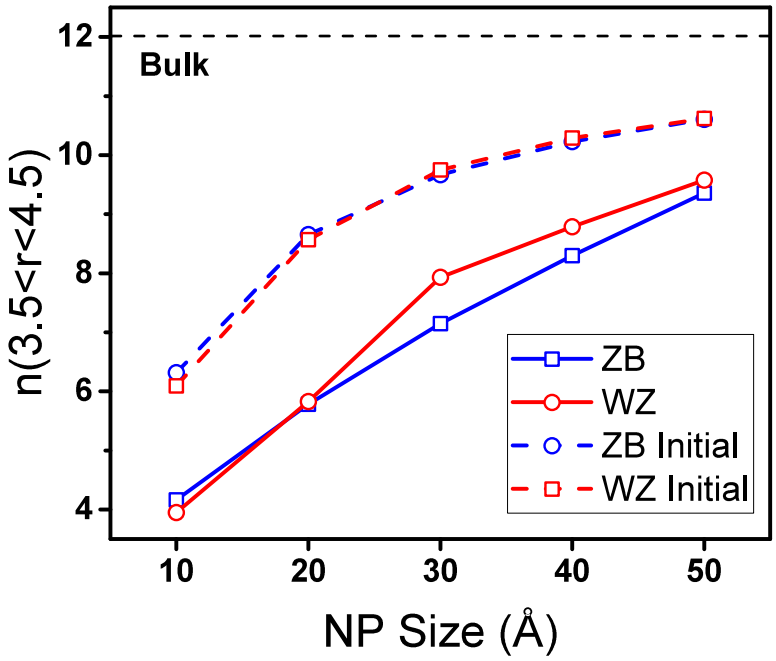

(f)

Figure 4.1: RDF plots of Zn-Zn pairs for (a) 10, (b) 20, (c) 30, (d) 40 and (e) 50 Å NPs. (f) shows the number of Zn-Zn pairs whose distances are between 3.5 and 4.5 Å, $n(3.5 < r < 4.5) = 4\pi \int_{3.5}^{4.5} \rho r^2 G(r) dr$. Dashed lines show the corresponding plots for the NPs with the same size but with an unrelaxed structure.

A general trend of losing crystallinity with decreasing the size of NPs can be recognized in RDF diagrams in Fig. 4.1. In ideal ZB and WZ structure, the first peak of Zn-Zn RDF diagram appears at 3.84 Å. For 10 and 20 Å NPs the position of this peak is changed and the Zn-Zn distance is reduced. All other peaks after 3.84 Å seem to fade away in these small NPs. These two features of RDF diagrams of 10 and 20 Å NPs suggest that these NPs lose their inital crystal structures after relaxation. NPs bigger than 20 Å show the crystalline RDF diagrams, suggesting that considerable portion of the NP structure keeps the crystalline order. The difference between RDF peaks intensities of unrelaxed and relaxed NP decreases as the size of the ZnS NP increases. This suggests that increasing the size of the ZnS NP enhances its crystal structures after relaxation. There is a tiny peak that emerges before the first neighbour's peak and its intensity increases by decreasing the size of the NPs. In other words, the intensity of this peak increases while the crystal structure loses stability. Hamad et al. reported the Zn-Zn RDF diagrams similar to what we observed for 10 and 20 Å NPs for small clusters which adopt double-bubble structures [40]. They related the appearance of the first tiny peak to the formation of 4-rings of 3-coordinated atoms in the bubble-like structures.

Figure 4.1f shows $n(3.5 < r < 4.5) = 4\pi \int_{3.5}^{4.5} \rho r^2 G(r) dr$ for ZnS NPs with different sizes as well as bulk structures. For a periodic system, this quantity is equal to the coordination number. Due to the undercoordinated surface atoms, this number is lower for NPs and decreases by decreasing the size of the NP (because the surface to volume ratio is higher in smaller NPs). The difference between the $n(3.5 < r < 4.5)$ of relaxed and unrelaxed configurations is an indication of the deviation of the relaxed structure from the ideal NP structure.

1 and 2 nm NPs

As mentioned before, the main characteristic of the bubble and onion like double bubble (where a network of 4-coordinated atoms connects the inner and outer bubble clusters) structures, is that the majority of atoms are three-coordinated. The coordination number (CN) of atom A was calculated by counting the number of dissimilar atoms (B) within a 3 Å distance from atom A. The 3 Å distance was chosen according to the first and second peaks in the Zn-S RDF diagram of periodic bulk ZnS (corresponding to the first and second dissimilar neighbours), which are 2.35 and 4.5 Å, respectively. Figure 4.2 represents the results of CN calculations for 10 and 20 Å NPs.

Since the initial configurations were made of perfect ZB and WZ structures, all undercoordinated atoms in the initial configurations ($CN < 4$) are located on the surface. Due to the higher surface-to-volume ratio of 10 Å NP, its initial configuration has more undercoordinated atoms compared to the 20 Å NP. Figure 4.2a shows that all atoms in 10 Å NP

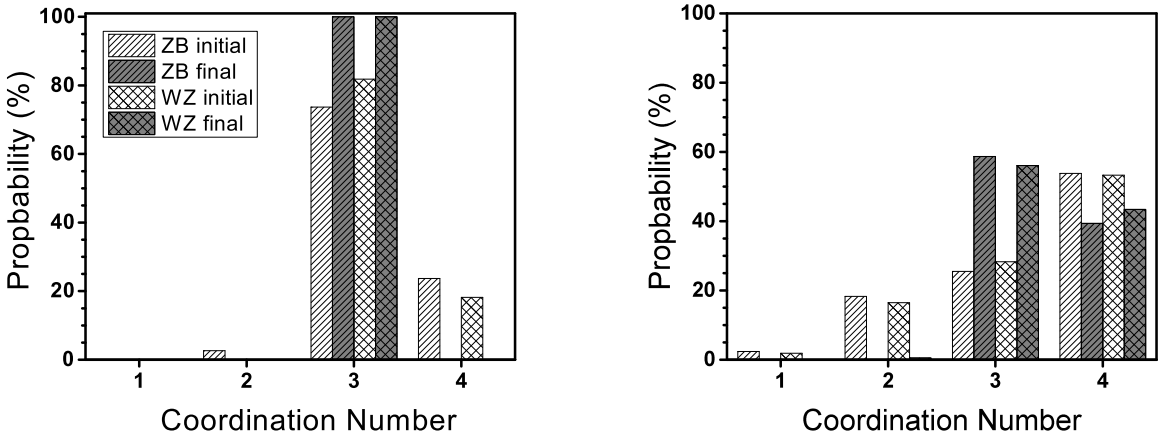

(a)

(b)

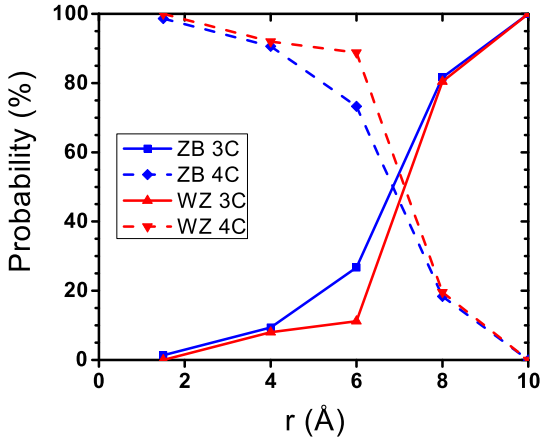

(c)

Figure 4.2: Distribution of atomic coordination number in initial and final configurations of (a) 10 Å and (b) 20 Å NPs. (c) Shows the probability of finding 3- and 4-coordinated atoms in 20 Å ZB and WZ NPs as a function of distance from the centre of NP.

become 3-coordinated after relaxation at 300 K. This confirms the stability of the bubble-like structure for 1 nm ZnS NPs which has been also shown by previous studies [3, 40]. In contrast, a considerable number of 4-coordinated atoms are detected in the relaxed 20 Å NPs, indicating that it is not likely that the atoms rearranged into a bubble-like structure (Fig. 4.2b). Figure 4.2b also shows that all the atoms become 3- or 4-coordinated after the relaxation and there is no 1- or 2-coordinated atoms in the final configuration of 20 Å NPs. The probability of finding 3- and 4-coordinated atoms in 20 Å NPs as a function of distance from the centre of the NP is represented in Fig. 4.2c. This figure also shows that the majority of atoms located in the cores of NPs ($r < 5$Å) keep their 4-coordinated structure. For both ZB and WZ NPs, the probability of finding 3-coordinated atoms increases as we approach the surface, but they increase with different rates. It seems the 4-coordinated structure is less stable in the 20 Å ZB NP.

To understand the nature of the 4-coordinated structure at the core of 20 Å NPs, we calculated the RDF for Zn-Zn and S-S pairs as well as the Honeycutt-Andersen (HA) indices [123] for atoms located in the core of the NPs. Four HA indices are defined as follows: the first index represents the RDF peak number to which the atomic pair of interest belongs and is usually equal to one (first neighbours). The second index is the number of common nearest neighbours of the atomic pair of interest. The third index counts the number of common neighbours which form a bond and the fourth one is used to differentiate clusters with identical sets of the first three indices but different configurations. HA indices can be used to identify the local FCC and HCP arrangements. It has been shown that the 1421 bond type is characteristic of the FCC crystal, while in the HCP structure, 1422 bonds are also predominant [124]. HA indices of Zn-Zn and S-S pairs can be used to track structural changes, since Zn and S atoms have FCC and HCP arrangements in ZB and WZ structures, respectively. The 12xx and 13xx bond families represent the short-range order by forming rhombus clusters, usually considered as a sign of a disordered system [125]. Figure 4.3 represents the RDF and HA indices for the core atoms of 20 Å NPs ($r < 5$Å). Both RDF and HA were calculated from the trajectories of the last 1 ns of simulations.

Figure 4.3 shows that structures of the cores of both NPs considerably diverge from the initial crystal structure. A large number of 1201 and 1311 bond types also indicates a highly distorted structure. Although almost all central atoms are still 4-coordinated in the relaxed 20 Å NPs, they have lost their initial crystal structure. Apparently, the structural change is more severe in the ZB structure. This can be deduced from the stronger first RDF peak and lower number of 1201 and 1311 bonds in WZ NP (Figure 4.3b). The tiny peak before the first neighbour peak is also observed in the core Zn-Zn RDFs, showing that 4-rings have also formed in the 4-coordinated cores of 20 Å NPs. The formation of 4-rings has been reported in the crystallization of ZnS from an amorphous structure [126]

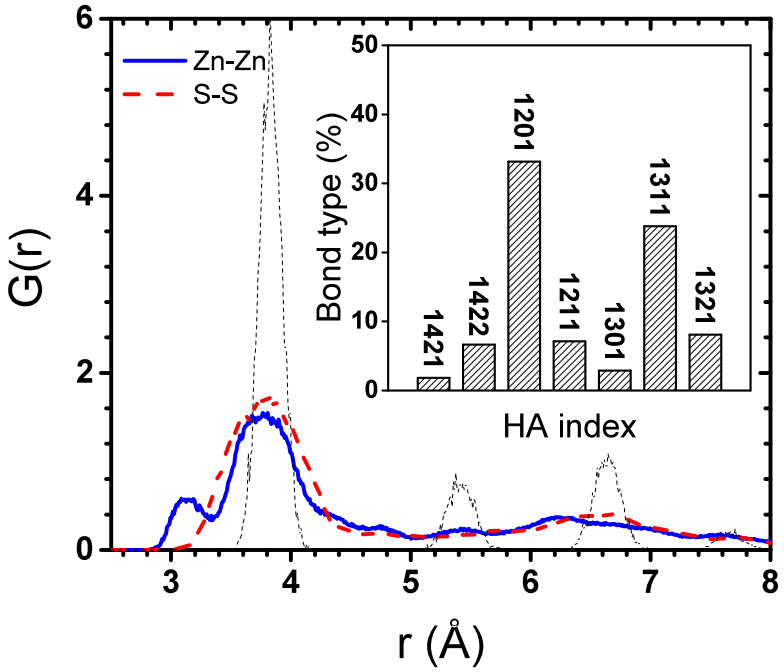

(a)

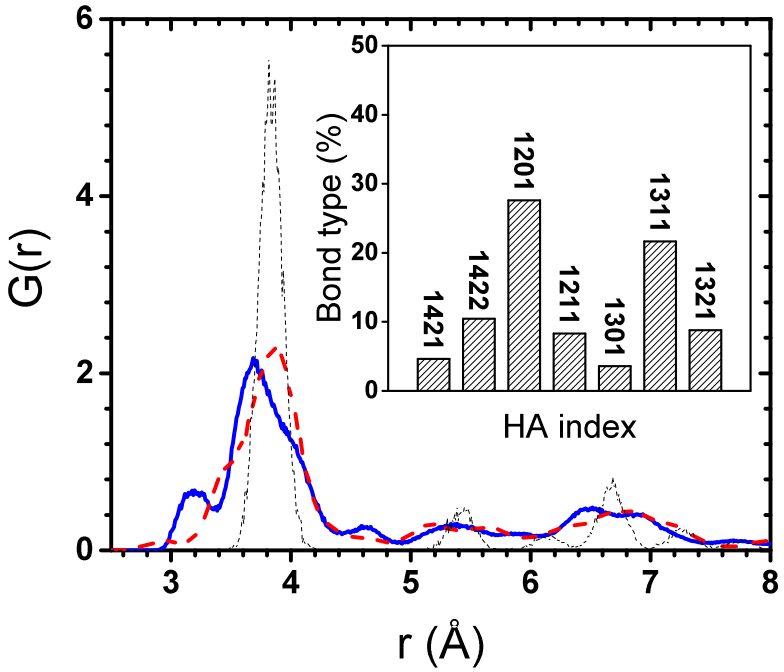

(b)

Figure 4.3: RDF of Zn-Zn and S-S pairs at the core ($r < 5$Å) of 20 Å ZnS NPs with initial (a) ZB and (b) WZ structures. Inset plots are HA indices for the same NP. Dashed lines show the corresponding plots for the NPs with the same size but with an unrelaxed structure. All calculation were done using trajectories of the last 1 ns of the simulations.

and simulated annealing [40]. This peak is missing in the S-S RDFs because 4-rings adopt a rhombus shape in which S atoms stay farther from each other. The bigger length of S-S pairs occurs because repulsive forces are stronger between anions in ionic components. In the ZB and WZ structures, Zn-Zn and S-S distances are identical, but once NP loses its crystal structure, S ions have the opportunity to repel each other and stay further away causing Zn-Zn distances to decrease. This explains why Zn-Zn RDF peaks for 10 and 20 Å NPs shift to the right compared to the unrelaxed RDF peaks (Figure 4.1). The deviation from the ideal crystal structure becomes more severe by coming closer to the surface, where the atoms have more freedom to move, i.e., the S-S distances increase more and Zn-Zn distances become shorter. When the atomic arrangement deviates from the nominal crystal structure of the NPs, the atomic bond angles are also altered. Perfect ZB and WZ crystals show a single peak angular distribution with a maximum located at 109.47°, which is the tetrahedral bond angle. Any deviation from this angular distribution is an indication of deviation from the crystal structure. Figure 4.4 shows the distribution of Zn-S-Zn and S-Zn-S angles at different distances from the centre of 20 Å ZB and WZ NPs.

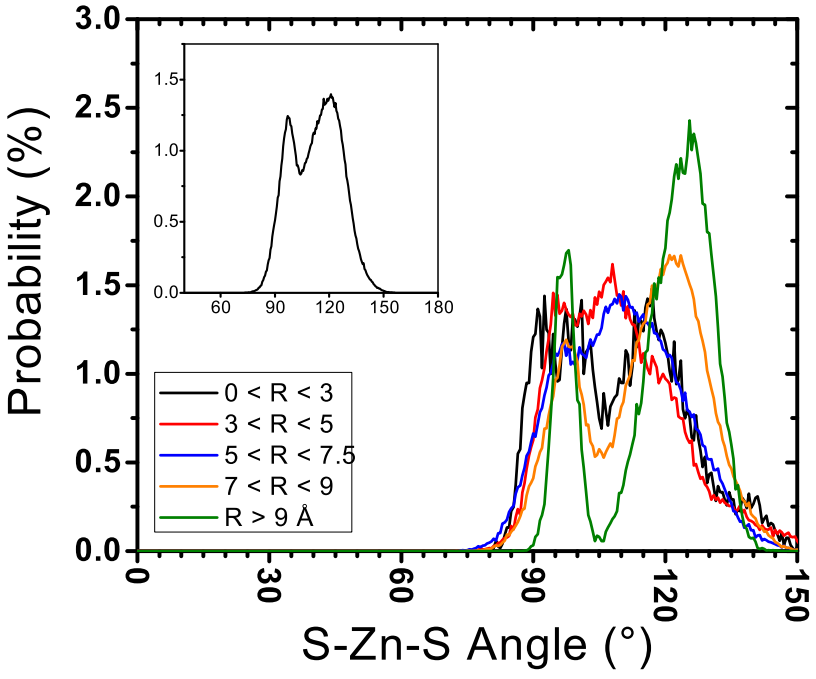

(a)

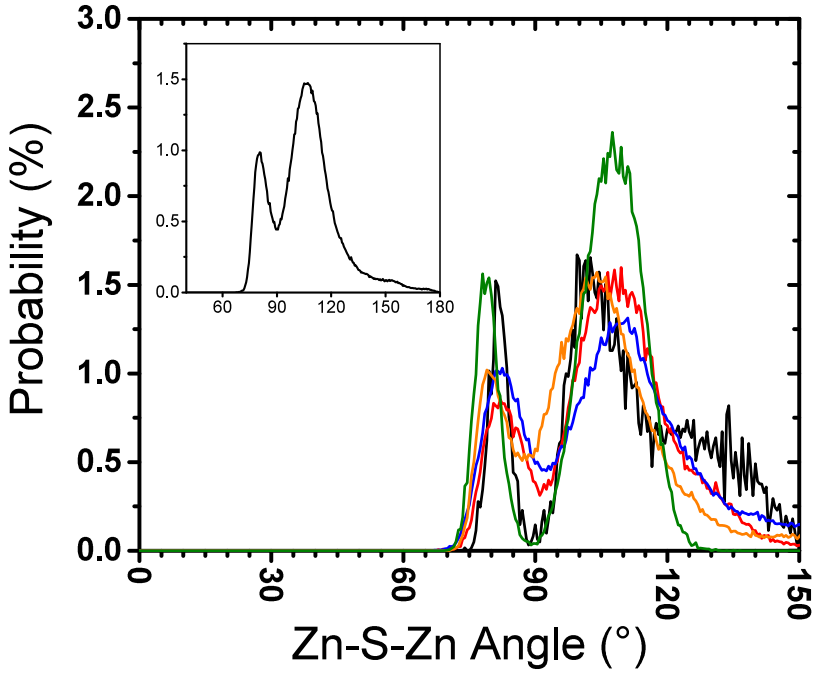
Probability (%)
Zn-S-Zn Angle (°)
3.0
2.5
2.0
1.5
1.0
0.5
0.0
0
30
60
90
120
150
1.5
1.0
0.5
0.0
60
90
120
150
180

(b)

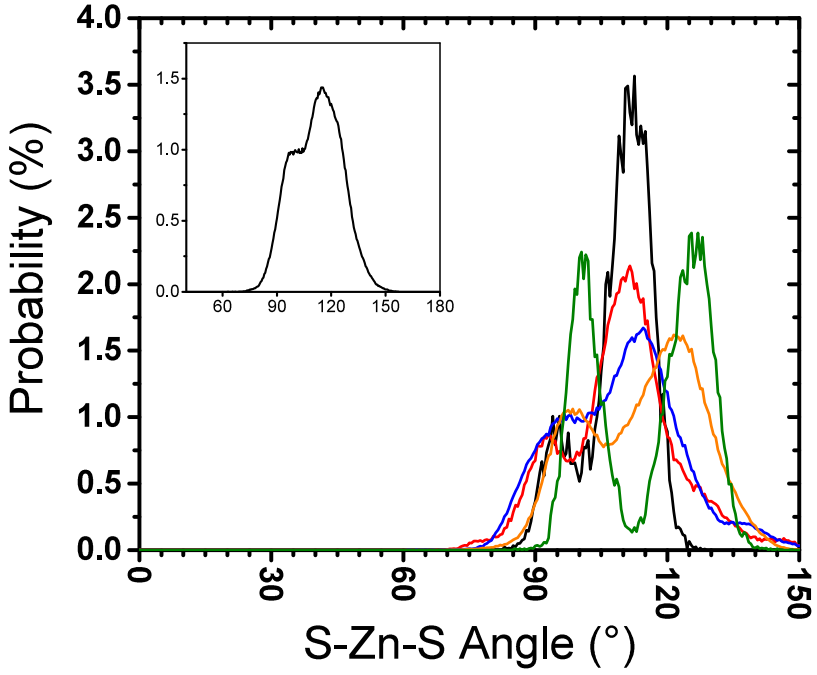
Probability (%)
S-Zn-S Angle (°)
4.0
3.5
3.0
2.5
2.0
1.5
1.0
0.5
0.0
0
30
60
90
120
150
1.5
1.0
0.5
0.0
60
90
120
150
180

(c)

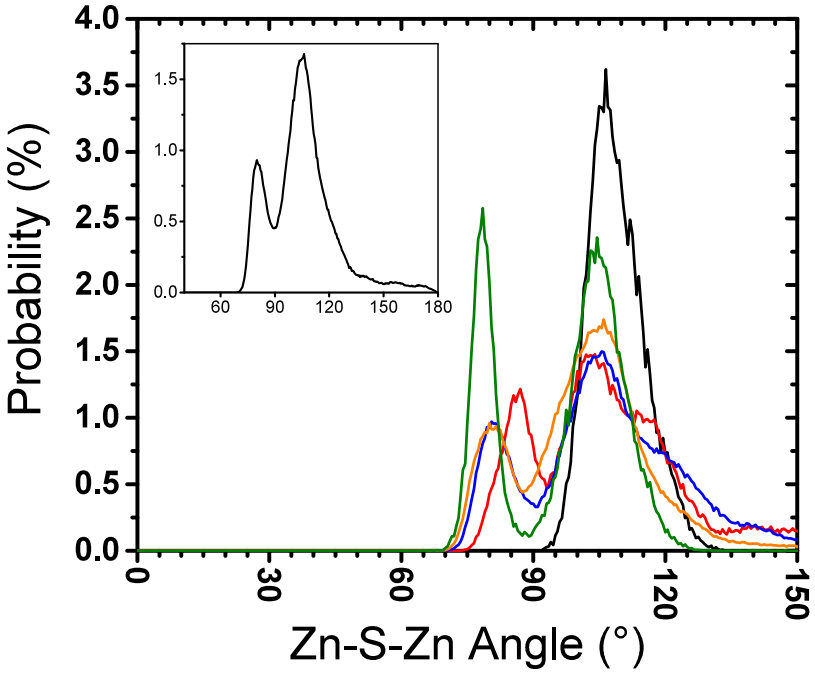

(d)

Figure 4.4: Angular distribution over the last 1 ns of relaxation at 300 K for 20 Å NPs with initial (a,b) ZB and (c,d) WZ structures. Different colours correspond to different distances of the vertex of the angle (central atom) from the centre of the NP. Inset plots are overall angular distributions.

While a small portion of atoms at the centre of the 20 Å WZ NP ($r < 3$Å) show a tetrahedral angular distribution (Fig. 4.4c-4.4d), ZB NP shows a completely distorted angular distribution, even for the central atoms. This further confirms that the tetrahedral bond structure is more stable in WZ NPs. Similar to Fig. 4.3, transformation from the single-peak to the double-peak angular distribution in Fig. 4.4 shows that the atomic structure of the cores of 20 Å NPs deviates from the tetrahedral structure, although atoms are still 4-coordinated. In the double peak angular distribution, the first peak corresponds to the formation of 4-rings where the angles are smaller. Generally, Zn-S-Zn angles are smaller than S-Zn-S angles because once the deviation from the tetrahedral bond structure occurs, Zn-Zn and S-S distances become shorter and bigger than their equilibrium distances in the crystal structure (the first peak in the unrelaxed RDF), respectively. As mentioned before, this deviation becomes more significant closer to the surface where atoms have more freedom to move. This movement causes the S-Zn-S and Zn-S-Zn angular distributions to move to the right and the left, respectively. The intensity of the 4-rings' peak in the angular distribution becomes significantly greater when R $>$ 9 Å showing the higher probability of forming 4-rings on the surface. Figure 4.5 shows the final configurations of 10 Å and the

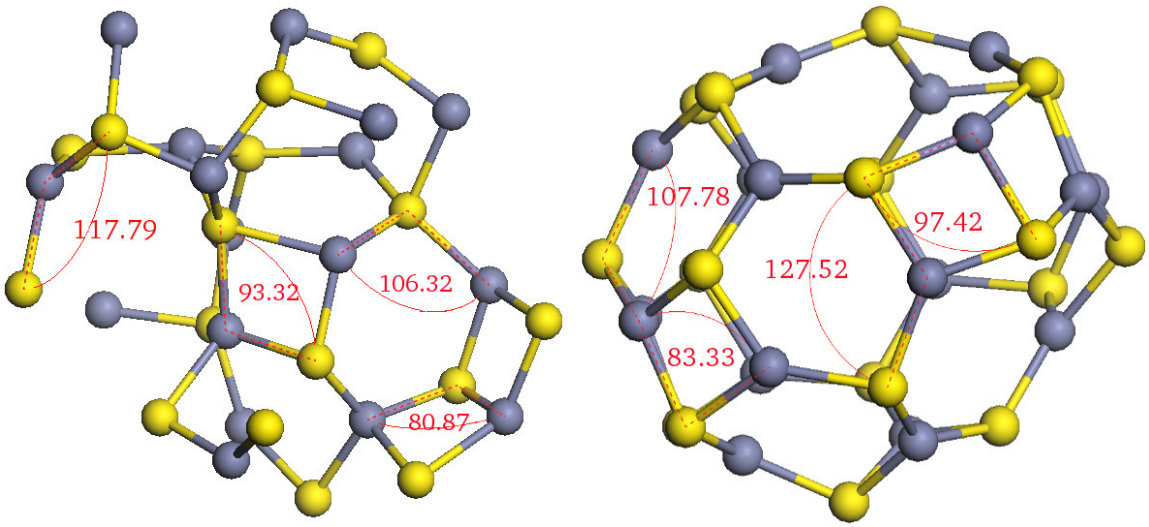

(a) (b)

Figure 4.5: Final configurations of (a) atoms at the core of 20 Å ZB NP ($r < 5$ Å) and (b) 10 Å ZB NP (yellow and grey spheres are S and Zn ions, respectively).

core of 20 Å ZB NPs.

All atoms at the core of 20 Å ZB NP are 4-coordinated, while the 10 Å ZB NP final configuration is made entirely of 3-coordinated atoms. Figure 4.5 shows that the S-Zn-S and Zn-S-Zn atomic angles between the 3-coordinated atoms on the surface differ from the 4-coordinated atoms in the core.

3 to 5 nm NPs

The above analyses confirm that the structure of the 20 Å ZnS NPs consists of 3-coordinated atoms on the surface and a distorted structure of 4-coordinated atoms in the core. The 4-coordinated atoms mainly lose their tetrahedral structure and arrange into 4- and 6-rings. However, small number of atoms at the core of 20 Å NP ($r < 3$Å) with the WZ initial structure still keep their tetrahedral arrangement. The initial structure seems to completely fade away in the ZB NP. Based on these observations, we can expect bigger NPs to have a structure, including the 4-coordinated atoms with the tetrahedral arrangement at the core, followed by a shell that includes the distorted structure of 4-rings and 6-rings of 4-coordinated atoms which connects 3-coordinated surface atoms to the core. The same analyses were performed to study the structural changes in the bigger NPs. Figure 4.6 shows the CN distribution of 30, 40 and 50 Å NPs.

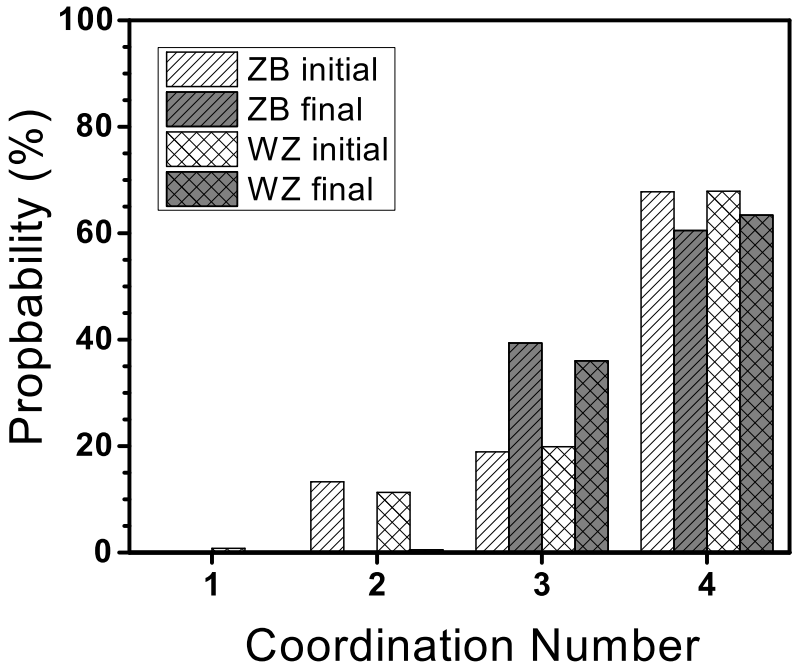
ZB initial
ZB final
WZ initial
WZ final
Propbability (%)
Coordination Number
0
20
40
60
80
100
1
2
3
4

(a) 30 Å

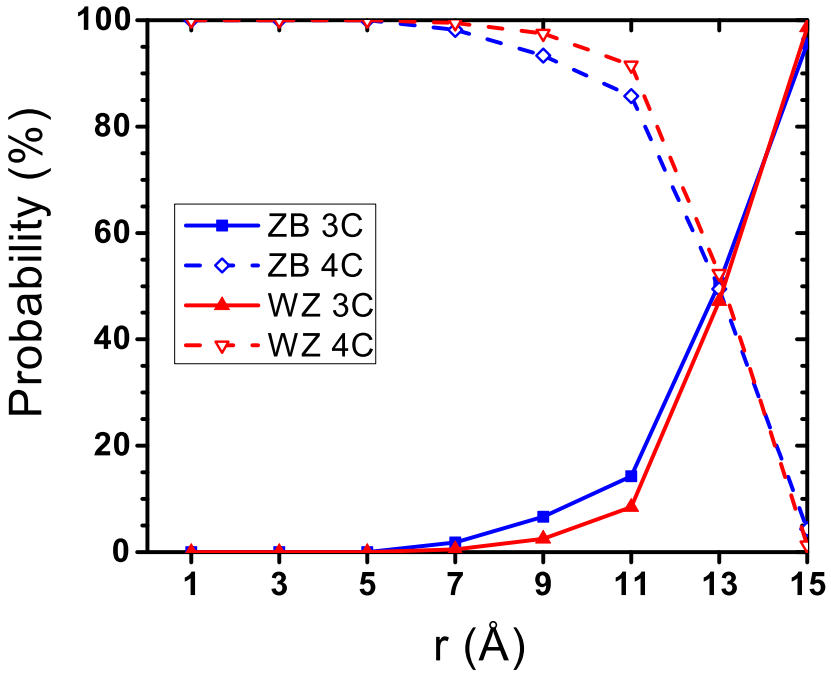
ZB 3C
ZB 4C
WZ 3C
WZ 4C
Probability (%)
r (Å)
0
20
40
60
80
100
1
3
5
7
9
11
13
15

(b) 30 Å

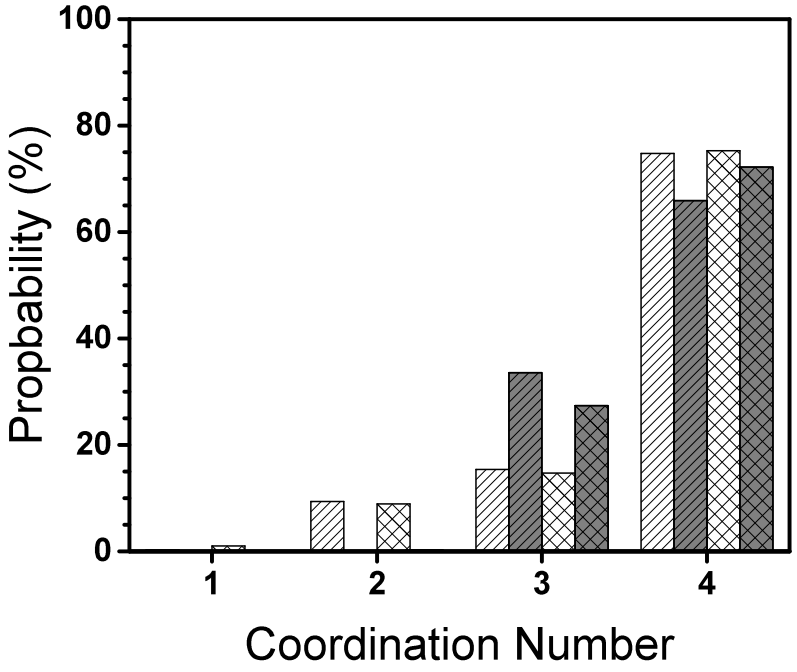
Propbability (%)
100
80
60
40
20
0
1
2
3
4
Coordination Number

(c) 40 Å

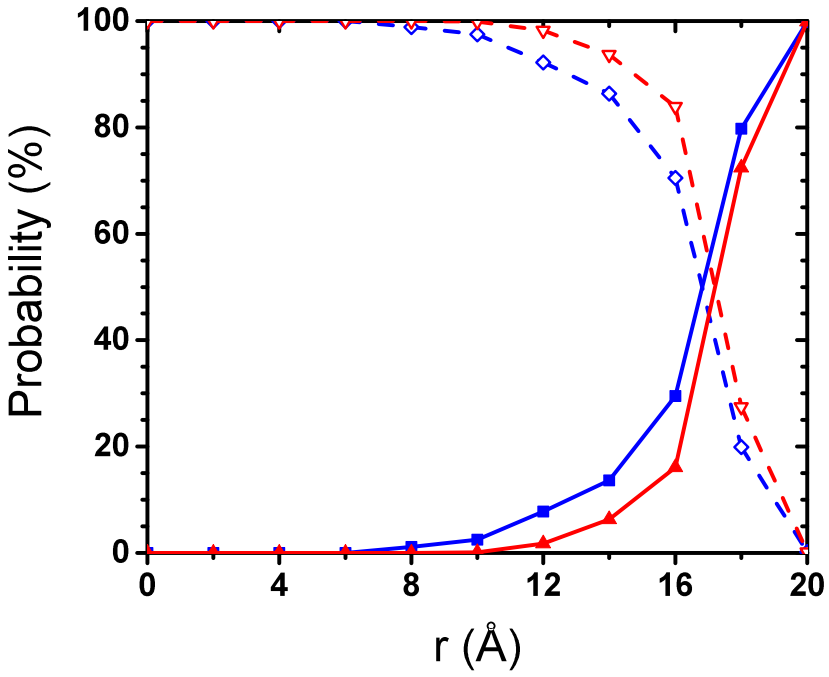
Probability (%)
100
80
60
40
20
0
0
4
8
12
16
20
r (Å)

(d) 40 Å

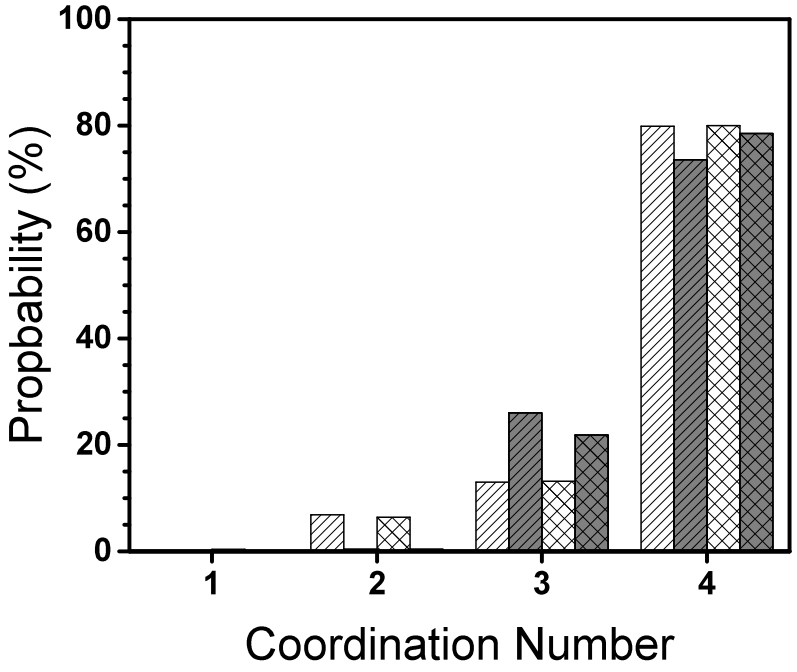

(e) 50 Å

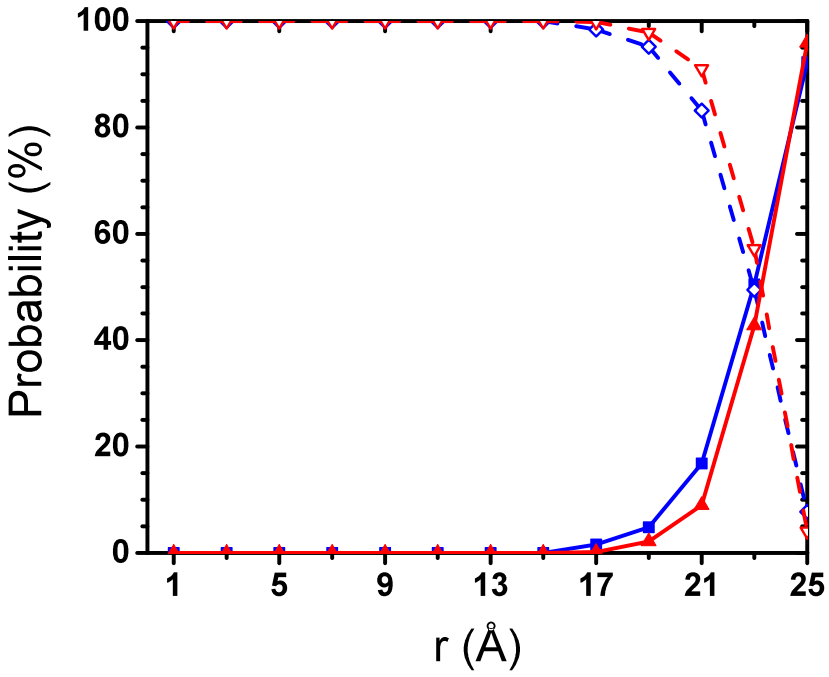

(f) 50 Å

Figure 4.6: CN distribution for (a,b) 30Å, (c,d) 40Å, and (e,f) 50Å NPs. Bar plots (left column) show the probability of finding atoms with different CNs in the initial and final configurations. Line plots (right column) show probability of finding a 4- or 3-coordinated atom at different distances from the centre during the last 1 ns of simulations.

Comparing Fig. 4.6 with Fig. 4.2b, we can see that unlike the 20 Å NPs, the 4-coordinated atoms are dominant in bigger NPs. The stability of the 4-coordinated structure increases by increasing the size of NPs. Similar to what was observed in 20 Å NP, the ZB structure is less stable than the WZ structure. Figures 4.6b, 4.6d and 4.6f show that a 50% probability for 3- and 4-coordinated atoms is located at around 1 Å beneath the surface. This distance, which was also observed for 20 Å NPs (Fig. 4.2c), shows that in all NPs ranging in size from 20 Å to 50 Å, the 3-coordinated structure is only limited to the surface. However, in 20 Å NPs, the surface relaxation causes a pervasive structural change, resulting in the disappearance of the tetrahedral structure. Thus, it seems that using the probability of finding 3-coordinated atoms in NPs is not a good way to quantify the stability of tetrahedral structure. As when we analyzed for 20 Å NPs, we calculated the angular distribution in different distances from the centre of NPs to track the change in tetrahedral structure. Figure 4.7 shows the S-Zn-S angular distribution calculated using trajectories of the last 1 ns of simulations.

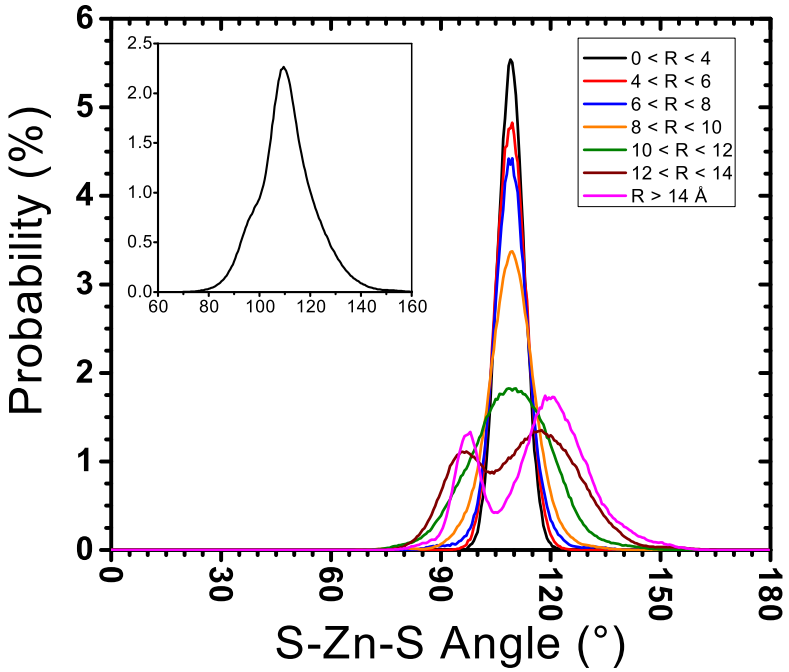
Probability (%)
S-Zn-S Angle (°)
0 < R < 4
4 < R < 6
6 < R < 8
8 < R < 10
10 < R < 12
12 < R < 14
R > 14 Å

(a) 30 Å

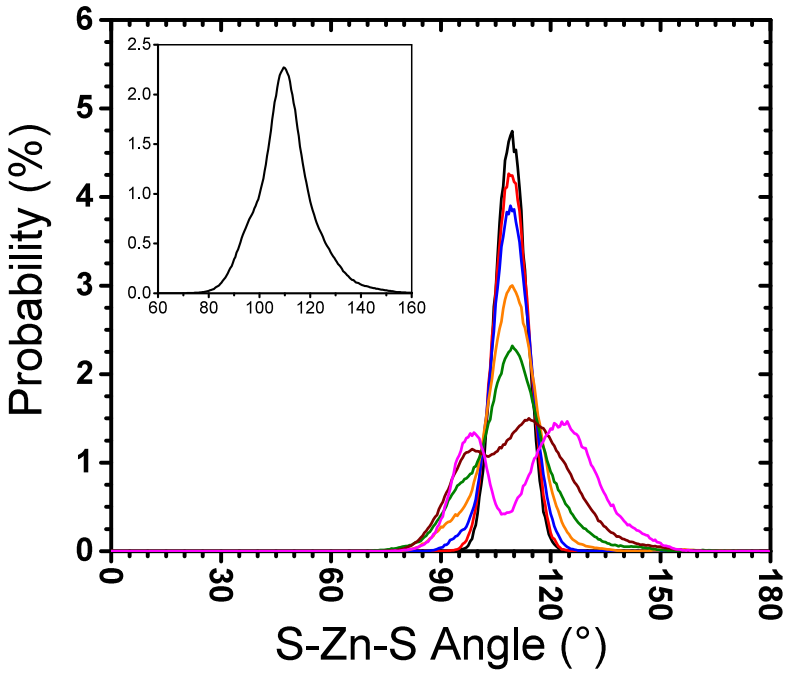
Probability (%)
S-Zn-S Angle (°)

(b) 30 Å

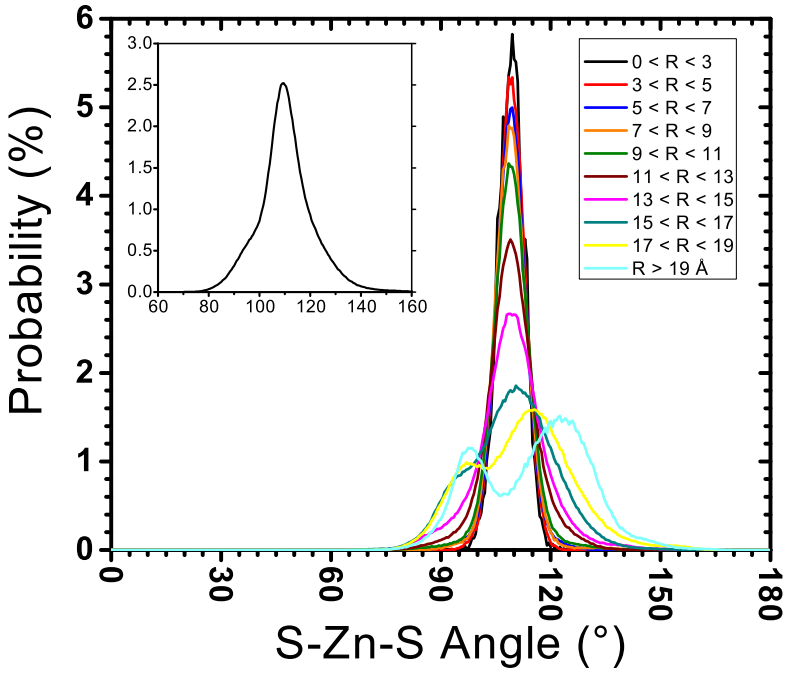
Probability (%)
S-Zn-S Angle (°)
0 < R < 3
3 < R < 5
5 < R < 7
7 < R < 9
9 < R < 11
11 < R < 13
13 < R < 15
15 < R < 17
17 < R < 19
R > 19 Å

(c) 40 Å

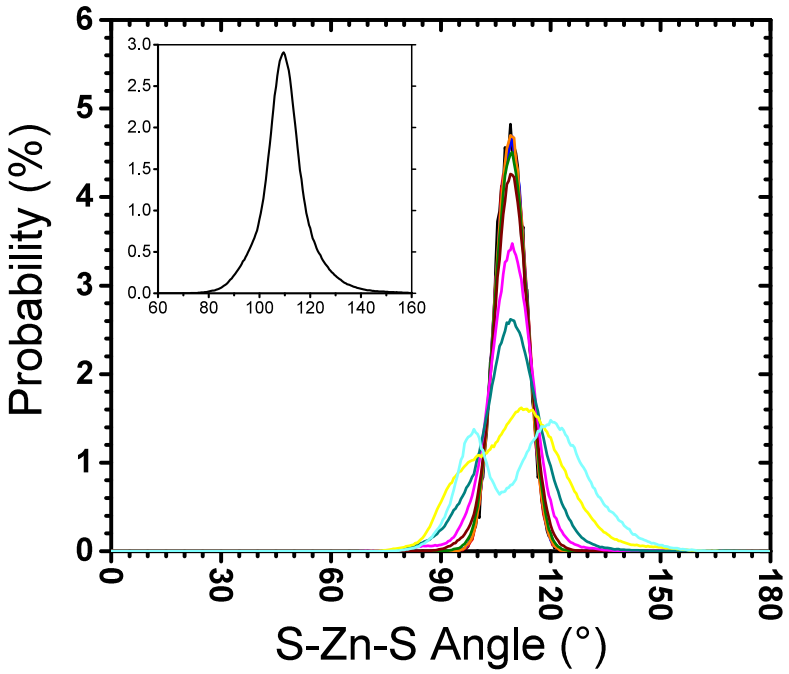
Probability (%)
S-Zn-S Angle (°)

(d) 40 Å

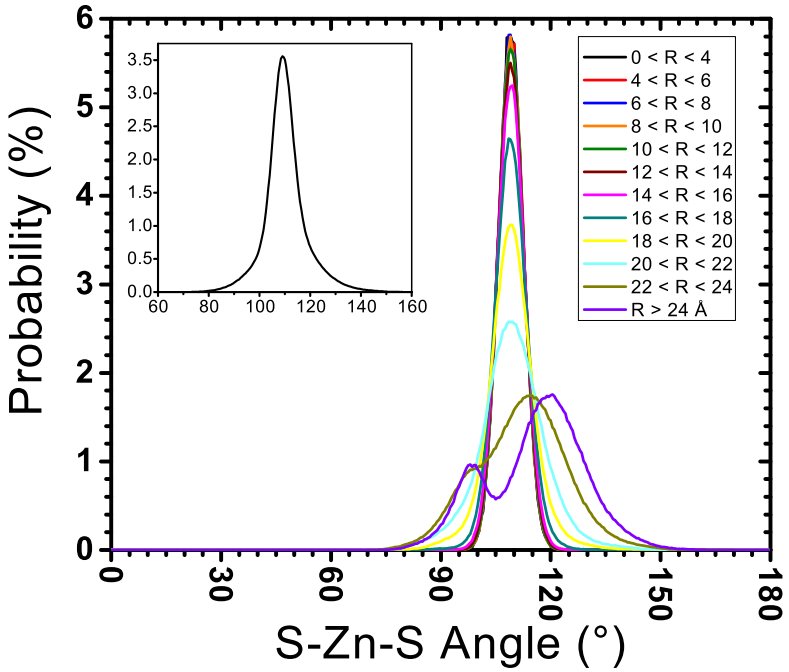

(e) 50 Å

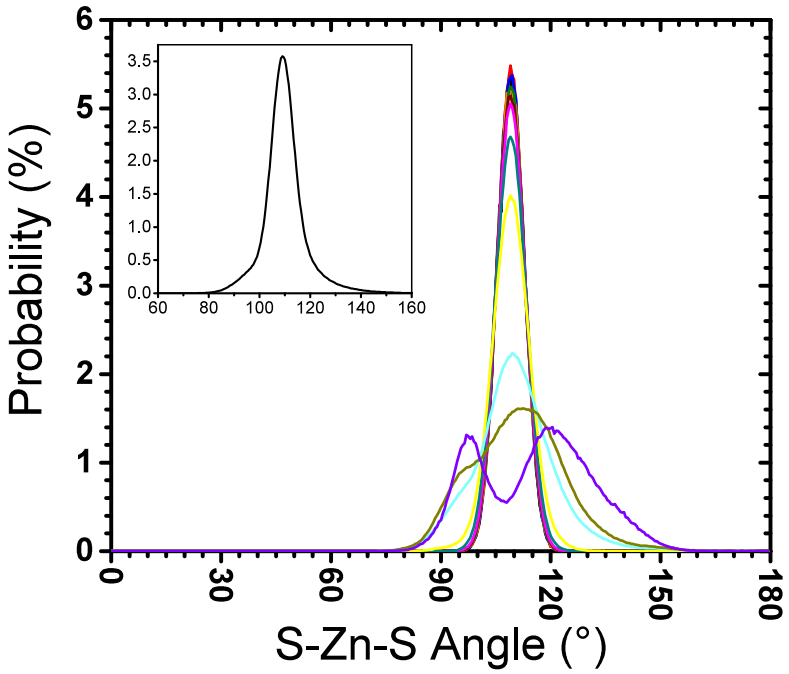

(f) 50 Å

Figure 4.7: Angular distribution over thr last 1 ns of relaxation at 300 K for 30 Å NPs with initial (a,b) ZB and (c,d) WZ structures. Different colours correspond to different distances of the vertex of the angle (central atom) from the centre of the NP. Inset plots are overall angular distributions.

Figure 4.7 shows that all NPs with sizes ranging from 30 Å to 50 Å have shown strong tetrahedral peaks at their centres. Compared to WZ NPs, the tetrahedral angular distributions of the central atoms in ZB NPs have a higher intensity. However, the intensity of the tetrahedral peak in ZB NPs decreases at a higher rate as it approaches the surface. The lower intensity of the tetrahedral angular distribution at the centre of WZ NPs is probably due to the anisotropic thermal vibration in WZ crystal, which causes the tetrahedral angle to vibrate in a wider range. The anisotropy of thermal vibration of WZ ZnS has been reported in DFT calculations [127]. Moreover, it is well known that real WZ lattices of II-VI semiconductors deviate from the ideal WZ structure [49]. It has been already shown that the potential formulation used in this study successfully reproduces the real WZ structure of ZnS at 300 K [128]. This difference can make the angle of the tetrahedral bond deviate slightly from the ideal tetrahedral angle (109.47 °) in the real WZ structure. This effect is also the main reason of the different polar behaviour of ZB and WZ structures. This behaviour is explained in more details later. Except for atoms at the very centre of NPs ($r < 5$Å), all other tetrahedral angular distributions in 30 and 40 Å WZ NPs are stronger than those in ZB NPs. This suggests that WZ NPs have a more stable tetrahedral structure.

As shown in Fig. 4.6, 3-coordinated atoms become dominant from almost 1 Å underneath the nominal radius of NPs. In Fig. 4.7, we can see that these atoms show a double-peak angular distribution in which both peaks have almost the same intensity. The first peak is due to the formation of 4-rings on the surface. In all diagrams, we can see that the deviation from single-peak to double-peak distribution starts from almost 5 Å underneath the surface. Since Fig. 4.6 shows that almost all atoms are still 4 coordinated at this distance, the formation of the double-peak distribution can be attributed to the distorted 4-coordinated structure (similar to what we observed at the core of 20 Å NPs). Double-peak distributions move to the right as we approach to the surface. This is because the S-Zn-S angles become bigger on the surface as atoms have more freedom to move.

Root Mean Square Displacement

To verify the formation of the distorted 4-coordinated structure under the surface, we also calculated the root mean square displacement of atoms with respect to their initial positions. In RMSD calculations the position of atoms in each time step is corrected to remove the NP's centre of mass rotation and movement effect. Figure 4.8 shows the average RMSD of atoms at different distances from the centre.

Apparently, the RMSD of centres of all NPs is negligible except for 20 Å NPs. This verifies the angular distribution results which showed that all NPs except for the 20 Å NPs kept their tetrahedral structures at their centres. Excluding the 20 Å NPs, Fig. 4.8 also

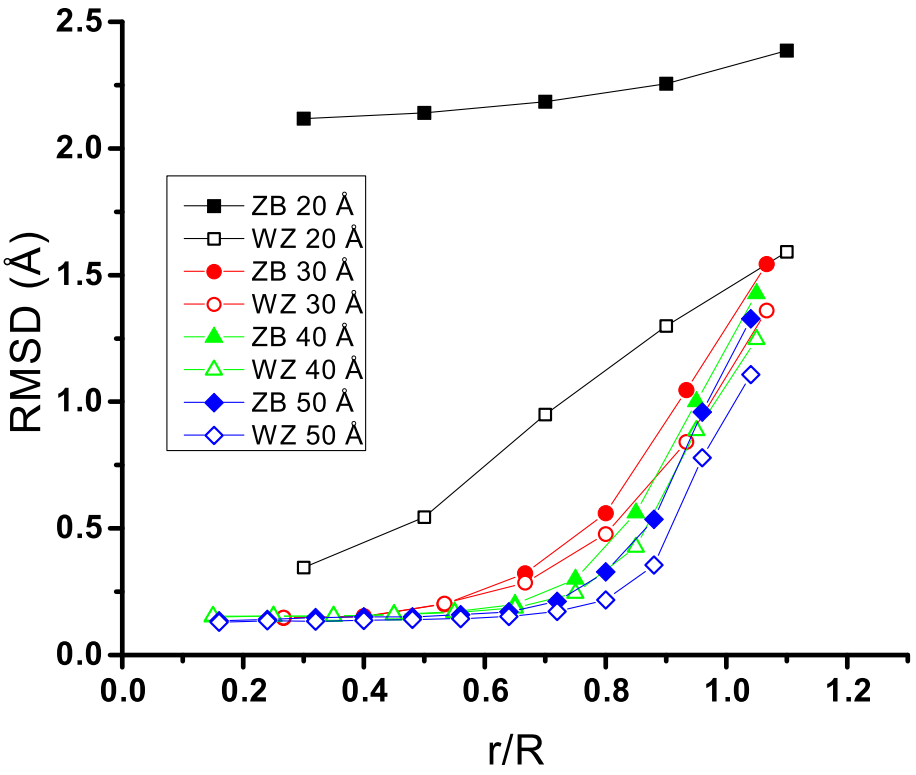

Figure 4.8: RMSD calculated for atoms located in a shell confined between r and r - 2 Å. R is the radius of the NP.

shows that RMSD plots for all NPs start to diverge from the plateau from about 5 Å beneath the surface. As mentioned before, the large displacement of atoms in this region can be a sign that distorted 4-coordinated structure was formed. The formation of distorted 4-coordinated structure was also characterized by the appearance of double-peak angular distributions in Fig. 4.7.

3-Phase Structure

The above observations and analyses confirm the three-phase structure of ZnS NPs: a) a crystalline core which maintains the initial tetrahedral bond structure, b) a distorted network of 4-coordinated atoms which surrounds the crystalline core, and c) a surface structure which includes 4 and 6-rings of 3-coordinated atoms. We further quantify these three phases using the bond angle and coordination number of each atoms as follows: 4-coordinated atoms whose all bond angles range between 100° and 120° are considered as tetrahedral atoms (4CT); the 4-coordinated atoms which have at least one angle out of the aforementioned range are categorized as not tetrahedral 4-coordinated atoms (4CNT); and finally, the 3-coordinated atoms (3C) which form the surface structure. According to the previous analyses, all atoms in the relaxed ZnS NPs should belong to one of these categories. Results of these calculations are illustrated in Fig. 4.9 using two different graphical representations. Line plots show the probability of finding each atom type at different distances from the centre. Each dot in the scatter plots represents an atomic position during the last 1 ns of simulations. For clarity, only the position of atoms located in the central slab ($-2\text{Å} < Z < 2\text{Å}$) of NPs is shown. Moreover, to avoid redundancy, only the results for 20 and 50 Å NPs are represented.

(a)

(b)

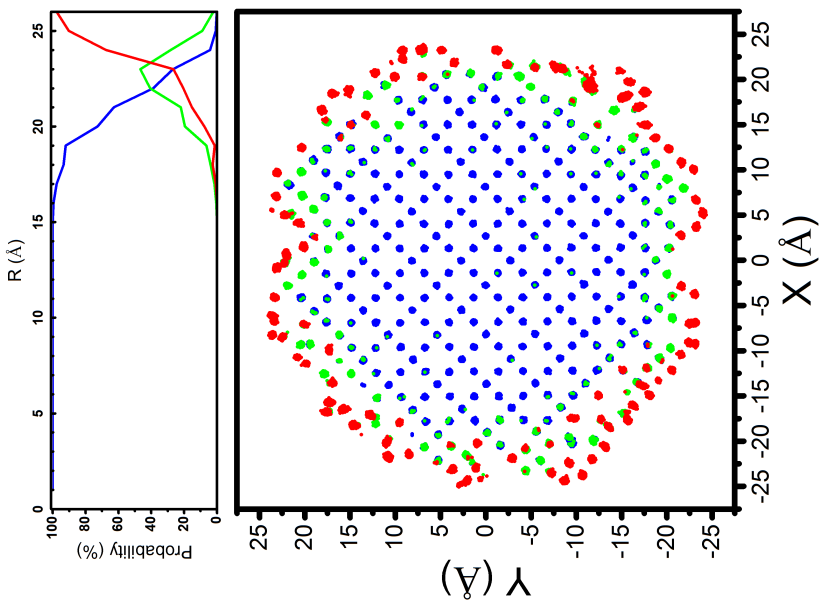

(c)

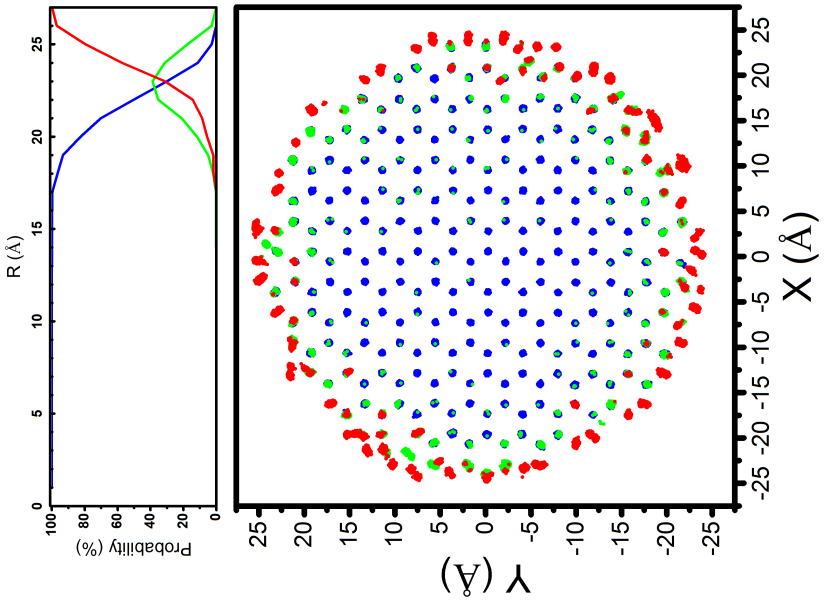

(d)

Figure 4.9: Representation of three atom types in the last 1 ns of relaxation of (a) 20 Å ZB, (b) 20 Å WZ, (c) 50 Å ZB and (d) 50 Å WZ NPs. 4CT: 4-coordinated atoms whose all bond angles are between 100° and 120° (tetrahedral atoms), 4CNT: 4-coordinated atoms which have at least one angle out of the aforementioned range (not tetrahedral 4-coordinated atoms), and 3C: 3-coordinated atoms (surface atoms). Scatter plots show the distribution of different atom types in a slab with $-2 < Z < 2$ and line plots show the probability of finding each atomic type in a shell confined between R and R - 1 Å. Different atomic types are distinguishable by different colours.

Figure 4.9a confirms the complete disappearance of the tetrahedral structure in the 20 Å ZB NP. In contrast, a small portion of tetrahedral atoms is detected in the centre of 20 Å WZ NP. Figures 4.9c and 4.9d also show that the deviation from the tetrahedral structure begins from about 5 Å beneath the surface. This 5 Å thickness of distorted structure, which has also been observed in Fig. 4.8, suggests that 30 to 50 Å ZnS NPs, regardless of their size or initial crystal structure, experience a similar surface relaxation which results in a network of 3-coordinated atoms on the surface followed by a couple of layers of distorted 4-coordinated atoms. This similarity is of great importance because it can result in the same surface properties that can control the interaction of NPs with the surrounding environment. Atoms located on the edges and corners of surface facets are more under-coordinated (1- and 2-coordinated) and more prone to chemical and electrochemical reactions [129]. The surface behaviour can be greatly changed if the faceted nature of the NPs' surfaces disappears, and the coordination number of all the atoms on the surface is turned to three. Figure 4.10 confirms that the similar surface structures of ZnS NPs leads to similar surface energies as well.

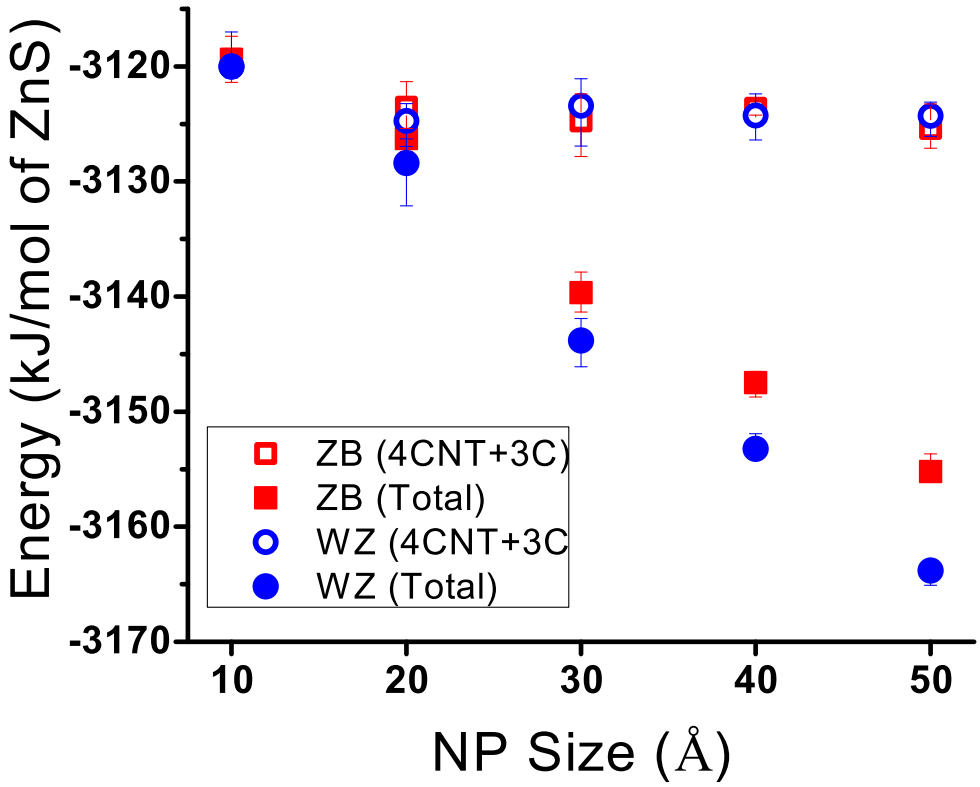

Figure 4.10: The average potential energy of ZnS NPs after relaxation. The energy of the surface layers (4CNT+3C atoms) was calculated via subtracting the energy of the crystalline core from the total energy of the NP.

The energy of the surface atomic layers including 4CNT and 3C atoms was estimated by subtracting the total energy of NP from the energy of the crystalline core. The energy of the ZB and WZ lattices has been calculated from NPT simulations of the periodic bulk structures. The energy of the crystalline core of NPs was then calculated by multiplying the number of 4CT atoms by the energy per atom obtained from the simulation of the bulk structures. The average number of 4CT, 4CNT and 3C atoms and the average total energy of NPs were calculated from the last 1 ns of simulations.

Figure 4.10 shows that the total energy of a NP decreases as the size increases. This is expected, as by increasing the size, the surface-to-volume ratio decreases and the structure of the NP also transforms from more amorphous-like to more crystalline-like, and energy approaches the level of bulk energy. However, the energy of the surface atoms (open symbols) is independent of both the initial crystal structure and the size of the NP.

4.2.2 Dipole Moment

The dipole momentum is calculated in this study to examine the effect of structural change. Dipole-dipole interactions are of a great importance as they are shown to be the governing factor in the agglomeration [45], oriented attachment [46], and stabilization of superlattice structures [47] of non-metallic NPs. There has been considerable number of studies on finding the origin of large permanent dipole in ionic NPs. A large DM is expected in WZ NPs due to the polar nature of WZ lattice but the DM is expected to be absent in ZB NPs, due to the T_d symmetry of ZB lattice. Li and Alivisatos's study on CdSe nanorods showed that a permanent DM was proportional to the volume of nanorods. They considered the origin of the DM was due to the natural polar character of the WZ structure [48]. Nann and Schneider have also shown that small crystallographic deviations from the ideal WZ structure could result in a large permanent dipole moment [49]. In contrast, Shim and Guyot-Sionnest have shown a large DM in both WZ CdSe and ZB ZnSe nanocrystals which were linearly dependent on the radius [44]. Since the large DM has been observed for both ZB and WZ structures, they concluded that this linear size dependence was not due to the polar character of the WZ lattice but to the faceted surface structure of nanocrystals. A subsequent study of Shanbhag and Kotov showed that minor deviations from a symmetric tetrahedral shape of ZB CdS nanocrystals could result in large DMs [50]. Cho et al. have shown that the dipole moment of PbSe nanocrystals with a centrosymmetric rocksalt lattice was large enough to result in the formation of nanowires through the oriented attachment of nanocrystals [51]. Considering a random distribution of polar facets and the probability of lacking of central symmetry, they showed that about 89% of possible shapes of PbSe nanocrystals was polar. The self-assembly of ZnS nanocrystals into ellipsoidal shapes has also been explained by charge-charge, charge-dipole, and dipole-dipole interactions of non-

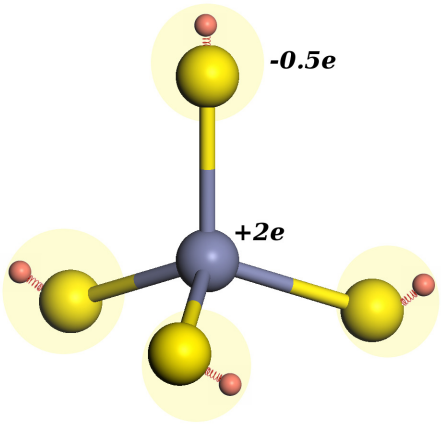

Figure 4.11: Tetrahedron model used to calculate the bulk dipole moment.

symmetric ZnS NCs along the [111] direction [52].

All the previous studies explain the dipole moment in NCs with a cubic crystal lattice via the deviation of distribution of surface ions from the central symmetry. In contrast, WZ NCs polarity is mainly related to deviation of WZ lattice from the idea tetrahedral bond structure. In this study we will systemically quantify the effect of surface and bulk asymmetry of ZnS NPs on the total DM. We also propose the dynamical structural relaxation of NPs (which is explained in previous section) as another major parameter controlling the DM. We used MD trajectories to calculate the total DM of a NP as

$$\overrightarrow{DM} = | < \sum_{i} q_i r_i > | \tag{4.3}$$

where q_i and r_i are the charge and the position vector of ion i, respectively. To study the effect of the crystal structure of NPs on their final DM, the natural DM of ZB and WZ lattices was calculated first using trajectories of the 1 ns NPT simulation of bulk structures at 300 K and 0 atm. We used the simple-point charged model of Nann and Schneider [49] to calculate the bulk DM. In this model, the DM is calculated for each Zn-S tetrahedron unit as shown in Fig. 4.11. In each Zn-S tetrahedron, the Zn ion caries the elemental charge of +2e and each S ion (core plus shell) caries 25% of the Zn charge. For an ideal tetrahedral bond structure, where all atomic bond lengths are equal and all bond angles are equal to 109.47 °, the DM is equal to zero.

As expected, DM calculations show that bulk ZB structure has no natural DM while the WZ lattice is considerably polar. The average natural DM for each WZ ZnS tetrahedron unit was calculated to be 0.3855 D in the opposite direction of the c axis. This is in an

agreement with Nann and Schneider calculations, which confirms the natural DM of real WZ structure as a consequence of the slight C_{3v}-distortion of the elementary tetrahedron in real wurtzite [49].

As explained in the Methods section, making initial configurations of NPs is started by cutting spheres from perfect ZB and WZ lattices and followed by removing excessive ions from the surface to achieve charge neutrality. In this paper, when we refer to the initial configurations, we are talking about the initial configurations after charge neutralization. Configurations before the charge neutralization are called as-cut configurations. The charge neutralization of ionic NPs as-cut structures has usually been achieved by randomly removing excessive ions from the surface. However, this method could not ensure the symmetry of the initial configurations. The asymmetry of distribution of positive and negative ions on the surface can cause a DM for initial configurations. We noticed that except for 10 and 20Å NPs (in which the initial crystal structure is entirely removed after relaxation), the final structures' DM magnitude and direction is strongly dependent on the initial DM. To study the effect of structural evolution during the NPs' relaxation on the final DM, we needed to remove this artificial effect of initial structures. We did this using a method other than the random removing of excessive ions from the surface, which results in non-polar initial configurations. Details of our charge neutralization method are explained in the Methods section. For each NP size, 10 different, non-polar initial structures were randomly chosen and relaxed through NVT simulations. Figure 4.12 shows the DM per ZnS calculated for ZB and WZ NPs using 10 ns NVT simulations at 300 K. Trajectories of the last 1 ns of simulations were used to calculate the DM.

Figure 4.12 shows polarities of ZnS NPs as a function of NPs size. This figure shows that the DM is evolving differently in ZB and WZ NPs. While the magnitude of the DM per ZnS is decreasing continuously by increasing the size of ZB NPs, it drops and then increases as the WZ NPs size increases. Another major difference between ZB and WZ NPs polar behaviours is the direction of the DM vectors. The directions of DM vectors of relaxed ZB NPs with different initial configurations show no correlation and change randomly. However, the WZ NPs' DM vectors become more aligned with -Z direction as the size increases. Since the initial structures of NPs are not polar (or negligibly polar in WZ NPs), DMs of final configurations are pure products of structural evolutions of NPs at 300 K. As the ZB lattice remains non-polar at 300 K, divergence from the ideal tetrahedral structure which happens on the atomic layers near surface (aforementioned 4CNT and 3C structures) is the main reason of polarity of relaxed configurations of ZB NPs. The random direction of final DM vectors can also be justified by the fact that the deformed surface structure of a ZB NP has a random atomic arrangement.

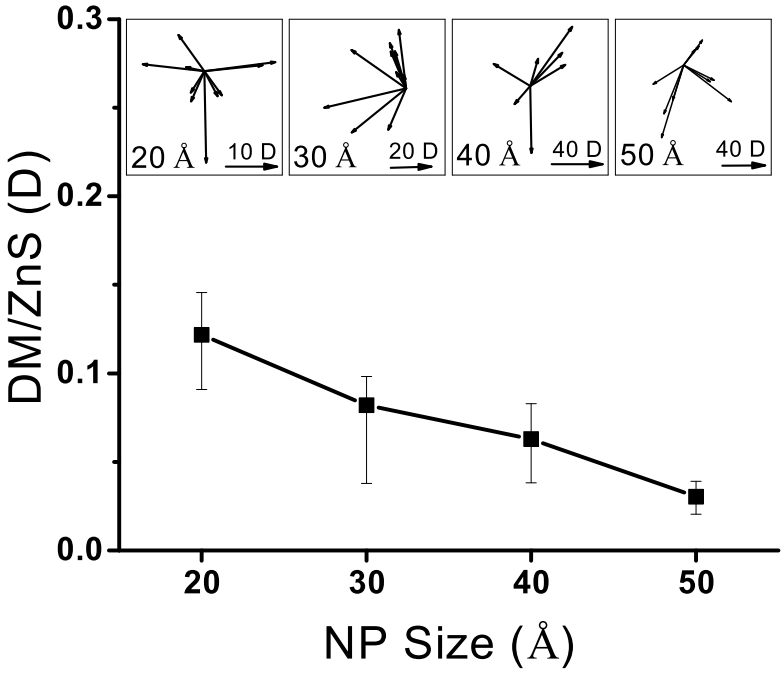

(a)

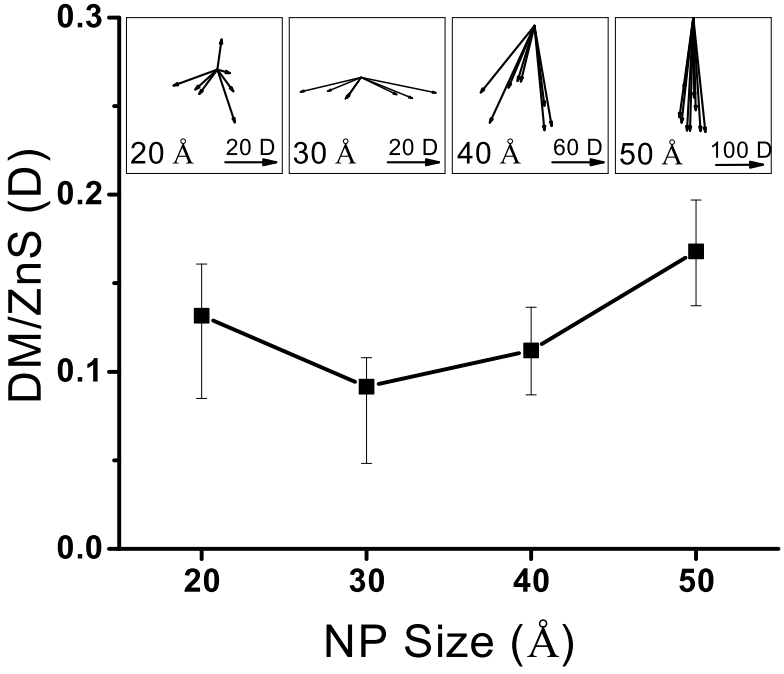

(b)

Figure 4.12: The DM of ZnS NPs calculated using the last 1 ns simulations. (a) and (b) show the DM of ZB and WZ NPs, respectively. Insets show the projected image of the DM vectors on the XZ plane.

For 20 Å WZ NP whose entire tetrahedral structure is almost vanished, the direction of DM is randomly changed for different initial configurations similar to ZB NPs. It also seems that the DM magnitude of 20 and 30 Å WZ NPs is similar to the corresponding ZB NPs, but starts to increase afterwards. Unlike the ZB structure, we showed that the WZ lattice is considerably polar at 300 K and the direction of the WZ bulk DM vector is aliened with -Z direction. As the WZ NP becomes bigger, the size of the bulk tetrahedral structure increases (number of 4CT ions) and this will consequently increase the magnitude of the bulk DM in Z direction. This is the reason why DM vectors become more aligned with the Z direction as the size of the WZ NP increases. It also explains why the polar behaviour of 20 and 30 Å WZ NPs, in which deformed surface structure is dominant, is similar to ZB NPs but starts to diverge after 30 Å when the polar crystalline core of WZ NPs becomes the dominant portion of the structure. As the size of the NP increases, the polarity converges to the bulk value. As a result, one should expect that the DM per ZnS magnitude of ZB and WZ NPs approach the bulk values which are 0.0 and 0.3855 D, respectively.

The DM caused by surface atoms of a WZ NP can be calculated by subtracting the DM caused by the crystalline core from the total DM of the NP. The bulk DM of WZ NPs was estimated by multiplying the number of tetrahedral units (number of Zn 4CT atoms) by 0.3855 D (the DM for each tetrahedral unit of WZ lattice). Figure 4.13 shows the DM per ZnS caused by the deformed surface structures of WZ NPs along with the total DM of ZB NPs.

Apparently, the magnitude of DM caused by surface structure of WZ NPs is similar to the DM of ZB NPs. This is another indication confirming that the surface structure of ZB and WZ NPs is similar. Figure 4.13 also shows that the effect of the surface dipole becomes less significant as the size of NPs increases. This is because the deformed surface structure of NPs becomes smaller comparing to bulk tetrahedral structure, as the size of a NP increases.

4.3 Discussion

In this paper, we studied the structural evolution of freestanding ZnS NPs having initial ZB and WZ crystal structures and ranged in size from 1 to 5 nm. We found that except for the 10 and 20 Å NPs, the final configurations of ZnS NPs with both initial crystal structures consisted of three regions: a) a crystalline core which kept the initial tetrahedral bond structure (4CT), b) a region of distorted 4-coordinated atoms which formed 4- and 6-rings (4CNT), and c) 3-coordinated atoms which covered the surface of NPs (3C). In the relaxed structure of 10 Å NPs all of the atoms were 3-coordinated, confirming the formation of the bubble-like structure. For 20 Å NPs, the structure relaxation removed the initial tetrahedral bond structure (region a) entirely. Our structural analyses showed that the surface

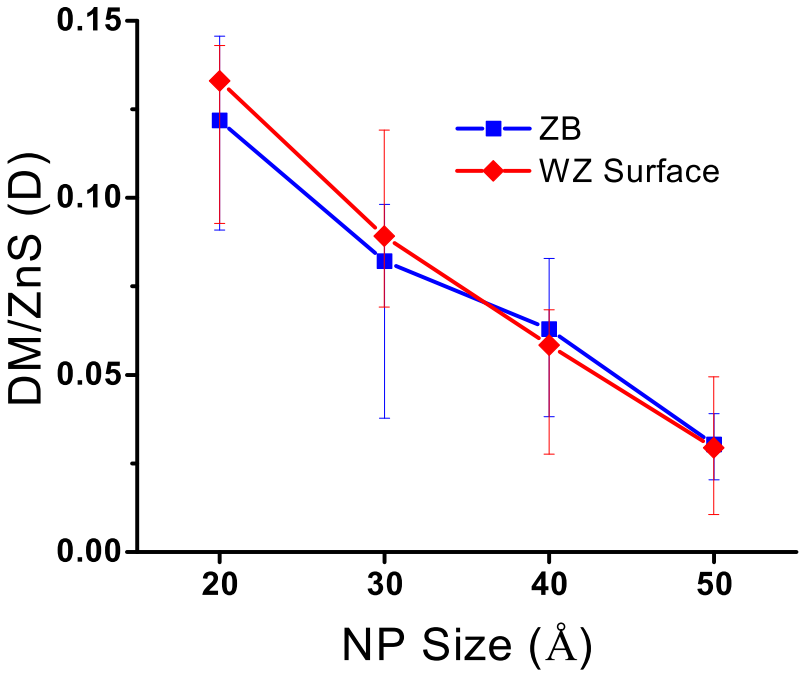

Figure 4.13: The DM per ZnS caused by the deformed surface structure.

structure of both ZB and WZ NPs ranging from 2 to 5 nm in size was similar and consisted of 3C and 4CNT atoms. This similarity may result in similar surface properties such as the the surface energy. These analyses also showed that tetrahedral bond structure was more stable in WZ NPs and that ZB NPs experienced more severe structural relaxations.

The effect of the structural evolution of NPs on the dipole moment was also studied. To study the pure effect of structural evolutions, non-polar initial configurations were used for simulations. Results of dipole moment calculations showed that non-polar ideal structures of NPs changed to polar structures after relaxation at 300 K. Since the tetrahedral core of ZB NPs has a non-polar nature, the polarity occurred in these NPs because their surface configurations deviated from the tetrahedral bond structure. There was no specific direction for a dipole moment vector of a ZB NP and the direction changed randomly for different configurations. In contrast, dipole moment vectors of WZ NPs became more aligned with -Z direction as the NP size increased. This was due to the polar nature of WZ lattice, which was shown to have dipole moment of 0.3855 D per ZnS molecule. By increasing the size of the WZ NP, the crystalline polar core became more dominant and controlled the dipole moment magnitude and direction. For NPs smaller than 3 nm, where 4CNT and 3C atoms were predominant, DMs of ZB and WZ NPs were similar due to the similarity of the surface structures. As the size of the NP increased, the 4CT atoms started to control the DM. As a result, ZB and WZ NPs became less and more polar, respectively. By subtracting the

dipole moment caused by the crystalline core from the total dipole moment, we calculated the surface dipole moment for WZ NPs. It was shown that surface dipole moment of WZ NPs was in the same range as dipole moment of ZB NPs, which again confirmed the similar surface properties of ZnS NPs in the range of 2 to 5 nm.

4.4 Methods

4.4.1 Initial configurations construction

The initial configurations of NPs ranging in size from 1 to 5 nm were generated by cutting spheres from perfect ZB and WZ super-lattices. Due to the tetrahedral symmetry of the ZB lattice, for each ion I(x,y,z), there exists a similar symmetric-ion I'(-x,-y,-z) in ZB as-cut configurations. Ions I and I' make a symmetric-group II', which has zero DM in all directions (X, Y and Z). Since all ions should belong to a symmetric-group, the total DM of the as-cut configuration would then be zero. WZ belongs to the C_{3v} point group, which has lower symmetry than T_d. While T_d makes DM to be zero in all X, Y and Z directions, C_{3v} symmetry only ensures zero DM in the X and Y directions. For each ion I(x,y,z) in the C_{3v} point group, there exist two similar symmetric-ions I'(x',y',z) and I"(x",y",z) such OI, OI' and OI" vectors make 120°angles. As the DM of symmetric-group II'I" in the (0001) plane (XY plane) is zero and each ion should belong to a symmetric group, the total DM of WZ the as-cut configuration will be zero in the X and Y directions.

Since the initial configurations of NPs are not necessarily charge-neutral, excess ions were removed from the surface to achieve electroneutrality. The charge neutralization of ionic NPs' as-cut structures has usually been achieved by randomly removing excessive ions from the surface. However, this method cannot ensure the symmetry of distribution of positive and negative ions on the surface and may result in a DM for initial configurations. In this study, instead of individual ions, symmetric groups were removed randomly from the surface to obtain non-polar initial configurations. It means that excessive ions should be removed in groups of 2 or 3 from ZB and WZ as-cut configurations, respectively. Depending on the total number of excessive ions, complete charge neutrality may not be accessible by removing symmetric ions from the surface. If the total number of excessive ions is not a multiple of two, we will end up having one remaining excessive ion in the NP after removing symmetric groups. Similarly, one or two excessive ions may remain if the total number of excessive ions is not a multiple of three in WZ NPs. In those cases, one or two remaining ions would be removed from the bulk of the as-cut configuration in a way that does not affect the symmetry.

For each of ZB and WZ NPs, 10 initial configurations with the lowest energies were

chosen. As the initial DMs of WZ NPs are not necessarily zero in the Z direction, one more condition was added to enssure that the initial configurations have the lowest DMs (negligible in respect to the final DM after the relaxation). A large number of repetitions (no less than 1,000,000) were performed to make sure that all possible combinations of removing excessive ions from the surface were covered. It is worth noting that initial configurations of WZ NPs were made out of the ideal WZ super-lattice so the probable DM of initial WZ configurations was just due to the asymmetry of distribution of surface ions in the Z direction, but not the asymmetry of the bulk structure. We noticed that for NPs greater than 2 nm, using either the random removing of ions or symmetric groups would not significantly affect the final structure and energy of NPs, but would affect their final DMs.

4.4.2 Simulation Details

A detailed comparison of the different available ZnS empirical potentials in the literature was published in our previous study [128]. Among all available potentials for ZnS, we chose the potential developed by Hamad et al. [37] for this work. Surface properties are of great importance when studying nanostructures. It has been shown that surface properties calculated by this potential have the best agreement with results of experimental and first-principle studies. Furthermore, this potential has successfully reproduced some other ZnS properties such as crystal structures, mechanical properties, thermal expansion and pressure-induced phase transformation. Moreover, developers of the empirical force field used in this study have validated its accuracy in predicting the energy of small ZnS clusters. They did so by comparing the force field results with the first-principle calculations [38, 40]. In their later study, they also emphasized the ability of this force field in modeling the surface properties of the small ZnS clusters by comparing $(ZnS)_n$ clusters (n = 2 - 7) optimized with both DFT and IP, which gave a deviation of less than 0.1 Å for bond distances, and less than 51 for angles [3]. Considering the importance of the surface effect in small NPs, we also performed first-principle calculations to validate the accuracy of this force field in predicting the energy and structure of 1 nm ZnS NPs. We performed DFT geometry optimization using the DMol^3 [130, 131] code and PW91 exchange-correlation functional [132] with effective core potentials and a double numerical plus polarization basis set. The energy, structure and dipole moment of 1 nm ZnS NPs were calculated and compared with the empirical interatomic potential results. This comparison, details of which are provided in Appendix A, shows that the properties of geometry optimized NPs achieved by interatomic potential agree strongly with the DFT results. MD simulations of ZnS NPs were run in vacuum and the canonical ensemble using DL_Poly [101] simulation code. All simulations were run at 300 K, and the Nosé-Hoover thermostat was used to control the temperature. A time step of 0.5 fs was used, and simulations were carried out for no less than 10 ns.

Chapter 5

Structure of ZnS nanoparticles in water

5.1 Introduction

In the past two decades, interesting optoelectronic properties of II-VI semiconductor nanomaterials have made research on this technology strive and many potential applications have been proposed. Biomedical imaging is one of these applications in which quantum dots (QDs), florescent II-VI semiconductor nanomaterials, have shown a promising future. Unique optical properties such as size-tunable photoluminescence, broad excitation band and narrow emission band, good resistance to photobleaching and stability in metabolic systems make these materials good candidates to substitute organic fluoroscopes for biomedical imaging applications [26]. However, serious concerns were raised early in their development about toxicity and safety, especially because the most studied II-VI semiconductor nanomaterials contain cadmium (CdSe, CdTe and CdS) which is known to be highly carcinogenic for living systems [27]. Although modifications such as adding ZnS shell or polyethylene glycol (PEG) coating have been suggested to modify QDs with toxic elements, it has been shown that their cytotoxicity can only be partially alleviated, but not completely eliminated [28, 133]. Zn based QDs such as ZnS has been introduced as a suitable alternative for QDs with Cd components since Zn is considered to be an essential biological element [29]. Furthermore, the band gap of ZnS is more than 1 eV wider than the others in the II-VI family, which enables a wider spectrum to be tuned by varying size of ZnS nanostructures. Unfortunately, ZnS nanoparticles (NPs) have shown intrinsic potential to undergo uncontrollable structural evolutions in ambient conditions which has limited their applicability [20]. Accordingly, structural stability of ZnS NPs have been highlighted in experimental and numerical studies.

A modified version of this chapter has been prepared for publication in Journal of Physical Chemistry C as **M. Khalkhali, H. Zeng, Q. Liu and H. Zhang**, "**Structural evolutions of ZnS nanoparticles in hydrated and bare states**"

At ambient temperature and pressure, zinc-blende ($ZB : F\bar{4}3m$) is the most stable crystal structure of the bulk ZnS while wurtzite ($WZ : P6_3mc$) is more stable above 1020 °C. Structural behavior of ZnS NPs, however, deviates from the bulk greatly, due to their large surface to volume ratio which means significant portion of atoms are undercoordinated. Undercoordinated atoms can reside on surface facets (3-coordinated), edges (2-coordinated) or corners (1-coordinated) of a NP. Due to their broken bonds, undercoordinated atoms on the surface cause an excess free energy for a NP comparing to the bulk which can result in alteration of phase stability behavior. One approach to predict stable configuration of a NP is to calculate frequent crystalline surface energies and construct the most stable shape using Wulff construction. Such an approach applied by Barnard et al. showed that ZB rhombic dodecahedron enclosed entirely by non-polar 110 facets is the most stable ZnS shape regardless of the NP size [42]. However adding polar facets to ZB nanostructures will make core/shell crystalline/amorphous structure thermodynamically favorable. Furthermore, deviation from rhombic dodecahedron enables some thermodynamic paths from ZB to WZ transformation by decreasing the size [43]. While this approach provides valuable thermodynamic information about phase stability of the ZnS NPs, it does not come close to dynamics. Moreover, Wulff configurations can not be made in all sizes and more realistic model of a NP includes imperfect facets, edges and corners which affect the NP's surface energy significantly.

Molecular dynamics (MD) is a suitable alternative to study the structural evolution of nanostructures in realistic sizes and time scales. In our previous study, we used MD simulations to study structural evolution of 1 to 5 nm ZnS NPs with initial WZ and ZB crystal structures [134] in vacuum. Simulation results revealed that relaxed configurations of ZnS nanoparticles larger than 3 nm consist of three regions: a) a crystalline core in which atoms keep their initial 4-coordinated tetrahedral bond structure, b) a region of distorted 4-coordinated atoms which environs the crystalline core, and c) the surface of the NP entirely made of 3-coordinated atoms. Decreasing the size of the ZnS nanoparticle to 2 nm will result in disappearance of the crystalline core and further reducing the size will result in formation of bubble like structure at which all atoms are 3-coordinated. Formation of bubble-like or onion-like structures which predominantly consist of arrangements of three-coordinated atoms is also reported in small $(ZnS)_n$ clusters ($n < 80$) relaxed through global minimization [38, 39]. Study of the larger NPs with the same method revealed that BCT structure, which is not observed experimentally, to be generally more stable than others [3]. However, the energy of WZ clusters were found to be so close to BCT ones and it was suggested that their relative energies may be reversed by solvation effects [3]. Early MD study on a 3 nm free standing ZB ZnS NP suggested ZB to WZ phase transformation at 300 K [2]. Although we reported more relative stability of WZ NPs, no phase transformation was noticed in 10 ns MD simulations.

It is well-known that surface ligands, like surfactants or solvent molecules, can alter NPs structure and properties through changing the surface energy. In the case of QDs, understanding the effect of surface adsorbed water on their structure, optoelectronic properties and toxicity is of great importance for biomedical (*in vivo*) applications. As a result, hydrated ZnS nanocrystals have been surveyed considerably. In one of the earliest work on this context, Zhang et. al. showed that ZnS NPs exhibit reversible structure transformation accompanying absorption and desorption of methanol and water [35]. This structural changed was identified by enhancement of crystallinity by absorption of water and reappearance of distorted structure by substituting water with ethanol. MD simulation performed by the same group confirmed that crystallinity of ZnS NPs is increased in presence of surface adsorbed water [2, 78]. Effect of water on enhancement of crystallinity of ZnS NPs has been reported in other theoretical and experimental studies as well [135–137].

In addition to alternating optoelectronic properties of a single NP, structural and configurational changes can also affect intrinsic forces between NPs. Semiconductor NPs interactions can be decomposed into coulomb and van der Waals components. Although NPs are generally charge neutral, they exhibit large static permanent dipoles causing considerable coulomb interactions [44]. Dipole-dipole interactions are of great importance in non-metallic nanoparticles, as they are found to govern the behavior of mixture of NPs which can vary from agglomeration to self-assembly into ordered structures. Zhang and Banfield showed that dipole-dipole interactions are the main driving force for oriented attachment of ZnS NPs [46]. ZnS nanowires with length as long as 10 µm have been successfully fabricated via oriented attachment of ZnS nanocrystals [53]. In our previous work, we showed that non-polar initial configurations of bare NPs (free standing NPs in vacuum) become polar after relaxation at 300 K. Since the tetrahedral core of ZB NPs has a non-polar nature, polarity of these NPs is due to the deviation of their surface configurations from the tetrahedral bond structure. There is no specific direction for the dipole moment (DM) vector of a ZB NP and it changes randomly for different configurations. On the other hand, DM vectors of WZ NPs become more aligned to -Z direction as the NP size increases. This is due to the polar nature of WZ lattice which was shown to have DM of 0.3855 D per ZnS molecule. DM of ZB and WZ NPs are in the same range when their sizes are smaller than 3 nm. In this size range, crystalline core is not predominant and DM of NPs is controlled by the surface structure. Due to the similarity of surface structures of WZ and ZB NPs, their dipole moments are in the same range. By increasing the size, DMs are converging to the bulk values. This makes ZB and WZ NPs less and more polar, respectively.

This study aims to extend our understanding of structural evolution of ZnS NPs, specially in hydrated state. As mentioned before, understanding the behavior of ZnS NPs in

aqueous environment is of the great importance for their potential biomedical application. For medical imaging applications, the QDs' site of action is *in vivo* which is mainly an aqueous media. As a result, the structural stability of ZnS QDs in water can govern their applicability for proposed biomedical applications. In addition to a structural stability of a single QD, interactions between complex set of these noncrystalline materials should be considered. It has been shown that structural transformation in ZnS nanoparticle can occur as a result of agglomeration [31, 33] and aggregation [34, 97]. In this study, we compare the structural evolutions of hydrated and bare ZnS NPs and study the effect of these evolutions on dipole moment and interactions between NPs.

5.2 Simulation Details

The initial configuration of NPs starts with cutting quasi-spherical shapes from ideal crystal lattices. These structures are not necessarily charge neutral so the excess ions should be removed from the surface to achieve electroneutrality. Charge neutralization is usually achieved by randomly removing of excessive ions from the surface. This method can not ensure the symmetry of distribution of the positive and negative ions on the surface after charge neutralization and may result in charge-neutral but polar initial configurations. In this study, we made charged-neutral, nonpolar initial configurations through symmetric removing of excessive ions from the surface. Process of making nonpolar initial configurations is explained in details in our previous study [134]. Five different initial configurations were chosen for each size. Due to the nonpolar nature of the initial structures of NPs, any change in their polarity is the results of their structural evolutions.

In comparison with other available empirical potentials for ZnS, potential developed by Hamad et al. [37] is shown to be more accurate to model ZnS bulk and surface properties at room temperature [128]. The accountability of this potential in modeling the surface effect in small ZnS clusters is also validated by comparing the interatomic potential results with the first-principle single point energy calculation [38, 39] and geometry optimization [3] [134]. Hence, this empirical potential is used to model ZnS in this study. The parameter of water potential is taken from consistent valence force field (CVFF) [138] and the ZnS-water interaction is modeled using the parameters proposed in the study on the embryonic stage of ZnS formation from aqueous solution [41].

Constant temperature and pressure simulation of ZnS NPs in water was performed using the DL_Poly [101] simulation code, periodic boundary condition, and the Nosé-Hoover thermostat and barostat. A time step of 0.5 fs was used and the size of the simulation box was chosen such that the interaction of the hydrated NP with its images in neighboring boxes was negligible. Considering the long range charge-charge and dipole-dipole interac-

tions of NPs, simulation box sizes were chosen to be at least 3 nm bigger than the diameter of the NPs to meet the minimum image criterion. To model the effect of presence of water on NP structural evolution accurately, it is important to let the water around the NP to equilibrate and absorb to the NP surface before letting the NP to relax. To achieve this, we first energy minimized the water structure while the NP was fixed using *zero temperature dynamics* module within DL_Poly. This will let us to repair any water-water or water-ZnS close contact before performing dynamics. This step is followed by 100 ps NVT simulation at 300 K in which the NP is still kept fixed. After equilibrating water around NPs, NPs let to relax during 100 ps NVT simulation which is followed by at least 10 ns NPT simulation at 300 K and 0 atm.

The fundamental question for any classical MD simulation is that if the simulation has been running long enough to satisfy ergodicity. In other words, MD simulation should be long enough so the system under study can explore all the energetically relevant configurations. This ideal condition, however, is not always achievable in practical situations. Different configurations of the system may be separated by high free-energy barriers which makes it impossible to observe the structural transformations in the time scale of MD simulation.

One approach to overcome the energy barriers and achieve the lowest energy configurations is to use global minimization techniques like simulated annealing which basically mimics high temperatures at which kinetics is much faster. As mentioned in Introduction, such a technique was applied on ZnS NPs ranging in size between 1-4 nm revealed bubble-like configurations for small ZnS clusters and BCT crystal structure for bigger NPs [3]. Simulated annealing is applicable for bare NPs, however, it does not have a physical meaning in the case of hydrated NPs. Another approach to explore the configurational space is to use methods such as Metadynamics which facilitate sampling the phase space. To make the best use of these methods, however, we need to have a clear picture of the classical MD results first. We need to know what are the limits achievable by MD to decide how to pass them by other methods.

In practice, equilibrium is examined by monitoring the thermodynamic properties during the MD simulation. The most common property which is readily available in each MD simulation is the potential energy. For bare NPs, we observed that the potential energy of the system reaches the equilibrium long before 10 ns. In the case of hydrated NPs, however, the potential energy of system is mainly dominated by the large number of water molecules and monitoring it cannot reflect the equilibration of the structures of the NPs. Therefore, we used parameters other than potential energy such as root mean square displacement (RMSD) and 4th order Steinhardt parameter, Q_4 [139]. RMSD was chosen because it can

show the changes of the atomic arrangements on the surface and in the bulk while Q_4 can reflect the evolution in the crystal structure of the NP. After running simulations for 8 ns, structural parameters were monitored carefully and simulations were stopped if these parameters did not change greatly for at least 2 ns (see the Appendix B for more details). All the analysis were done using the trajectories of the last 500 ps of simulations.

5.3 Results and Discussion

5.3.1 Structure of ZnS NPs

As explained in our previous work, some cares should be taken when using RDF to evaluate the structural evolution of a NP. Due to the undercoordinated atoms on the surface, the intensities of RDF peaks of the unrelaxed NP is lower than the periodic system with the same structure, while the positions of peaks are identical. At very small sizes like 1 nm, high order RDF peaks would disappear even for the unrelaxed structure. As a result, it is more accurate to compare each NP's RDF diagram with its unrelaxed state rather than the periodic system. In Figure 5.1, RDF diagrams of unrelaxed NPs are calculated by cutting spheres with the same sizes from the trajectories of a 1 ns NPT simulation of the periodic systems. Moreover, the number density of the bulk ZnS is used as the normalizing factor for all RDF calculations. This makes the intensities of RDFs of NPs with different sizes to be in the same order of magnitude. The Zn-Zn RDF diagrams ($g(r)$) for ZB and WZ NPs are shown in Figure 5.1. The number of Zn-Zn pairs whose distances are between 3.5 and 4.5 Å ($n(3.5 < r < 4.5) = 4\pi \int_{3.5}^{4.5} \rho r^2 g(r) dr$), is also represented in this figure. For a periodic mono-atomic system, this quantity is equal to the coordination number. Similar to RDF peak intensities, $n(3.5 < r < 4.5)$ for a NP is smaller compared to the bulk and its value approaches the bulk value as the size of the NP increases.

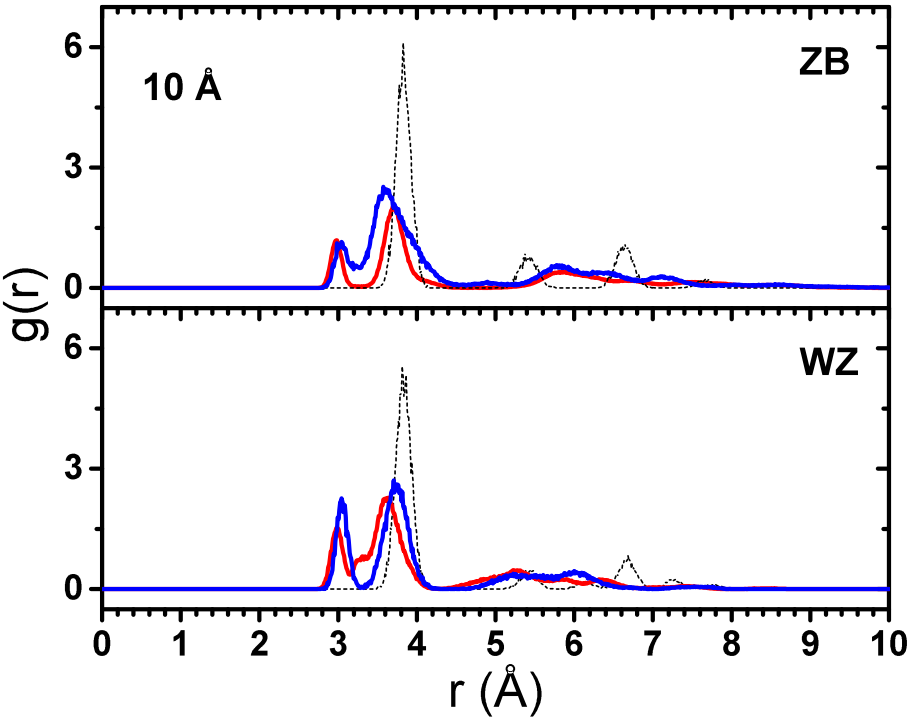

(a)

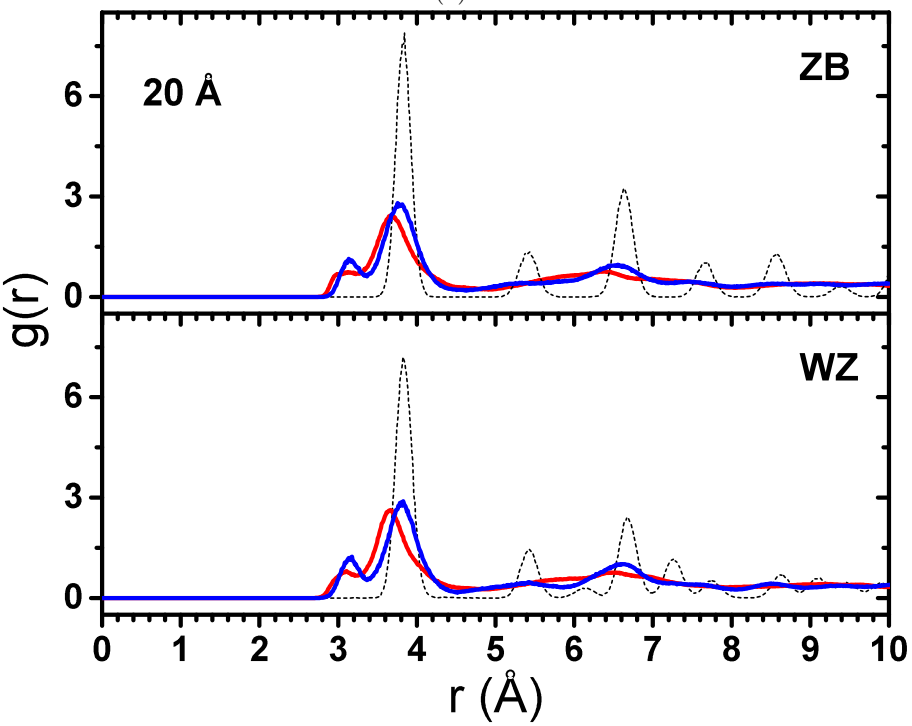

(b)

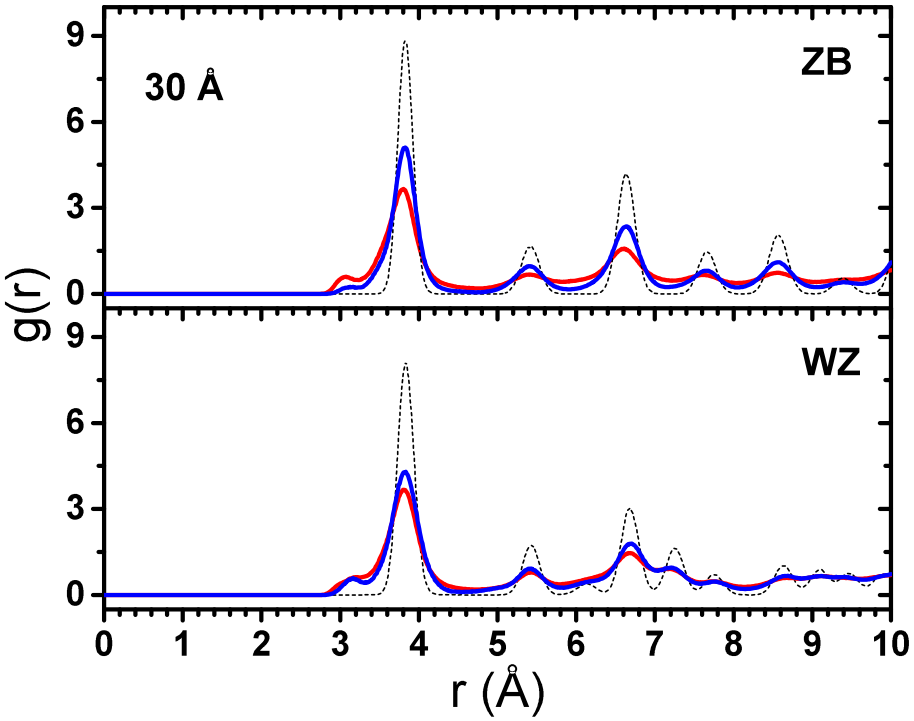

(c)

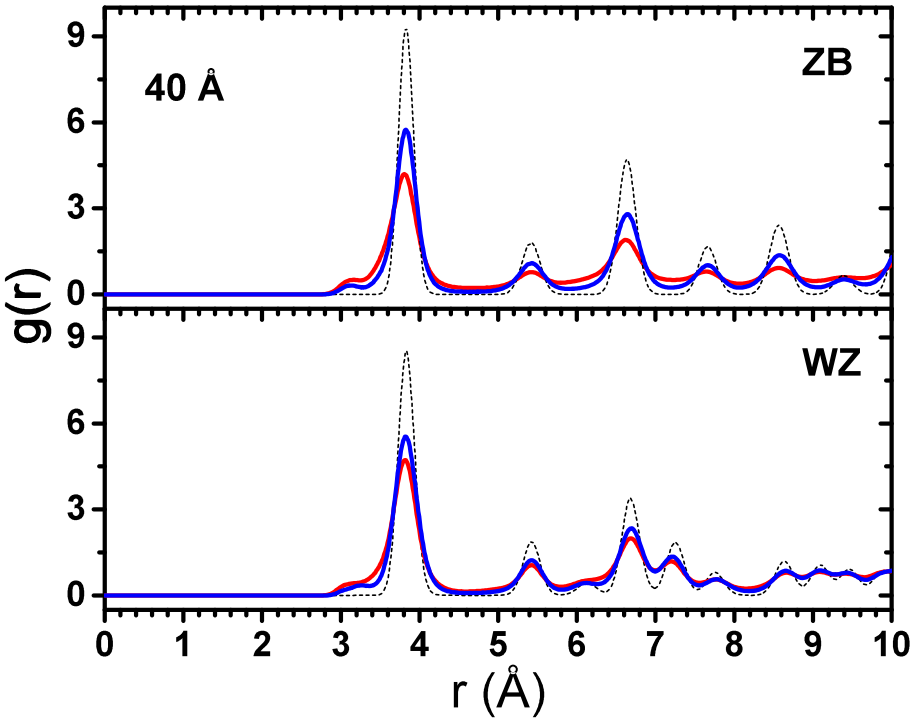

(d)

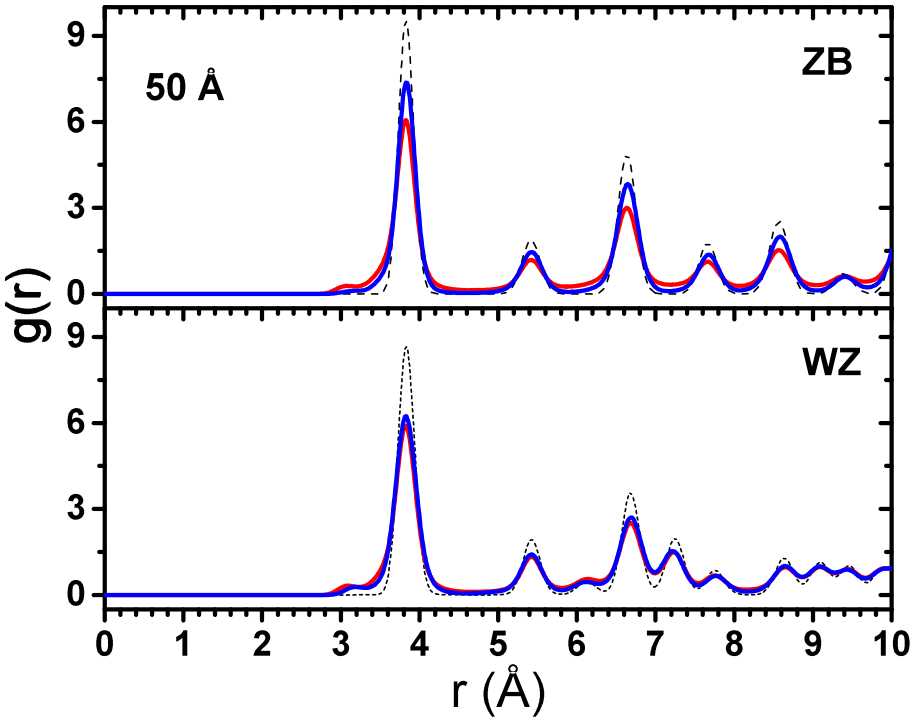

(e)

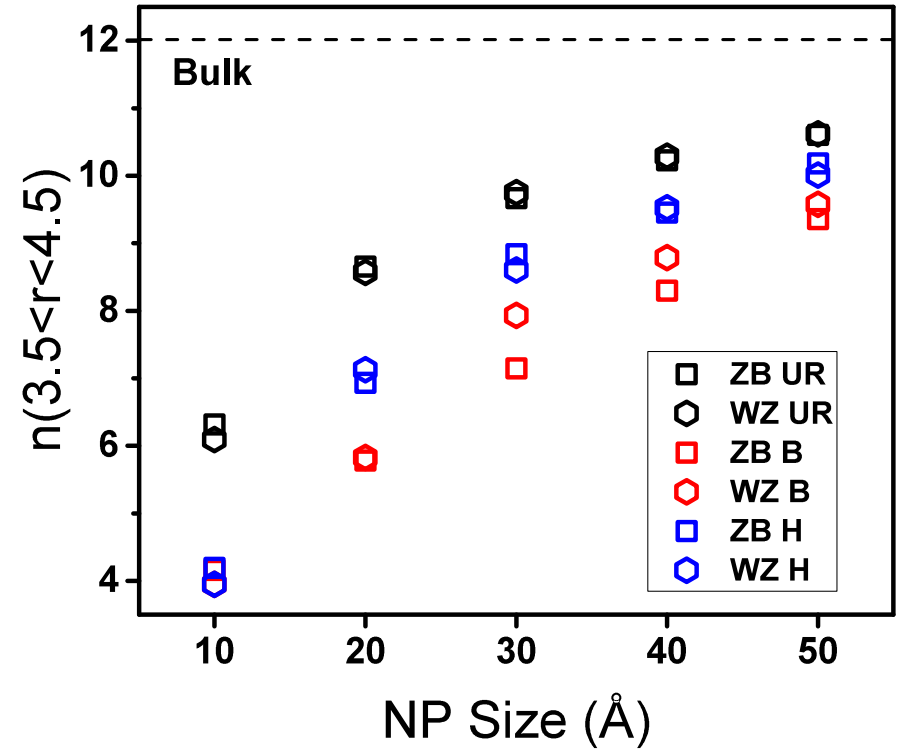

(f)

Figure 5.1: RDF plots for Zn-Zn pairs in (a) 10, (b) 20, (c) 30, (d) 40, (e) 50 Å ZnS NPs in bare (red line) and hydrated (blue line) states. (f) shows The number of Zn-Zn pairs whose distances are between 3.5 and 4.5 Å ($n(3.5 < r < 4.5) = 4\pi \int_{3.5}^{4.5} \rho r^2 g(r) dr$). UR, B and H stand for the unrelaxed, relaxed bare and relaxed hydrated NPs, respectively.

It has been shown before that 10 and 20 Å bare NPs, with both initial ZB and WZ structures, lose their crystal order after relaxation. 10 Å bare NPs adopt bubble-like structure while 20 Å bare NPs consist of distorted 4-coordinated structure in the core and a network of interconnected 3-coordinated atoms on the surface. Figure 5.1a shows that the RDF diagrams of hydrated and bare 10 Å NPs are comparable showing no clear crystallinity. This indicates that in this small size, 4-coordinated structure may not be stable even in the hydrated state.

20 Å NPs which completely lost their crystal structure in the vacuum, however, show more crystalline RDF in hydrated state. Higher order RDF peaks which were completely disappeared in bare NPs can be recognized in hydrated ones. Although the bigger NPs show clear crystalline RDF diagrams in both vacuum and water, the intensity of RDF peaks of hydrated NPs is higher. This shows that presence of water enhances the crystallinity of NPs. The difference between the RDF intensities of hydrated and bare NPs decreases as the size of NPs increases. In other words, the structure of bare and hydrated NPs become more similar as the size of NPs increases. Another interesting point about Figure 5.1 is that the difference between RDF diagrams of bare and hydrated NPs with WZ structure is smaller than ZB NPs. This can be due to the more structural stability of the bare WZ NPs compared to the bare ZB NPs [134]. One other possibility is that this order may change in presence of water and hydrated ZB NPs show higher structural stability.

In Figure 5.1f, $n(3.5 < r < 4.5)$ of the hydrated (H) state lies between the unrelaxed (UR) and bare (B) states, showing the structure of hydrated NPs is more similar to the unrelaxed structure. The RDF analyses show that the structure of hydrated NPs with both crystal structures are generally more crystalline but it does not give us information about the structure of surface of NPs. To study the surface structure of hydrated NPs and to check if the three phase structure is also forming in presence of water we need more structural analyses. The three phase structure of bare NPs is made of a crystalline core in which atoms keep their tetrahedral bond structure, a distorted 4-coordinated region where the bond structure deviates from tetrahedral, and a network of interconnected 3-coordinated atoms on the surface. The bond length and angular distribution diagrams are shown in Figure 5.2.

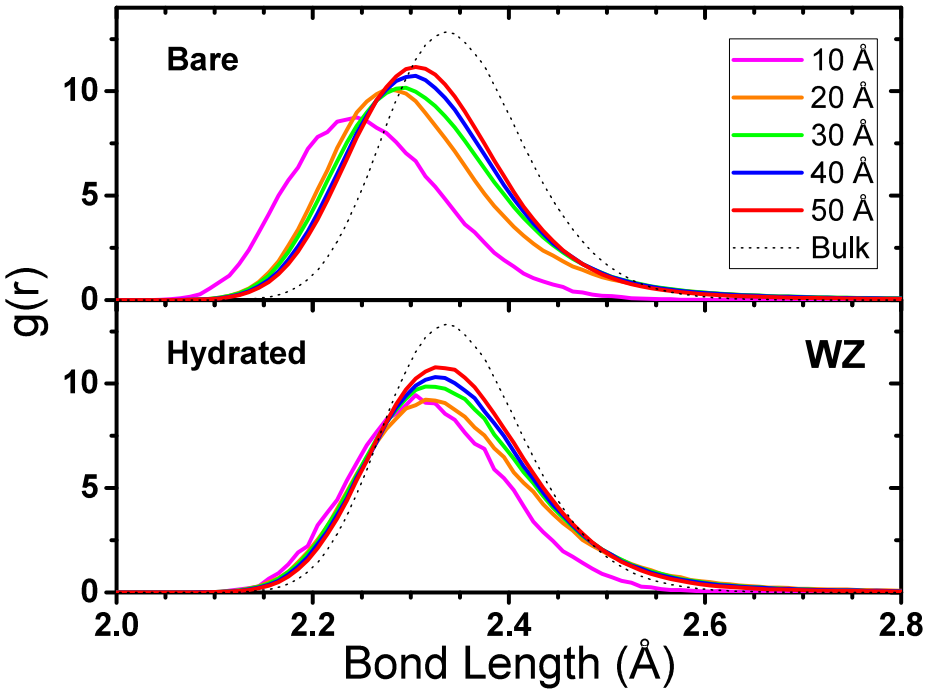
Bare
10 Å
20 Å
30 Å
40 Å
50 Å
Bulk
Hydrated
WZ
g(r)
0
5
10
2.0
2.2
2.4
2.6
2.8
Bond Length (Å)

(a)

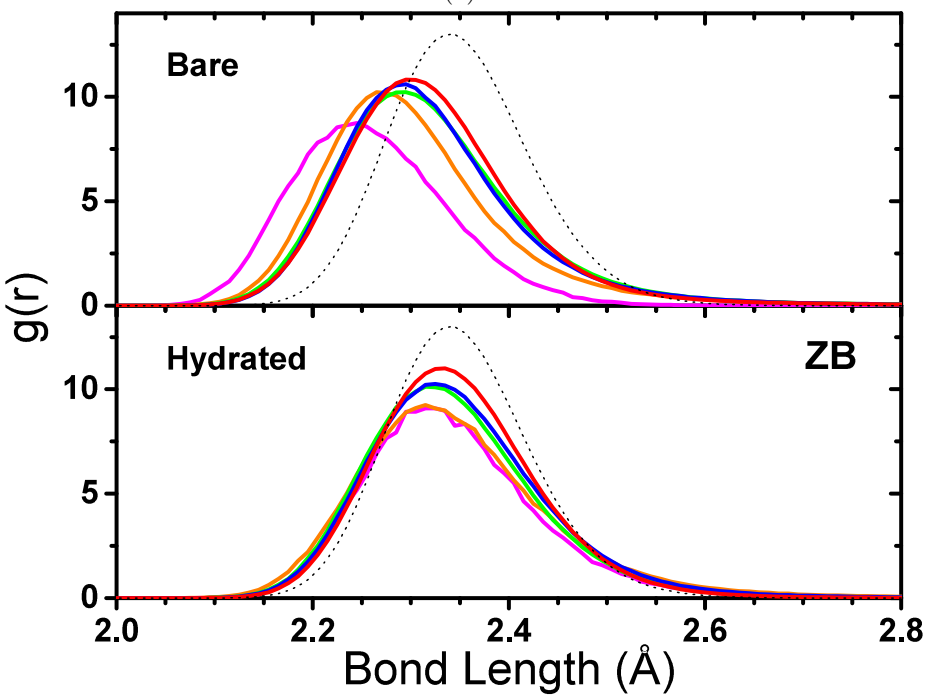
Bare
Hydrated
ZB
g(r)
0
5
10
2.0
2.2
2.4
2.6
2.8
Bond Length (Å)

(b)

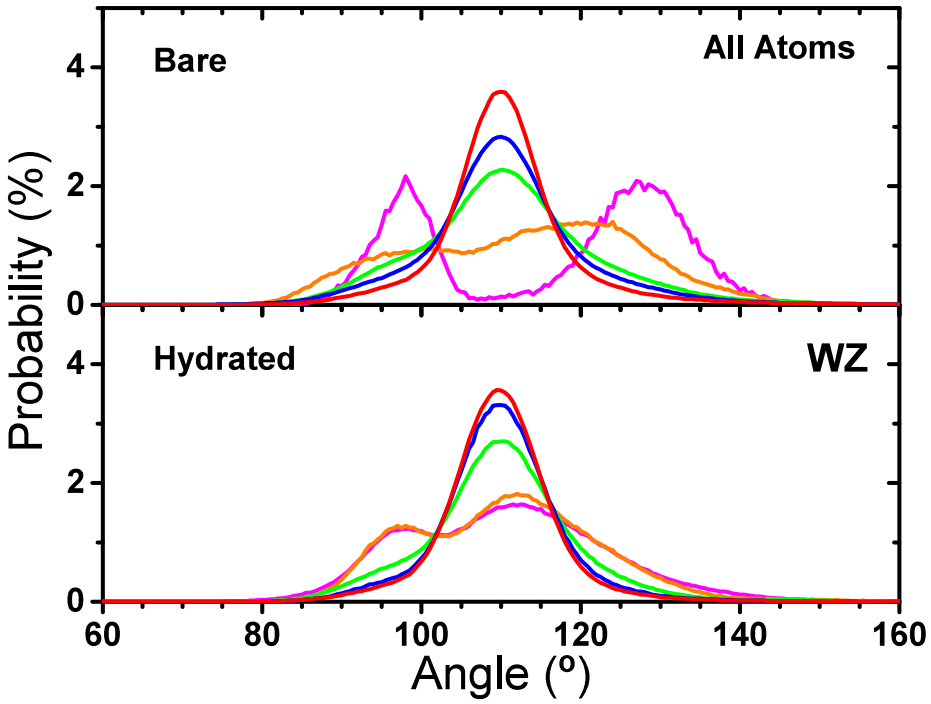
Bare
All Atoms
Hydrated
WZ
Probability (%)
Angle (º)
0
2
4
60
80
100
120
140
160

(c)

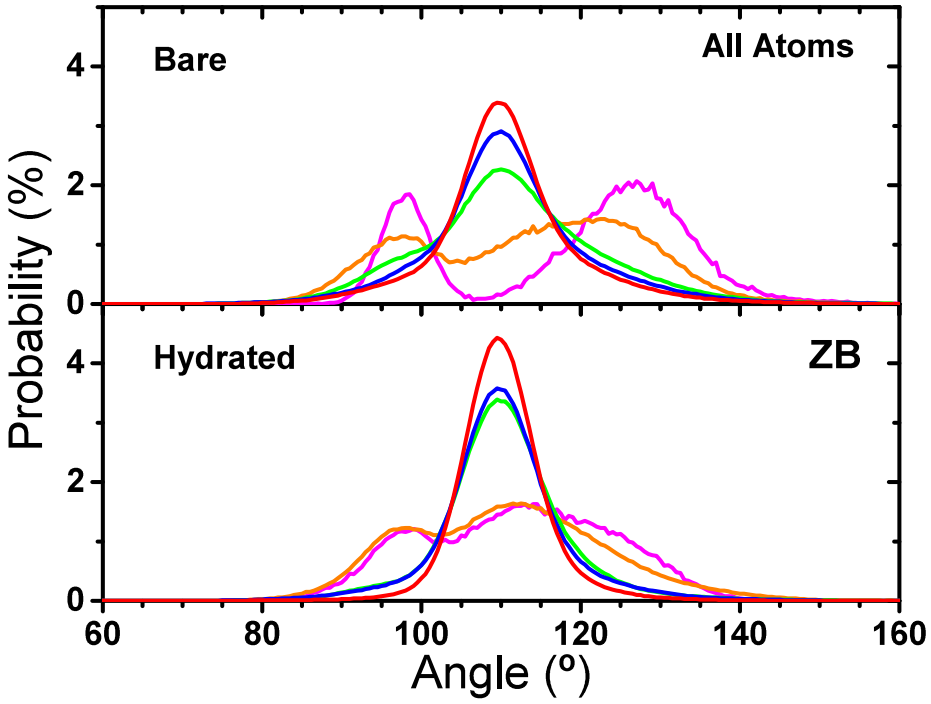
Bare
All Atoms
Hydrated
ZB
Probability (%)
Angle (º)
0
2
4
60
80
100
120
140
160

(d)

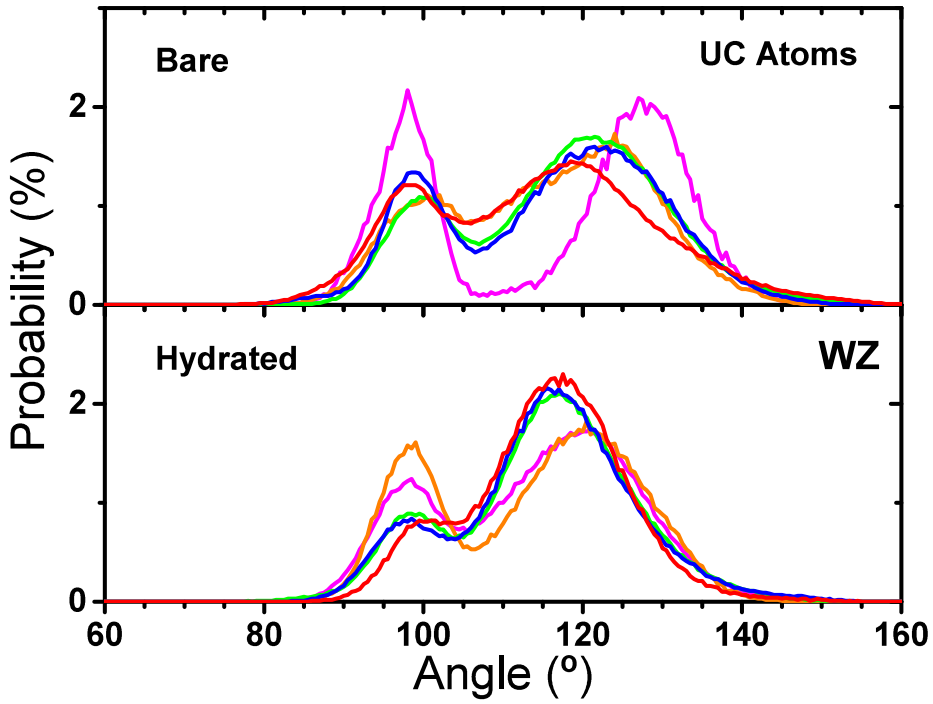

(e)

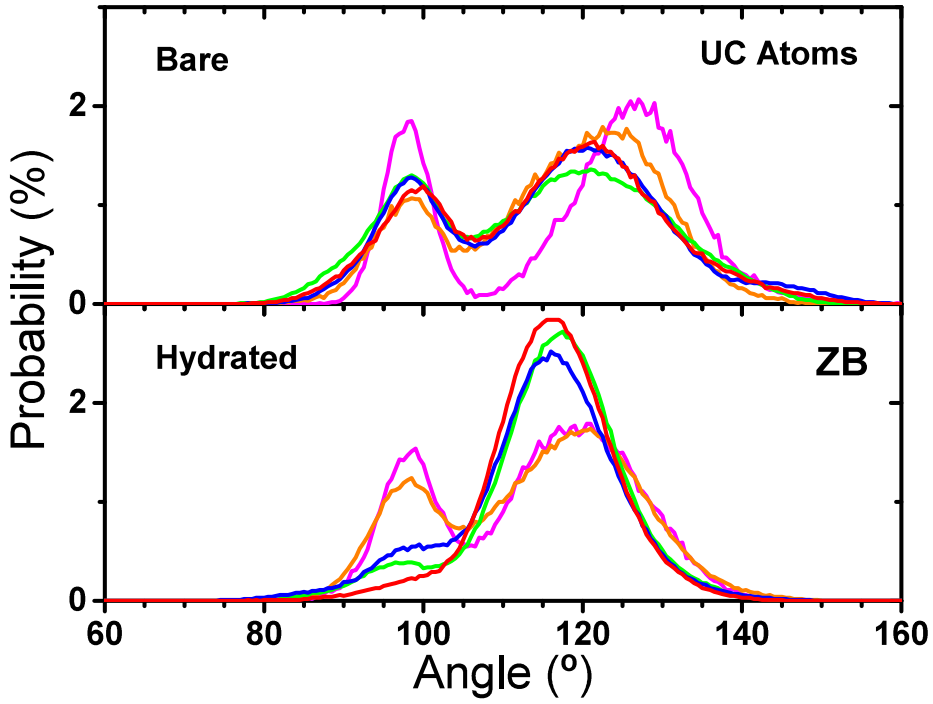

(f)

Figure 5.2: The bond length and bond angle distribution in bare and hydrated ZnS NPs. (a) and (b) show the bond length distribution of WZ and ZB NPs, respectively. The all-atom angular distributions for WZ and ZB NPs are shown in (c) and (d), respectively. (e) and (f) show the angular distributions calculated using only undercoordinated atoms.

Figures 5.2a and 5.2b show that the Zn-S bond length in bare NPs is lower than bulk. Shrinkage of the bond length in bare NPs is related to the formation of the interconnected 3-coordinated surface structure which causes a compressive surface tension. By increasing the size of the bare NP, the surface to volume ratio decreases and the surface effect becomes weaker, consequently. This effect can be seen in Figures 5.2a and 5.2b where the Zn-S bond length in bare NPs is approaching to the bulk value by increasing the size. Hydrated NPs however, show bond lengths much closer to the bulk value and the effect of the increasing of the size on the bond length is not as significant as bare NPs.

Ideal ZB and WZ lattices have tetrahedral bond structures in which all bond angles are equal to 109.47°. Transformation of a 109.47° single peak to a double peak angular distribution is the sign of the deviation from tetrahedral bond structure. We have shown previously [134] that the first peak in the double peak angular distribution is the sign of the formation of 4-rings of Zn and S while the second peak is usually due to the 6-rings. Once the bond structure of ZnS deviates from tetrahedral, anions (S^{2-}) which have the stronger tendency to repel each other would find the opportunity to increase their distance forcing cations (Zn^{2+}) to approach each other. That is why 4-ring acquire rhombic shape in which S-Zn-S angles are bigger than Zn-S-Zn angles. Shorter Zn-Zn distances in 4-rings also causes the emergence of a tiny peak in Zn-Zn RDF diagram before the first Zn-Zn nominal distance in crystal structure. 4-rings can form in both distorted 4-coordinated bulk and 3-coordinated surface structures. As undercoordinated atoms on the surface have more freedom to move, S atoms can increase their distances more, making Zn-S-Zn angles bigger. Thus, angular distribution of surface atoms shifts to the right in respect to distorted 4-coordinated structure beneath surface.

In Figures 5.2c and 5.2d, 10 Å bare NPs which are entirely made of 3-coordinated atoms show a clear double peak angular distributions. Nonetheless, the hydrated 10 Å NPs are different and resembles the double-peak angular distribution of the 20 Å bare NPs. This indicates that bubble structure was not formed in 10 Å hydrated NPs. The angular distributions also show that the 10 and 20 Å NPs have distorted structures in both bare and hydrated states. As the size of a ZnS NPs increases, their angular distributions in both bare and hydrates states approach the bulk. NPs bigger than 30 Å show single-peak angular distributions but the peak intensities of the bare WZ NPs seem to be slightly lower than bare ZB NPs. It was shown that this difference is due to the anisotropic thermal vibration in WZ crystal which can make the bond angles to vibrate in a wider range [134]. Similar to what was observed in RDF diagrams, it seems the effect of water on ZB NPs is more significant than WZ ones.

Examination of Figures 5.2e and 5.2f shows than undercoordinated atoms of bare NPs

with both ZB and WZ initial structures ranging in size between 2 and 5 nm have similar angular distributions. This is due to the similar surface structure of bare NPs which was shown to consist of interconnected 3-coordinated atoms. This structure is recognized by a double-peak angular distribution with two peaks around 100° and 120° which have comparable intensities [134]. The angular distribution of undercoordinated atoms in hydrated NPs, however, does not have these characteristics. Moreover, the angular distributions of hydrated ZB and WZ NPs do not resemble. This shows that the 3-coordinated structure is not forming on the surface of the hydrated NPs and their surface structure not similar either.

To further investigate the internal and surface structure of NPs we examine the coordination number and tetrahedral order parameter at different distances from centre of NPs. Previously, we used atomic coordination number and bond angles to categorize 4-coordinated atoms into two tetrahedral and not tetrahedral groups. Here, we use an order parameter to track the level of deviation from tetrahedral bond structure in different parts of the NPs. The tetrahedral order parameter (Q^T) of Chau and Hardwick [140] indicates the deviation from perfectly tetrahedral bond structure and ranges from 0 (random bond structure) to 1 (perfectly tetrahedral arrangement). For each 4-coordinated atom in ZB or WZ structures, the atomic tetrahedral order parameter is defined as

$$q_i^T = 1 - \frac{3}{8}\sum_{j=1}^{3}\sum_{k=j+1}^{4}\left(cos\ \theta_{ijk} + \frac{1}{3}\right)^2 \tag{5.1}$$

where θ_{ijk} is the bond angle between the central atom i and two of its closest dissimilar neighbors j and k. Tetrahedral order parameter of NP then can be calculated as

$$< Q^T >= \frac{1}{N}\sum_{i=1}^{N} < q_i > \tag{5.2}$$

where $< ... >$ denoted the ensemble average. Figure 5.3 shows the average coordination number and tetrahedral order parameter at different distances from the centre of NPs.

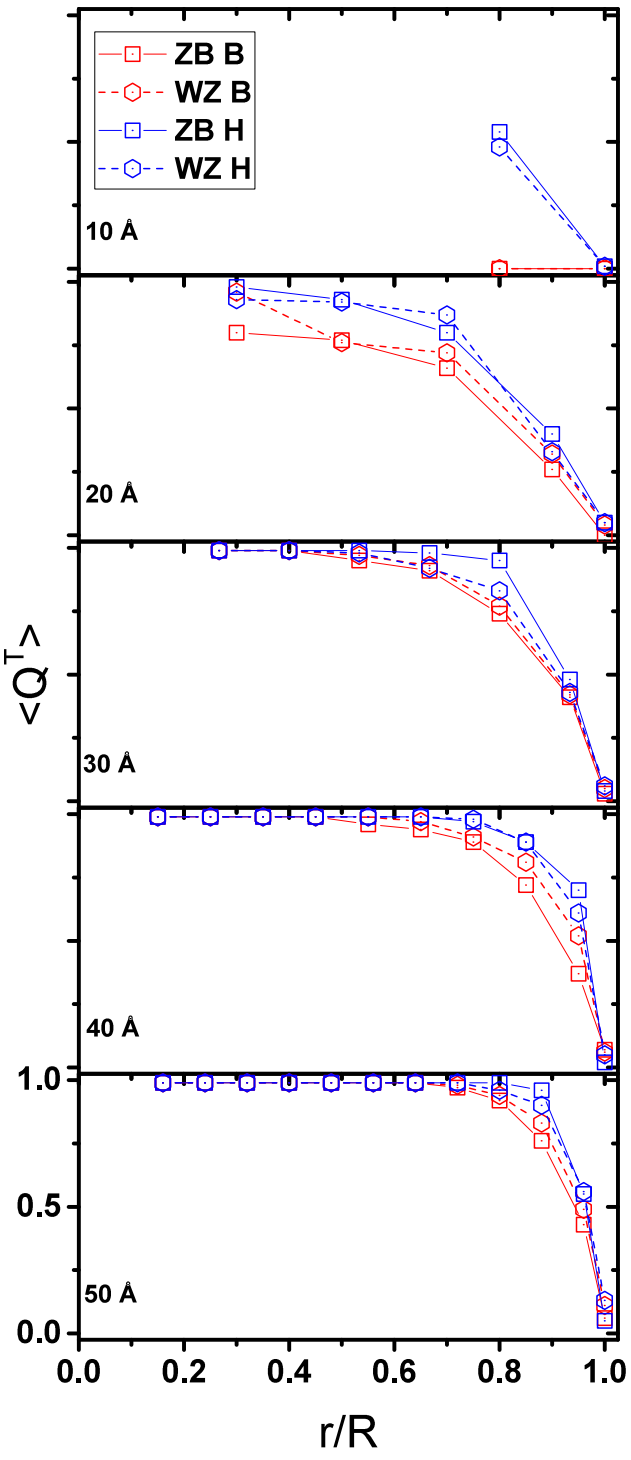

(a)

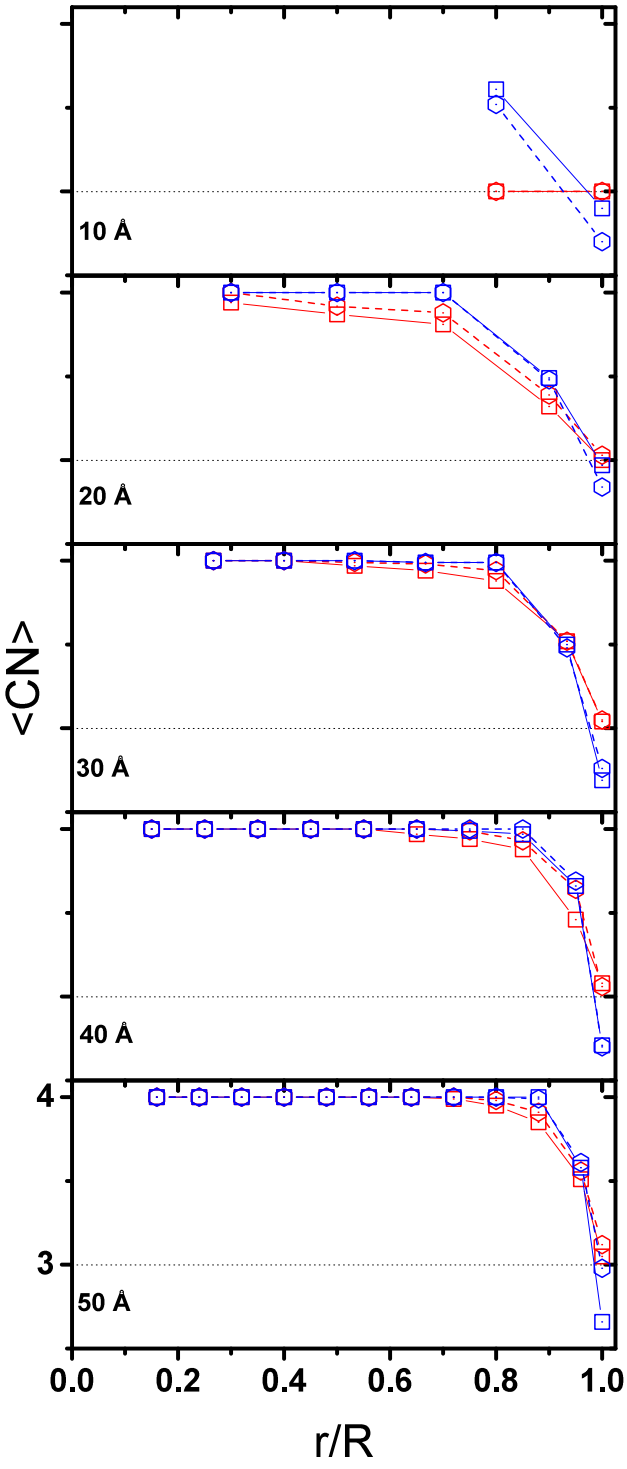

(b)

Figure 5.3: Average tetrahedral order parameter (a) and coordination number (b) at different distances from centre of ZnS NPs. r and R are the distance from the centre and radius of NPs, respectively.

Due to the bubble-like structure, there is no 4-coordinated atom in bare 10 Å NPs so

$< Q^T >$ can not be calculated. On the other hand, Figure 5.3b shows that the $< CN >$ is bigger than 3 at the centre of the hydrated 10 Å NPs meaning that 4-coordinated atoms still exist. More over, the average CN on the surface of these NPs is smaller than three which shows atoms on the surface are not entirely 3-coordinated. These two observations reveal that hydrated 10 Å NPs did not form bubble-like (in which all atoms are 3-coordinated) or onion-like (where two bubbles are connected through a network of 4-coordinated atoms) structures. Considerably low value of $< Q^T >$ at the centre of the hydrated 10 Å NPs (Figure 5.3a) shows that the bond structure of 4-coordinated atom deviates from the tetrahedral greatly.

It was shown previously that atoms with tetrahedral bond structure can be detected at the very centre of bare 20 Å WZ NPs while they are completely disappear in bare ZB NPs with the same size. The low $< Q^T >$ at the centre of bare 20 Å WZ NP in Figure 5.3a also confirms this. However, the same figure shows a tetrahedral bond structure at the centre of the hydrated 20 Å ZB NP. In fact, it can be seen that $< Q^T >$ of hydrated NPs with all sizes and crystal structures are generally higher than bare NPs which shows more stability of the tetrahedral bond structure in hydrated NPs. It has been shown that WZ NPs have more structural stability when they relax in vacuum. This can be also observed in Figure 5.3a where the $< Q^T >$ plots of bare WZ NPs lie above the ZB ones. However, the tetrahedral order parameter of ZB NPs in hydrated state is generally higher that WZ NPs.

Figure 5.3b shows that unlike the bare NPs, the average CN of surface atoms in hydrated NPs is smaller than three. Similar to angular distribution in Figures 5.2e and 5.2f, this indicates that the interconnected 3-coordinated surface structure which was observed in bare NPs was not formed in hydrated NPs and atom with lower coordination numbers remained on the surface. Examining the coordination number of the surface atoms in detail showed that almost all atoms on the surface of relaxed hydrated NPs are either 2- or 3-coordinated. In some rare cases, interaction with water causes the 1-coordinated Zn atoms to leave the surface of the NP but generally, 1-coordinated atoms changed their coordination number by surface relaxation. The RMSD of the undercoordinated atoms is calculated to examine the surface structure of NPs in more detail. Correction of atomic positions to remove centre of mass movement and rotation is important before calculating RMSD, specially for small hydrated NPs which have large movement in water. The average RMSD of undercoordinated Zn and S atoms in respect to the initial configuration of NPs are shown in Figure B.1.

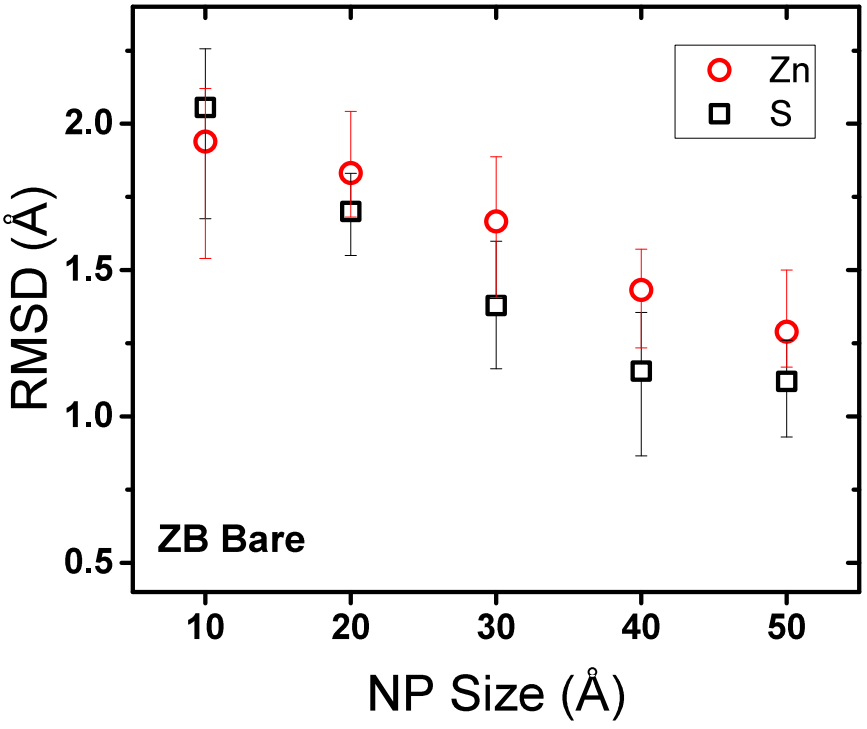
Zn
S
RMSD (Å)
2.0
1.5
1.0
0.5
ZB Bare
10
20
30
40
50
NP Size (Å)

(a)

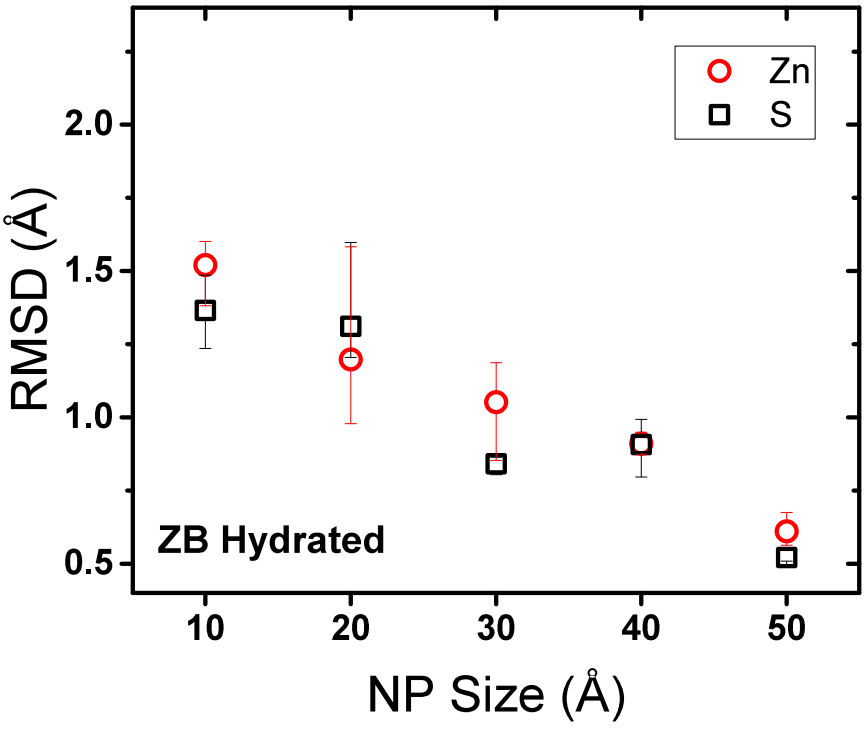
Zn
S
RMSD (Å)
2.0
1.5
1.0
0.5
ZB Hydrated
10
20
30
40
50
NP Size (Å)

(b)

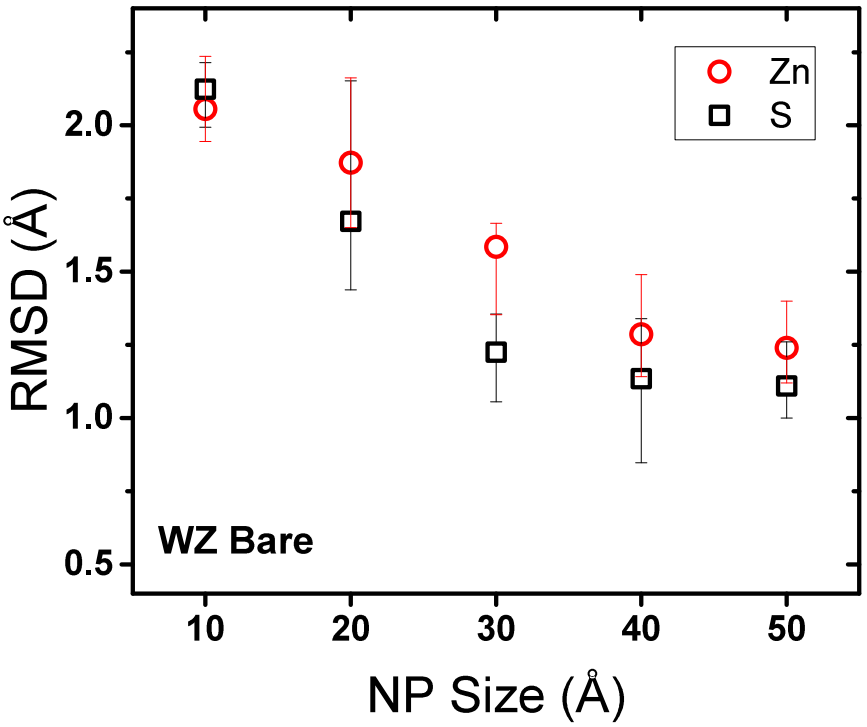

(c)

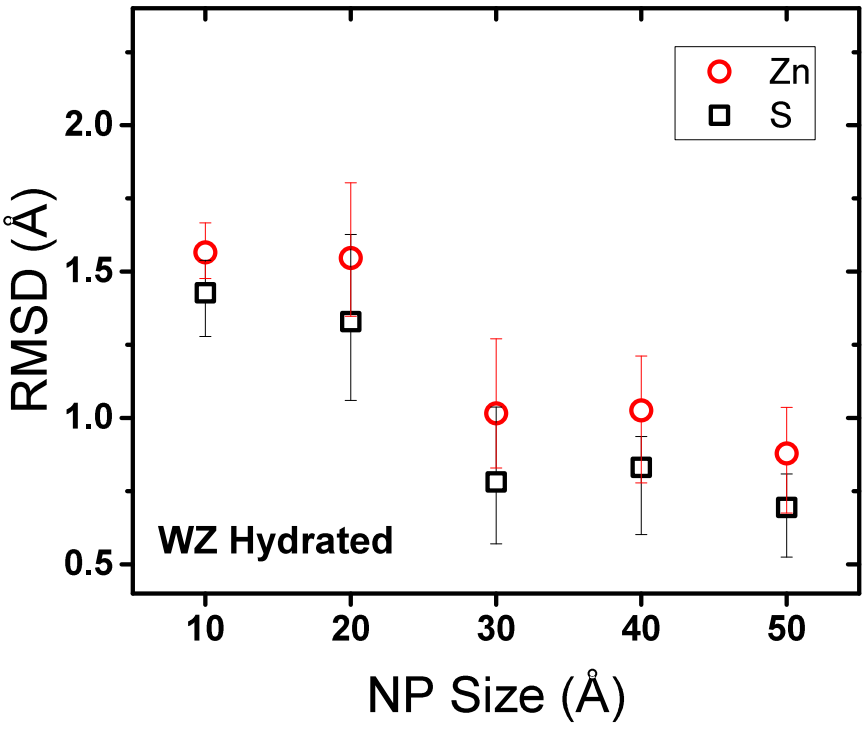

(d)

Figure 5.4: RMSD of Zn and S atom in (a) ZB bare, (b) ZB hydrated, (c) WZ bare, and (d) WZ hydrated NPs. RMSD is calculated in respect to the initial configurations of NPs. Error bars show the difference between values obtained from different initial configurations.

As expected, Figure 5.4 shows that the overall RMSD of atoms in hydrated NPs is lower than bare NPs indicating that NPs experience less severe structural changes when they are relaxed in water. In other words, the structure of hydrated NPs are more similar to the initial structures before relaxation which also means they have more crystalline structure. The RMSD of undercoordinated Zn atoms is generally higher than S atoms in bare NPs due to the higher mobility of Zn atoms. Zn atoms seems to have higher mobility than S atoms on the surface of hydrated WZ NPs as well while the RMSD of undercoordinated Zn and S atoms is close to each other in hydrated ZB NPs. In both hydrated and bare states, the overall RMSD is decreasing by increasing the size due to the lower structural changes in bigger NPs. According to RMSD results, we may expect the hydrated NPs to be less polar since their structure is more similar to initial non-polar configurations. In the next section, we study the polarity of bare and hydrated NPs in more detail.

5.3.2 Polarity as a function of structural evolutions

Previously, we showed that relaxation of ZnS NPs with non-polar and charge-neutral initial configurations in vacuum, results in final structures with the polar nature [134]. The same dipole moment (DM) calculations were done for hydrated NPs in this study. As a result, DMs reported for hydrated NPs are pure DMs without considering the solvent effect. Figure 5.5 shows the DM calculation results for hydrated and bare ZB NPs.

Since bulk ZB structure has a non-polar nature, polarity of relaxed NPs is due to the deviation of the arrangement of the surface atoms from the ideal ZB structure. Figure 5.5 shows that the magnitude of DM of a hydrated ZB NPs is considerably bigger than the bare NPs with the same sizes. This shows that less deviation of hydrated NPs' structures from the initial configurations which was shown by RMSD calculations, would not make them less polar. However, Figure 5.5b shows that the magnitude of normalized DM (DM per ZnS) for hydrated NPs decreases by increasing the size similar to what was observed for bare ZB NPs. The difference between magnitude of the normalized DM of hydrated and bare ZB NPs also decreases as the NP become bigger. As the size of the NP increases, the portion of NP structure which deviates from the initial nonpolar configuration decreases. This makes the surface effect less significant and the structure of bare and hydrated NPs more similar. The randomness of the direction of the DM vectors also shows that the polarity of ZB NPs in both bare and hydrated states is controlled by the surface structure. Thus, the different polarity of bare and hydrated ZB NPs is attributed to their different surface structures.

The atomic structure of the surface of bare NPs consists of a network of interconnected 3-coordinated atoms which are connected to the crystalline core of the NP through a layer of distorted 4-coordinated structure. This arrangement makes the surface of bare NPs to

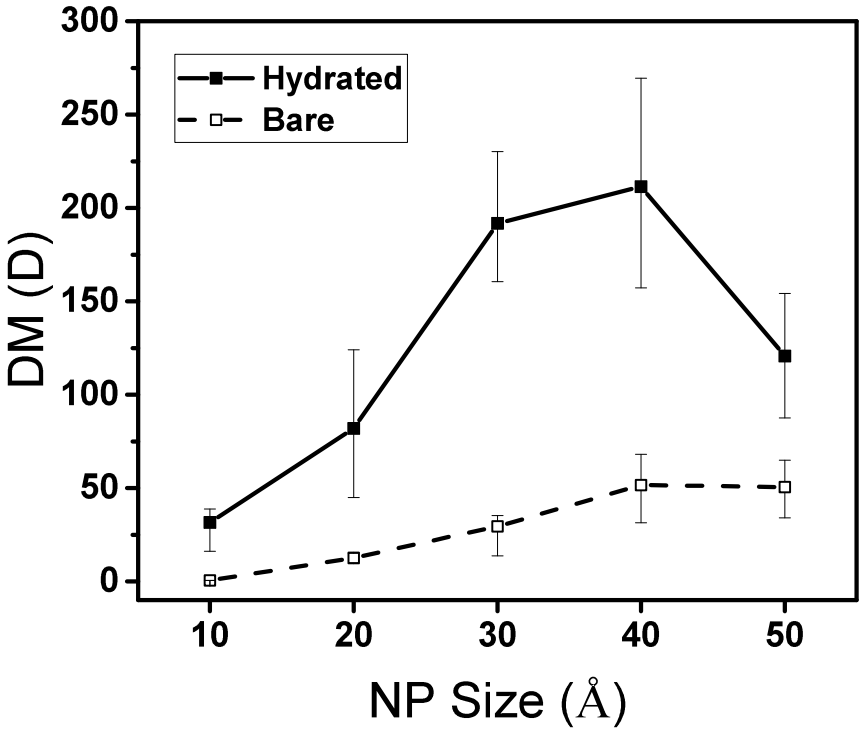

(a)

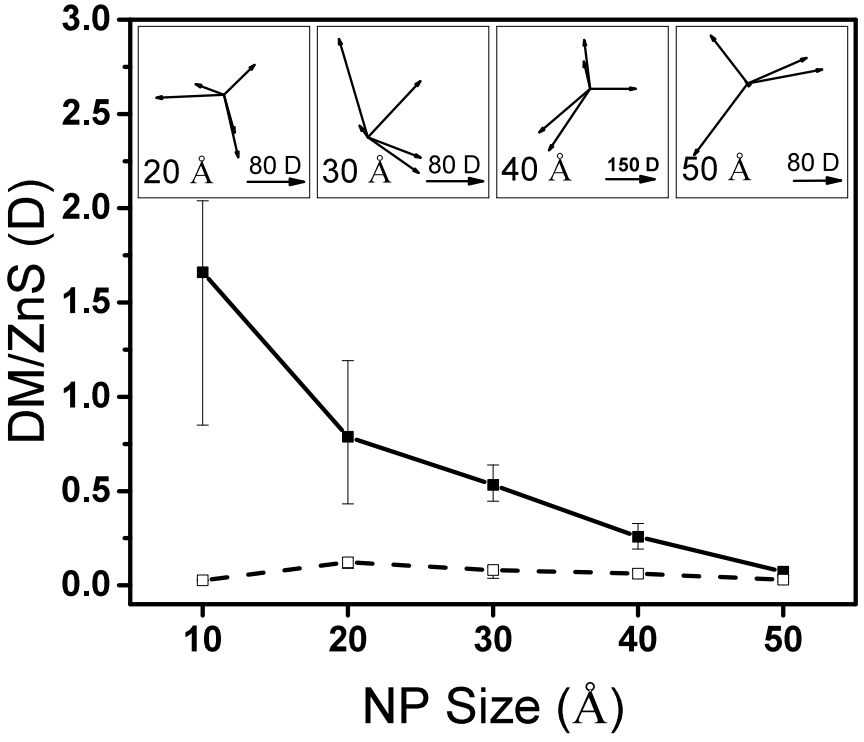

(b)

Figure 5.5: Variation of (a) DM and (b) DM per ZnS molecule with the size of bare and hydrated ZB NPs. Inset plots show the the projected image of the DM vectors of hydrated NPs on the XZ plane.

have a liquid like structure which is homogeneously distributed all over the surface and is similar in all NPs. The homogeneous nature of the surface structure of bare NPs, lowers the DM caused by the surface atoms. In the extreme case of the very small NPs (D = 1 nm) where the bubble-like structure is formed, the arrangement of atoms is close to a spherical shell which has the maximum symmetry. To further clarify this, the structures of bare and hydrated 30 Å ZB NP is shown in figure 5.6.

The three phase structure of bare NPs can be clearly recognized in Figure 5.6a where the high tetrahedrally ordered centre is surrounded by a layer of 4-coordinated atoms with a distorted bond structure and the surface is entirely made of 3-coordinated atoms. Both distorted 4-coordinated and 3-coordinated surface structures seem to be interconnected and continuous. On the surface of the hydrated 30 Å ZB NP however, the 2-coordinated atoms can still be found after relaxation. Moreover, there is no continuous distorted 4-coordinated structure beneath the surface of the hydrated NP and tetrahedral seems to be stable up to the surface of the NP. Another important difference between surface relaxation in water and vacuum is how the CN of atoms changes during relaxation. When the NP is relaxed in vacuum, all undercoordinated atoms try to increase their CN and become 3-coordinated to lower the surface energy. However, it was observed that some of the surface atoms which were 3-coordinated in the initial configuration lower their CN to 2 after relaxation in water. This shows that for some of the surface atoms, it is energetically more favorable to break a bond with ZnS structure and form a bond with water Which increases the inhomogeneity of the surface structure of the hydrated NPs. Hydrated NPs experience less overall structural evolutions which results in lower RMSD and more crystalline structures. However, their surface relaxation is less homogeneous comparing to the bare NPs which results in the higher DM in the hydrated NPs.

We have shown before that the bulk WZ structure at 300 K shows a natural DM of 0.3855 D per ZnS along the Z direction because of the slight C_{3v}-distortion of the elementary ZnS tetrahedron [134]. The magnitude of DM of the bare ZnS NPs with both crystal structures are similar when the size of the NPs is smaller than 30 Å. This is due to the fact that crystalline core is not the dominant part of the NP structure and the surface structures of the bare WZ and ZB NPs are similar. When the size of the bare NP increases, the crystalline core becomes dominant part of the NP structure so DM approaches to the bulk value, consequently. As a result, the DM of the bare WZ NP becomes more aliened to the Z direction and its magnitude converges to 0.3855 D per ZnS molecule when the size increases. Figure 5.7 shows the DM of bare and hydrated WZ NPs as a function of the NP size.

Figure 5.7a shows that the DM of both hydrated and bare WZ NPs increases by increasing the size. However, the DM of hydrated WZ NPs is bigger that the bare NPs. Figure

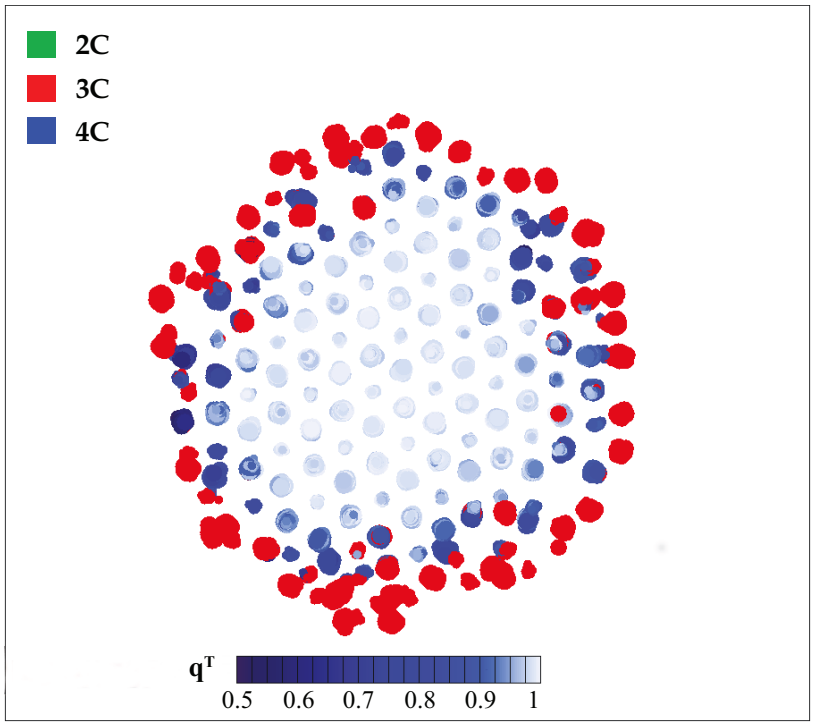

(a)

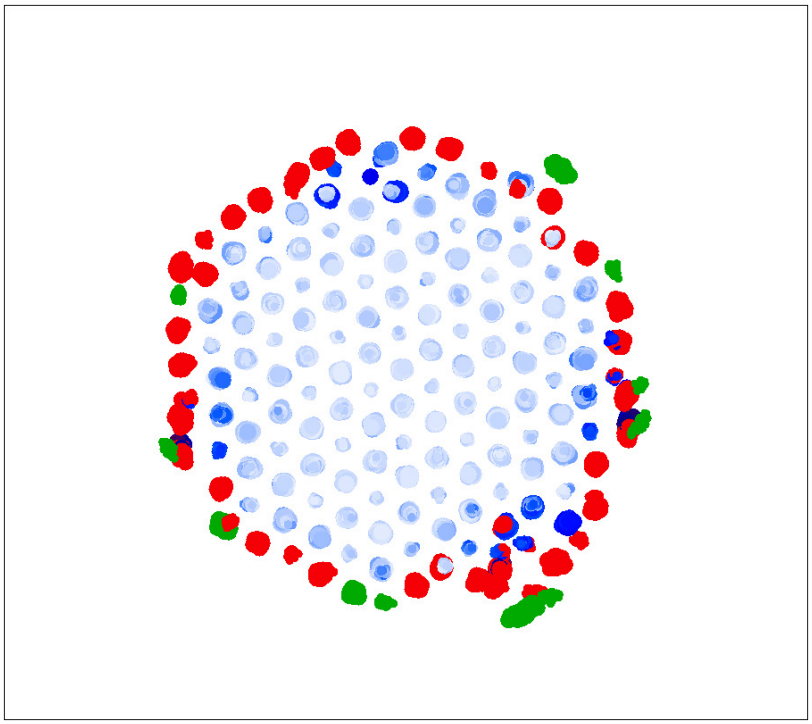

(b)

Figure 5.6: Projection of atomic positions in the last 500 ps of relaxation of (a) bare and (c) hydrated 30 Å ZB NP. The cross-section is viewed along the [111] direction and the big and small circles represent S and Zn atoms, respectively. 4-coordinated atoms are colored with respect to their tetrahedral order parameter, q^T. For clarity, only the position of atoms located in the central slab ($-6\text{Å} < x + y + z < 6\text{Å}$) are shown.

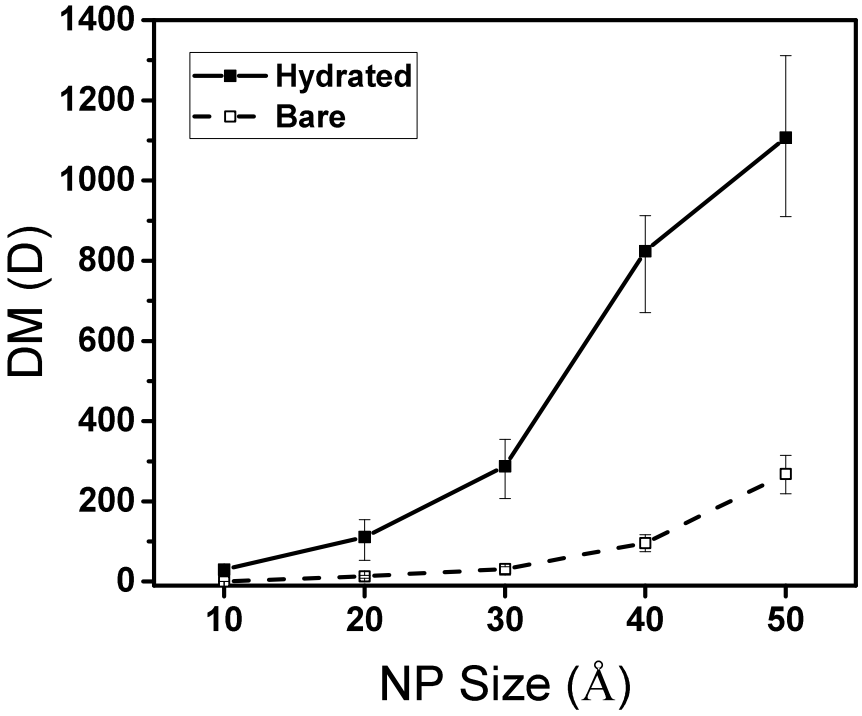

(a)

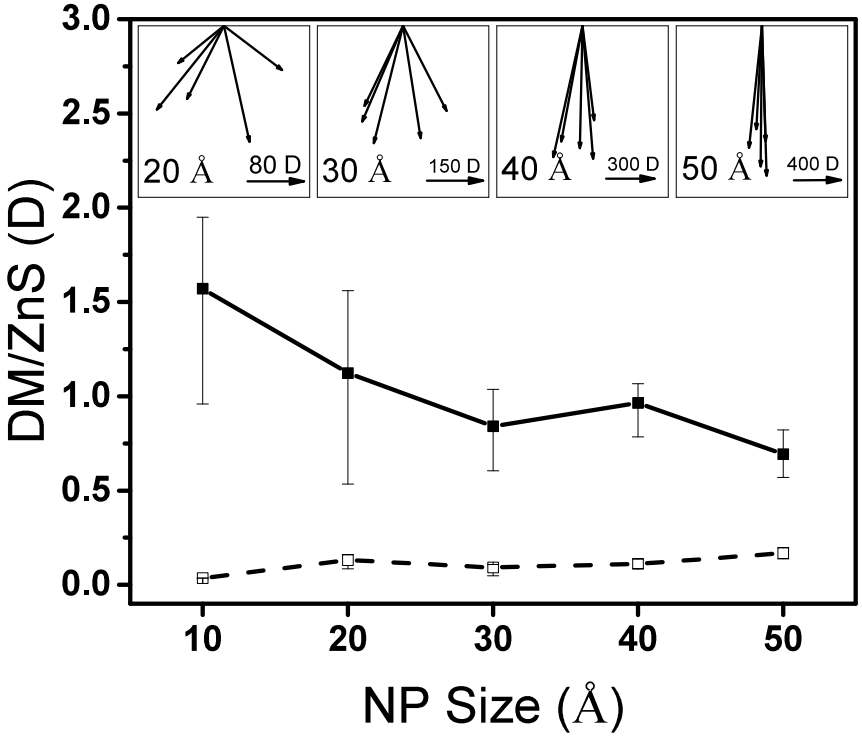

(b)

Figure 5.7: Variation of (a) DM and (b) DM per ZnS molecule with the size of bare and hydrated ZB NPs. Inset plots show the the projected image of the DM vectors of hydrated NPs on the XZ plane.

5.7a shows that DM per ZnS is also higher in the hydrated WZ NPs. As the hydrated NPs has more crystalline structure, this difference can be attributed to the polar nature of the WZ lattice. However, the fact that DM of hydrated 50 Å WZ NP is still much bigger than the natural DM of bulk WZ shows that the large DM of hydrated WZ NPs is not solely due to their more crystalline structure. Similar to ZB NPs, the surface of WZ NPs has less homogeneous structure than the bare NPs and this can result in higher DMs. However, The large difference between DM magnitude of bare and Hydrated WZ NPs shows that the effect of the surface is more significant in hydrated WZ NPs.

In WZ structure, (0001) is the most compact and a polar crystallographic surface. First principle studies has been shown that relaxation of Zn-terminated (0001) includes a large displacement of Zn atoms toward the bulk which ends up to a surface reconstruction very similar to the one of the non-polar (1010) surface [141, 142]. We also modeled relaxation of Zn and S (0001) surfaces in water and vacuum using MD at 300 K and obtained the same results. The simulations showed that Zn atoms move down to locate in the underlying S layer. Relaxation of S-terminated (0001) planes, however, does not include large movement of S ions. In our WZ NPs, the positive and negative end of all NPs in Z direction is terminated by Zn and S (0001) surfaces, respectively. This tells us that we should expect a large movement of positively charged Zn ions toward the -Z direction which can cause a large DM in the same direction. The structure of relaxed bare and hydrated 30 Å WZ NP is shown in Figure 5.8 to demonstrate this surface relaxation.

Figure 5.8 clearly shows the difference between relaxation of bare and hydrated WZ NPs in Z direction. More faceted structure of the hydrated NP is accompanied by large surface relaxation in Zn-terminated (0001) surface.This relaxation includes a large movement of Zn atoms toward the -Z direction which makes final structure of Zn-terminated (0001) surface to be flatten. This kind of surface reconstruction was also reported by other studies using different interatomic potentials [143]. It was shown that the the final {0001} surfaces are flattened to a near-hexagonal net which can effect the tetrahedral bond structure of the underlying layers in the bulk of NP as well. Thus, the effect of the Zn-terminated (0001) surface relaxation on the underlying atomic layers is probably the reason of lower tetrahedral order parameter and wider angular distribution which was observed for hydrated WZ NPs. The same surface relaxation happened in the first stages of the relaxation of WZ NPs in vacuum. By continuing the relaxation and formation of the 3-phase structure, the initial strain caused by relaxation of Zn-terminated (0001) surface is released and DM decreases. The more faceted configuration of the hydrated WZ NPs, however, is the reason of their larger polarity. The equivalent WZ (0001) plane in ZB structure is (111) surface. Due to the T_d symmetry of ZB structure there are 4 sets of (111) planes in ZB which gives a more homogeneous distribution to the (111) facets on the surface of a ZB NP. As a result,

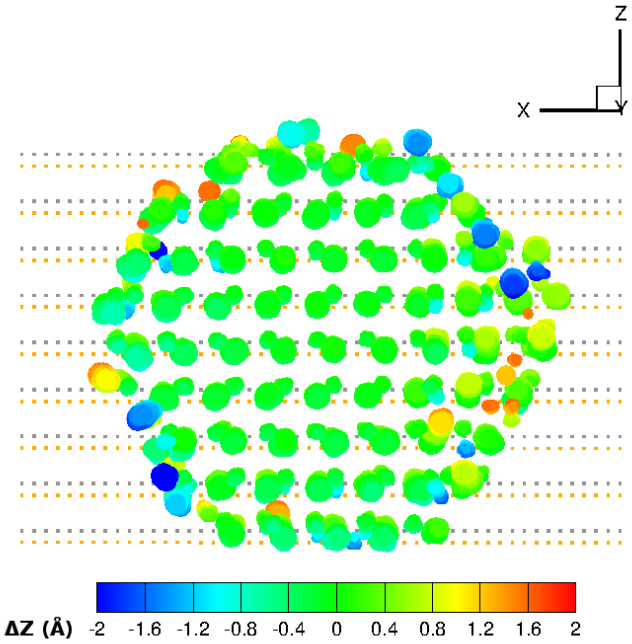

(a)

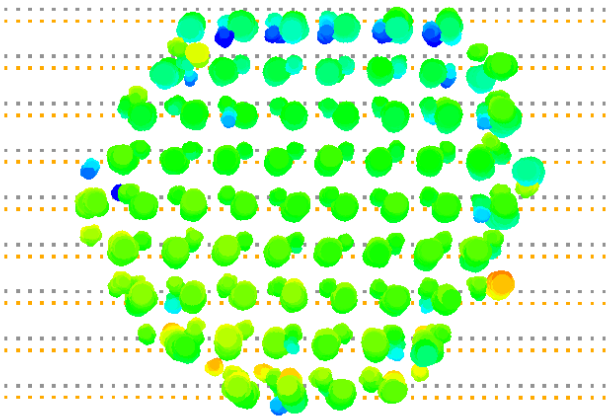

(b)

Figure 5.8: Projection of atomic positions in the last 500 ps of relaxation of (a) bare and (c) hydrated 30 Å ZB NP. The cross-section is viewed along the +Y direction and the big and small circles represent S and Zn atoms, respectively. Dashed lines represent the initial position of (0001) planes and color map shows the atomic displacement in Z direction.For clarity, only the position of atoms located in the central slab (-6Å $< y <$ 6Å) are shown.

the effect of polar facets relaxation on the total DM of the hydrated ZB NP is less significant.

5.3.3 The structure of water

To understand the interaction between water and ZnS NPs, we studied the water structure around NPs in more details. In addition to stabilize the surface, the structure of water around the NP can play an important role in interaction of NP with the aqueous solution such as adsorption/desorption reactions of aqueous ions on the surface of NPs. The partial RDF diagrams between surface atoms of 30 Å NPs and water molecules are shown in Figure 5.9.

In theory, water adsorption to the NPs surface can happen through formation of Zn-O bonds, S-H bonds or mixture of both bond types. Figure 5.9 shows that water adsorbs to the NPs surface mainly through Zn-O interactions. Examination of partial RDF diagrams for other sizes shows that Zn-O bond length is varying between 2.1 and 2.2 Å while S-H bond length lies between 2.4 and 2.5 Å. These values are in a good agreement with CPMD results for hydrated $(ZnS)_n$ clusters (n = 4[78], 33 and 116 [137]). The structure of hydrated Zn^{2+} ion has thoroughly been studied by various experimental and theoretical methods. It has been shown that preferred hydration state of Zn^{2+} is six-coordinated. Experimentally measured Zn-O bond length for six coordinated Zn^{2+} cation varies between 2.07 to 2.1 Å [144, 145] which has been also confirmed by DFT studies have [146, 147]. In the fitting procedure used to derive parameters of Water-ZnS potential no data from solvation of Zn^{2+} was used, however, it was shown that the correct octahedral coordination is obtained for Zn^{2+} with a distance of 2.07 Å between the ion and the water molecules [41]. We also performed the MD simulation of solvation of S^{2-} ion in water. More water molecules (9 - 11) was found in the first coordination shell of S^{2-} ion with the average S-H distance of 2.4 Å. Shorter Zn-O distance suggests stronger Zn-O bond in respect to S-H bonds. This can be attributed to the difference between the Pauling electronegativities of O and Zn (3.44-1.65 = 1.79) which is larger than that between S and H (2.58-2.20 = 0.38) [78].

The first peak in the Zn-O RDF diagram represents the first hydration shell around the NP at which water molecules are tightly bond to the NP surface. The statics and dynamics of water at the first hydration shell can be explained using two quantities: average number of coordinated water (n_w), and water residence time (τ). These two parameters have been used in experimental studies on ions in water [144], and theoretical studies to describe water properties near flat surfaces [148] and nanoparticles [149, 150]. Average number of coordinated water for each atom on the surface of the NP was calculated by counting the number of water molecules whose centre of mass lies within the first hydration shell distance. We used the definition proposed by Impey et al. [151] to calculate water residence time. In this

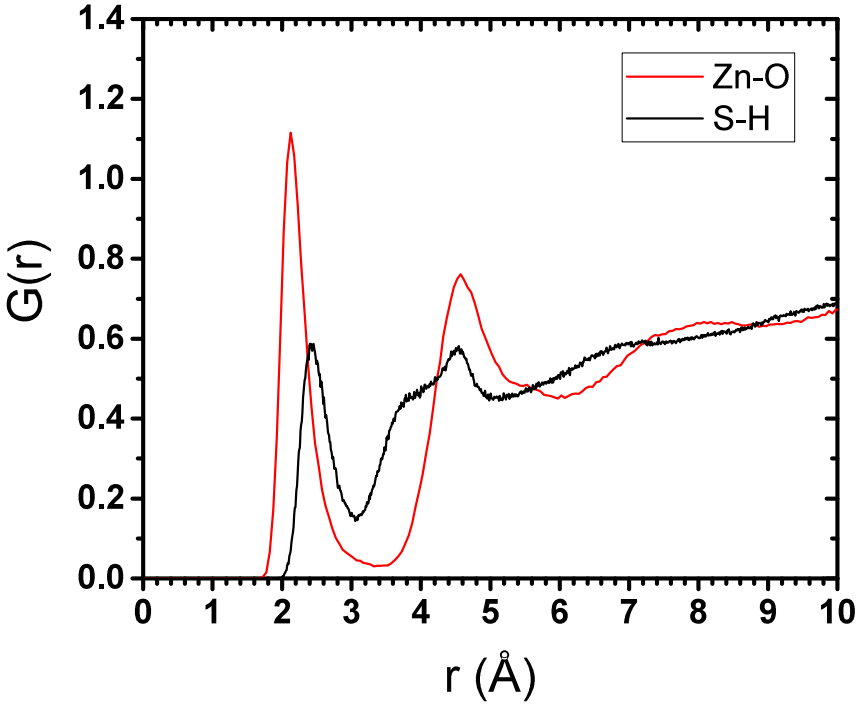

(a)

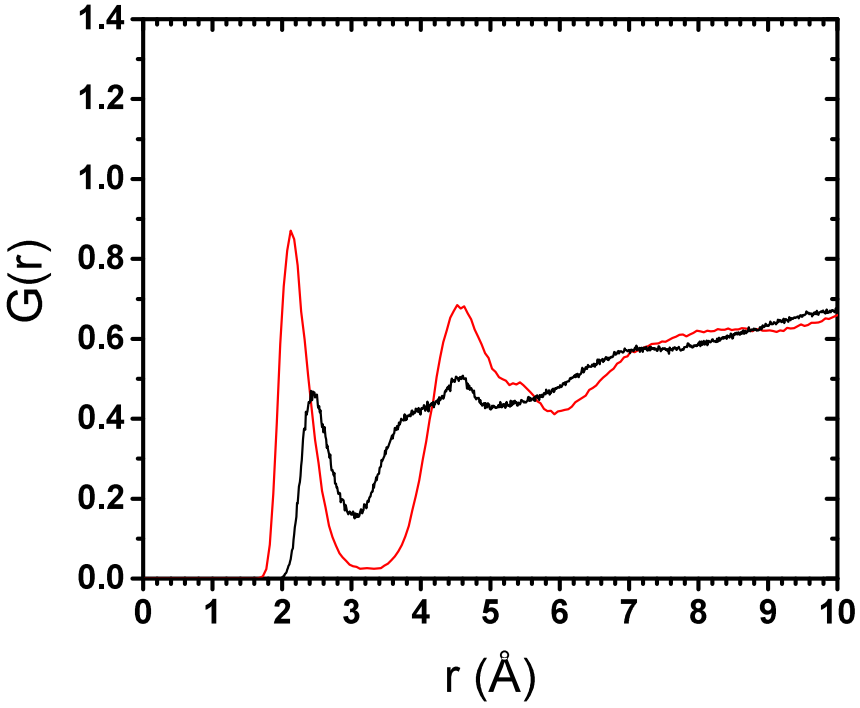

(b)

Figure 5.9: Partial RDF diagrams of Zn(surface)-O(water) and S(surface)-H(water) pairs for 30 Å ZnS NPs with initial (a) ZB and (b) WZ crystal structures.

definition, water residence time for each ion is calculated from residence-time correlation function, which is defined as

$$< n(t) >=< \frac{1}{N_0} \sum_{i=1}^{N_0} P_i(t_0, t; t^*) > \tag{5.3}$$

where $< ... >$ denotes the time average, N_0 is the number of the coordinated water around the ion at the time t_0 and $P_i(t_0, t; t^*)$ is a property of water molecule i which can take values of 0 or 1. $P_i(t_0, t; t^*)$ equals to 1, if water molecule i is within the first hydration shell at the time t_0 and $t_0 + t$ and have not left the first hydration shell for any continuous period longer than t^*. Under all other circumstances, it takes the value 0. Following the original work of Impey et al., we set t^* equal to 2 ps [151]. From this definition it is apparent that $n(0) = 1$. The water residence time at the first hydration shell can be obtained now by integration of $< n(t) >$:

$$\tau = \int_0^\infty < n(t) > dt \tag{5.4}$$

Figure 5.10 shows the average number of coordinated water molecules and the average residence time of water in the first hydration shell. These properties were calculated using the trajectories of the last 500 ps of simulations.

Figure 5.10a shows that the number of coordinated water and water residence time is higher around 2-coordinated surface atoms. Surface atoms with lower coordination numbers have more ability to adsorb water to compensate their under-coordination. Similar to what was observed for S^{2-} and Zn^{2+} ions in water, the average coordinated water number around surface S atoms is higher in Figure 5.10a. However, Figure 5.10b shows that there is a large difference between water residence time near surface Zn and S atoms. Water molecules in the first hydration shell of surface Zn atoms show a high stability while the residence time near S atoms is almost negligible. Large difference between water residence time around Zn and S atoms, shows again that water molecules mainly adsorb to the surface of NPs through Zn-O interactions. The long residence time specially near 2-coordinated Zn atoms can effect the surface properties of hydrated NPs greatly. In catalyst applications for instance, the affinity of undercoordinated atoms which considered as reaction sites can be influenced by water molecules in the first hydration shell. The almost immobile water molecules near 2-coordinated Zn atoms can also affect the observable dipole moment of the NP.

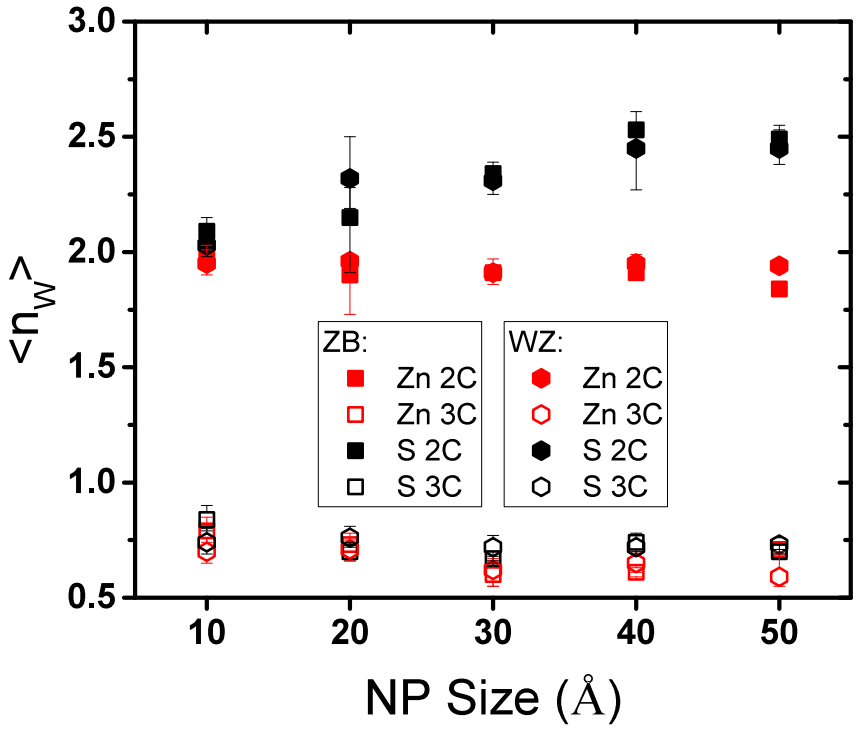

(a)

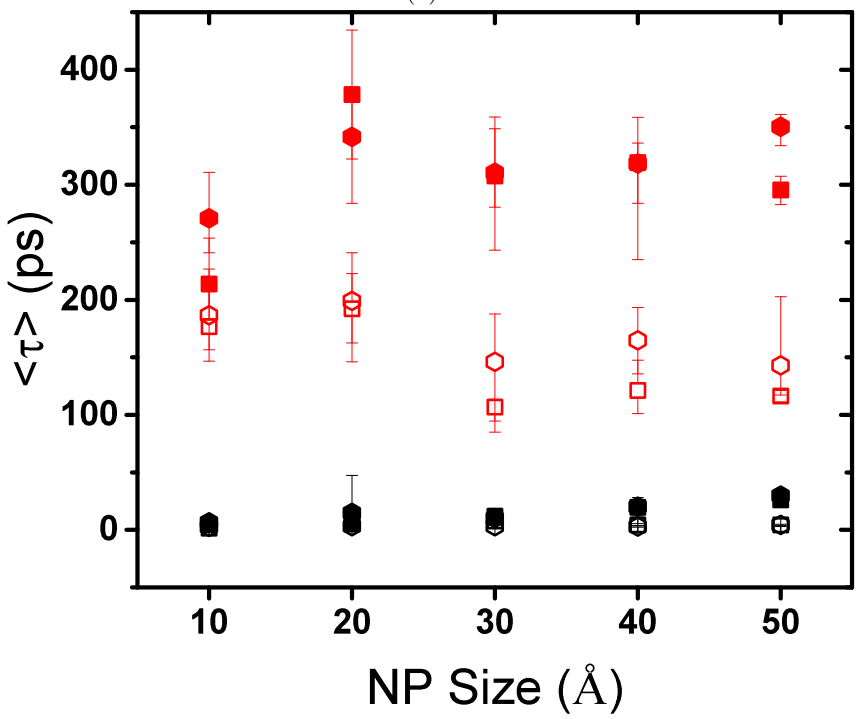

(b)

Figure 5.10: Water properties within the first hydration shell distance from the surface atoms during the last 500 ps of simulations. (a) average coordinated water number and (b) average water residence time near surface.

Figure 5.10a also shows that adsorption of water to the surface of NPs depends on the local structure of the surface. Type of atoms (Zn or S) and their CN (2 or 3) affects the water structure near a surface site. Accordingly, the water structure around the NP is heterogeneous and the first hydration shell is not continuous. The position of water molecules within the first hydration shell distance (< 3Å) from the surface of 30 Å ZB and WZ NPs are shown in Figure 5.11. To make it possible to show the whole surface of NPs, positions of Water molecules are represented in the Spherical Polar Coordinates.

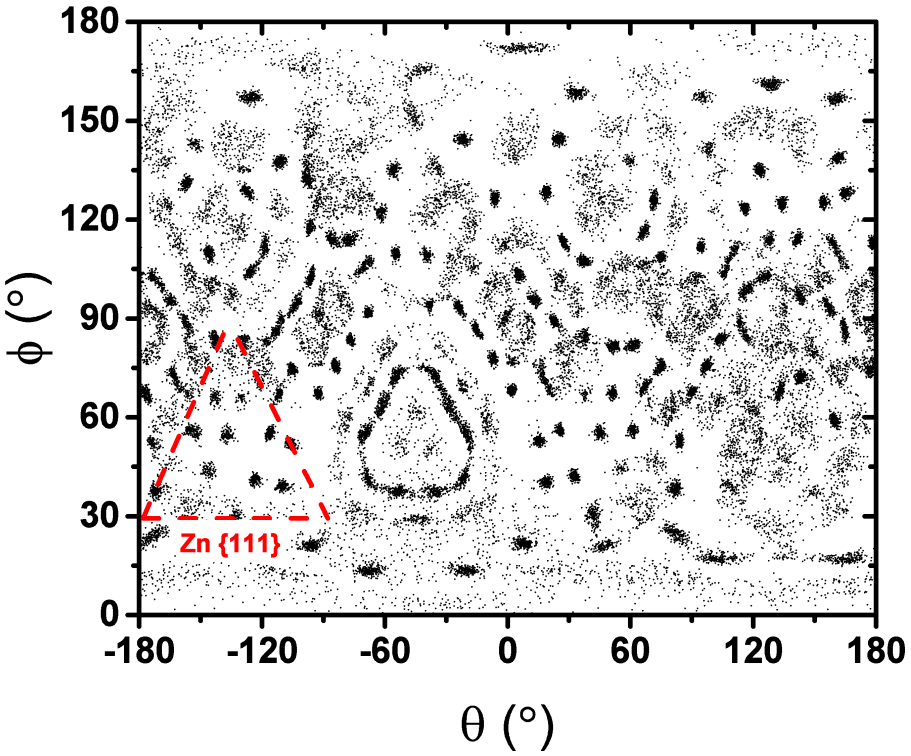

(a)

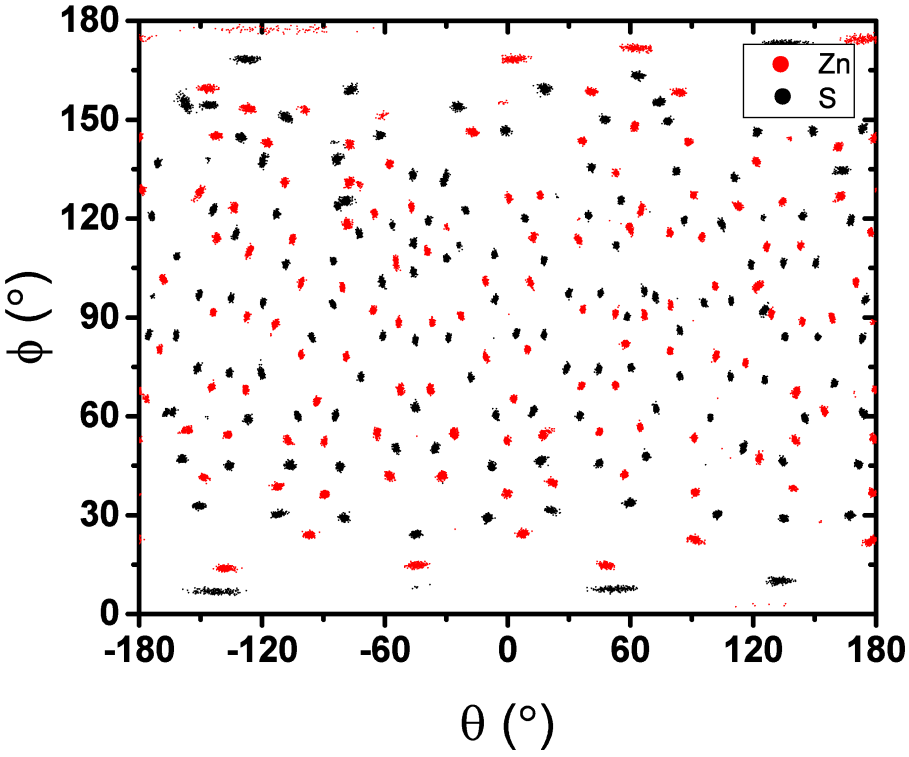
Zn
S
180
150
120
90
60
30
0
ϕ (°)
-180
-120
-60
0
60
120
180
θ (°)

(b)

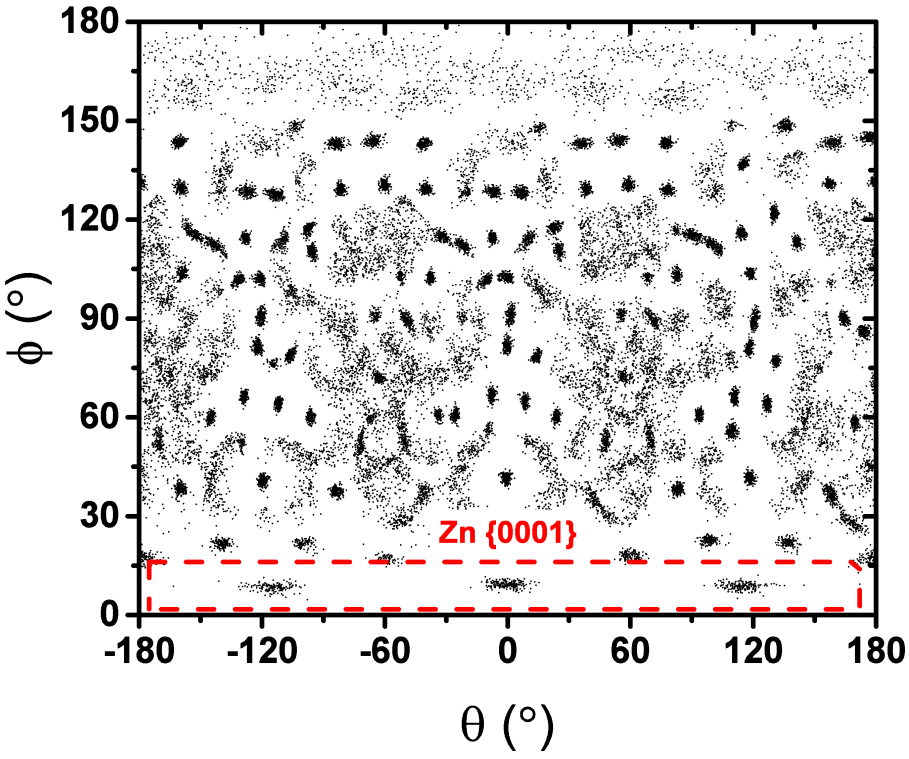
Zn {0001}
180
150
120
90
60
30
0
ϕ (°)
-180
-120
-60
0
60
120
180
θ (°)

(c)

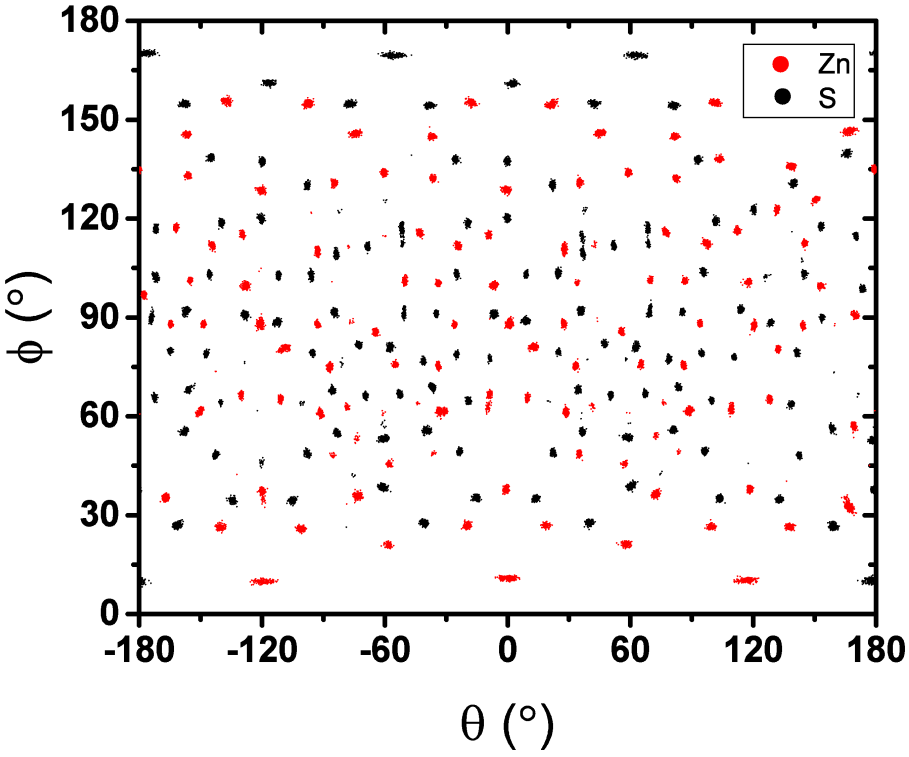

(d)

Figure 5.11: Projection of positions of water molecules in the first hydration shell and surface Zn and S atoms of 30 Å ZB and WZ NPs in the $\theta\phi$ plane of the Spherical Polar Coordinates. (a) and (c) are positions of water molecules within the first hydration shell distance from the surface of ZB and WZ NPs, respectively. (b) and (d) show the position of surface Zn and S atoms in the same NPs, ZB and WZ, respectively. θ is the azimuthal angle in the xy-plane from the x-axis with $0 \leq \theta < 2\pi$, ϕ is polar angle from the positive z-axis with $0 \leq \phi \leq \pi$. Each point in the graphs represent one atomic (or molecular in case of water) position during the last 500 ps of simulations.

As shown in Figure 5.11, the water structure of in the first coordination shell strictly depends on the position of Zn atoms on the surface. The positions of water molecules can be fit on the positions of Zn atoms on the surface. The position of the Zn-terminated (111) and (0001) facets in the ZB and WZ NPs are shown in the Figures 5.11b and 5.11d as an example. It can be trivially seen that corresponding S-terminated planes did not caused any order in the water structure.

5.4 Conclusions

The structural evolutions of bare and hydrated ZnS NPs with two initial crystal structures, ZB and WZ, and ranging in size between 1 to 5 nm are compared in this work. Different structural analyses such as radial distribution function, angular distribution, tetrahedral

order parameter and root mean square displacement performed on relaxed NPs showed that the 3-phase structure which was previously reported for the bare NPs was not formed in hydrated NPs. The 3-phase structure of bare NPs consists of a crystalline core followed by a layer of distorted 4-coordinated atoms and surface structure which entirely made of interconnected 3-coordinated atoms. Despite the more crystalline bulk of the hydrated NPs, their surface structure is not as homogeneous as bare NPs. The layer of distorted 4-coordinated atoms was not observed and bulk of NP remains its tetrahedral bond order almost up to the surface. 2-coordinated atoms which disappear after relaxation of NPs in vacuum were observed on the surface of hydrated NPs as well.

The structural evolution of ZnS NPs in vacuum and water affects their polarity. Initially non-polar ZnS NPs show polar behaviour after relaxation. When the size of the bare NP is smaller than 3 nm, the surface is dominant portion of NP structure and controls the polarity. Due to the similar surface structure of bare WZ and ZB NPs they show similar dipole moments. In bare NPs bigger than 3 nm, polarity is controlled by volume. This makes ZB and WZ NPs less and more polar, respectively (WZ crystal structure has a natural dipole moment at 300 K due to the slight C_{3v}-distortion of the elementary ZnS tetrahedron). Despite the more crystalline structure, hydrated ZB NPs showed a considerable polarity specially in small sizes. It has been shown than this polarity is due to the inhomogeneous surface relaxation in hydrated NPs. On the other hand, liquid like surface structure which is the result of the homogeneous structural deformation, lowers the dipole moment in bare NPs. In spite of the different dipole moment magnitudes of hydrated and bare ZB NPs, they both follow the same trend by increasing the size and become less polar. Hydrated WZ NPs showed more complicated surface relaxation. It is shown than relaxation of Zn-terminated (0001) surface of hydrated WZ NPs causes a large dipole moment in the Z direction. As a result, WZ NPs show a strong polarity in water and their dipole moment does not converge to the bulk WZ value even in sizes as big as 5 nm.

Analyses on water structure showed that water molecules are adsorbed to the surface of ZnS NPs mainly through Zn-O interactions. Despite of higher number of coordinated water molecules in the first hydration shell of surface S atoms, the residence time of water near S atoms is negligible. On the other hand, long residence time of water near undercoordinated Zn atoms, especially 2-coordinated Zn atom, showed that some water molecules become almost immobile in the vicinity of the surface Zn atoms. This results show that the water adsorption is depended on the local structure of the NP surface which results in a discontinuous first hydration shell. The position of water molecules in the first hydration shell of NPs showed to have the same pattern as the arrangement of surface Zn atoms.

Chapter 6

Conclusion and future works

Throughout this work we have studied the structural stability of ZnS nanoparticles as a function of crystal structure, size and environment mainly through employing the molecular dynamics simulations. We began with a focus on finding the proper empirical potential to model ZnS in nano-scale. The performance of five different empirical potentials for ZnS were tested and compared in Chapter 3. These potential functions of ZnS were developed by Wright and Jackson [90], Hamad et. al. [37], Wright and Gale [91], Grünwald et. al. [88], and Benkabou et. al. [92]. To avoid redundancy, we named the potentials by their short terms as IP1, IP2, IP3, IP4 and IP5, respectively.

It was shown that the lattice constants of ZB and WZ phases calculated by all empirical potentials are in acceptable agreement with the experiment. However, the lattice constant of RS phase calculated by IP3 and IP5 were not in an agreement with experimental values. This also happened for mechanical properties as elastic constants calculated for RS phase using IP3 and IP5 diverge greatly from those calculated by other potentials. We showed that mechanical and structural properties of RS phase calculated by IP3 potential can be improved by modifying its 3-body cut-off distance. Study of the phonon dispersion relations of ZB and WZ phases showed that all empirical potentials were able to reproduce acoustic branch except for IP1. None of potentials could predict optical phonons accurately and it was worse for IP5 as there was no LO/TO splitting due to the charge neutral atoms. IP1 was also unable to make the experimentally observed surface structure of ZnS. All other empirical potentials produced correct relaxed surface structures, however, IP2 and IP3 results were in the better agreement with the experiment. Pressure induced phase transformation was successfully predicted by IP1, IP2 and IP4. It is also shown that changing the 3-body cut-off distance would enable IP3 to show the pressure induced phase transformation as well. P-V relation calculated by IP2 represents better agreement with experimental results. Thermal expansion and potential hyper surface calculated by IP2 also showed a better agreement with experimental results and DFT calculations. Overall, one general comment can not be made on reliability of particular empirical potentials. The choice of

potential is highly depended on the application that molecular mechanic simulation aims for. Each of these potentials is designed to reproduce some specific ZnS properties. Except for IP5, we were able to run molecular dynamic simulations for temperatures as high as 1500 K. However, more care should be taken when using potentials that include shell model to perform high temperature molecular dynamics simulations. Very small time steps are needed to make shell model work in high temperatures which usually makes simulations too slow to be practical. Simulation speed is also highly depended on the complexity of the potential formulation. Thus, potentials like IP4 offer much higher simulation speed than more complicated ones like IP3.

The structural evolution of bare ZnS NPs having initial ZB and WZ crystal structures and ranged in size from 1 to 5 nm was investigated in Chapter 4. It was shown that for NPs bigger than 30 Å, the final configurations consists of three regions: a) a crystalline core which keeps its tetrahedral bond structure, b) a region of distorted 4-coordinated atoms which surrounds the core by forming 4- and 6-rings, and c) a network of interconnected 3-coordinated atoms which covers the surface of NPs. In the relaxed structure of 10 Å NPs all of the atoms are 3-coordinated, confirming the formation of the bubble-like structure. For 20 Å NPs, the structure relaxation removes the initial tetrahedral bond structure (region a) entirely. Our structural analyses showed that both ZB and WZ NPs ranging from 2 to 5 nm in size adopt a similar surface structure which includes regions b and c. This similarity may result in similar surface properties such as the surface energy. Although the tetrahedral bond structure is more stable in WZ NPs, we did not observe any phase transformation from ZB to WZ during 10 ns MD simulations. Results of dipole moment calculations showed that non-polar ideal structures of the bare NPs changes to the polar structures after relaxation at 300 K. Since the tetrahedral core of ZB NPs has a non-polar nature, the deviation of the surface structure from the ideal tetrahedral bond arrangement is the reason of their polar behaviour. Due to the randomness of the arrangement of the atoms on the surface, there was no specific direction for the dipole moment vector of the ZB NPs. In contrast, dipole moment vectors of WZ NPs becomes more aligned with -Z direction as the NP size increases. This is due to the polar nature of the WZ lattice, which was shown to have a dipole moment of 0.3855 D per ZnS molecule. By increasing the size of the WZ NP, the crystalline polar core becomes more dominant and controls the dipole moment magnitude and direction. For NPs smaller than 3 nm, where surface structure is predominant, the magnitude of dipole moments of ZB and WZ NPs are similar due to the similarity of the surface structures. As the size of the NP increases, the crystalline core becomes the dominant part of the NPs structure making ZB and WZ NPs less and more polar, respectively.

The structural evolutions of bare and hydrated ZnS NPs were compared in Chapter 5.

Structural analyses performed on the relaxed structures showed that the 3-phase structure which was observed in the bare NPs is not formed in hydrated NPs. The structure of hydrated NPs is generally more crystalline. Despite the more crystalline bulk of the hydrated NPs, their surface structure is not as homogeneous as the surface structure of the bare NPs. The layer of distorted 4-coordinated atoms was not observed and bulk of NP remains its tetrahedral bond order almost up to the surface. 2-coordinated atoms which disappeared after relaxation of NPs in vacuum were observed on the surface of hydrated NPs. The inhomogeneity of the surface structure of hydrated ZB NPs results in a considerable polarity specially in small sizes. On the other hand, liquid like surface structure which is the result of the homogeneous structural deformation, lowers the dipole moment in bare NPs. In spite of the different dipole moment magnitudes of hydrated and bare ZB NPs, they both follow the same trend by increasing the size and become less polar. Hydrated WZ NPs showed more complicated surface relaxation. It is shown than relaxation of Zn-terminated (0001) surface of hydrated WZ NPs causes a large dipole moment in the Z direction. As a result, WZ NPs show a strong polarity in water and their dipole moment does not converge to the bulk WZ value even in sizes as big as 5 nm. Analyses of the water structure around NPs showed that the arrangement of water molecules in the first hydration shell highly depends on the arrangement of under-coordinated Zn atom on the surface. This is because of strong interaction between NPs' zinc atoms and oxygen in water molecules which causes water molecules to adsorb to the surface of ZnS NPs mainly through Zn-O interactions. Despite the higher number of coordinated water molecules in the first hydration shell of surface S atoms, the residence time of water near S atoms is negligible. On the other hand, long residence time of water near undercoordinated Zn atoms, especially 2-coordinated Zn atom, showed that some water molecules become almost immobile in the vicinity of the surface Zn atoms.

Overall, this study shows that ZnS NPs structure can dynamically change and its evolution depends on crystal structure, size and environment. The particle-particle and particle-environment interactions are also affected by the structural evolution of NPs. This study clearly shows that there is still plenty to investigate in this field. some aspect of our work which we could not complete and propose for future studies are:

- This study highlights that improving the available ZnS empirical potentials is still desirable. We found the potential developed by Hamad et al. [37] the most suitable one to study the noncrystalline ZnS. But, this should be emphasized that the order of the structural stability of ZB and WZ phases is not predicted accurately by this or other available empirical potentials in literature. The fact that the most stable structure of ZnS NPs predicted by this potential using the global minimization technique is the unphysical BCT phase shows that, developing a more accurate potential can be the subject of the future studies. It also may be desirable to develop more stable

force fields in high temperatures to investigate structure of ZnS NPs as a function of temperature. Developing parameter of more powerful force fields such as ReaxFF, can enable the study of surface reactions such as Cu-Zn uptake or surface dissociation.

- The fundamental question for any classical molecular dynamics simulation is that if the simulation has been running long enough to satisfy ergodicity. In other words, MD simulation should be long enough so the system under study can explore all the energetically relevant configurations. This ideal condition, however, is not always achievable in practical situations. Different configurations of the system may be separated by high free-energy barriers which makes it impossible to observe the structural transformations in the time scale of MD simulation. We tried to apply the metadynamics method to investigate phase space of ZnS NPs. This would be an exiting topic for the future studies as size and shape dependent phase transformation in ZnS NPs has been proposed in numerical and experimental studies.

- The first principle calculations can be used in conjunction with molecular dynamics simulations to study the effect of structural changes of ZnS NPs on their optoelectronic properties. Simulation of dynamics of structural evolution in long time scales such as those reported in this study is still beyond the reach of the first principle simulations. However, these methods can be used to investigate the optoelectronic properties of NPs at different stages of MD relaxation. This can provide useful information regarding the life time and performance quality of ZnS quantum dots in different conditions.

Bibliography

[1] N. C. Anheier, Nature 523 (2015) 39–40.

[2] H. Zhang, F. Huang, B. Gilbert, J. F. Banfield, The Journal of Physical Chemistry B 107 (2003) 13051–13060.

[3] S. Hamad, C. R. A. Catlow, Journal of Crystal Growth 294 (2006) 2–8.

[4] Y. C. Cheng, C. Q. Jin, F. Gao, X. L. Wu, W. Zhong, S. H. Li, P. K. Chu, Journal of Applied Physics 106 (2009) 123505.

[5] C. B. Duke, Journal of Vacuum Science & Technology A: Vacuum, Surfaces, and Films 2 (1984) 515.

[6] S. Ves, U. Schwarz, N. Christensen, K. Syassen, M. Cardona, Physical Review B 42 (1990) 9113–9118.

[7] S. Desgreniers, L. Beaulieu, I. Lepage, Physical Review B 61 (2000) 8726–8733.

[8] R. Roberts, G. White, T. Sabine, Australian Journal of Physics 34 (1981) 701–706.

[9] B. Moss, The Journal of Chemical Physics 78 (1983) 7503.

[10] N. Giovambattista, S. V. Buldyrev, H. E. Stanley, F. W. Starr, Physical Review E - Statistical, Nonlinear, and Soft Matter Physics 72 (2005) 1–12.

[11] Z. Jin, P. Gumbsch, K. Lu, E. Ma, Physical Review Letters 87 (2001) 12–15.

[12] C. L. Soles, R. M. Dimeo, D. a. Neumann, A. Kisliuk, A. P. Sokolov, J. Liu, A. F. Yee, W. L. Wu, Macromolecules 34 (2001) 4082–4088.

[13] W. Steffen, B. Zimmer, a. Patkowski, G. Meier, E. Fischer, Journal of Non-Crystalline Solids 172-174 (1994) 37–42.

[14] F. H. Stillinger, T. a. Weber, The Journal of Chemical Physics 81 (1984) 5095.

[15] H. Zhang, D. J. Srolovitz, J. F. Douglas, J. a. Warren, Acta Materialia 55 (2007) 4527–4533.

[16] T. Sakuma, K. Shibata, S. Hoshino, Solid State Ionics 53-56 (1992) 1278–1281.

[17] H. E. Castillo, C. Chamon, L. F. Cugliandolo, J. L. Iguain, M. P. Kennett, Physical 68 (2003) 41.

[18] K. E. Drexler, Bulletin of Science, Technology and Society 24 (2004) 21–27.

[19] Nanotechnologies – Vocabulary – Part 2: Nano-objects, ISO/TS 80004-2:2015, 2015.

[20] C. Feigl, S. P. Russo, a. S. Barnard, Journal of Materials Chemistry 20 (2010) 4971.

[21] J. Foresman, A. Frisch, Exploring Chemistry with Electronic Structure Methods: A Guide to Using Gaussian, Gaussian Pittsburgh, PA, 2 edition, 1996.

[22] D. Sholl, J. A. Steckel, Density Functional Theory: A Practical Introduction, Wiley-Interscience, 2009.

[23] M. a. Reed, J. N. Randall, R. J. Aggarwal, R. J. Matyi, T. M. Moore, a. E. Wetsel, Physical Review Letters 60 (1988) 535–537.

[24] W. Leutwyler, S. Bürgi, H. Burgl, Science 271 (1996) 933–937.

[25] M. Bruchez Jr., Science 281 (1998) 2013–2016.

[26] N. Hildebrandt, ACS Nano 5 (2011) 5286–5290.

[27] V. Brunetti, H. Chibli, R. Fiammengo, A. Galeone, M. A. Malvindi, G. Vecchio, R. Cingolani, J. L. Nadeau, P. P. Pompa, Nanoscale 5 (2013) 307–17.

[28] K. Tsoi, Q. Dai, Accounts of Chemical Research 46 (2012) 662–671.

[29] Y. Yang, J. Lan, Z. Xu, T. Chen, T. Zhao, T. Cheng, J. Shen, S. Lv, H. Zhang, Nanotoxicology 8 (2014) 107–16.

[30] L. Shao, Y. Gao, F. Yan, Sensors (Basel, Switzerland) 11 (2011) 11736–51.

[31] S. Qadri, E. Skelton, D. Hsu, A. Dinsmore, Physical Review B 60 (1999) 9191–9193.

[32] G. Murali, D. Reddy, Optoelectronics and Advanced Materials 5 (2011) 928–931.

[33] C. Yang, Y. Liu, H. Sun, D. Guo, X. Li, W. Li, B. Liu, X. Zhang, Nanotechnology 19 (2008) 095704(1–5).

[34] F. Huang, B. Gilbert, H. Zhang, J. Banfield, Physical Review Letters 92 (2004) 155501.

[35] H. Zhang, B. Gilbert, F. Huang, J. Banfield, Nature 424 (2003) 1025–1029.

[36] B. Gilbert, H. Zhang, F. Huang, J. F. Banfield, Y. Ren, D. Haskel, J. C. Lang, G. Srajer, A. Jürgensen, G. a. Waychunas, The Journal of chemical physics 120 (2004) 11785–95.

[37] S. Hamad, S. Cristol, C. R. A. Catlow, Journal of Physical Chemistry B 106 (2002) 11002–11008.

[38] E. Spano, S. Hamad, C. Catlow, Journal of Physical Chemistry B 107 (2003) 10337–10340.

[39] E. Spanó, S. Hamad, C. Catlow, Chemical communications (2004) 864–865.

[40] S. Hamad, C. R. A. Catlow, E. Spanó, J. M. Matxain, J. M. Ugalde, The journal of physical chemistry. B 109 (2005) 2703–9.

[41] S. Hamad, S. Cristol, C. R. a. Catlow, Journal of the American Chemical Society 127 (2005) 2580–2590.

[42] a. S. Barnard, C. a. Feigl, S. P. Russo, Nanoscale 2 (2010) 2294–301.

[43] C. a. Feigl, A. S. Barnard, S. P. Russo, Physical chemistry chemical physics : PCCP 14 (2012) 9871–9.

[44] M. Shim, P. Guyot-Sionnest, The Journal of Chemical Physics 111 (1999) 6955–6964.

[45] W. Yan, S. Li, Y. Zhang, Q. Yao, S. D. Tse, The Journal of Physical Chemistry C 114 (2010) 10755–10760.

[46] H. Zhang, J. F. Banfield, CrystEngComm 16 (2014) 1568–1578.

[47] D. V. Talapin, E. V. Shevchenko, C. B. Murray, A. V. Titov, P. Kral, Nano letters 7 (2007) 1213–9.

[48] L. Li, A. Alivisatos, Physical Review Letters 90 (2003) 097402.

[49] T. Nann, J. Schneider, Chemical Physics Letters 384 (2004) 150–152.

[50] S. Shanbhag, N. a. Kotov, The journal of physical chemistry. B 110 (2006) 12211–7.

[51] K. Cho, D. V. Talapin, W. Gaschler, C. B. Murray, Journal of the American Chemical Society 127 (2005) 7140–7.

[52] B. Peng, D. Chen, Z. Deng, T. Wen, X. Meng, X. Ren, J. Ren, F. Tang, Chemphyschem : a European journal of chemical physics and physical chemistry 11 (2010) 3744–51.

[53] G. Zhu, S. Zhang, Z. Xu, J. Ma, X. Shen, Journal of the American Chemical Society 133 (2011) 15605–12.

[54] J. E. Mayer, The Journal of Chemical Physics 1 (1933) 270–279.

[55] P.P. Ewald, ANNALEN DER PHYSIK 64 (1921) 253–287.

[56] Kittel, Introduction to solid state physics, 2007.

[57] T. Darden, D. York, L. Pedersen, The Journal of Chemical Physics 98 (1993) 10089.

[58] R. a. Jackson, C. R. a. Catlow, Studies in Surface Science and Catalysis 52 (1989) 203–208.

[59] R. A. Buckingham, The Classical Equation of State of Gaseous Helium, Neon and Argon, 1938.

[60] B. D. Jr, A. Overhauser, Physical Review 122 (1958) 90–103.

[61] M. T. Dove, Introduction to Lattice Dynamics, Cambridge University Press, Cambridge, 1993.

[62] P. J. D. Lindan, M. J. Gillan, J. Phys: Condens. Matter 5 (1993) 1019.

[63] P. Mitchell, D. Fincham, Journal of Physics: Condensed Matter 5 (1993) 1031–1038.

[64] M. Allen, D. Tildesley, Computer Simulation of Liquids, Clarendon Press, 1989.

[65] W. G. Hoover, Physical Review A 31 (1985) 1695–1697.

[66] S. Nosé, Molecular Physics 52 (1984) 255–268.

[67] H. C. Andersen, The Journal of Chemical Physics 72 (1980) 2384–2393.

[68] M. Parrinello, a. Rahman, Journal of Applied Physics 52 (1981) 7182–7190.

[69] S. Melchionna, G. Ciccotti, B. Lee Holian, Molecular Physics 78 (1993) 533–544.

[70] P. Hohenberg, W. Kohn, Physical Review 136 (1964) B864.

[71] W. Kohn, L. J. Sham, Physical Review 140 (1965).

[72] R. Dronskowski, Computational Chemistry of Solid State Materials: A Guide for Materials Scientists, Chemists, Physicists and others, 2007.

[73] J. C. Slater, Physical Review 36 (1930) 57–64.

[74] S. F. Boys, Proceedings of the Royal Society A: Mathematical, Physical and Engineering Sciences 200 (1950) 542–554.

[75] S. B. Qadri, E. F. Skelton, a. D. Dinsmore, J. Z. Hu, W. J. Kim, C. Nelson, B. R. Ratna, Journal of Applied Physics 89 (2001) 115.

[76] S. Hamad, S. M. Woodley, C. R. A. Catlow, Molecular Simulation 35 (2009) 1015–1032.

[77] T. Akiyama, K. Sano, K. Nakamura, T. Ito, Japanese Journal of Applied Physics 46 (2007) 1783–1787.

[78] H. Zhang, J. R. Rustad, J. F. Banfield, The journal of physical chemistry. A 111 (2007) 5008–14.

[79] C. a. Feigl, A. S. Barnard, S. P. Russo, CrystEngComm 14 (2012) 7749.

[80] M. Grünwald, K. Lutker, a. P. Alivisatos, E. Rabani, P. L. Geissler, Nano letters (2012) 2–7.

[81] T. Mandal, P. K. Maiti, C. Dasgupta, Physical Review B 86 (2012) 024101.

[82] N. Finkelstein, International Journal of Mineral Processing 52 (1997) 81–120.

[83] H. M. Steele, K. Wright, I. H. Hillier, Physics and Chemistry of Minerals 30 (2003) 69–75.

[84] D. Simpson, T. Bredow, A. Chandra, G. P. Cavallaro, A. R. Gerson, Journal of Computational Chemistry 32 (2011) 2022–2030.

[85] J.-h. Chen, Y. Chen, Y.-q. Li, Transactions of Nonferrous Metals Society of China 20 (2010) 1121–1130.

[86] M. Porento, P. Hirva, Surface Science 576 (2005) 98–106.

[87] B. Bag, B. Das, B. Mishra, Minerals Engineering 24 (2011) 760–765.

[88] M. Grünwald, A. Zayak, J. B. Neaton, P. L. Geissler, E. Rabani, The Journal of chemical physics 136 (2012) 234111.

[89] M. E. Tuckerman, G. J. Martyna, The Journal of Physical Chemistry B 104 (2000) 159–178.

[90] K. Wright, R. Jackson, Journal of Materials Chemistry 5 (1995) 2037–2040.

[91] K. Wright, J. Gale, Physical Review B 70 (2004) 035211.

[92] F. Benkabou, H. Aourag, M. Certier, Materials Chemistry and Physics 66 (2000) 10–16.

[93] J. Fan, Multiscale Analysis of Deformation and Failure of Materials, Wiley, 2011.

[94] J. Tersoff, Physical Review Letters 56 (1986) 632–635.

[95] J. Tersoff, Physical Review B 39 (1989) 5566–5568.

[96] K. Wright, G. Watson, American Mineralogist 83 (1998) 141–146.

[97] H. Zhang, J. Banfield, Nano Letters 4 (2004) 713–718.

[98] K. Wright, The Canadian Mineralogist 47 (2009) 615–623.

[99] J. D. Gale, A. L. Rohl, Molecular Simulation 29 (2003) 291–341.

[100] G. Gao, K. Van Workum, J. David Schall, J. a. Harrison, Journal of physics. Condensed matter : an Institute of Physics journal 18 (2006) S1737–50.

[101] I. T. Todorov, W. Smith, K. Trachenko, M. T. Dove, Journal of Materials Chemistry 16 (2006) 1911.

[102] M. L. Cohen, J. R. Chelikowsky, Electronic Structure and Optical Properties of Semiconductors (Springer Series in Solid-State Sciences), Springer, 2012.

[103] J. D. Klerk, Journal of Physics and Chemistry of Solids 28 (1967) 1831–1837.

[104] D. Berlincourt, H. Jaffe, L. Shiozawa, Physical Review 129 (1963) 1009–1017.

[105] J. Jamieson, H. D. Jr, Journal of Physics and Chemistry of Solids 41 (1980) 963–964.

[106] C. F. Cline, Journal of Applied Physics 38 (1967) 1944.

[107] N. Uchida, Journal of Applied Physics 43 (1972) 971.

[108] E. Chang, G. Barsch, Journal of Physics and Chemistry of Solids 34 (1973) 1543–1563.

[109] CRC, Handbook of Chemistry and Physics, 94th Edition, CRC Press, 94 edition, 2013.

[110] G. Lucovsky, R. Martin, E. Burstein, Physical Review B 4 (1971) 251–262.

[111] J. V. Vechten, Physical Review 182 (1969) 181–905.

[112] J. M. Siqueiros, R. Machorro, L. E. Regalado, Applied optics 27 (1988) 2549–53.

[113] D. Parry, Surface Science 49 (1975) 433–440.

[114] J. Yang, F. Zhu, Q. Zhang, Y. Wu, X. Wu, S. Qin, J.-C. Dong, D.-L. Chen, Chinese Physics Letters 30 (2013) 046101.

[115] B. Moss, R. K. McMullan, T. F. Koetzle, The Journal of Chemical Physics 73 (1980) 495.

[116] D. Barlow, Journal of Physics and Chemistry of Solids 74 (2013) 406–409.

[117] J. Heyd, J. E. Peralta, G. E. Scuseria, R. L. Martin, The Journal of chemical physics 123 (2005) 174101.

[118] M. J. Lucero, T. M. Henderson, G. E. Scuseria, Journal of physics. Condensed matter : an Institute of Physics journal 24 (2012) 145504.

[119] K. Kudin, G. Scuseria, Physical Review B 61 (2000) 16440–16453.

[120] M. J. Frisch, G. W. Trucks, H. B. Schlegel, G. E. Scuseria, M. A. Robb, J. R. Cheeseman, G. Scalmani, V. Barone, B. Mennucci, G. A. Petersson, H. Nakatsuji, M. Caricato, X. Li, H. P. Hratchian, A. F. Izmaylov, J. Bloino, G. Zheng, J. L. Sonnenberg, M. Hada, M. Ehara, K. Toyota, R. Fukuda, J. Hasegawa, M. Ishida, T. Nakajima, Y. Honda, O. Kitao, H. Nakai, T. Vreven, J. A. Montgomery Jr., J. E. Peralta, F. Ogliaro, M. Bearpark, J. J. Heyd, E. Brothers, K. N. Kudin, V. N. Staroverov, R. Kobayashi, J. Normand, K. Raghavachari, A. Rendell, J. C. Burant, S. S. Iyengar, J. Tomasi, M. Cossi, N. Rega, J. M. Millam, M. Klene, J. E. Knox, J. B. Cross, V. Bakken, C. Adamo, J. Jaramillo, R. Gomperts, R. E. Stratmann, O. Yazyev, A. J. Austin, R. Cammi, C. Pomelli, J. W. Ochterski, R. L. Martin, K. Morokuma, V. G. Zakrzewski, G. A. Voth, P. Salvador, J. J. Dannenberg, S. Dapprich, A. D. Daniels, O. Farkas, J. B. Foresman, J. V. Ortiz, J. Cioslowski, D. J. Fox, Gaussian09 Revision D.01, 2012.

[121] Z. Li, B. Liu, S. Yu, J. Wang, Q. Li, B. Zou, T. Cui, Z. Liu, Z. Chen, J. Liu, The Journal of Physical Chemistry C 115 (2011) 357–361.

[122] F. Huang, J. F. Banfield, Journal of the American Chemical Society 127 (2005) 4523–9.

[123] J. Honeycutt, H. Andersen, Journal of Physical Chemistry 94305 (1987) 4950–4963.

[124] H. Tsuzuki, P. S. Branicio, J. P. Rino, Computer Physics Communications 177 (2007) 518–523.

[125] L. Hui, D. Feng, W. Jinlan, B. Xiufang, W. Guanghou, The Journal of Chemical Physics 114 (2001) 6413.

[126] D. C. Sayle, B. C. Mangili, J. Klinowski, T. X. T. Sayle, Journal of the American Chemical Society 128 (2006) 15283–91.

[127] S. Q. Wang, Applied Physics Letters 88 (2006) 061902(1–3).

[128] M. Khalkhali, Q. Liu, H. Zhang, Modelling and Simulation in Materials Science and Engineering 22 (2014) 085014.

[129] N. Tian, Z.-Y. Zhou, S.-G. Sun, Y. Ding, Z. L. Wang, Science 316 (2007) 732–5.

[130] B. Delley, The Journal of Chemical Physics 92 (1990) 508.

[131] B. Delley, Journal of Chemical Physics 113 (2000) 7756–7764.

[132] J. P. Perdew, Y. Wang, Physical Review B 45 (1992) 13244–13249.

[133] Y. Wang, R. Hu, G. Lin, I. Roy, K. T. Yong, ACS Applied Materials and Interfaces 5 (2013) 2786–2799.

[134] M. Khalkhali, Q. Liu, H. Zeng, H. Zhang, Scientific Reports 5 (2015) 14267.

[135] C. M. Goodell, B. Gilbert, S. J. Weigand, J. F. Banfield, The Journal of Physical Chemistry C 112 (2008) 4791–4796.

[136] J. M. Azpiroz, E. Mosconi, F. D. Angelis, The Journal of Physical Chemistry C 115 (2011) 25219–25226.

[137] J. Azpiroz, E. Mosconi, J. M. Ugalde, F. D. Angelis, The Journal of Physical Chemistry C 118 (2014) 3274–3284.

[138] K. F. Lau, H. E. Alper, T. S. Thacher, T. R. Stouch, The Journal of Physical Chemistry 98 (1994) 8785–8792.

[139] P. Steinhardt, D. Nelson, M. Ronchetti, Physical Review B 28 (1983).

[140] P.-L. Chau, a. J. Hardwick, Molecular Physics 93 (1998) 511–518.

[141] M. Houssa, B. van den Broek, E. Scalise, G. Pourtois, V. V. Afanas'ev, a. Stesmans, Physical chemistry chemical physics : PCCP 15 (2013) 3702–5.

[142] X. Zhang, H. Zhang, T. He, M. Zhao, Journal of Applied Physics 108 (2010).

[143] B. J. Morgan, P. a. Madden, Physical chemistry chemical physics : PCCP 9 (2007) 2355–2361.

[144] H. Ohtaki, T. Radnai, Chemical Reviews 93 (1993) 1157–1204.

[145] P. D'Angelo, V. Barone, G. Chillemi, N. Sanna, W. Meyer-Klaucke, N. V. Pavel, Journal of the American Chemical Society 124 (2002) 1958–1967.

[146] N. Díaz, D. Suárez, K. M. Merz Jr, Chemical Physics Letters 326 (2000) 288–292.

[147] M. Pavlov, P. E. M. Siegbahn, M. Sandström, The journal of physical chemistry. A 102 (1998) 219–228.

[148] D. Spagnoli, D. J. Cooke, S. Kerisit, S. C. Parker, Journal of Materials Chemistry 16 (2006) 1997.

[149] D. Spagnoli, B. Gilbert, G. a. Waychunas, J. F. Banfield, Geochimica et Cosmochimica Acta 73 (2009) 4023–4033.

[150] D. Spagnoli, J. P. Allen, S. C. Parker, Langmuir 27 (2011) 1821–1829.

[151] R. W. Impey, P. a. Madden, I. R. McDonald, Journal of Physical Chemistry 87 (1983) 5071–5083.

[152] M. Bonomi, D. Branduardi, G. Bussi, C. Camilloni, D. Provasi, P. Raiteri, D. Donadio, F. Marinelli, F. Pietrucci, R. a. Broglia, M. Parrinello, Computer Physics Communications 180 (2009) 1961–1972.

[153] I. A. I. Frenkel, Kinetic Theory of Liquids, Dover, New York, 1955.

[154] J. E. Lennard-Jones, A. F. Devonshire, Proceedings of the Royal Society of London A: Mathematical, Physical and Engineering Sciences 170 (1939) 464–484.

[155] a. V. Granato, Physical Review Letters 68 (1992) 974–977.

[156] A. KANIGEL, J. ADLER, E. POLTURAK, International Journal of Modern Physics C 12 (2001) 727–737.

[157] D. Kuhlmann-Wilsdorf, Physical Review 140 (1965).

[158] J. M. Kosterlitz, D. J. Thouless, Journal of Physics C: Solid State Physics 6 (1973) 1181–1203.

[159] R. M. J. Cotterill, Physical Review Letters 42 (1979) 1541–1544.

[160] S. F. Edwards, M. Warner, Philosophical Magazine A 40 (1979) 257–278.

[161] L. Burakovsky, D. Preston, R. Silbar, Physical Review B 61 (2000) 15011–15018.

[162] S. T. Chui, Physical Review B 28 (1983) 178–194.

[163] H. Kleinert, Gauge Fields in Condensed Matter, World Scientific, Singapore, Teaneck, NJ, 1989.

[164] N. F. Mott, R. W. Gurney, Trans. Faraday Soc. 35 (1939) 364–368.

[165] R. a. Quinn, J. Goree, Physical review. E, Statistical, nonlinear, and soft matter physics 64 (2001) 051404.

[166] R. Lipowsky, Physical Review Letters 57 (1986) 2876.

[167] M. Li, W. Johnson, W. Goddard, Physical Review B 54 (1996) 12067–12072.

[168] F. Lund, Physical Review Letters 69 (1992) 3084–3087.

[169] F. A. Lindemann, Physikalische Zeitschrift 11 (1910) 609–612.

[170] J. Gilvarry, Physical Review 102 (1956) 308–316.

[171] J. Bilgram, Physics Reports 153 (1987) 1–89.

[172] H. Löwen, Physics Reports 237 (1994) 249–324.

[173] R. Finken, M. Schmidt, H. Löwen, Physical Review E - Statistical, Nonlinear, and Soft Matter Physics 65 (2002) 1–9.

[174] S. N. Luo, A. Strachan, D. C. Swift, Journal of Chemical Physics 122 (2005) 0–5.

[175] H. J. Fecht, W. L. Johnson, Nature 334 (1988) 50–51.

[176] L. C. Gallington, A. Bongiorno, Journal of Chemical Physics 132 (2010) 0–6.

[177] M. Born, J. Chem. Phys. 7 (1939) 591.

[178] G. H. Wannier, The Journal of Chemical Physics 7 (1939) 810.

[179] T. V. Ramakrishnan, M. Yussouff, Physical Review B 19 (1979) 2775–2794.

[180] S. Di Nardo, J. H. Bilgram, Physical Review B 51 (1995) 8012–8017.

[181] E. Burke, J. Q. Broughton, G. H. Gilmer, The Journal of Chemical Physics 89 (1988) 1030–1041.

[182] H. Zhang, P. Kalvapalle, J. F. Douglas, Journal of Physical Chemistry B 115 (2011) 14068–14076.

[183] C. Donati, J. Douglas, W. Kob, S. Plimpton, P. Poole, S. Glotzer, Physical Review Letters 80 (1998) 2338–2341.

[184] C. Donati, S. C. Glotzer, P. H. Poole, W. Kob, S. J. Plimpton, Physical review. E, Statistical physics, plasmas, fluids, and related interdisciplinary topics 60 (1999) 3107–3119.

[185] R. a. Riggleman, K. Yoshimoto, J. F. Douglas, J. J. De Pablo, Physical Review Letters 97 (2006) 1–4.

[186] H. Zhang, D. J. Srolovitz, J. F. Douglas, J. a. Warren, Proceedings of the National Academy of Sciences of the United States of America 106 (2009) 7735–7740.

[187] G. Adam, J. H. Gibbs, The Journal of Chemical Physics 43 (1965) 139–146.

[188] L. Gránásy, T. Pusztai, T. Börzsönyi, J. a. Warren, J. F. Douglas, Nature materials 3 (2004) 645–650.

[189] L. Gránásy, T. Pusztai, G. Tegze, J. a. Warren, J. F. Douglas, Physical Review E - Statistical, Nonlinear, and Soft Matter Physics 72 (2005) 1–15.

[190] I. Saika-Voivod, R. K. Bowles, P. H. Poole, Physical Review Letters 103 (2009) 1–4.

[191] A. Sanz, A. Nogales, T. a. Ezquerra, Macromolecules 43 (2010) 29–32.

[192] L. Wang, C. Peng, Y. Wang, Y. Zhang, Physics Letters, Section A: General, Atomic and Solid State Physics 350 (2006) 69–74.

[193] T. Kawasaki, H. Tanaka, Proceedings of the National Academy of Sciences 107 (2010) 14036–14041.

[194] E. Sanz, C. Valeriani, E. Zaccarelli, W. C. K. Poon, P. N. Pusey, M. E. Cates, Physical Review Letters 106 (2011) 1–4.

[195] R. W. Cahn, Nature 323 (1986) 668–669.

[196] W. A. Curtin, Physical Review B 39 (1989).

[197] B. Pluis, D. Frenkel, J. van der Veen, Surface Science 239 (1990) 282–300.

[198] R. Ohnesorge, H. Löwen, H. Wagner, Physical Review E 50 (1994) 4801–4809.

[199] R. Lipowsky, U. Breuer, K. C. Prince, H. P. Bonzel, Phys. Rev. Lett. 64 (1990) 2105.

[200] A. F. Voter, S. P. Chen, in: Materials Research Society Symposium Proceedings, Boston.

[201] B. J. Alder, W. G. Hoover, T. E. Wainwright, Physical Review Letters 11 (1963) 241–243.

[202] B. J. Alder, D. M. Ceperley, E. L. Pollock, International Journal of Quantum Chemistry 22 (1982) 49–61.

[203] P. Choquard, J. Clerouin, Physical Review Letters 50 (1983) 2086–2089.

[204] C. R. Berardi, K. Barros, J. F. Douglas, W. Losert, Physical Review E - Statistical, Nonlinear, and Soft Matter Physics 81 (2010) 1–5.

[205] C. a. Murray, R. a. Wenk, Physical Review Letters 62 (1989) 1643–1646.

[206] K. J. Naidoo, J. Schnitker, J. D. Weeks, Molecular Physics 80 (1993) 1–24.

[207] H. M. Thomas, G. E. Morfill, Nature 379 (1996) 806–809.

[208] W.-T. Juan, Z.-H. Huang, J.-W. Hsu, Y.-J. Lai, L. I, Physical Review E 58 (1998) R6947–R6950.

[209] C.-H. Chiang, L. I, Physical Review Letters 77 (1996) 647–650.

[210] X. M. Bai, M. Li, Physical Review B - Condensed Matter and Materials Physics 77 (2008) 1–13.

[211] J. Broughton, G. Gilmer, J. Weeks, Physical Review B 25 (1982) 4651–4669.

[212] M. Dzugutov, S. I. Simdyankin, F. H. M. Zetterling, Physical review letters 89 (2002) 195701.

[213] a. Anikeenko, N. Medvedev, Physical Review Letters 98 (2007) 1–4.

[214] A. Anikeenko, N. Medvedev, A. Bezrukov, D. Stoyan, Journal of Non-Crystalline Solids 353 (2007) 3545–3549.

[215] H. Tanaka, T. Kawasaki, H. Shintani, K. Watanabe, Nature materials 9 (2010) 324–331.

[216] U. R. Pedersen, T. B. Schrø der, J. C. Dyre, P. Harrowell, Physical Review Letters 104 (2010) 1–4.

[217] A. Haji-Akbari, M. Engel, S. C. Glotzer, Journal of Chemical Physics 135 (2011).

[218] S. M. Foiles, M. I. Baskes, M. S. Daw, Physical Review B 33 (1986) 7983–7991.

[219] S. Plimpton, Journal of Computational Physics 117 (1995) 1–19.

[220] J. W. Daniel, Numerische Mathematik 10 (1967) 125–131.

[221] P. Yunker, Z. Zhang, a. G. Yodh, Physical Review Letters 104 (2010) 2–5.

[222] H. Fecht, Z. Fu, W. Johnson, Physical Review Letters 64 (1990) 1753–1756.

[223] Rehn 59 (1987) 2987–2990.

[224] M. a. Parshin, C. Laermans, D. a. Parshin, V. G. Melehin, Physica B: Condensed Matter 316-317 (2002) 549–551.

[225] R. Zangi, S. a. Rice, Physical review letters 92 (2004) 035502.

[226] a. H. Marcus, J. Schofield, S. a. Rice, Physical review. E, Statistical physics, plasmas, fluids, and related interdisciplinary topics 60 (1999) 5725–5736.

[227] E. R. Weeks, Science 287 (2000) 627–631.

[228] H. Zhang, D. J. Srolovitz, J. F. Douglas, J. a. Warren, Physical Review B - Condensed Matter and Materials Physics 74 (2006) 1–10.

[229] D. Stauffer, A. Aharony, Introduction to Percolation Theory, 2nd ed, Taylor & Francis, London, Bristol, PA, 1994.

[230] K. Nordlund, Y. Ashkenazy, R. S. Averback, a. V. Granato, Europhysics Letters (EPL) 71 (2007) 625–631.

[231] F. W. Starr, J. F. Douglas, S. Sastry, Journal of Chemical Physics 138 (2013).

[232] A. S. Keys, A. R. Abate, S. C. Glotzer, D. J. Durian, Nat Phys 3 (2007) 260–264.

[233] J. F. Douglas, J. Dudowicz, K. F. Freed, Journal of Chemical Physics 125 (2006).

[234] R. a. Riggleman, J. F. Douglas, J. J. De Pablo, Journal of Chemical Physics 126 (2007).

[235] K. H. Nagamanasa, S. Gokhale, R. Ganapathy, a. K. Sood, Proceedings of the National Academy of Sciences of the United States of America 108 (2011) 11323–11326.

[236] T. O. E. Skinner, D. G. a. L. Aarts, R. P. a. Dullens, Journal of Chemical Physics 135 (2011).

[237] J. F. Douglas, T. Ishinabe, A. M. Nemirovsky, K. F. Freed, J. Phys. A: Math. Gen. 29 (1993) 1835.

[238] C. a. Murray, D. H. Van Winkle, Physical Review Letters 58 (1987) 1200–1203.

[239] Y. Tang, a. J. Armstrong, R. C. Mockler, W. J. Osullivan, Physical Review Letters 62 (1989) 2401–2404.

[240] A. H. Marcus, S. a. Rice, Physical Review E 55 (1997) 637–656.

[241] J. Douglas, D. Leporini, Journal of Non-Crystalline Solids 235-237 (1998) 137–141.

[242] J. F. Douglas, Computational Materials Science 4 (1995) 292–308.

[243] E. B. Stukalin, J. F. Douglas, K. F. Freed, Journal of Chemical Physics 129 (2008).

[244] Y. Zhou, X. Jin, Physical Review B - Condensed Matter and Materials Physics 71 (2005) 1–9.

[245] F. W. Starr, S. Sastry, J. F. Douglas, S. C. Glotzer, Physical review letters 89 (2002) 125501.

[246] L. Larini, a. Ottochian, C. De Michele, D. Leporini, Nature Physics 4 (2008) 42–45.

[247] A. M. Alsayed, M. F. Islam, J. Zhang, P. J. Collings, A. G. Yodh, Science 309 (2005) 1207–1210.

[248] H. Shiba, A. Onuki, T. Araki 66004 (2008) 6.

[249] M. D. Ediger, SPATIALLYHETEROGENEOUSDYNAMICS IN SUPERCOOLED LIQUIDS, 2000.

[250] H. Sillescu, Journal of Non-Crystalline Solids 243 (1999) 81–108.

[251] M. T. Cicerone, M. D. Ediger, The Journal of Chemical Physics 104 (1996) 7210–7218.

[252] S. Sengupta, S. Karmakar, C. Dasgupta, S. Sastry, Physical Review Letters 109 (2012) 1–5.

[253] W. Kob, H. C. Andersen, Phys. Rev. E 51 (1995) 4626–4641.

[254] M. G. Zemlyanov, V. K. Malinovskii, V. N. Novikov, P. P. Parshin, A. P. Sokolov, JETP Lett 49 (1989) 602.

[255] E. Duval, A. Boukenter, B. Champagnon, Physical Review Letters 56 (1986) 2052–2055.

[256] a. Mermet, N. V. Surovtsev, E. Duval, J. F. Jal, J. Dupuy-Philon, a. J. Dianoux, Europhysics Letters (EPL) 36 (1996) 277–282.

[257] M. Russina, F. Mezei, Physical review letters 85 (2000) 3630–3633.

[258] H. Shintani, H. Tanaka, Nature materials 7 (2008) 870–877.

[259] K. Chen, M. L. Manning, P. J. Yunker, W. G. Ellenbroek, Z. Zhang, A. J. Liu, a. G. Yodh, Physical Review Letters 107 (2011) 1–5.

[260] M. L. Manning, a. J. Liu, Physical Review Letters 107 (2011) 2–5.

[261] P. Tan, N. Xu, A. B. Schofield, L. Xu, Physical Review Letters 108 (2012) 1–5.

[262] A. Ghosh, V. K. Chikkadi, P. Schall, J. Kurchan, D. Bonn, Physical Review Letters 104 (2010) 2–5.

[263] R. P. Feynman, Physical Review 90 (1953) 1116–1117.

[264] R. P. Feynman, Physical Review 94 (1954) 262–277.

[265] R. P. Feynman, Physical Review 91 (1953) 1291–1301.

[266] W.-T. Juan, L. I, Physical Review Letters 80 (1998) 3073–3076.

[267] A. Paciaroni, A. Bizzarri, S. Cannistraro, Physical Review E 57 (1998) R6277–R6280.

[268] C. a. Angell, K. L. Ngai, G. B. McKenna, P. F. McMillan, S. W. Martin, Journal of Applied Physics 88 (2000) 3113–3157.

[269] G. N. Greaves, F. Meneau, O. Majérus, D. G. Jones, J. Taylor, Science (New York, N.Y.) 308 (2005) 1299–1302.

[270] Y. Li, H. Y. Bai, W. H. Wang, K. Samwer, Physical Review B - Condensed Matter and Materials Physics 74 (2006) 1–4.

[271] D. Kaya, N. L. Green, C. E. Maloney, M. F. Islam, Science (New York, N.Y.) 329 (2010) 656–658.

[272] T. S. Grigera, V. Martín-Mayor, G. Parisi, P. Verrocchio, Nature 422 (2003) 289–292.

[273] M. E. Manley, M. Yethiraj, H. Sinn, H. M. Volz, A. Alatas, J. C. Lashley, W. L. Hults, G. H. Lander, J. L. Smith, Physical Review Letters 96 (2006) 3–6.

[274] H. N. Bordallo, E. V. Boldyreva, J. Fischer, M. M. Koza, T. Seydel, V. S. Minkov, V. a. Drebushchak, A. Kyriakopoulos, Biophysical Chemistry 148 (2010) 34–41.

[275] M. E. Manley, a. J. Sievers, J. W. Lynn, S. a. Kiselev, N. I. Agladze, Y. Chen, a. Llobet, a. Alatas, Physical Review B - Condensed Matter and Materials Physics 79 (2009) 2–6.

[276] M. E. Manley, B. Fultz, R. J. McQueeney, C. M. Brown, W. L. Hults, J. L. Smith, D. J. Thoma, R. Osborn, J. L. Robertson, Physical Review Letters 86 (2001) 3076–3079.

[277] a. J. Sievers, S. Takeno, Physical Review Letters 61 (1988) 970–973.

[278] C. Reichhardt, C. J. Olson Reichhardt, Physical review letters 90 (2003) 095504.

[279] a.V. Granato, Journal of Physics and Chemistry of Solids 55 (1994) 931–939.

[280] H. R. Schober, in: S. Hunklinger, W. Ludwig, G. Weiss (Eds.), Vol. 1, World Scientific, Singapore, 1989, p. 444.

[281] A. M. Nieves, T. Sinno, Journal of Chemical Physics 135 (2011).

[282] J. Farago, Physica D: Nonlinear Phenomena 237 (2008) 1013–1020.

[283] M. Peyrard, J. Farago, Physica A: Statistical Mechanics and its Applications 288 (2000) 199–217.

[284] T. Dauxois, M. Peyrard, A. Bishop, Physical Review E 47 (1993) 684–95.

[285] G. Tsironis, S. Aubry, Physical Review Letters 77 (1996) 5225–5228.

[286] S. Flach, G. Mutschke, Physical Review E 49 (1994) 5018–5024.

[287] G. C. S. Lee, J. C. M. Li, Physical Review B 39 (1989) 9302–9311.

[288] a. Savin, L. Manevitch, Physical Review B 58 (1998) 11386–11400.

[289] F. W. Starr, J. F. Douglas, Physical Review Letters 106 (2011) 1–4.

[290] R. a. Riggleman, J. F. Douglas, J. J. de Pablo, Soft Matter 6 (2010) 292.

[291] C. Zener, Acta Crystallographica 3 (1950) 346–354.

[292] A. Gray-Weale, P. a. Madden, Journal of Physical Chemistry B 108 (2004) 6624–6633.

[293] S. Hull, Reports on Progress in Physics 67 (2004) 1233–1314.

[294] N. Kamaya, K. Homma, Y. Yamakawa, M. Hirayama, R. Kanno, M. Yonemura, T. Kamiyama, Y. Kato, S. Hama, K. Kawamoto, A. Mitsui, Nature materials 10 (2011) 682–686.

[295] B. a. Pazmiño Betancourt, J. F. Douglas, F. W. Starr, Soft Matter (2012) 241–254.

[296] B. M. Voronin, S. V. Volkov, Journal of Physics and Chemistry of Solids 62 (2001) 1349–1358.

[297] M. T. Hutchings, K. Clausen, M. H. Dickens, W. Hayes, J. K. Kjems, P. G. Schnabel, C. Smith, Journal of Physics C: Solid State Physics 17 (2000) 3903–3940.

[298] J. P. Goff, W. Hayes, S. Hull, M. T. Hutchings, Journal of Physics: Condensed Matter 3 (1999) 3677–3687.

Appendix A

Comparison between DFT and IP results for the geometry optimization of the 1 nm nanoparticle

Table A.1: Comparison between DFT and IP (interatomic empirical potential) results for the geometry optimization of the 1 nm zinc blende (ZB) and wurtzite (WZ) ZnS nanoparticles.

Property	**Method**	**ZB**	**WZ**
$\Delta E^1_{IP}(eV)$	IP	-1.415	-1.700
	DFT	-1.089	-1.272
$\Delta E^*_{DFT}(eV)$	IP	-0.859	-0.911
	DFT	-1.03	-1.17
RMSD (Å)	IP	1.63	1.72
	DFT	1.34	1.41
Average Bond Length (Å)	IP	2.321	2.333
	DFT	2.355	2.350
Average Bond Angle (°)	IP	107.913	106.588
	DFT	130.130	103.970
Average Coordination Number[2]	IP	3.101	3.000
	DFT	2.942	2.955
Dipole Moment[3](D)	IP	1.475	1.938
	DFT	1.389	1.867

1. $\Delta E = E_f - E_0$. Geometry optimization performed using IP and DFT methods. Single point energy calculation was performed for initial and final structures after geometry optimization. Subscript of ΔE shows the method used for the single point energy calculations. In the IP method which includes shell model, we let the shells of S atoms to relax during energy calculations.

2. Average coordination numbers of the initial configurations of the ZB and WZ nanoparticles were 2.895 and 2.636, respectively.

3. Dipole moment was calculated using the DFT method.

Appendix B

Monitoring the structural evolution of hydrated ZnS nanoparticles during MD simulation

Root mean square displacement (RMSD) and the 4th order Steinhardt parameter, Q_4 were used to monitor the structural changes in the hydrated ZnS nanoparticles (NPs). After running MD simulations for 8 ns in the NPT ensemble, simulations were stopped if these parameters did not change abruptly for at least 2 ns. Figure SB.1 shows the evolution of RMSD in the 10 ns NPT simulations. RMSD is calculated with respect to the initial unrelaxed configurations of NPs.

The 4th order Steinhardt parameter, Q_4 was calculated using the PLUMED software [152]. The order in the first coordination shell around an atom can be conveniently measured using Steinhardt order parameters. As explained in the PLUMED manual, Steinhardt parameters can be utilized in a variety of different ways to perform this measurement. Instead of simply taking the norm of Steinhardt parameters and calculating Q_4, we used more complicated approach which calculates "local Q_4". This parameter shows the extent which orientation of the atoms in the first coordination sphere of an atom match the orientation of the central atom. For more details about different methods of calculation of Steinhardt order parameter, readers are referred to the PLUMED manual. Evolution of the "local Q_4" during the 10 ns NPT simulation of ZnS NPs is represented in Figure SB.2.

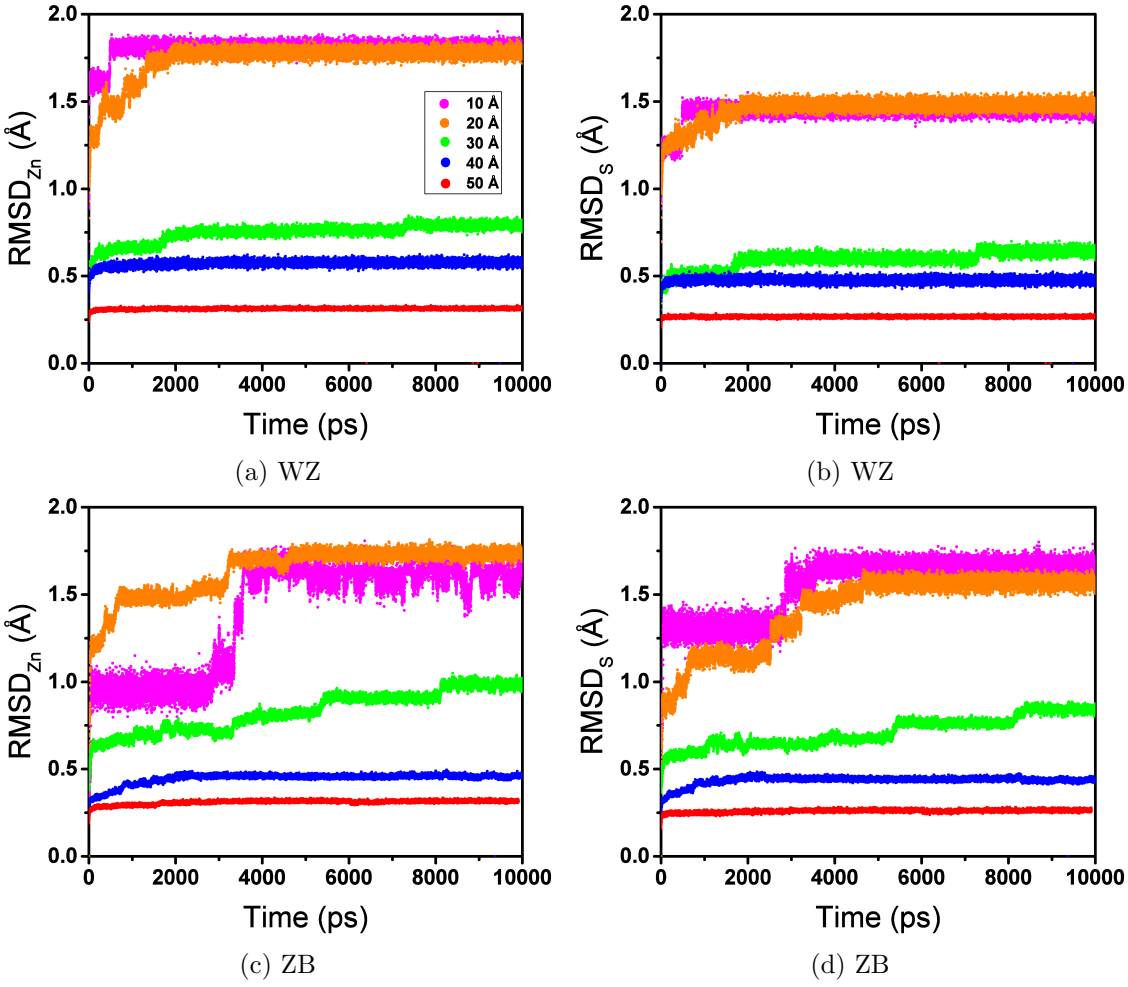

(a) WZ (b) WZ

(c) ZB (d) ZB

Figure B.1: Evolution of RMSD during the 10 ns NPT simulation of ZnS NPs. (a) and (b) are related to WZ NPs and show RMSD of Zn and S atoms, respectively. (c) and (d) are the similar calculations for the ZB NPs.

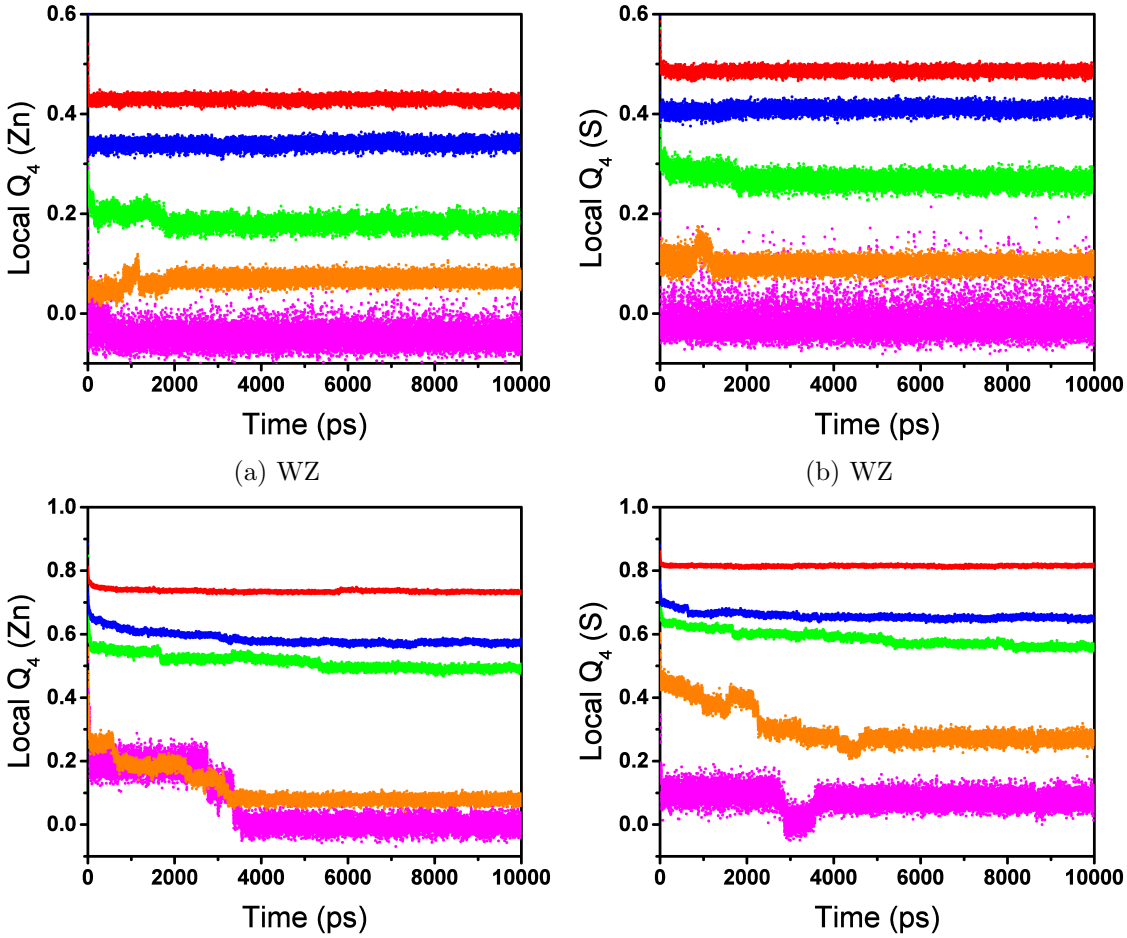

(a) WZ (b) WZ

(c) ZB (d) ZB

Figure B.2: Evolution of local Q_4 during the 10 ns NPT simulation of ZnS NPs. (a) and (b) are related to WZ NPs and show the local Q_4 of Zn and S atoms, respectively. (c) and (d) are the similar calculations for the ZB NPs.

Appendix C

Surface properties of ZnS in vacuum and water

As a part of this study, the surface properties of ZB and WZ ZnS is studied in the vacuum and water. The results of surface energy calculations are represented in Table C.1. The surface properties represented in this section are calculated using 3D periodic boundary conditions within DL_POLY software which is different from the method used to calculated surface properties in Chapter 3.

Table C.1: Surface energy calculations for ZB and WZ crystallographic planes in vacuum and water.

Condition	E_1^* (eV)	E_2^* (eV)	$E_2 - E_1$ (eV)	Area (Å^2)	E_s (J/m^2)
			ZB		
(110)					
Vacuum - 0 K	-25508.444	-25442.324	66.120	993.392	0.533
Vacuum - 300 K	-25448.889	-25383.184	65.705	1001.119	0.526
Water - 300 K	-26007.991	-25960.422	47.569	1001.119	0.381
(111) - Zn					
Vacuum - 0 K	-25508.444	-25424.650	83.794	811.101	0.828
Vacuum - 300 K	-25448.889	-25365.000	83.889	817.411	0.822
Water - 300 K	-25870.384	-25817.128	53.256	817.411	0.522
(111) - S					
Vacuum - 0 K	-25508.444	-25405.000	103.444	811.101	1.022
Vacuum - 300 K	-25448.889	-25346.439	102.450	817.411	1.004
Water - 300 K	-25823.258	-25737.000	86.258	817.411	0.845
(100) - Zn					
Vacuum - 0 K	-28697.000	-28547.000	150.000	1053.652	1.140
Vacuum - 300 K	-28630.000	-28487.000	143.000	1119.572	1.023

Continued on the next page

Table C.1 – Continue

Condition	E_1^* (eV)	E_2^* (eV)	$E_2 - E_1$ (eV)	Area (Å^2)	E_s (J/m^2)
Water - 300 K	-29256.587	-29167.501	89.086	1119.572	0.637
(100) - S					
Vacuum - 0 K	-28697.000	-28530.610	166.390	1053.652	1.265
Vacuum - 300 K	-28630.000	-28474.000	156.000	1119.572	1.116
Water - 300 K	-29249.801	-29149.000	100.801	1119.572	0.721
WZ					
(0001)-Zn					
Vacuum - 0 K	-26632.000	-26511.860	120.140	1040.846	0.925
Vacuum - 300 K	-26566.000	-26456.000	110.000	1015.734	0.868
Water - 300 K	-27018.032	-26941.000	77.032	1015.734	0.608
(0001)-S					
Vacuum - 0 K	-26632.000	-26484.070	147.930	1040.846	1.139
Vacuum - 300 K	-26566.000	-26431.000	135.000	1015.734	1.065
Water - 300 K	-27018.032	-26917.000	101.032	1015.734	0.797
(1010)					
Vacuum - 0 K	-26632.000	-26564.490	67.510	943.884	0.573
Vacuum - 300 K	-26566.000	-26502.000	64.000	962.003	0.533
Water - 300 K	-26970.152	-26920.000	50.152	962.003	0.418
(1120)					
Vacuum - 0 K	-26632.000	-26564.340	67.660	1021.779	0.530
Vacuum - 300 K	-26566.000	-26502.000	64.000	1041.399	0.492
Water - 300 K	-26970.152	-27001.000	46.062	1041.399	0.354

Appendix D

String-like Cooperative Motion in Homogeneous Melting

D.1 Abstract

Despite the fundamental nature and practical importance of melting, there is still no generally accepted theory of this ubiquitous phenomenon. Even the earliest simulations of melting of hard discs by Alder and Wainwright indicated the active role of collective atomic motion in melting and here we utilize molecular dynamics simulation to determine whether these correlated motions are similar to those found in recent studies of glass-forming (GF) liquids and other condensed, strongly interacting, particle systems. We indeed find string-like collective atomic motion in our simulations of "superheated" Ni crystals, but other observations indicate significant differences from GF liquids. For example, we observe neither stretched exponential structural relaxation, nor any decoupling phenomenon, while we do find a Boson peak, findings that have strong implications for understanding the physical origin of these universal properties of GF liquids. Our simulations also provide a novel view of "homogeneous" melting in which a small concentration of interstitial defects exerts a powerful effect on the crystal stability through their initiation and propagation of collective atomic motion. These relatively rare point defects are found to propagate down the strings like solitons, driving the collective motion. Crystal integrity remains preserved when the permutational atomic motions take the form of ring-like atomic exchanges, but a topological transition occurs at higher temperatures where the rings open to form linear chains similar in geometrical form and length distribution to the strings of GF liquids. The local symmetry breaking effect of the open strings apparently destabilizes the local lattice

A modified version of this chapter has been published as **H. Zhang, M. Khalkhali, Q. Liu, and J. F. Douglas**, "**String-like Cooperative Motion in Homogeneous Melting**", *J. Chem. Phys.*, 138, 12A538 (2013).

structure and precipitates crystal melting. The crystal defects are thus not static entities under dynamic conditions, such as elevated temperatures or material loading, but rather are active agents exhibiting a rich non-linear dynamics that is not addressed in conventional "static" defect melting models.

D.2 Introduction

The theory of melting has developed rather slowly and there is still no fundamental theory of this ubiquitous phenomenon. Melting has been conceived of in terms of the proliferation of vacancies [153], interstitials [154–156] and dislocations [157–161] upon heating where these "excitations" are argued to progressively decrease the shear modulus of the crystal until there is a complete loss of rigidity, resulting in the melted fluid state. Chui [162] has emphasized the importance of the self-organization of dislocations to form low angle grain boundaries (GBs), an effect that makes the melting transition first order [162, 163]. Many other authors have emphasized the propensity for lattice defect structures to self-organize into more extended defect structures [162–168]. There is also the Lindemann approach to melting, [169–174] which is based on a consideration of the global instability of the crystal lattice. In this perspective, melting is associated with a dynamical instability defined by the thermodynamics of the crystal. In particular, melting is then characterized by a condition at which the mean square atomic displacements become sufficiently large in comparison to the mean interatomic lattice spacing. Basically, this condition defines the point at which the lattice globally loses its structural integrity. Finally, we mention approaches based on thermodynamic instability criteria that the entropy of the crystal exceeds the fluid entropy [175, 176] or the vanishing of the crystal shear modulus [177, 178].

All these models consider melting in terms of time averaged equilibrium properties and focus on the derivation of the conditions under which melting occurs, and on the thermodynamic nature of the melting transition [179]. These approaches entirely neglect local dynamical phenomena involved in the progressive change of state of the material from a locally ordered to a disordered state or the reverse of this process, "freezing". Measurements of freezing provide ample evidence of large scale fluctuations in dynamic light scattering measurements [180], an effect attributed to some kind of large scale collective atomic motion at the crystallization front [181]. In a previous paper [182], we investigated both heterogeneous melting and freezing in Ni nanoparticles (NPs) and found that the collective atomic motion

took exactly the same form as strongly interacting disordered particle systems such as GF liquids. In NP melting, the collective motion and associated crystal disordering initiated from the NP surface, while in NP freezing the ordering process initiated instead from the interface of an ordered region ("seed") within the NP. In both NP melting and freezing, however, the transition between the solid and liquid states took the form of a propagating wavefront in which string-like collective atomic motion occurred in the interfacial region of the propagating front, evidencing the highly collective nature of the non-equilibrium ordering and disordering processes in these NPs [182]. Curiously, the length distribution of the string-like collective motions, localized within the interfacial regions of these propagating fronts, has always been found to be nearly exponential in the number of particles (atoms) involved. This property is also characteristic of equilibrium GF liquids [183–185], and the interfacial dynamics of GBs [186] and NPs at equilibrium [142], suggesting that a local equilibrium approximately prevails at the propagating ordering and disordering interfaces.

While string-like collective motion evidently plays an important role in the dynamics of ordering and disordering processes, the physical significance of this collective dynamics is not yet entirely clear. In GF liquids, the growth of the average extent of this collective motion (average number of particles moving collectively) has been directly related to the growth of the activation energy for structural relaxation [187], providing significant insight into the astronomical growth of relaxation times associated with cooling GF liquids; presumably, this collective particle motion will have a similar significance for understanding aspects of the kinetics of melting and freezing. It seems likely that a better understanding of this "dynamic heterogeneity" will also provide insights into how collective particle motion influences crystal morphology [188, 189] and the propensity for crystal nucleation [190, 191]. Recent studies have emphasized that the dynamic heterogeneity of GF liquids is prevalent in the freezing of simple fluids, even hard sphere liquids, making the nucleation process more complicated than the simple model assumed by classical nucleation theory [192–194]. A predictive model of how the dynamic heterogeneity of glass-formation affects critical nucleus formation has not yet emerged, however. Further studies of the coupling of dynamic heterogeneity to both crystallization and melting are clearly required before such advances can be made on a systematic basis. In the present work, we seek a better understanding of the nature of the collective motion in the relatively "simple" process of homogeneous melting. Of course, melting in most materials is initiated by a heterogeneous nucleation process initiated from the free surface of the crystalline material [195–199], as in our former NP

study [182], or instead is initiated from GBs or other defects within the crystal [183, 184]. However, if these nucleation sources for melting are suppressed by modifying the crystal interface appropriately, and also by reducing defects within the crystal, then it is possible to "superheat" the crystal to well above its "equilibrium melting temperature", T_m^E. The present work considers the nature of this "homogeneous" melting process for crystalline Ni based on the same interatomic potential [200] as used before for polycrystalline Ni and Ni NPs, a choice that facilitates comparisons between these materials. We note that our homogeneous melting temperature T_m^E is not the liquid-solid coexistence temperature at zero pressure. Rather, it is the more practically defined temperature at which actual melting in our simulations occurs as a result of heating the crystal where interfacial effects on melting are suppressed through the use of periodic boundary conditions.

In some ways, superheating is just an inversion of the supercooling process found in GF liquids so we may expect some sort of collective atomic motion or some form of "dynamic heterogeneity" to arise in superheated crystals as well. Qualitative evidence for such heterogeneity has been apparent since the earliest simulations of melting in hard discs by Alder et al. [201, 202] where large-scale cooperative particle motion was found to be a conspicuous feature of the melting process. This type of permutational particle motion was also noticed long ago in the simulated melting of one-component plasmas [203] and measurements on granular fluid [204], colloidal fluid [205, 206] and dusty plasma [207–209] melting in near two dimensions. Quite recently there have been molecular dynamics studies of collective atomic motion associated with superheating of three dimensional crystals of Lennard-Jones particles [11, 210] where many aspects of dynamics heterogeneity in GF liquids are exhibited such as a strong growth of the non-Gaussian parameter, clusters of mobile particles, cooperative particle motion, etc. (These quantities are defined and examined below). Perhaps the most extraordinary aspect of these simulations is the significant rate of diffusion occurring in crystalline materials well below T_m^h, a temperature about 20% larger than T_m^E.

The appearance of highly correlated particle motion in association with bulk melting appears to be consistent with the entropy catastrophe model of melting introduced by Fecht and Johnson [175] where bulk melting was identified with the condition that the crystal entropy becomes equal to that of the equilibrium fluid, an instability condition dual to that of the liquid to crystallization when the liquid configurational entropy approaches that of the crystal upon sufficient supercooling [175]. Recent molecular dynamics simulations of

bulk melting in Ni and other metals (Al, Au, Pt) [176] have provided evidence supporting this instability explanation of bulk melting and Gallington and Bongiorno [176] further suggested that the rapid increase of the configurational entropy of the crystal to its liquid value upon heating is directly associated with cyclic atomic permutational atomic motion, providing a potential direct link between the thermodynamic instability based on entropy and the collective particle motion driving the melting process. However, accurate calculations of the configurational entropy of both the heated crystal and the Ni melt are required to better understand how the geometry of these collective atomic motions relate to the configurational entropy, molecular transport properties in the crystal, and the ultimate crystal stability. The present paper takes a first step in this direction by focusing on quantifying the nature (geometric size, fractal geometry, topological form) of the collective atomic motions in crystalline Ni near bulk melting.

What does it really mean for a crystal to be "dynamically heterogeneous" and how does this heterogeneity relate to the melting process itself. Bai and Li [210] suggest that the proliferation of permutational motion of the atoms in heated crystals actually drives the melting process under homogeneous melting conditions. In particular, they note the prevalence of two distinct types of string-like collective motion in melting - open and closed strings having the form of linear and ring "polymeric" structures. The atoms in the linear strings are characterized by a higher potential energy and significantly larger average vibrational amplitudes than surrounding particles and they provided qualitative evidence that these dynamical structures, rather than strings having a ring-like form, are nuclei for the liquid phase [210]. We look into this fascinating suggestion below.

The various proposed models of melting and simulations just described lead us to expect some kind of thermally activated defects to form during the course of melting and we may generally expect their self-organization into coherent structures that drive the bulk melting transition. While there is much evidence supporting this scenario, there has been very little quantification of these dynamic structures. Are these excitations related to some type of GB phenomenon [211]? What types of defects are formed in superheated crystals and what role do they play in the initiation and propagation of the evident collective motion? Can one effectively quantify this collective motion? What effect does this collective motion have on mass transport and the nature of structural relaxation in the superheated crystal? In particular, do we observe the characteristic "decoupling" phenomenon between mass and

momentum diffusion processes, the Boson peak and stretched exponential relaxation phenomena that are universally observed in GF liquids?

We can anticipate that this investigation of homogeneous melting to be revealing about the nature of GF liquids because these systems lack a basic feature of supercooled liquids, the packing of atoms, polymer chain segments or colloidal suspension particles into structures that are locally well-ordered and the local packing can be denser than any macroscopic crystal, e.g., icosahedral ordering for hard spheres [212–216]. Due to packing frustration, these clusters of excessively immobile particles organize into dynamic polymer structures that coexist with the strings of particles exhibiting cooperative motion, playing a role analogous to grain boundaries in polycrystalline materials. This type of clustering of molecules into relatively rigid, but dynamic, polymeric structures presumably cannot exist in crystals so that studying superheating affords an opportunity of investigating how collective atomic motion affects material dynamics (There are exceptions to this situation in certain quasi-crystal materials [217], however, and we hope to study melting in this type of crystal in the future to contrast with the present simulations on Ni.) Our simulations inform rather clearly on the separate effects created by the mobile and immobile particles in GF liquids. The decoupling phenomenon and the stretched exponential relaxation phenomena are simply not observable in the superheated crystal, and yet these materials exhibit highly collective motion involving cooperatively rearranging atoms and a Boson peak, much like any GF liquid. Evidently, the decoupling and stretched exponential relaxation phenomena of GF liquids can be attributed to the immobile particle clusters rather than correlated particle motion.

D.3 Simulation Details

Molecular dynamics simulations were performed to characterize melting of our bulk Ni material based on the same potentials that we have utilized before for simulating Ni GBs [186] and the interfacial dynamics and melting/freezing of Ni NPs [142, 182]. In particular, atomic interactions for Ni were described using the Voter-Chen [200] form of an Embedded Atom Method (EAM) [218] potential. A perfect crystal of face-centered cubic lattice was initiated first. The simulation cell consists of 13,500 atoms with a dimension of about 5 nm x 5 nm x 5 nm, oriented with crystallographic directions [100], [010] and [001] in the X-, Y- and Z-directions. In all simulations, periodic boundary conditions were applied in all direc-

tions and the isobaric-isothermal ensemble (NPT) was employed where the zero pressure and simulation box size were controlled by the Parrinello-Rahman method [68]; constant temperature (T) was maintained by the Nose-Hoover method [65, 66]. Uncertainties below are based upon a 95 % confidence interval. The MD simulations utilize LAMMPS [219], which was developed at the Sandia National Laboratories.

Bai and Li [210] found that the heating rate has a large effect on the bulk melting temperature T_m^h due to the fact that typical heat rate (1011 to 1013) K / s in molecular dynamics simulations does not allow the system to fully relax to reach equilibrium and will suppress some important kinetic processes in homogeneous melting. On the other hand, isothermal heating below T_m^h for an extended period of time would ensure the system to reach equilibrium, allowing us to probe kinetic processes that cannot be observed under continuous heating conditions. In this study, both continuous and isothermal heating methods are considered. Continuous heating was employed to determine T_m^h, where temperature was continuously changed from 300 K to 2000 K with a heating rate of $2 \times 10^1 1\ K/s$. The "equilibrium melting temperature" T_m^E of 1624 K was determined previously for this potential using solid-liquid co-existence technique [15]. In order to obtain a superheated crystal, isothermal heating simulations were also performed at T = 1800 K, 1840 K, 1880 K, 1900 K, 1920 K, 1940 K, 1950 K, 1960 K, 2000 K and 2100 K. At each T, the simulation was conducted for at least 4 ns and up to 6 ns. Our simulation results indicated that the crystal structure retained its integrity during the entire isothermal heating simulation for T values below 1950 K, while at T = 1960 K, the system potential energy increases abruptly after 0.6 ns, suggesting a solid to liquid transformation occurs at this T (i.e., T_m^h =1960 K). Figure D.1 shows a typical atomic configuration of the simulation cell at T = 1800 K, where the atoms are colored by their potential energy (see color map). Energy minimization using the conjugate gradient method [220] was also performed in quenching the equilibrium atomic configuration to obtain the information of stable defects in the simulation cell.

D.4 Results and Discussion

D.4.1 Bulk Melting Temperature

As in our previous papers [142], we first establish the value of T_m^h by calculating the potential energy per atom through continuous heating, and we then determine T_m^h as the T

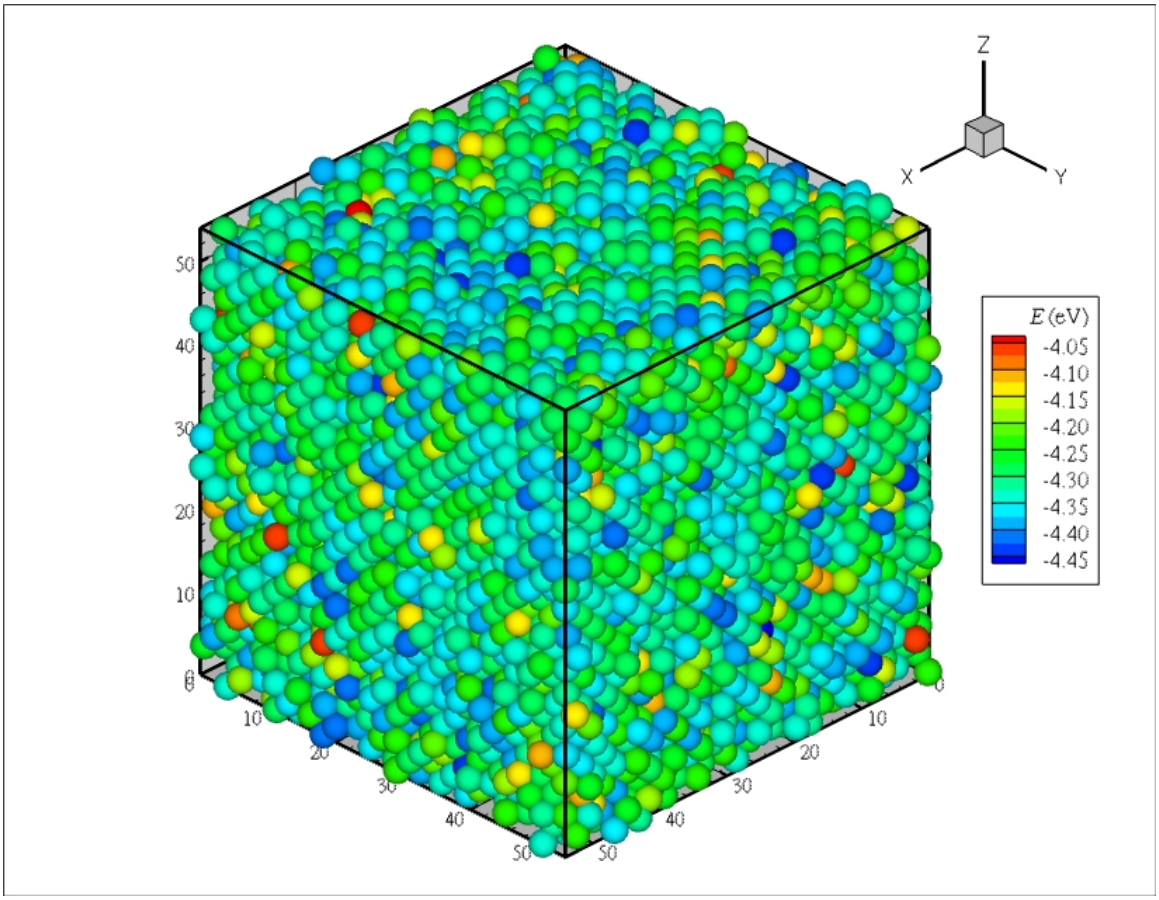

Figure D.1: Equilibrium atomic configuration of simulation cell at T = 1800 K. Atoms are colored by potential energy.

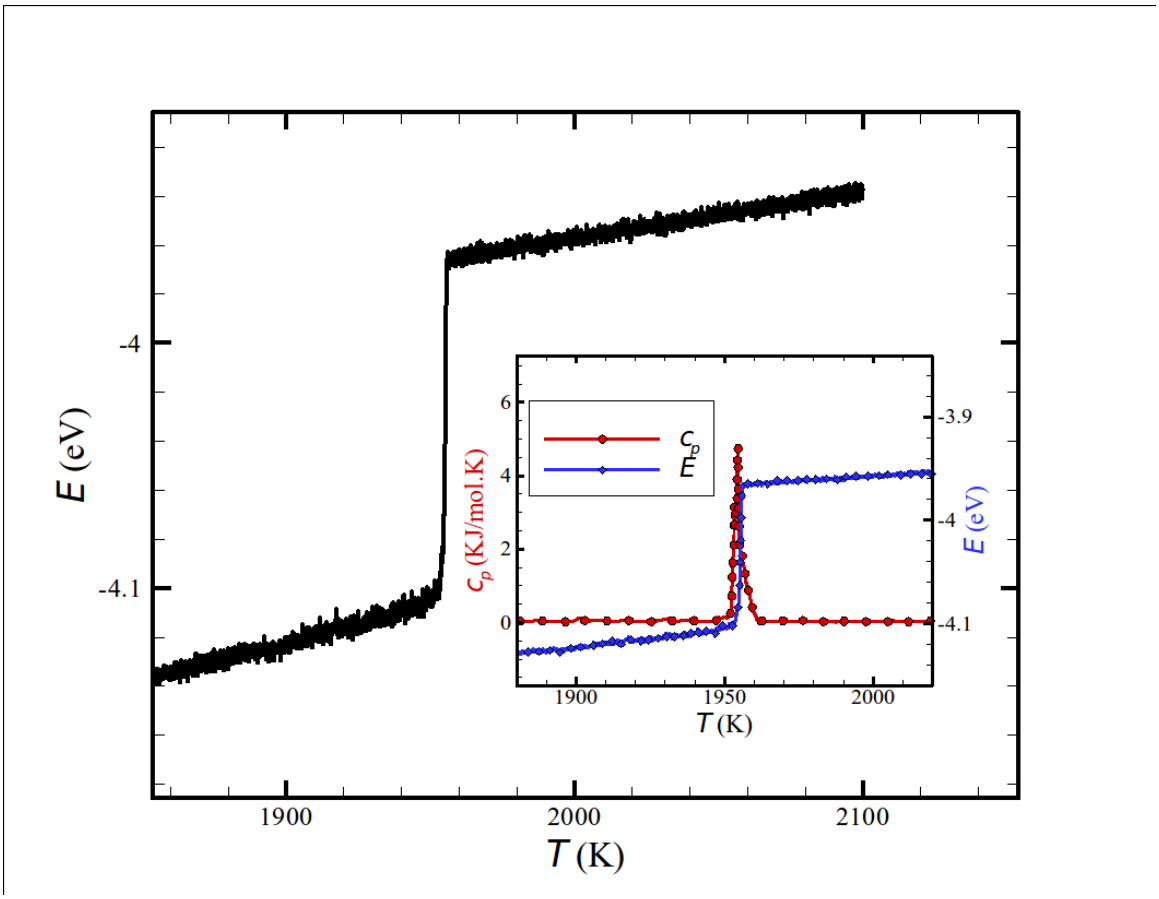

Figure D.2: Potential energy per atom versus temperature for bulk Ni. The heating rate in current simulations are $2 \times 10^1 1\ K/s$ where the potential energy in inset is averaged over every 5 ps.

at which there is an abrupt change in potential energy, reflecting the phase change of the material. We show the result of such a standard computation in Fig. D.2, where we see that the transition is rather sharp, appropriate for a phase transition of first order. The inset to this figure shows that this change in E gives rise to a very sharp disordering transition, as observed in measurements on the crystal-glass transition in both colloidal and molecular materials [221, 222]. Sharp transitions from crystal to an amorphous state have also been observed in metallic crystalline materials subjected to a critical amount of irradiation [223, 224].

D.4.2 Van Hove Correlation Function

We first characterize basic aspects of rate of molecular diffusion and the extent of dynamic heterogeneity in the superheated crystal. Both of these quantities can be quantified to a

degree with the self-part of the van Hove correlation function $G_s(r, \Delta t)$, which describes the probability distribution of the position r of an atom after a time t. Mathematically, the van Hove correlation function can be written as:

$$G_s(r, \Delta t) = \frac{1}{N} \langle \sum_{i=1}^{N} \delta(\mathbf{r}_i(\Delta t) - \mathbf{r}_i(0) - r) \rangle \tag{D.1}$$

When Δt is small, $G_s(r, \Delta t)$ is Gaussian, meaning the atom undergoes harmonically localized motion. As the time interval Δt increases, generally we expect to observe non-Gaussian behavior. By looking at $G_s(r, \Delta t)$ at different time intervals, we can trace the path that the atom takes as it moves through the system and quantify these changes in terms of atomic displacement. The non-Gaussian parameter α_2 is one of the basic measures of dynamic heterogeneity,

$$\alpha_2(\Delta t) = \frac{3 < r_4(\Delta t) >}{5 < r_2(\Delta t) >^2} - 1 \tag{D.2}$$

where $r(t)$ is the displacement of an atom after a time interval, Δt.

Figure D.3 inset shows the self-part of the van Hove correlation function on a reduced radial coordinates (rescaled by r_0, which is the interatomic distance at the T of interest) for the simulation cell at T = 1800 K, 1880 K and 2100 K with Δt = 150 ps, 150 ps, and 5 ps, respectively. The multiple peaks centering at successive nearest-neighbor distances in $G_s(r)$ imply a "hopping" motion to preferentially quantized distances, a phenomenon emphasized before by Bai and Li [210].

These hopping peaks are pronounced and such peaks are also characteristic for two-dimensional fluids exhibiting hexatic ordering, a condition that is likewise an intermediate state between a crystal and fully disordered liquid [225] (This phenomenon is further illustrated as a function of time in Appendix E). A large non-Gaussian parameter has been noted before in the phenomenology of diffusion in fluids approaching their melting transitions in systems in two and three dimensions. Below we define "mobile" particles as those exceeding the van Hove function minimum position after a characteristic time t^* at which

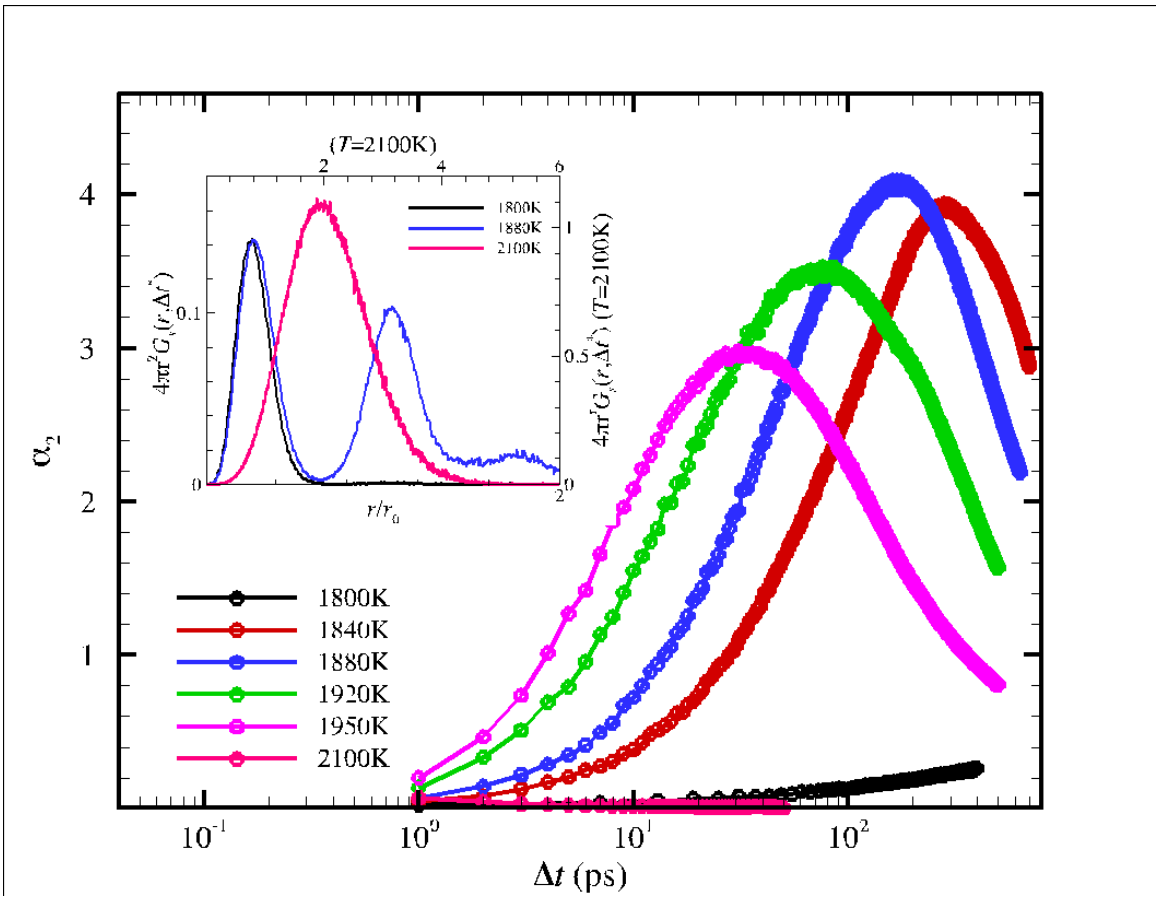

Figure D.3: The non-Gaussian parameter α_2 as a function of time interval Δt for a range of T. Temperatures are shown in the bottom left of figure. The inset shows the van Hove function $G_s(r, \Delta t)$ describing the probability for particle displacement from a particle position at the origin ($r = 0$) at Δt = 150 ps for T = 1800 K and T = 1880 K while at Δt = 5 ps for T = 2100 K. As T_m^h is approached, $G_s(r, \Delta t)$ develops multiple peaks above T = 1800 K, reflecting a "hopping" motion of the atoms (see text). At T = 1800 K, α_2 is rather small, indicating a nearly harmonic localization of the Ni atoms in the crystal. The minimum in the van Hove function occurs near 0.6 (See Appendix E for further details and illustration).

α_2 exhibits a maximum.

D.4.3 Cooperative Atomic Motion in Bulk Melting

Cooperative particle dynamics is one of the most characteristic features of the dynamics of GF fluids. Both atomistic simulations [183–185] and experiments [226] on glass-forming colloidal [227] and granular fluids [226] exhibit string-like collective motion and MD simulations [15, 186, 228] have recently shown that this type of motion also occurs in the dynamics of GB [186] and the interfacial [142] and melting dynamics of NPs [182]. We next apply methods originally developed to identify this type of correlated motion in GF liquids [183] to our simulations of the dynamics bulk melting. First, we review the definition of collective atomic displacement motion [183].

As a first step in identifying collective particle motion, we must identify the "mobile" atoms in our system. In GF liquids, the "mobile" atoms (atoms with enhanced mobility relative to Brownian motion) are defined by comparing the self-part of the van Hove correlation function $G_s(r)$, describing the probability distribution that a particle initially at the origin makes a displacement to the spatial distance $r(t)$ after a time t, for the strongly interacting particle fluid to an ideal uncorrelated liquid exhibiting Brownian motion where $G_s(r)$ reduces to a simple Gaussian function by the central limit theorem [The diffusion coefficient D is defined to be the same in the interacting and non-interacting $G_s(r)$] [183].

Since "mobile" atoms are essentially those particles moving a distance $r(t)$ larger than the typical amplitude of an atomic vibration after a decorrelation time Δt, but smaller than the second nearest-neighbor atomic distance, we mathematically identify these mobile particles, as in previous studies of GB dynamics and the interfacial dynamics of NP [142, 186], by a threshold atomic displacement condition, $0.6r_0 < |\mathbf{r}_i(\Delta t) - \mathbf{r}_i(0)| < 1.2r_0$, involving the average bulk crystal interatomic spacing, r_0. (See Fig. E.1 in Appendix E for motivation of the minimal displacement cut-off.) We find the mobile particles cluster in space and their size distribution is highly reminiscent of percolation clusters (which have a fractal dimension near 2.5 in three dimensions and a power-law size distribution with an exponent [229] near -2; we summarize these results in Appendix E.) The fraction of mobile particles at the characteristic time t^* seems to be insensitive to the temperature in the range of 1840 K and

1950 K (about 5 % to 6 % of total atoms in the system.) A previous study has identified the mobile atom clusters in incipiently melting bulk Cu crystals [230] based on a EAM potential model, where they find similar results and where they emphasize the similarity of this size distribution of mobile particles to supercooled liquids [10, 17, 231]. Given this former characterization of mobile particle clusters in incipiently melting crystals, we do not further emphasize the geometrical characteristics of the mobile particles in the present work.

The identification of correlated atomic motion requires a consideration of the relative displacement of particles. Collective atom motion means that the spatial relation between the atoms is preserved to some degree as the atoms move. Specifically, mobile atoms i and j are considered to be within a collective atom displacement string if they remain in each other's neighborhood, and we specify this proximity relationship by, $min[|\mathbf{r}_i(\Delta t) - \mathbf{r}_i(0)|, |\mathbf{r}_i(0) - \mathbf{r}_i(\Delta t)| < 0.43 r_0$, as in past studies of GF liquids, the dynamics of GB, [183, 228] and the interfacial dynamics of Ni NPs [142]. Application of this criterion reveals that the collective particle motion in the superheated Ni crystal takes the form of "strings" (see Figure D.3 for illustration). The nature of this motion is remarkably similar to previous simulations on the atomic dynamics of GF liquids [183] and the atomic dynamics of GBs in polycrystalline materials [186, 232].

The mean "string length" is defined as the average,

$$\overline{n}(\Delta t) = \sum_{n=2}^{\infty} n P(n, \Delta t), \tag{D.3}$$

which we advocate as a measure of the scale of cooperative particle motion in strongly interacting liquids rather generally. $P(n, \Delta t)$ is the probability of finding a string of length n in time interval Δt. String properties are defined at a characteristic decorrelation time $\Delta t = t^*$ at which the mean string length in Eq. D.1 has a maximum [15, 183–185]. Previous work [15, 185] has established that the average string length in GF liquids grows upon cooling, along with the effective activation energy for structural relaxation. This finding accords with the Adams and Gibbs (AG) theory of relaxation in GF liquids [187], where the strings are identified [183] with the vaguely defined "cooperatively rearranging regions" of the AG theory. Strings are thus of practical interest since they are correlated with the rela-

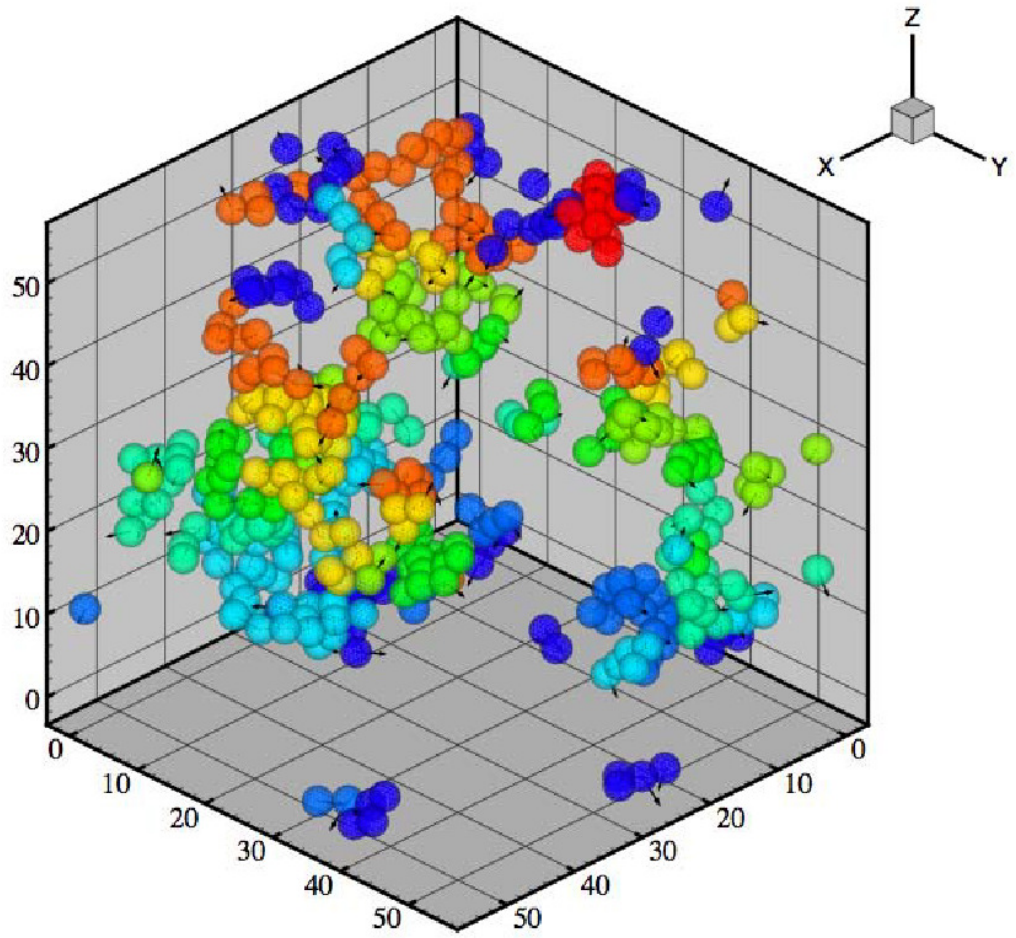

Figure D.4: String-like collective atomic motion in the superheated bulk Ni crystal at T = 1880 K. The lines denote Ni atoms that belong to the same collective atom movement and the colors are introduced to discriminate between different string events.

tive strength of the T-dependence of transport properties (see below), perhaps the defining property of GF fluids.

String-like cooperative atomic motion is prevalent in all GF liquids examined to date (including water, polymer fluids, metallic glass-forming liquids, concentrated colloidal suspensions and even strongly driven granular fluids [183, 185, 227, 232, 233].) It is apparently a *universal property* of the dynamics of strongly interacting fluids where a strong reduction in the particle mobility and an enormous change in the rate of structural relaxation are found in association with the growth of string-like correlated motion upon approaching the glass transition. We think it is significant that these *same* structures arise in superheated crystals. To further establish the nature of the strings, we determine some of their other properties.

We next examine the nature of the atomic motion occurring in the superheated crystal to determine if it follows this general pattern of "frustrated fluid" dynamics seen in supercooled liquids. The colored atoms in Fig. D.4 represent the initial atomic positions ($t = 0$) and the displacement arrows point to their positions at a later time Δt. This string-like atomic motion occurs "randomly" , i.e., without much obvious correlation to the crystal lattice structure and these motions superficially resemble the collective motion found previously in supercooled liquids [142]. We next consider the size distribution of these strings of collective motion and the T dependence of their average size, $L \equiv < n >$.

Atomistic simulations of glass-forming liquids [183] indicate that the distribution of string lengths $P(n)$ is generally an exponential function of n,

$$P(n) \sim (-n/ < n >), \tag{D.4}$$

to an excellent approximation. Figure D.5 shows the distribution of string lengths at $\Delta t = t^*$, where the mean string length $n(\Delta t)$ exhibits a maximum [The time dependence of $\overline{n}(\Delta t)$ is not shown (See refs. [15, 183, 184])].

The distribution of the string length n in the heated bulk Ni crystal is the *same* as found in GF liquids [234], the atomic dynamics of GB in simulated polycrystalline Ni [186]

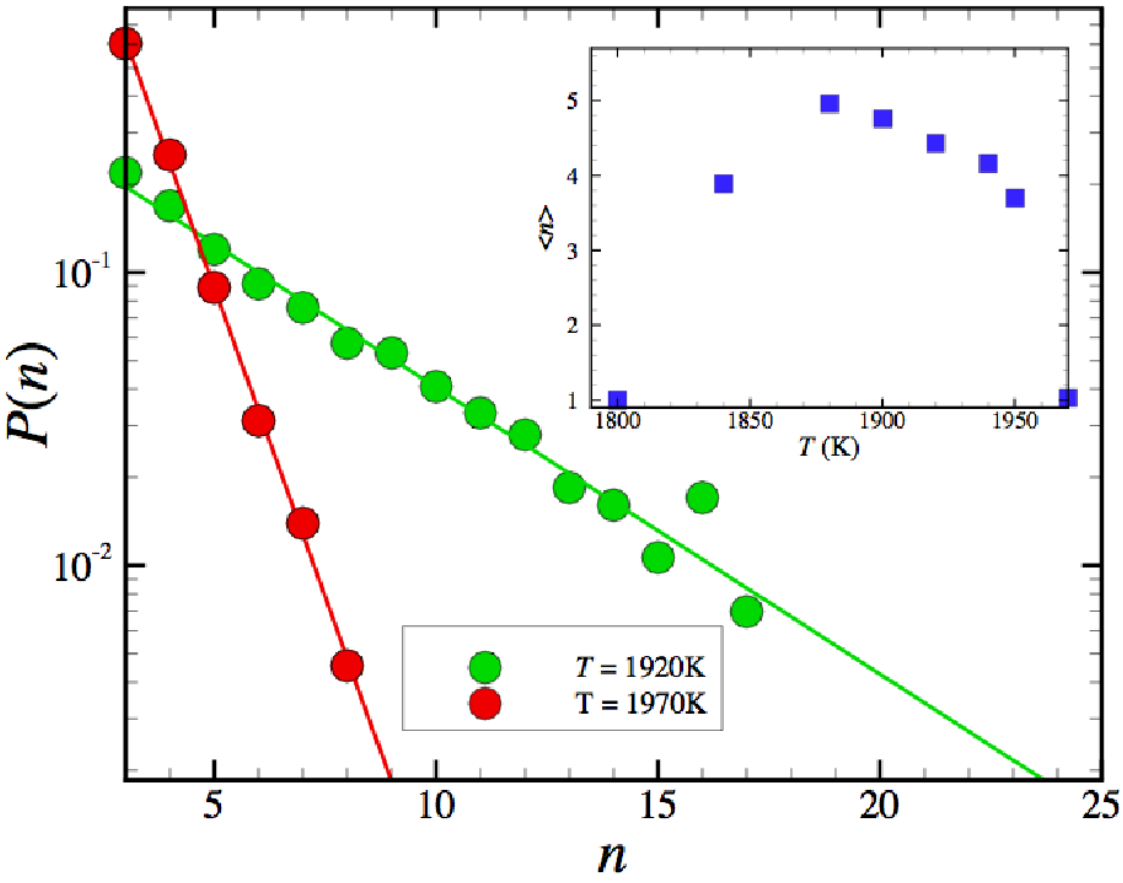

Figure D.5: The string size distribution at T = 1920 K and T = 1970 K. Inset shows the T dependence of the average string length $< n >$.

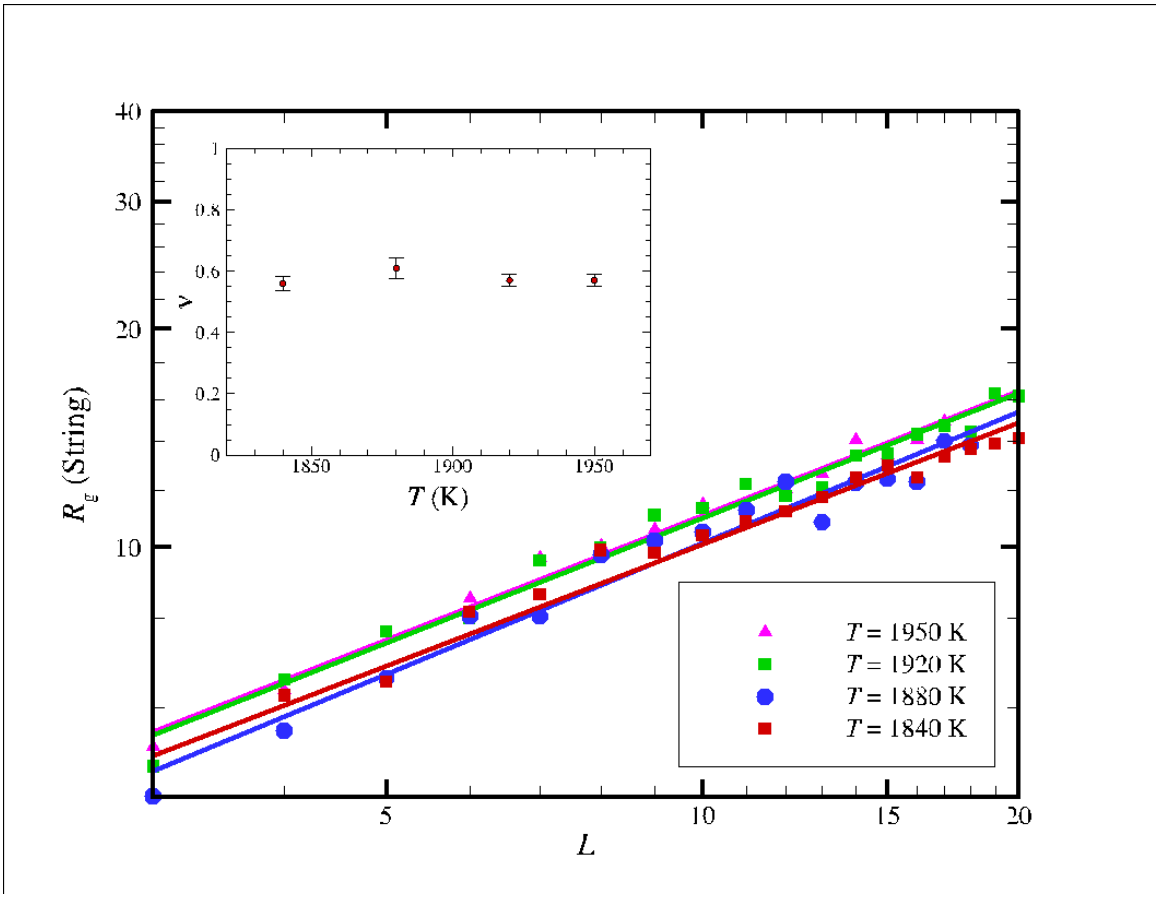

Figure D.6: Scaling of string radius of gyration R_g with its length L as $R_g \sim L^{\nu}$, where the inset shows $\nu = 1/d_f$ as a function of T. The exponent ν is about 0.6, corresponding to a fractal dimension $d_f \approx 5/3$ of self-avoiding walks [10].

and colloidal measurements [235, 236] of polycrystalline materials and interfacial dynamics of Ni NPs [142]. Figure D.6 indicates the radius of gyration R_g of the strings versus their mass and the scaling exponent ν describing how their average size (R_g) increases with the length is near $\nu \approx 0.6$, a value characteristic of self-avoiding walks [237]. This type of scaling behavior has also been observed for strings of monomers in a coarse-grained GF polymer melt [231].

We have also examined the possibility of a topological transition between strings having open linear chain and closed polymer ring topologies since Bai and Li have suggested that open strings can be identified with the liquid "nuclei" that initiate the melting process. Figure D.7 shows the variation of the number of linear chains of collective atomic motion in comparison to the number of ring atomic permutational atomic exchange motions. We indeed find that linear chains proliferate near T_m^h while the ring atom exchanges exhibit

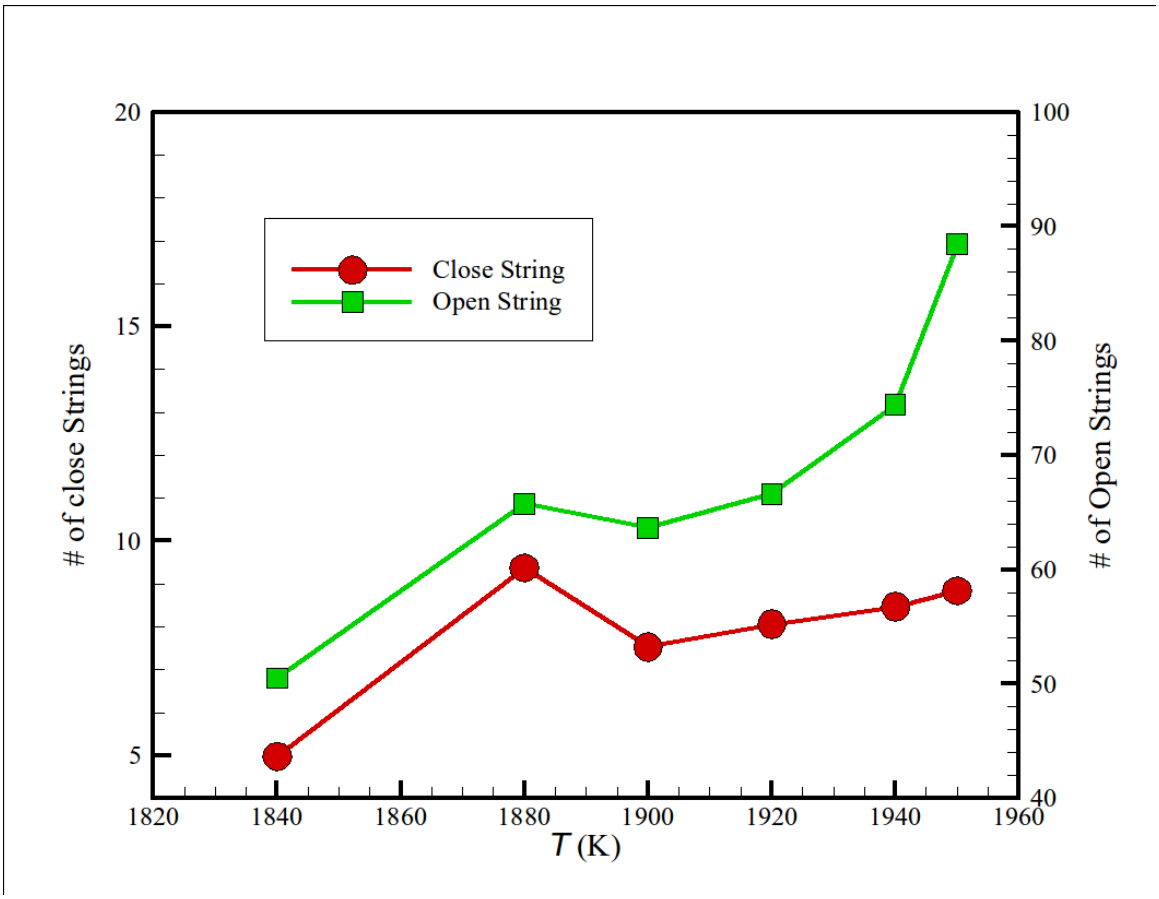

Figure D.7: The number of open strings and close strings as a function of T.

a maximum at a lower T that is close to the value at which the average string length L exhibits a maximum (See Fig. D.5). The proliferation of the open strings is not as singular as we expected, however. This may represent finite size effects near T_m^h and future work should consider a systematic finite size analysis to refine the current estimates.

While the full ramifications of this topological transition in the form of collective motion for homogeneous melting are not yet clear, the open strings clearly play a significant role in the homogeneous melting process, as suggested before Bai and Li. Our analysis of the open string/ring populations as a function of T serves to quantify the nature of this topological transition in the nature of the collective motion upon approaching the homogeneous melting transition. There have been earlier observations of this string-like motion in association with crystal melting and we next discuss some of these observations briefly.

The appearance of string-like collective motion in connection with melting has been long

known from simulations of hard disc melting by Alder and Wainwright [201, 202] and the melting of two-dimensional lattice of Lennard-Jones particles [206]. This type of particle permutation motion has also been observed in particle tracking measurements of melting in quasi-two dimensional lattices of colloidal particles [205, 238–240], quasi-two dimensional driven granular fluids [204] and simulations of the melting of quasi-two dimensional plasma crystals [165, 203, 207]. It is thus not surprising that we see prevalent string-like collective motion in our simulations of melting in Ni crystals. What is somewhat surprising is that the size distribution and geometrical form of the excitations is so similar in geometrical form to GF liquids. We next turn to some further comparisons of the dynamics of superheated crystals to GF liquids.

D.4.4 Impact of Dynamic Heterogeneity on the Dynamical Properties of Bulk Ni

There has been much speculation about how dynamic heterogeneity, as measured by α_2, and collective particle motion relate to some of the essential characteristics of GF liquids such as the breakdown of the Stokes-Einstein relation between the translational diffusion coefficient D and the structural relaxation time from the intermediate scattering function (or from dielectric or stress relaxation measurements) and the general observation of structural relaxation having the form of a stretched exponential rather than a simple exponential decay. Douglas and coworkers [233, 241–243] have made two predictions with regard to these basic phenomena of GF liquids that are germane to the current discussion of bulk melting. First, Douglas and Leporini [241, 242] have argued based on classical hydrodynamics that clustering in the form of immobile particle clusters alters mass and momentum diffusion differently and that this effect simply explains the fundamental origin of the breakdown of the Stokes-Einstein relation. Stukalin et al. [243] found stretched exponential stress relaxation with a non-trivial "stretching" exponent β near 1/3 naturally arises from persistent self-assembled polymer structures and Douglas et al. [233] further argued that the immobile particle clusters of GF liquids are self-assembled "equilibrium" polymers so that non-trivial β exponent calculations of Stukalin et al. should directly apply to GF liquids.

In the context of the current bulk melting simulations, these model calculations and arguments imply that no decoupling should exist in superheated crystals and, moreover, the stretching exponent β is predicted to remain near 1. These expectations follow since

most of the particles in the crystal, at least at T well below T_m^h, are in a localized crystalline state, i.e., polydisperse immobile clusters of finite extent do not exist in the superheated crystal. We next check these predictions, which if confirmed, would offer significant insights into both supercooled liquids and superheated crystals. First, we examine the nature of caging and diffusion in the superheated crystal.

Caging, particle delocalization at melting point and diffusion

In Figure D.7, we plot the mean square displacement $< r^2 >$ of Ni atoms in our bulk Ni crystal over a range of T indicated in the figure. Following Jin et al. [11], we also plot the average root-mean-square particle displacement $< \Delta r^2 >^{1/2}$ compared with its equilibrium interparticle distance r_0. The fraction of particles for which the ratio $(< r^2 >^{1/2} /r_0)$ exceeds a critical Lindemann value ($\delta \equiv 0.20$; vibrational amplitude or the first peak position in van Hove plot near melting point), then provides an estimate of the fraction of atoms f in the liquid state [244].

Starr and coworkers [245] and Leporini and coworkers [246] describe how the caging time may be determined and consequently define the "Debye-Waller factor" (DWF), $< u^2 >$, as the mean square atomic displacement $< r^2 >$ after a particular decorrelation time characterizing the crossover from ballistic to caged atom motion. The mean square atomic displacement $< r^2 >$ in Fig. D.8 exhibits a well-defined plateau at short times that is also typical of "caging" in GF liquids and $< r^2 >$ at long times is diffusive. This allows us to determine D (the proportionality constant between $< r^2 >$ and t after the caged dynamics region atomic displacement), at least for a range of T below T_m^h. The upper inset of this figure shows that D/T, scales inversely with the time constant t^* at which the strings are defined so that the characteristic time t^* is a diffusive relaxation time.

The Lindemann criterion for homogeneous melting is different phenomenogically from the well know condition for the equilibrium melting temperature where the presence of an interface is implicit in the definition. We find that the mean square amplitude of atomic displacement in the vicinity of T_m^h is nearly equal its value on the boundary of the crystal at the onset of heterogeneous melting [142]. In particular, this critical displacement value is about $< u^2 >^{1/2} /r_0 \approx 0.27$, which is about twice as large as the Lindemann ratio value for our material undergoing heterogeneous melting. Our observations are consistent with

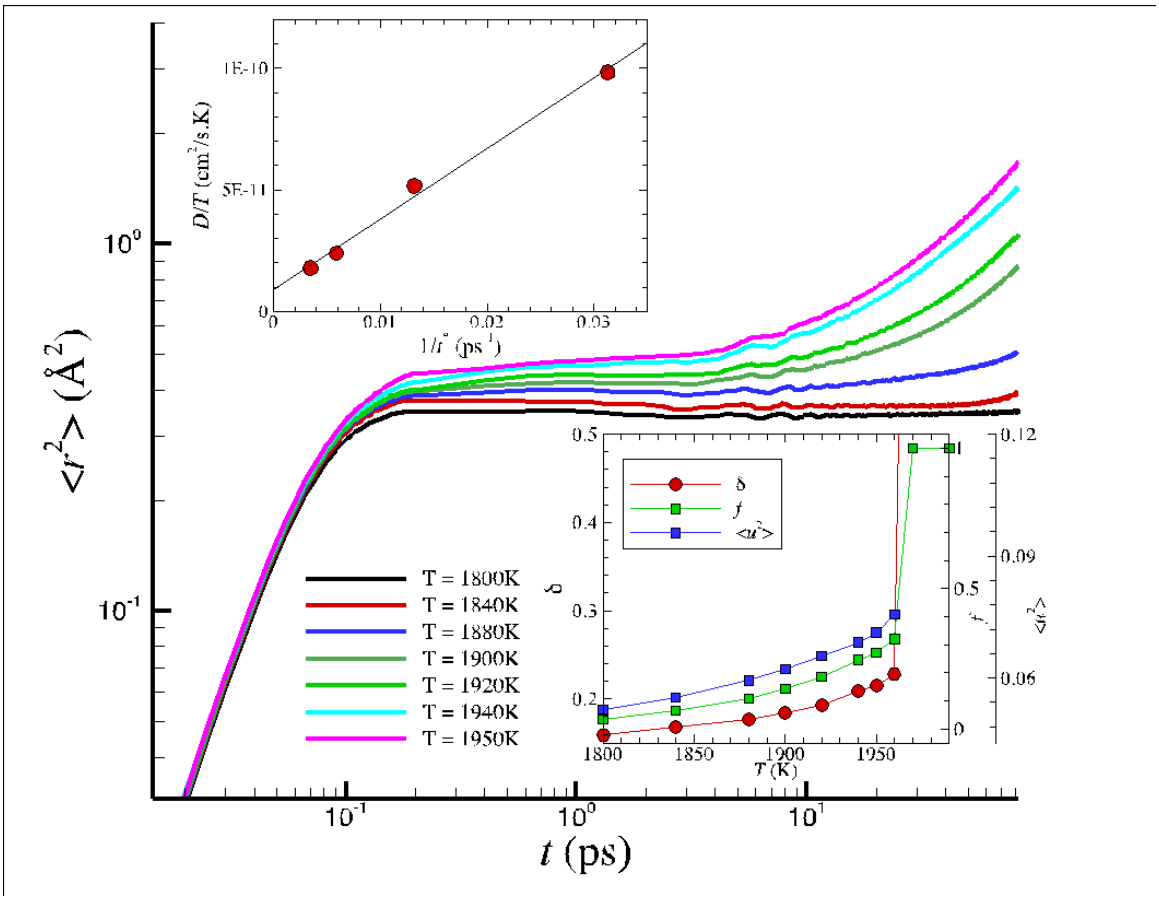

Figure D.8: Mean square displacement of bulk Ni at seven different temperatures. The bottom inset shows the temperature dependence of the Lindemann parameter, $\delta =< \Delta r^2 >^{1/2} /r_0$, describing the root mean square particle displacement relative to the average interatomic distance, the "Debye-Waller factor" (DWF), $< u^2 >$, and the fraction of "Lindemann particles" [11] as a function of T ($< \Delta r^2 >^{1/2} /r_0 > 0.2$; the magnitude 0.2 cut-off is prescribed by the peak position of the van Hove function in Figure D.8 and Fig. E.1). The top inset shows, D/T $1/t^*$, where D is the Ni atom diffusion coefficient and t^* is the time at which α_2 exhibits a maximum. This is a general result that holds as well for many GF liquids. The characteristic relaxation time t^* has the significance of a diffusive relaxation time, a quantity that in general can have a qualitatively different T dependence from the inverse structural relaxation time α_2 from the self-intermediate scattering function (See Fig. D.9).

simulations of bulk melting in crystals of LJ particles in three dimensions by Jin et al [11]. and with measurements on defect-mediated melting in bulk colloidal crystals [247]. The initiation of bulk homogeneous melting evidently requires a larger critical average displacement and this condition is more readily achieved at the interface of the crystal.

The lower inset to Fig. D.8 also shows that the fraction of mobile particles f, defined by the Lindemann particle definition above, increases in a parallel fashion to $< u^2 >$. Moreover, in the next section we find that f varies in direct proportionality to interstitial defect concentration in the crystal (each defect generating about 200 mobile particles so a small number of defects can be rather disruptive to the lattice). Below, we consider how lattice defect structures relate to these mobile particles and their active role in facilitating the collective particle motion seen in association with bulk melting.

Structural relaxation, decoupling, and the boson peak

The structural relaxation time is a basic property of a condensed material and we estimate this quantity from the self-intermediate scattering function $F_s(q,t)$ (see Fig. D.9), $F_s(q,t) =< exp\{-iq[r_i(t) - r_i(0)]\} >$, which is simply the Fourier transform of the particle displacement distribution function $G_s(r,t)$ described above. (The Fourier transform variable **q** is often termed the scattering "wave vector" .) After exhibiting a plateau associated with the particle caging phenomenon, $F_s(q,t)$ in GF liquids normally exhibits a "stretched exponential" variation,

$$F_s(q,t) \propto exp[-(t/\tau)^{\beta_s}] \;\; where \; 0 < \beta_s < 1. \tag{D.5}$$

$F_s(q,t)$ data for GBs and NPs both exhibit a normal trend for GF liquids, i.e., the "stretching exponent" β_s has a value near $\beta_s \approx 1/3$, i.e., $\beta_s = 0.34$ *and* 0.36 ± 0.02, for Ni GBs and 2 nm NPs, respectively. In stark contrast, the fitted value of β_s in our bulk Ni simulations is near 1 (i.e., β_s lies in the range 0.92 and 1.01). An exponential decay of the intermediate scattering function has also been found recently in simulations LJ particles in two dimensions by Shiba et al. [248]. It is then clear that β_s cannot be simply identified with development of collective atomic motion. We also consider the matter of

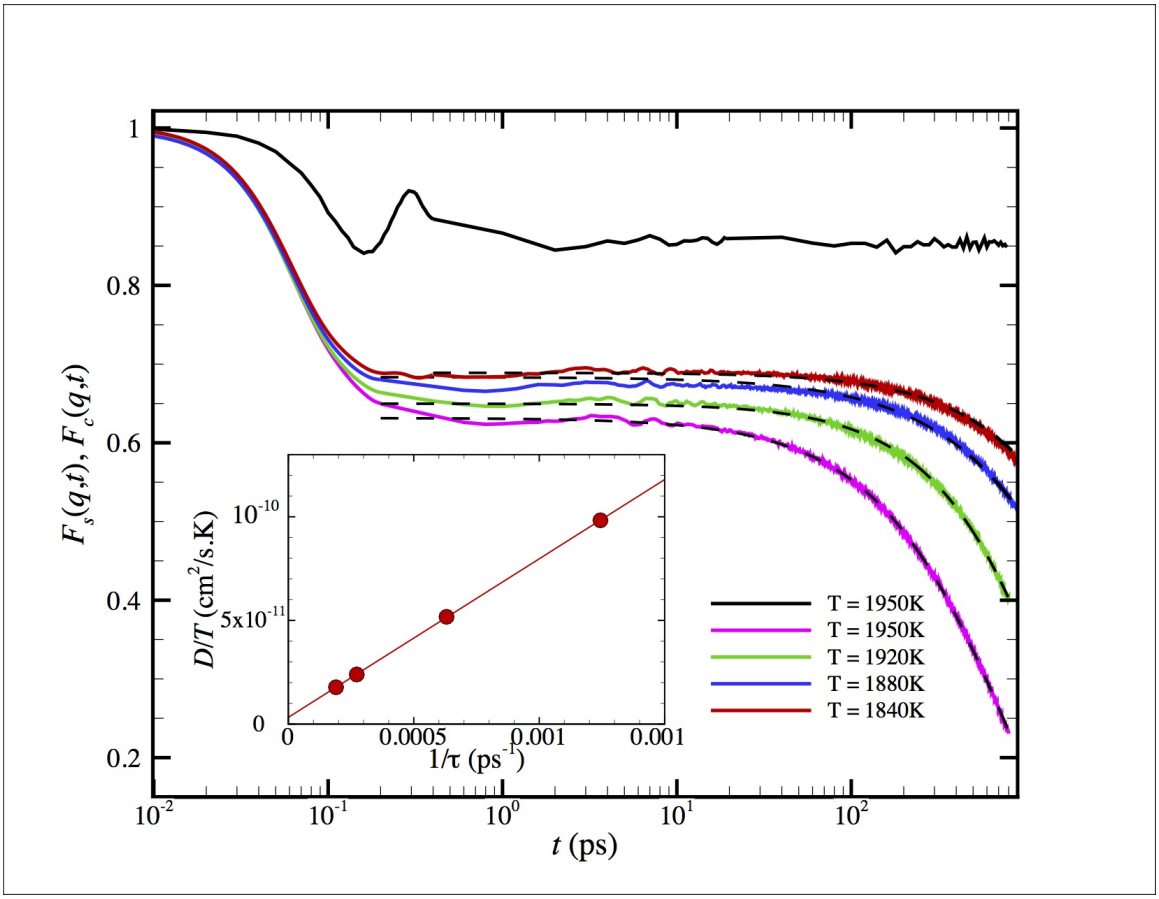

Figure D.9: The self-intermediate scattering function $F_s(q,t)$ in bulk Ni at T = 1840 K, 1880 K, 1920 K and 1950 K and the collective intermediate scattering function (the black solid curve) in bulk Ni at T = 1950 K. The dashed black curves are fits using where the apparent value of β varies between 0.92 and 1.01. Inset shows D rescaled by the temperature, D/T, as a function of the structural relaxation time, τ obtained from $F_s(q,t)$. Note that the collective intermediate scattering function $F_c(q,t)$ (solid line) does not decay to 0 in the crystal state and that this quantity exhibits collective density oscillations on a timescale on the order of a ps. We discuss this "Boson peak" feature below (see Fig. D.10).

decoupling. In the inset to Fig. D.9, we also examine the scaling relation between D/T and the structural relaxation time τ obtained from $F_s(q,t)$. We see that D/T in our superheated crystal scales inversely to τ so that the fractional power-law relation between these properties ("decoupling") often found in GF liquids [249–251] is not observed, despite the significant dynamic heterogeneity in the superheated crystal taking the form of strings.

The current simulations observations then strongly suggest that the decoupling between mass and momentum diffusion relaxation times and the stretching of structural relaxation in GF liquids both arise from the existence of polydisperse immobile particle clusters, as suggested before by Douglas and coworkers. By extension, increasing the spatial dimension in which the fluid is embedded should relieve packing frustration responsible for the immobile particle clusters so that increasing dimensionality should decrease the strength of decoupling and exponent stretching, while at the same time the collective motion would remain prevalent, approaching the nature of the superheated crystal. There are recent simulations of model GF liquids in variable spatial dimension that could be used to test these expected trends [252].

The decay of $F_s(q,t)$ reflects the facile diffusion of atoms within the superheated crystal due to collective motion, but the material is still a crystal so that its decay seems somewhat counter-intuitive. Actually, there is no real paradox and the crystalline nature of the material is apparent from the *collective intermediate scattering function* [253]. Normally, $F_s(q,t)$ and $F_c(q,t)$ are similar in GF liquids, but in a crystal, or any solid really, we expect instead that $F_c(q,t)$ should decay to a plateau after a transient inertial regime. In Figure D.9, we illustrate $F_c(q,t)$ for our bulk Ni crystal at T = 1950 K where we see that this quantity for our heated crystal does not decay to zero at long times.

The so-called Boson peak is another universal [254] feature of GF materials whose even qualitative interpretation remains controversial. Many authors attribute this feature in GF liquids to the existence of relatively stiff hypothetical nanoscale elastic heterogeneities having a log-normal size polydispersity [255, 256]. On the other hand, other authors have attributed the Boson peak to collective permutational atomic motions in the material [255, 257], In particular, Shintani and Tanaka [258] found evidence that the Boson peak involves "transverse collective vibrational motions" associated with "soft regions" in the disordered material and Chen et al. [259], Manning and Liu 260 and Tan et al. [261] have

all argued based on both experimental and simulation evidence that the Boson peak has its origin "soft spots" in glasses where some sort of correlated particle rearrangements are concentrated. Recent particle tracking measurements on colloidal fluids [262] have indicated that the Boson peak can be associated with hierarchical collective swirling particle motions that are reminiscent of Feymann" s conception of "rotons" in terms a vortex-like local stirring motion in the fluid [263–265] and of vortex motions often directly observed in dusty plasmas [200–202, 208, 266]. We certainly see swirling collective atomic motion in our crystal approaching bulk melting so do these heated crystals exhibit a Boson peak? The answer to this question should contribute to the ongoing intense discussion to the meaning of this scattering feature.

To address this question, we first calculate the power spectrum of the velocity autocorrelation function $VAF(t) \equiv < v(t)v(0) >$, which encodes basic information about the density of states of the material. In particular, the cosine transform (power spectrum) of $< v(t)v(0) > / < v(0)^2 >$ determines the vibrational density of states $g(\omega)$ [267]. Glass-forming liquids have an excess density of states at relatively low frequencies relative to crystals as one of their most distinctive features and $g(\omega)$ normalized by the Debye vibrational density of states $g_D(\omega)$, scaling as ω^2 for a crystal, normally exhibits a Boson peak" [268–271]. The $VAF(t)$ is related to the mean square particle displacement $< r^2 >$ by differentiation, $d^2 < r^2 > /dt^2 \propto VAF(t)$ and this is a good way of determining $VAF(t)$ if we have smooth data on a fine time mesh. We calculate the cosine transform of $VAF(t)$ of the Ni atoms in the bulk Ni crystal to obtain,

$$g(\omega) \sim \sum VAF(t) cos(2\pi\omega t)\Delta t. \tag{D.6}$$

Here $g(\omega)$ is divided by ω^2 to obtain the reduced density of states, $g(\omega)/\omega^2$. We see from Fig. D.10 that a heated bulk crystal does indeed exhibit a Boson peak, as in the case of glassy materials [268–272]. The observation of the Boson peak in our data supports its interpretation in terms of collective atomic rearrangement motions within the material rather than nanoscale stiff regions. We note that crystalline materials at low T do not normally exhibit a Boson peak, but lattice damage induced by fast neutron radiation [224] or material deformation [273] can induce this scattering feature to arise. Neutron scattering

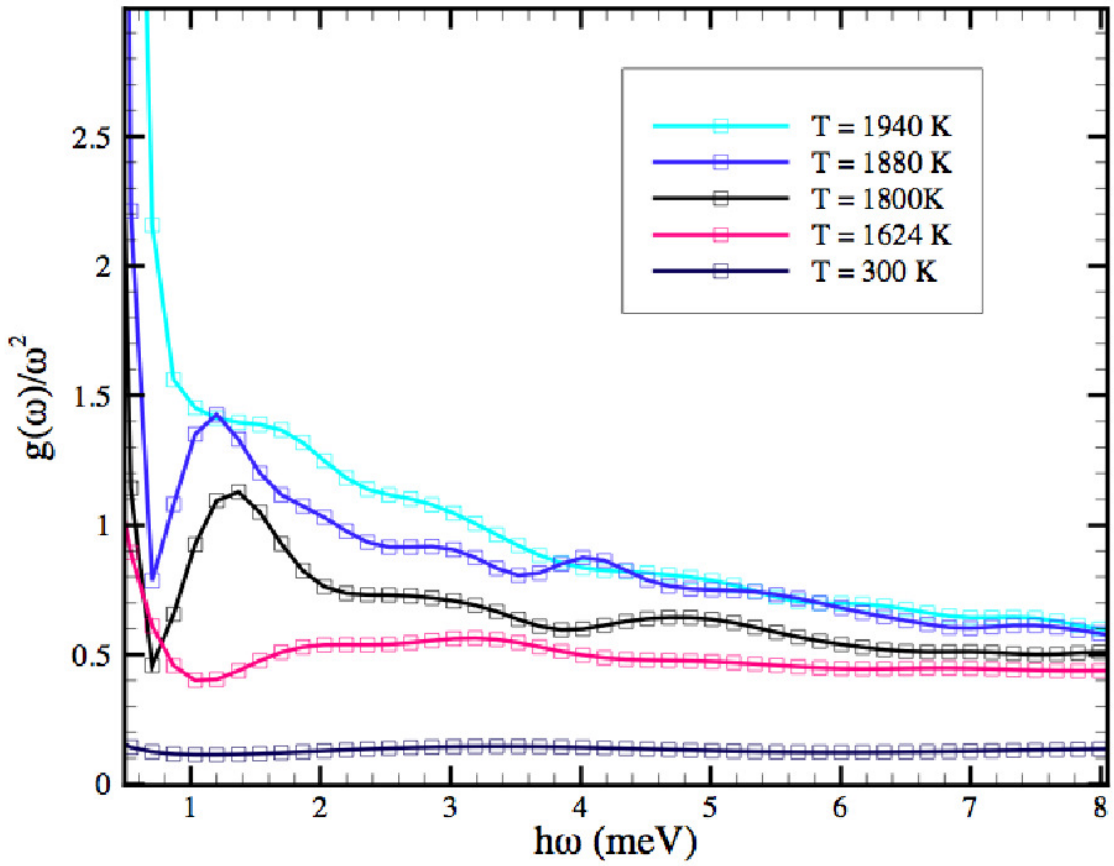

Figure D.10: Reduced vibrational density of states and Boson peak for Bulk Ni at five different temperatures. The variation of the position of the Boson peak with T is hard to resolve in our simulations, but is clear that the peak position blue shifts to smaller frequencies upon going from 1800 K to 1880 K, a trend that is opposite to the trend found in GF liquids [12, 13]. Our impression from the limited data, however, is that the trend is non-monotonic when a larger T range is considered, as in the string length L data in Fig. D.5.

measurements also show that simply heating crystals towards their melting point, as in our present simulations, can give rise to a Boson like peak feature [269, 274–277], consistent with our simulations.

D.4.5 String-like Collective Motion and Defects?

Another basic issue that we address by simulation is the suggestion that the strings have some relation to the formation of point defects within the melting crystal [278]. Granato and coworkers [230, 279] have made convincing arguments of the significance of interstitial defects in relation to melting by virtue of their relatively low activation energy in comparison

to dislocations, disclinations, stacking faults, etc [155, 279]. The fundamental significance of these defects in relation to bulk melting has also been emphasized by Stillinger and Weber [14]. Many aspects of crystals [14, 155, 279, 280] can indeed be rationalized by thermally excited interstitial defects, including the Boson peak phenomenon in irradiated crystals [155, 261, 262]. Nordlund et al. [230] have gone so far as to advocate the identification of "strings" of collective atomic motion with chains of interstitial defects, which is a testable proposition. While the arguments of Granato and coworkers are conjectural, it is certainly plausible that disclinations play a significant role in the initiation of the collective string-like atomic motion. We next explore this possibility.

To identify whether string-like collective motion can be unambiguously identified or associated with some kind of point defects or dislocation related structures, we performed energy quenches of our superheated crystals at T = 1840 K, 1880 K, 1920 K and 1950 K and simply examined the nature of the defect structures that resulted. At each T, we sampled at least 10 independent atomic configurations (spaced by 200 ps) for energy quench. The defect concentration was then averaged over these independent simulations so that defects were not introduced artificially but instead arose naturally from thermal fluctuations within the material. The result of this analysis surprised us since we had intuitively anticipated seeing thermally generated GBs. Instead, as shown in Fig. D.11, the defects are simple point defects such as vacancies and interstitials, in line with the reasoning of Granato and coworkers [155, 230, 279] (A vacancy is just a vacant lattice site and an interstitial is an atom that occupies an off-lattice position within the crystal, often in the form of a "split interstitial" atomic pair located near a lattice position.).

We see that the density of interstitial defects (Fig. D.12) increases with heating, but their concentration remains small and their positions are relatively uncorrelated. Recent studies of inherent structures in crystals undergoing bulk or homogeneous melting have come to a similar conclusion [281]. We must conclude that the defect structures in the superheated crystal do not appear to be particularly interesting at first glance; they certainly do not suggest at first an obvious origin for the string-like collective motion described above.

A striking aspect of our quantitative estimation of the self-interstitial concentration as a function of T in Figure D.12 is the rather small concentration of these defects over a wide T range below T_m^h. However, these defects are pregnant in their capacity in creating mobile particles in the crystal and to establish this fact we compare the interstitial concentration to

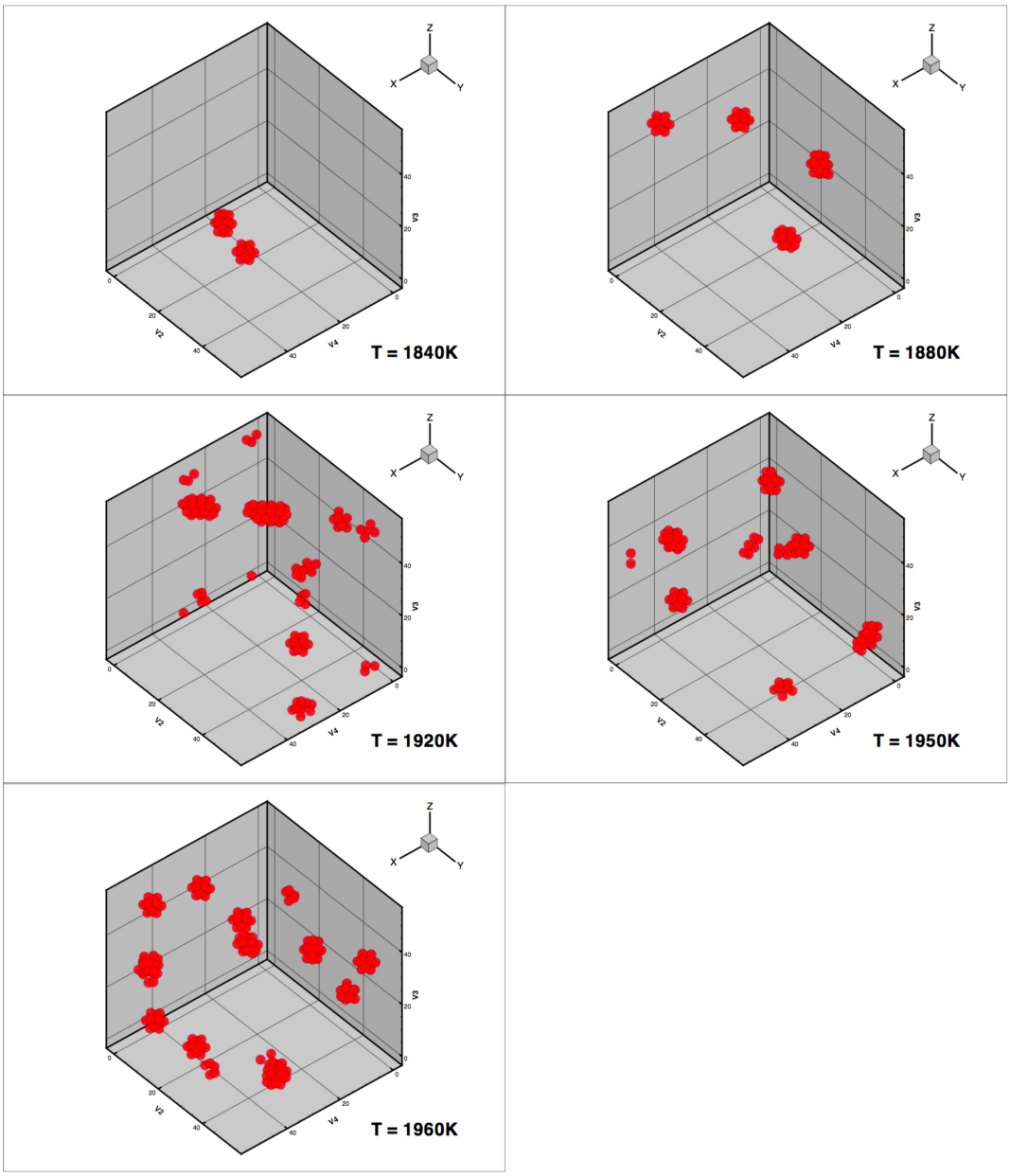

Figure D.11: Defects exhibited in Ni crystal following energy minimization at different temperatures. Only non-fcc atoms are displayed in the figure for clarity. The defects observed correspond to simple interstitials. The density of these defects does increase with heating, but their concentration is rather small and their positions seem to be relatively uncorrelated in space. Stillinger and Weber [14] have provided insightful visualizations and discussion of this type of defect.

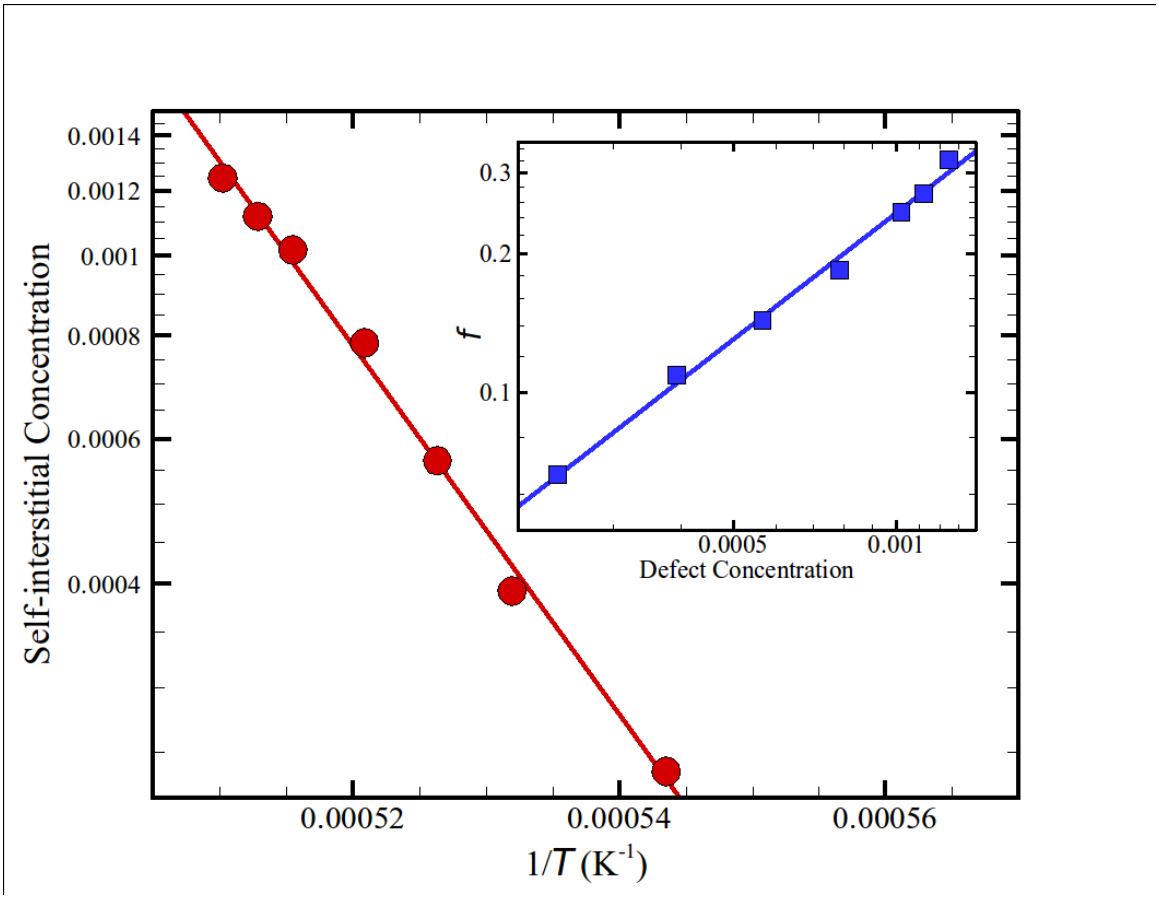

Figure D.12: The self-interstitial concentration as a function of T. Inset shows the correlation between self-interstitial and Lindemann particle concentrations at different T.

the Lindemann particle concentration indicated in Fig. D.8. We find that these concentrations are proportional to a high approximation and we then see that each interstitial defect creates about a 20-fold increase of relative number of Lindemann particles. The proliferation of interstitial defects and mobile particles by the Lindemann criterion are evidently directly related.

The slope of the Arrhenius curve in Fig. D.12 allows us to estimate the activation energy E_{int} for self-interstitial formation under superheating conditions, $E_{int} \approx 4.5$ eV. The concentration of these defects near the homogeneous melting temperature is extrapolated to be a fraction of a percent, i.e., 0.13 %. (Every vacancy created must be associated with a self-interstitial and these may be considered a "Frenkel pair" so that the self-interstitial concentration equals the vacancy concentration). Granato et al. [155, 279] nd Feynman [263–265] have correspondingly emphasized that while the concentration of these defects may be small, they can nonetheless have a potent effect on the shear modulus of the crystal. Convinced of the importance of these defects by Granato" s arguments and the observations above, we inquire further into how these defects might be related to string-like collective motion.

So how might self-interstitial defects relate to the strings discussed above? In order to probe this question quantitatively, we consider a typical string event at $T = 1840$ K and analyze energy and displacement fluctuations over the course of the string lifetime, t^*. Figure D.13a illustrates the specific string under consideration, corresponding to our superheated Ni crystal at T = 1840 K. In Figure D.13b, we examine the potential energy for Ni atoms within this representative string and Fig. D.13c shows particle displacements $\Delta r/r_0$ for these same string atoms. The potential energy is taken the difference between the average energy over 1 ps and the average energy over the string lifetime $t^* = 250$ ps for each atom in string. The atomic displacements are taken with respect to its initial position, rescaled by the distance to its neighbor along the string; its value can then be positive or negative depending on its relative position to the neighbor. The y-axis denotes time in units of the caging time (same time for which $< u^2 >$ is defined). Plots of this kind are conventional in studies of energy localization in one-dimensional chains of non-linear oscillators where they are termed "hypsometric plots" [282–286]. The color map legends of these figures define the magnitude of the potential energy and particle displacement jumps. These figures show the local energy variation in the string along with the displacement of the atoms

along the string [See Fig. D.13c]. This process is signaled by a propagating wave of energy jump events that are shown as small red segments in Fig. D.13b. After having displaced, the particle positions then become relatively stable. Figures D.13b and D.13c then show that energy of each atom becomes relatively large just before the diffusive jump and this transient energy rise is somehow related to the energy barrier for jumping. What is driving these local potential energy changes and propagating atomic motion?

We next chose an atomic configuration just before the jump of atom 1 occurs and then perform an energy quench to see if there is a defect in the neighborhood of this position. After energy minimization, we find two self-interstitial defects in this quench: one at atom 1, described above, and the other located next to a vacancy that atom 1 is about to occupy. These observations clearly suggest that interstitial defect pairs serve as *initiators* of string-like cooperative motion in our heated crystal. If we continue the quench process, the interstitial defects are observed to propagate along the string, i.e., each atom involved in string-like motion transiently becomes an interstitial as these excitations move down the string, resulting in a net displacement of a whole group of atoms. Evidently, the interstitial propagates down the string in the form of a *soliton*, driving atomic successive displacements within the string. A chain-like nearest neighbor atomic motion driven by interstitial defect movement was previously observed by Lee and Li [287] in connection with incipient bulk melting where it was further recognized that chain closure in the form of rings results from interstitial-vacancy annihilation. However, the connection of this motion to the collective motion found in GF liquids was not appreciated in this early work and the geometrical properties of this collective motion were not examined in any detail.

We then see that former suggestions that string-like motion can be equated with interstitial defect chains and GBs [278] are untenable. Nonetheless, the interstitial defects play a significant role in initiating the collective motion that we observe in association with bulk melting. The appearance of soliton-like excitations driving particle displacements in our simulations first surprised us, but the proliferation solitonic excitations has been predicted for melting in polymer crystals [288] so this phenomenon might have been anticipated.

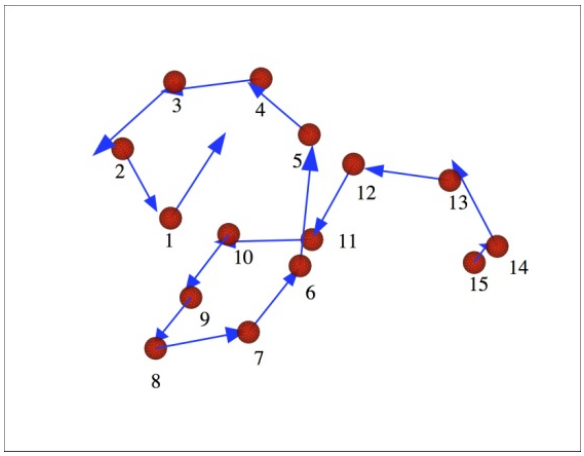

(a)

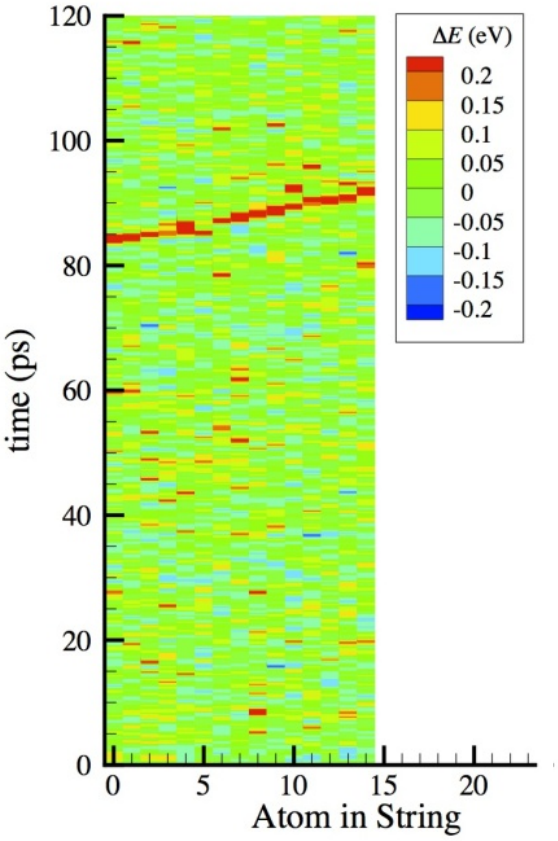

(b)

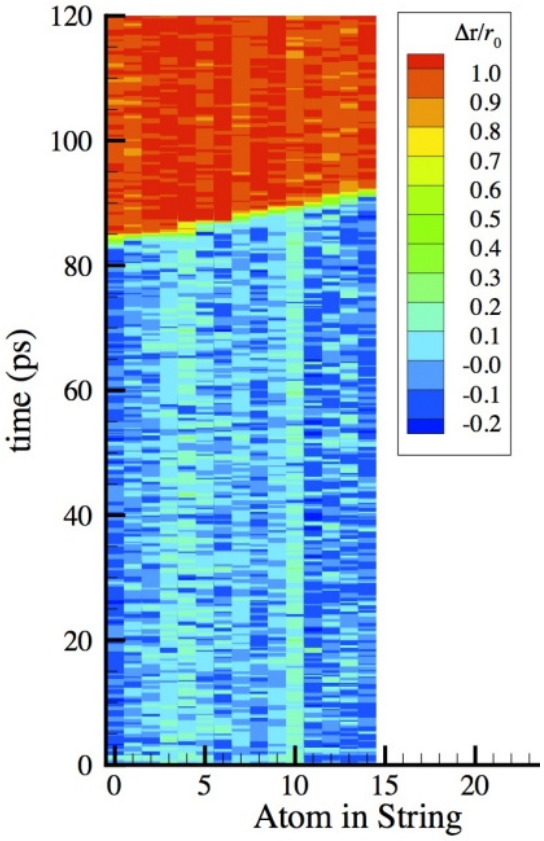

(c)

Figure D.13: (a) A typical string with a member of 15 atoms at $T = 1840$ K. (b) Potential energy fluctuations of atom that is involved in collective string-like motion over the timescale of 120 ps (b) Relative displacements ($\Delta r/r_0$) fluctuation of atoms within string. .

D.5 Conclusions

The emergence of the solid state from the liquid state upon cooling and the liquid state from the solid state upon heating are both cooperative phenomena characterized by collective particle motions that play an active role in the conversion of one state to the other and that affect the dynamics of materials near their solidification or "softening" points. Previous work has extensively characterized the collective motion in "supercooled" or glass-forming liquids [183–185] and shown the significance of string-like collective motion for understanding the strong temperature dependence of the transport properties of these complex fluids [289] and interfacial dynamics of grain boundaries in polycrystalline materials [186] and the interfacial dynamics of nanoparticles [142]. Simulation has also shown that the dynamics of both melting and freezing of nanoparticles involves the propagation of ordering and disordering interfaces at which collective atomic motion is prevalent, taking a form similar to the collective motions of glass-forming liquids. Although we have focused on Ni nanoparticles, we expect this phenomenon to arise in almost any type of nanoparticle and to arise in the heterogeneous melting and freezing of any type of crystal. We can also expect that the same type of cooperative motion to be important for understanding the physical aging properties of condensed materials and changes of the relaxation times and transport properties in applied fields such as temperature or applied stresses or physical confinement effects. We have already found cooperative atomic motion to be modified for the grain boundary mobility of polycrystalline Ni subjected to applied stresses and the relaxation dynamics of thin glass-forming polymer films [185], but there are many other studies to be made to understand how perturbations of materials can be used to modify their properties based on this effect. Simulations have also suggested that the polycrystalline nature of many commonly encountered crystallizing materials, such as semi-crystalline polymers, is largely influenced by the collective dynamics of glass-formation [188] so that both the dynamics and the structural form of diverse materials is predicted to reflect the collective dynamics operating during the material solidification process, a behavior that can be controlled through the judicious use of molecular [185, 234, 290] and nanoparticle [289] additives that modulate the cooperative molecular motion depending on the geometrical properties of the additive and it interaction with the fluid. Recent simulation [190] has further shown that the occurrence of crystal nucleation in simulated silica can be strongly influenced by dynamic heterogeneity of the glass-forming liquids, an effect that probably has general significance in understanding the propensity of liquids to crystallize rather than form glasses at high degrees of cooling.

The present work focuses on string-like cooperative atomic motion that occurs in connection with homogeneous melting of "bulk" crystals under isothermal conditions where there are no interfaces (boundaries of the materials or defects within the material) to nucleate the melting process. As in our previous studies of ordering and disordering in condensed materials, we find that the atomic dynamics within a crystal approaching its melting point is highly collective and the cooperative atomic motion greatly facilitates molecular diffusion in the crystal before it melts at the homogeneous melting temperature T_m^h. We are again impressed by the extent to which string-like collective motion pervades the dynamics of condensed materials.

Our simulations provide a novel view of melting in which a small concentration of interstitial defect exert a powerful effect on the crystal stability through their initiation of collective particle motions that ultimately lead to a breakdown of lattice order and these defects drive significant atomic transport at temperatures below T_m^h in the form of a collective atomic permutational motion. The crystal integrity remains preserved for permutational atomic motions in the form of rings exchanges, but at higher temperatures we find a topological transition in these exchange motions into linear catenations of particle exchange events similar in geometrical form to glass-forming liquids. These motions evidently give rise to a local symmetry breaking of the local lattice structure that the crystal cannot sustain. We find that this collective atomic motion driving transport and melting is driven by propagating interstitial defect excitations that move down the chain of atoms that move in string-like coordination. The defects are not static entities under dynamic conditions of elevated temperatures or material loading. They exhibit a rich non-linear dynamics that are not captured in static defect models of melting.

The fact that permutational collective motion increases the rate of diffusion in heated crystals rather than decreasing the rate of diffusion in cooled liquids, as anticipated by Zener [291], underscores the different influence of collective motion on ordering and disordering process involving the emergence and loss of rigidity. We do not fully understand this striking difference, but we can appreciate that the emergence of a disordered solid state from a fluid involves the clustering of particles into fractal polydisperse, persistent and locally well-packed particles dynamic structures that must play an essential role in the viscoelastic properties of these complex fluids. This immobile particle clustering phenomenon

presumably does not arise in crystals below their melting point (unless they are highly damaged by applied stresses or radiation) so the study of superheating of crystals provides an opportunity to study which general properties of glass-formation derive from the mobile particles exhibiting collective string-like motion or for the immobile particles that are mainly responsible for the growth of the viscosity of cooled fluids approaching their glass transition. To address this issue, we examined three basic phenomena in our simulations of the melting of crystalline Ni crystals that arise universally in all glass-forming liquids - the occurrence of stretched exponential relaxation, a decoupling power law relation between the translational diffusion coefficient and the structural relaxation time of the cooled liquid and the occurrence of the Boson peak. None of these phenomena has a generally accepted interpretation in glass forming liquids, but models by Douglas and coworkers [233, 243] have indicated that both decoupling and stretched exponential relaxation in glass-forming liquids derive from structural heterogeneity taking the form of immobile particle clusters that do not exist in glass-forming liquids so that these phenomena are then expected to essentially not exist in heated crystals, despite the highly prevalent string-like collective motion that the simulations indicate is occurring in these systems and the strong resemblance of this collective motion that occurring in glass-forming liquids. Strikingly we find no decoupling or any appreciable stretching of the intermediate scattering function governing structural relaxation in the dynamically heterogeneous regime of our heated crystal approaching its melting point. Decoupling and stretched exponential relaxation in glasses are then suggested strongly to have their origin in the clustering of immobile particles and these phenomena have no general direct relation to the emergence of collective motion. The Boson peak has been interpreted both in terms of the emergence of relative stiff and soft nanoscale regions in regions in glass-forming liquids so that the investigation of the Boson peak in our heated Ni crystal also sheds light on the physical interpretation of this ubiquitous, but poorly understood phenomenon. We find a well-defined Boson peak in our simulations of bulk Ni in the superheated regime and we can infer that this phenomenon is consistent with models that attribute it to relatively high frequency and mobile particles exhibiting small-scale cooperative atomic motion. The study of superheated crystals then provides a laboratory for investigating essential aspects of glass-forming liquids since these materials exhibit a simpler type of "dynamic heterogeneity" than supercooled liquids.

As mentioned in the introduction, the general tendency for crystals to initiate their melting through heterogeneous nucleation at their boundaries due to the relatively large average

atomic displacements at these boundaries is the usual explanation of why it's more difficult to superheat crystals than it is to supercool liquids below their equilibrium melting temperature. It is normally rather difficult to perform measurements on real superheated crystals and homogeneous melting is thought to occur only under rather special circumstances. Consequently, our results on this type of melting might appear to have only academic interest.

Actually, there is an important class of crystalline materials that exhibit properties strikingly similar to those found in our simulations of heated Ni crystals and these materials, moreover, have great current interest in materials applications in the crucial field of energy storage. In particular, many crystals having a fluorite crystallographic structure exhibit extraordinarily high electrical conductivities [292, 293] as approaching values of ionic melts! This makes these materials extremely attractive as solid electrolyte materials for batteries, etc. [294] Apart from the superficial similarity of a high atomic mobility in these materials to our Ni crystal simulations when each type of crystal is heated, recent simulations [292] on PbF2, CaF2 and other superionic crystalline materials indicate that there is no stretching of intermediate scattering function , i.e., $\beta = 1$, and no decoupling between the ion diffusion coefficient and the electrical conductivity. Moreover, there is strong experimental and computational evidence for the role of interstitial defect formation, and associated collective motion, in these materials as well. All of these observations on superionic crystals accord with our simulations on heated Ni crystals with boundary effects removed so that homogeneous melting is prevalent. We expect that a detailed examination of previous simulations on superionic materials will reveal that we are actually dealing with a kind of homogeneous melting phenomenon.

One of the singular findings of our simulations on homogeneous melting in Ni is peculiar observation of a non-monotonic variation of the string length L with temperature, a feature that we have frankly never seen before in glass-forming liquids. The phenomenon is so unusual that we, and of course our reviewers, were naturally concerned that this might be a computational artifact due to some kind of non-equilibrium aging effect. However, we do not see any obvious evidence of aging effects in our simulations under the conditions investigated so we find it difficult to explain away this phenomenon as an artifact and we naturally wonder if anything like this has ever been seen experimentally? Given our suggestion that superionic crystals might be a system exhibiting incipient homogeneous melting, it is then natural to turn to the experimental literature on transport in superionic crystals

to see if this "weird" behavior has observed in these materials.

In glass-forming liquids, there is simulation evidence in the case of model polymer glass-forming materials [289, 295] indicating that the average scale of collective motion (string length L) is proportional to the activation energy governing structural relaxation so that large changes in transport and cooled liquids with temperature can be directly and transparently understood from a variation in the context of collective motion in these materials. In particular, these simulations support the identification of the strings with the abstract "cooperatively rearranging regions" of Adam and Gibbs. [187] Recent simulation and experimental studies have also found remarkable similarities between the temperature dependence of transport properties in superionic crystals and glass-forming materials [292] and, in particular, the Adam-Gibbs (AG) relation was found to *quantitatively* describe both the ion-diffusivity and electrical conductivity of simulated PbF2 and CaF2 super-ionic crystalline materials where the configurational entropy of the AG theory S_c was estimated from a determination of the difference between the material entropy, minus its value at the super-ionic transition temperature defining the onset of appreciable ion conductivity. The identification of the strings with the cooperative rearranging regions of AG in the context of heated crystals, the applicability of AG to heated crystal relaxation data, along with the hypothesis that such crystals might be identified with super-ionic materials, imply that the activation energy for the conductivity of super-ionic materials should exhibit the same peculiar maximum as the string length in our simulations at a temperature well below the melting temperature. Careful conductivity experiments [296] on a range of superionic crystals have indeed indicated the general occurrence of an activation energy maximum of this kind for a wide range of superionic crystalline materials. The maximum that we observe in the string length with temperature is broader than in many of the super-ionic crystalline material observations, but the strength of this feature is highly variable experimentally [292, 296] and, correspondingly, the variable "sharpness" of this activation energy peak, and in the specific heat, has been termed "fragility" by analogy with the use of this term in glass-forming materials [292]. By this classification scheme, our Ni crystal system is a relatively "strong" crystalline material (experimentally, PbF2 is much more fragile than CaF2 [292]). Finally, we mention that there is much neuron scattering evidence that the unusual transport properties in superionic materials are associated with interstitial defect generation [297, 298], as we have found for superheated Ni crystal. It is also notable that these crystalline materials exhibit a Boson peak [16], as in our simulations. All these striking

correspondences between our simulation findings for homogeneous melting of Ni crystals in bulk and the phenomenology of superionic crystals support our contention that superionic crystals are superheated crystals, or these materials are at least physically very much like them. The odd properties of superionic crystals have been since the early studies of them by Faraday [154, 163], but the extreme promise of these materials for applications relating to energy storage for electric vehicles, and wind and solar energy storage, is only recently becoming appreciated [294]. The further elucidation of the dynamics of these materials using the methods of the present paper should aid in the practical development of these promising materials.

Appendix E

String-like Cooperative Motion in Homogeneous Melting - Supplementary Material

The mobile atoms are identified as these particles by a threshold atomic displacement condition, $0.6r_0 < |\mathbf{r}_i(\Delta t) - \mathbf{r}_i(0)| < 1.2r_0$, involving the average bulk crystal interatomic spacing, r_0. While changing the cut-off value alters the number of mobile particles, the statistical properties of the size distribution are insensitive to this choice. We then define a 'mobile particle cluster' as the group of neighboring particles having a separation less than 1.2 times the interatomic spacing, r_0. The power-law cluster size distribution for the mobile particles in Fig. E.4 is characteristic of branched equilibrium polymers and the distribution of the mass of the mobile particles exhibits a similar exponent as observed before for heated crystals of Cu and model glass-forming liquids [17] (See Nordlund et al. [230]).

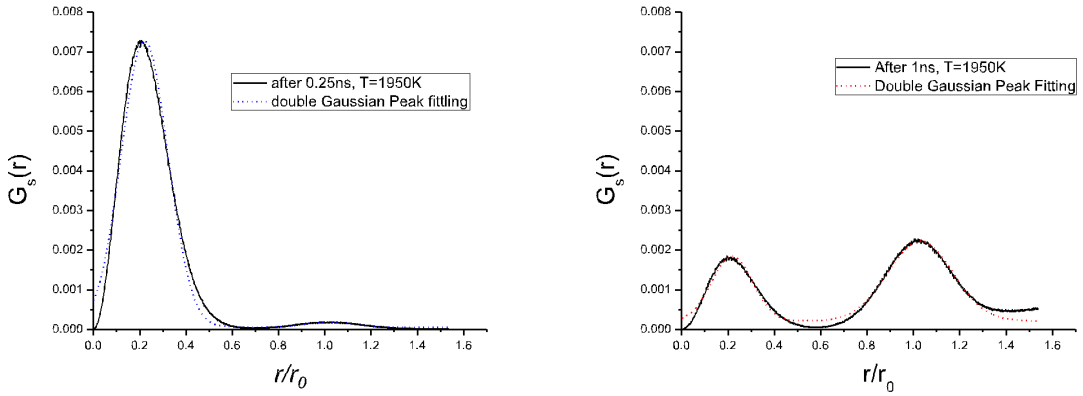

(a) (b)

Figure E.1: an Hove function $G_s(r,t)$ after a short time (0.25 ns) and longer time (1 ns) exhibiting a transformation from particle localization to a displacement to a distance about an interparticle distance away. A minimum in this curve at the reduced scale ≈ 0.6 defines a natural cut-off for defining the mobile particles.

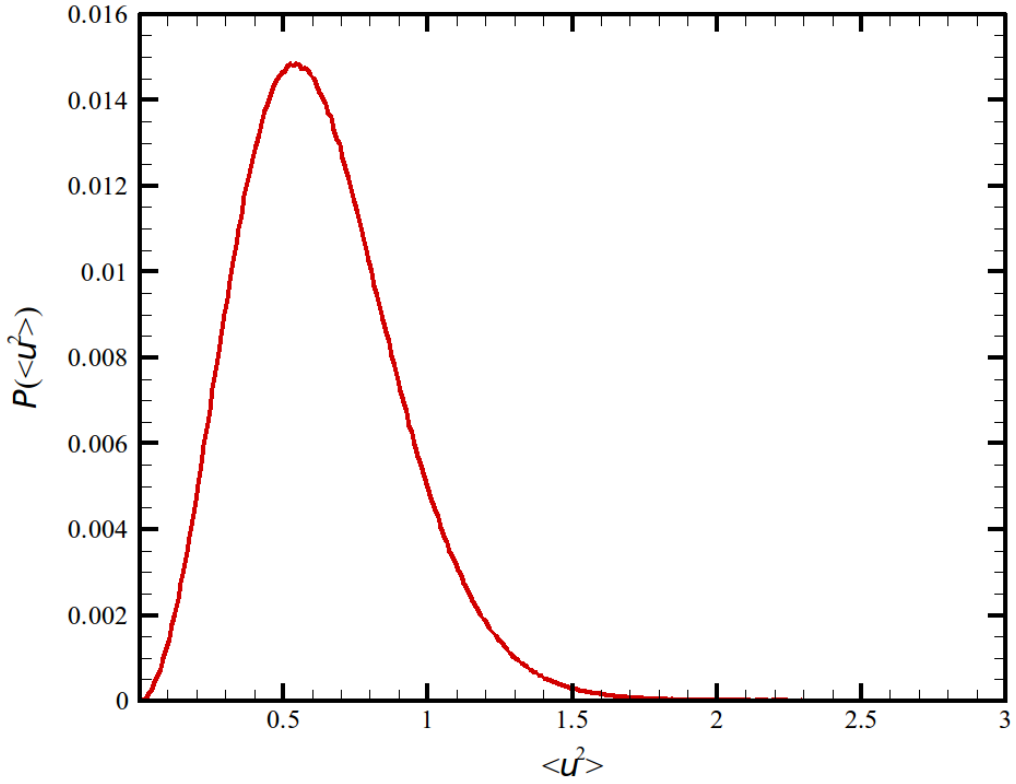

Figure E.2: The distribution of $< u^2 >$ at T = 1950 K. We note that the distribution of $< u^2 >$ does not exhibit any clear bimodal character, despite the clear multi-modal nature of $G_s(r,t)$ in Fig. E.1.

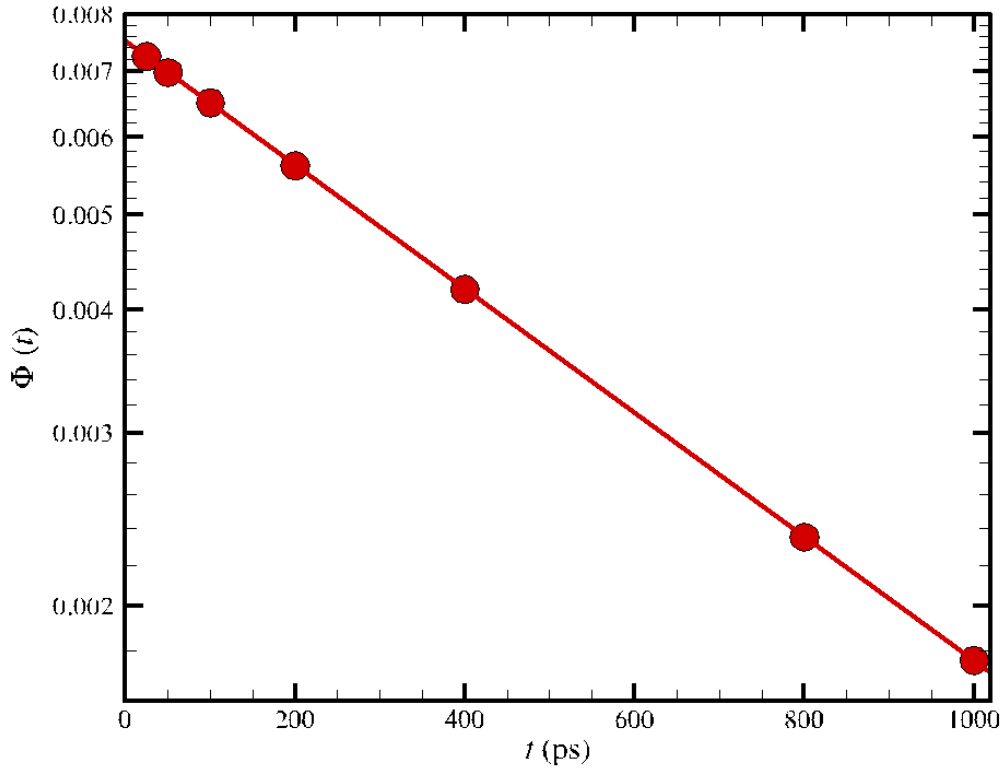

Figure E.3: Decay first peak height of $G_s(r,t)$ in Fig. E.1. The first peak magnitude at T = 1950 K, denoted $\Phi(t)$, decays an exponential function, $\Phi(t) = exp(-t/\tau)$, to a good approximation. The time constant τ fitted here is $\approx$ 700 ps, which is comparable to the structural relaxation time τ_s obtained from the self-intermediate scattering function ($\approx$ 800 ps; See Fig. D.9 in Appendix D). The structural relaxation time then reflects the persistence time of the particles in the immobile state, as in glass-forming liquids [10].

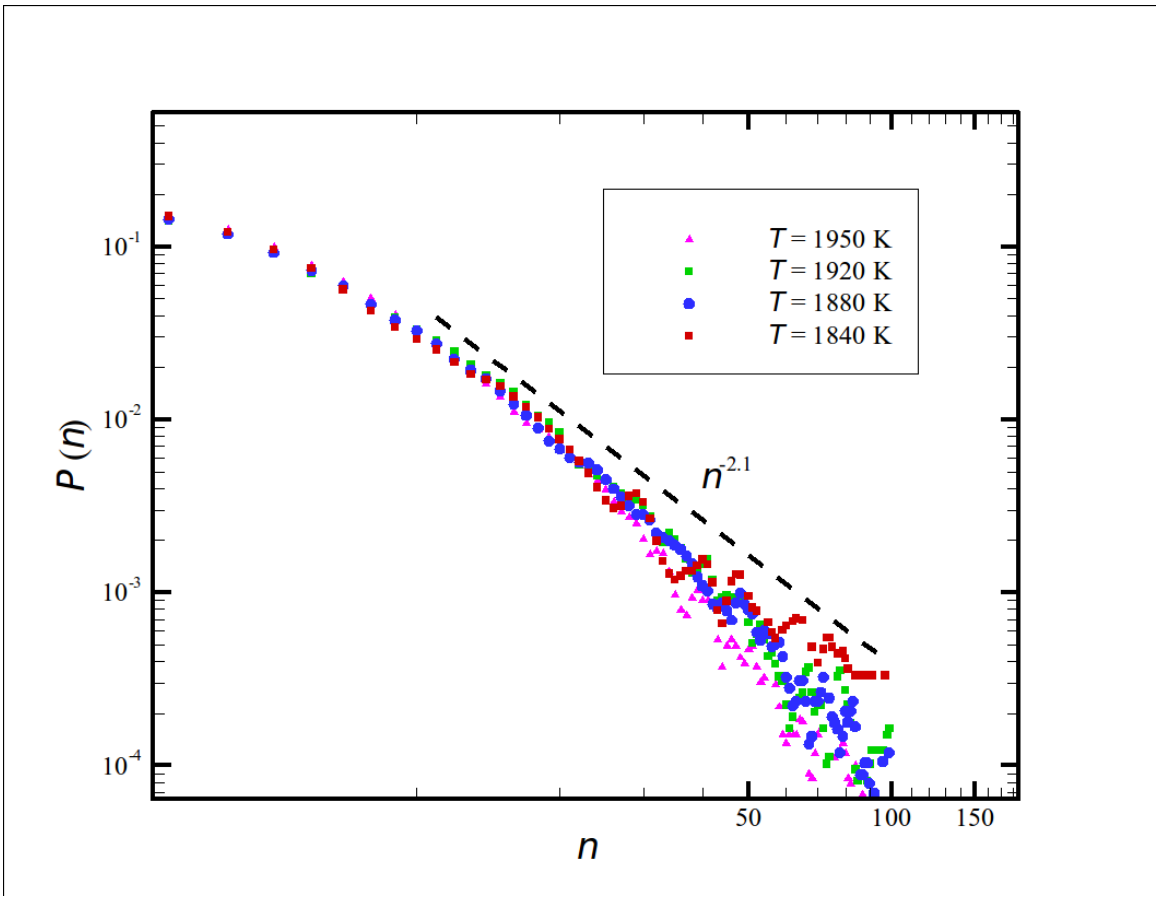

Figure E.4: The distribution of particle cluster sizes $P(n)$ for mobile atoms at four T . The inset shows the average cluster size for mobile particles as a function of time interval at different T.

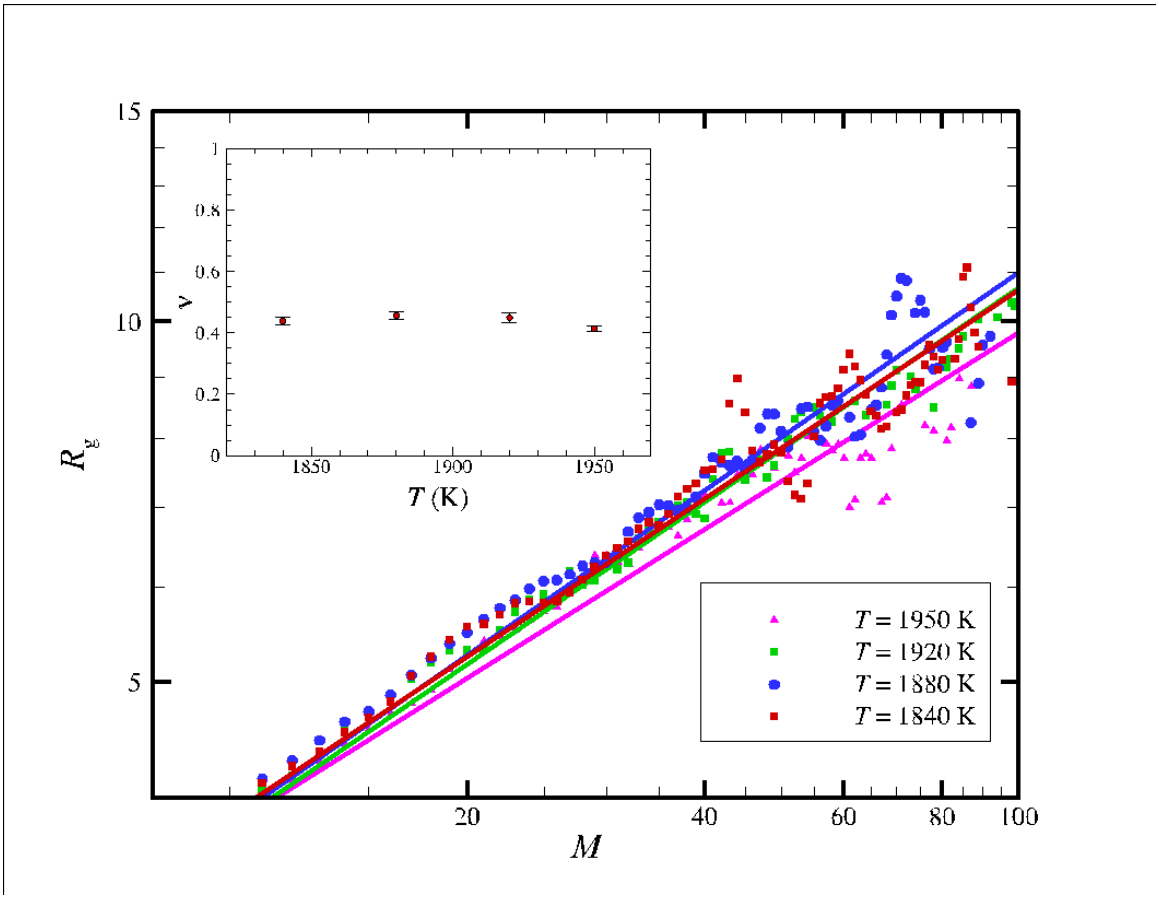

Figure E.5: Scaling of mobile particle radius of gyration R_g with its average mass M, $R_g \sim M^\nu$ where the inset shows $\nu = 1/d_f$ as a function of T. The exponent ν is about 0.4, corresponding to a fractal dimension df $d_f \approx 2.5$, consistent with branched equilibrium polymers with screened excluded volume interactions, i.e., percolation clusters [15, 16]. Recent simulation estimates of the mobile particles in a model polymer glass-forming liquid also indicate a fractal dimension of these clusters near 2.5 [17].